Dissertation
submitted to the
Combined Faculties for the Natural Sciences and for Mathematics
of the Ruperto-Carola University of Heidelberg, Germany
for the degree of
Doctor of Natural Sciences

Put forward by

Diplom-physicist:	Rolf Gerd Kuiper
Born in:	Haselünne, Niedersachsen, Germany
Oral examination:	December, 21st 2009

Modeling the formation of massive stars

Referees: Prof. Dr. Thomas Henning
Priv.-Doz. Hubert Klahr

To Svenja

Numerische Simulationen der Entstehung massereicher Sterne

Ich untersuche das sogenannte Strahlungsdruckproblem in der Entstehung massereicher Sterne mittels eines neu entwickelten, frequenzabhängigen Strahlungstransportverfahrens für hydrodynamische Simulationen. Die Auswirkungen des Strahlungsdrucks in Abhängigkeit der Beschaffenheit der stellaren Umgebung werden in ein-, zwei- sowie drei-dimensionalen Simulationen des Kollapses massereicher Molekülwolkenkerne ergründet. Im Gegensatz zu früheren Studien wird dabei eine weit überlegene Technik frequenzabhängiger Einstrahlung berücksichtigt. Dies ermöglicht eine räumliche Auflösung der näheren Umgebung des entstehenden Sterns von $(1.27\ \mathrm{AU})^3$ und die Berechnung der Entwicklung des Systems über mehrere hunderttausend Jahre. Die Effizienz des Strahlungstransportverfahrens erlaubt darüberhinaus erstmalig eine breit angelegte Studie numerischer Parameter sowie unterschiedlicher Anfangsbedingungen. Die Simulationen zeigen, dass es für eine korrekte Berechnung der stellaren Strahlungsrückwirkung unerlässlich ist, die sogenannte Staubkondensationsfront in das Rechengebiet miteinzubeziehen. In früheren Rechnungen, die dies nicht berücksichtigt haben, führt der dadurch künstlich erhöhte Strahlungsdruck zu einem unphysikalischen, abrupten Ende der Akkretionsphase. Meine Ergebnisse weisen dagegen den grundlegenden Unterschied auf, dass die um den Proto-Stern entstehende, massereiche Akkretionsscheibe den Strahlungsfluss in Richtung der optisch dünnen Atmosphäre umlenkt. Der Drehmomenttransport einer weit innen liegenden Gravitationsinstabilität ermöglicht die Aufrechterhaltung des Akkretionsstromes. Die Masse des so entstehenden Sterns wächst deutlich über die Grenzen hinaus, die in bisherigen wissenschaftlichen Untersuchungen gefunden wurden.

Modeling the formation of massive stars

I investigate the radiation pressure problem in the formation of massive stars using a newly developed frequency dependent radiation transport module for three-dimensional hydrodynamics simulations. The nature of the radiative impact depending on the morphology of the stellar environment is examined in one-, two-, and three-dimensional monolithic collapse calculations of massive pre-stellar cores. Contrary to previous research, a highly superior frequency dependent stellar feedback is considered, the vicinity of the forming star is resolved down to 1.27 AU, and the evolution is computed for a factor of ten longer. For the first time a broad survey of the parameter space is possible. The simulations demonstrate the need of including the dust condensation front to compute the radiative feedback correctly. Earlier calculations, which ignore these physics, lead to an artificial truncation of the accretion phase. The most fundamental result is that the formation of a massive accretion disk in slowly rotating cores bypasses the radiative flux through the optically thin atmosphere, enabling steady accretion. A revealed close-by gravitational instability in the disk drives a sufficiently high accretion rate to overcome the residual stellar radiation feedback. This mechanisms allow the star to grow far beyond any limit found in earlier calculations.

Contents

Abstract **7**

Contents **x**

Preface **11**

1 Introduction **13**
1.1 From molecular clouds to clumps to cores to massive stars - A journey through time and space . . . 14
1.2 The link between low-mass and high-mass star formation . . . 15
1.3 The radiation pressure problem in the formation of massive stars . . . 18
1.4 Self-gravitating radiation hydrodynamics in the formation of massive stars . . . 20
1.5 The approach to the problem . . . 21

2 Physics of the formation of massive stars **23**
2.1 Discretization of the computational domain . . . 24
2.2 Hydrodynamics . . . 26
2.3 Viscosity . . . 27
2.4 Gravity . . . 28
2.4.1 Central gravity and Poisson equation . . . 28
2.4.2 Tests of the Poisson solver . . . 29
2.5 Radiation transport . . . 39
2.5.1 Theory and numerics of the approximate radiation transport scheme . . . 40
2.5.2 Frequency dependent test of the approximate radiation transport . . . 46
2.5.3 Parallel performance tests of the approximate radiation transport module . . . 58
2.5.4 Radiative hydrodynamics shock tests . . . 60
2.6 Dust model . . . 64
2.7 Stellar evolution model . . . 66

3 Basic analytical solutions and concepts **69**
3.1 Circumstellar disks in equilibrium . . . 70
3.1.1 Classical keplerian motion . . . 71
3.1.2 Orbital motion in 'hot' disks . . . 71
3.1.3 Vertical stratification . . . 72
3.2 Free fall time . . . 73

3.3 Centrifugal radius . . . 75
3.4 Generalized Eddington limit . . . 77
3.5 Dust condensation radius . . . 79

4 Simulations of the formation of massive stars 81
4.1 Default initial conditions of the massive pre-stellar cores . . . 86
4.2 Spherically symmetric pre-stellar cores . . . 87
4.2.1 Convergence simulations . . . 87
4.2.2 The influence of the size of the sink cell . . . 89
4.2.3 Parameter scan of the initial pre-stellar core mass: The upper mass limit of spherically symmetric accretion . . . 91
4.2.4 Epochs and dynamics of the collapse of spherically symmetric pre-stellar cores . . . 94
4.3 Rotating axially and midplane symmetric pre-stellar cores . . . 101
4.3.1 Convergence simulations . . . 101
4.3.2 The influence of the size of the sink cell: Resolving the dust condensation front . . . 103
4.3.3 Parameter scan of the α-viscosity . . . 107
4.3.4 Comparison to Yorke & Sonnhalter (2002) . . . 109
4.3.5 Parameter scan of the initial pre-stellar core mass: Breaking through the upper mass limit of spherically symmetric accretion . . . 111
4.3.6 Epochs and dynamics of the collapse of rotating axially and midplane symmetric pre-stellar cores . . . 117
4.4 Three-dimensional simulations . . . 123
4.4.1 Resolving the dust condensation front . . . 123
4.4.2 The onset of radiation pressure driven outflows . . . 125
4.4.3 Disk fragmentation and binary formation . . . 125
4.4.4 Angular momentum transport and accretion in massive circumstellar disks . . . 129

5 Summary and outlook 133
5.1 Summary of the project . . . 133
5.2 Outlook on the future of the project . . . 138

Acknowledgements 139

A Constants, units, and variables 141

List of figures 149

List of tables 152

Bibliography 159

Preface

The content of this Ph.D. thesis is based on numerical studies I performed in the planet and star formation group of the Max Planck Institute for Astronomy during the years 2006-2009. For this purpose I developed a frequency dependent radiation transport module and a Poisson solver for three-dimensional hydrodynamics simulations. Both solvers as well as a dust and stellar evolution model based on tabulated data were implemented into our framework of the open source MHD code Pluto.

If not stated in the figure caption or text elsewhere, physical quantities are given in cgs units (based on cm, gram, and seconds), which are still the default units in astronomy. All equations and numerical expressions are numbered consecutively. Basic definitions or important equations are highlighted by gray boxes. Registers of constants, units, and variables are given in the attachment. A list of figures and tables as well as a complete bibliography are given at the end of the thesis.

The electronic version of the thesis in the pdf-format fully supports automatic cross-references and contains high-resolution images (in pdf-format) wherever possible.

1 Introduction

Massive stars are of great importance for a wide range of astrophysical problems. In spite of the fact that they are both rare and short-lived, they represent the major source of radiation energy in their stellar clusters. Therefore, they act as valuable tracers of star formation rates in distant galaxies. Additionally, the radiation emitted during a massive star's lifetime influences their lifetime is influencing the surroundings through various interactions such as heating and ionization of gas, evaporation of dust, and radiative forces leading to powerful stellar winds and outflows. Finally, when a massive star dies, it enriches its neighborhood with heavy elements. In this sense, massive stars are the main drivers of the morphological, dynamical and chemical evolution of their complex environments (Zinnecker & Yorke 2007; McKee & Ostriker 2007; Henning 2008).

However, knowledge about their formation is rather poor compared to the case of low-mass star formation. Observationally, this is mostly due to their larger average distances and the fact that they are deeply embedded in dense, opaque cores especially during their early evolutionary phases. Also, their short lifetime, rareness and complex environment pose difficulties for detailed observations. Nevertheless, current observational results, e.g. from the Spitzer Space Telescope Survey and millimeter interferometry, support the assumption that the basic concepts of star formation, including the collapse of an unstable gas and dust core, the formation of both bipolar outflows and jets as well as accretion disks, are valid throughout the whole range of stellar masses.

After positioning the formation of massive stars in a more global astrophysical context in Sect. 1.1 we will address these similarities and differences of high-mass to low-mass star formation in more detail in Sect. 1.2. From a theoretical point of view, assuming that the formation of high-mass stars is basically a scaled-up version of low-mass star formation, implies its own challenges: Their rapid evolution, especially the shorter Kelvin-Helmholtz contraction timescale, leads to the interaction of the accreting flow of gas and dust with the emitted radiation from the nuclear fusion of the newborn star (Shu et al. 1987). The impact of the resulting radiation pressure on the formation of massive stars is depicted in Sect. 1.3. Previous radiation hydrodynamics research regarding these issues are summarized in Sect. 1.4. We conclude the introductory chapter by motivating the basics of our approach to the radiation pressure problem in Sect. 1.5.

1.1 From molecular clouds to clumps to cores to massive stars - A journey through time and space

Recent observations indicate that the formation of massive stars can be described as a sequence of evolutionary phases with reasonable similarities to the formation of low-mass stars. These evolutionary phases are directly linked to their own specific spatial scale on which the change of the physical properties of the system will occur. Following the evolution in time therefore implies a closer and closer view from large towards small scales. In the following we recapitulate the evolutionary phases of the formation of massive stars.

Spiral galaxies can be considered as composed of stars and stellar remnants around a central black hole as well as material between the stars called the interstellar medium (ISM). Parts of the ISM that are much denser than average are often referred to as molecular clouds. Molecular clouds have masses of up to a few million solar masses, average temperatures of 10 K, and an extent of several pc. The closest massive star forming molecular cloud is the Orion molecular cloud. Several external impacts like nearby supernova explosions, the collisions of individual molecular clouds or tidal forces from galactic mergers can initiate the global gravitational collapse of such a molecular cloud. During its collapse the cloud will fragment hierarchically in clumps of about 1 pc in size harboring several dense cores approximately 0.1 pc in extent. An example of embedded cores detected in a molecular cloud is shown in Fig. 1.1. From these cores the individual stars will eventually form. A well-known example of a resulting star cluster is R136a near the center of the Tarantula nebula also known as 30 Doradus or NGC 2070. Amongst others, the R136a cluster contains about a dozen very massive and luminous stars at its center. The masses of these stars are estimated to lie between 30 and 80 $M_\odot$ (de Koter et al. 1998). Currently, there are 39 confirmed O3 stars in R136a (Lebouteiller et al. 2008). An image of the center of the Tarantula nebula as well as of the star cluster is shown in Figs. 1.2a and 1.2b respectively. Aside from this hierarchical classification, which is not even agreed upon by astronomers in the field, the terminology of clouds, clumps and cores is not very specific: The mass of an object called a molecular cloud, can range from several hundred to thousands of solar masses and a 'final' pre-stellar core can range from several solar masses up to hundreds of solar masses. The amount of further fragmentation of the pre-stellar cores is still unclear and an open question of ongoing research. Two diverse theoretical approaches - the so-called competitive

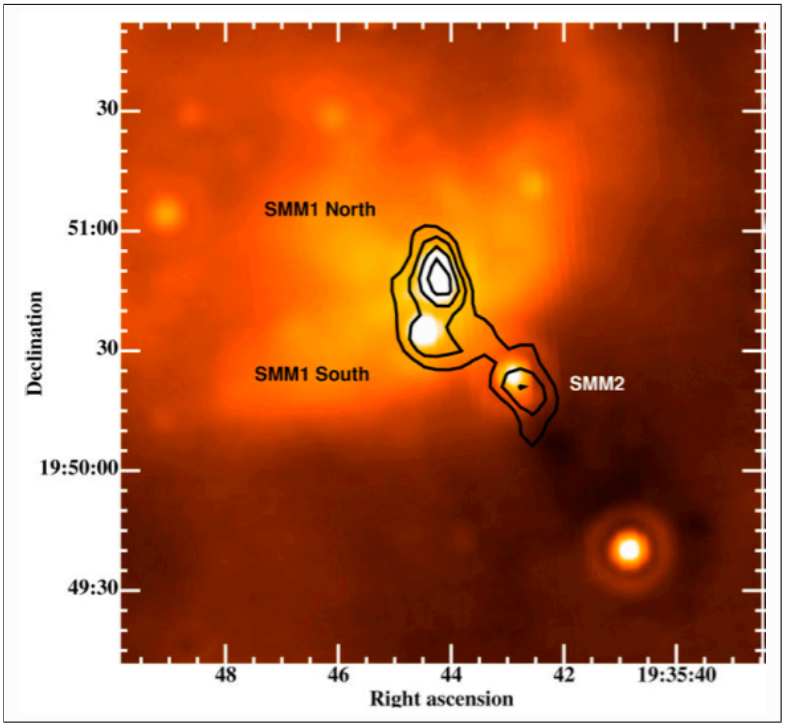

Figure 1.1: Observations of the star-forming region ISOSS J19357+1950. The image shows the 24 μm map of a part of the large scale cloud and the overlaid contours show the 450 μm emission visualizing the embedded cores. The extent of these cores in SMM1 North and SMM2 is roughly given by their FWHM of 0.3 to 0.4 pc (Author: Hennemann et al. (2008)).

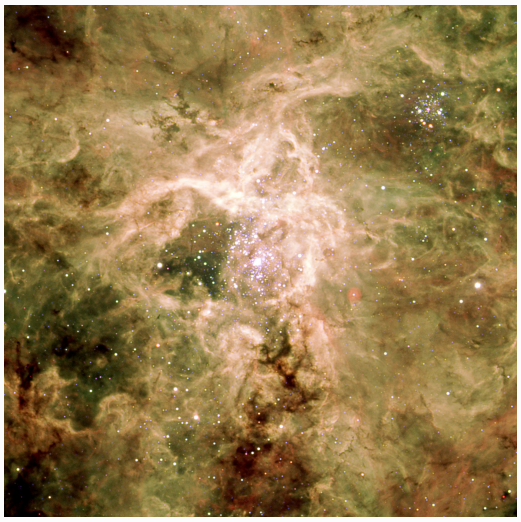

(a) R136a located in the center of the Tarantula Nebula.

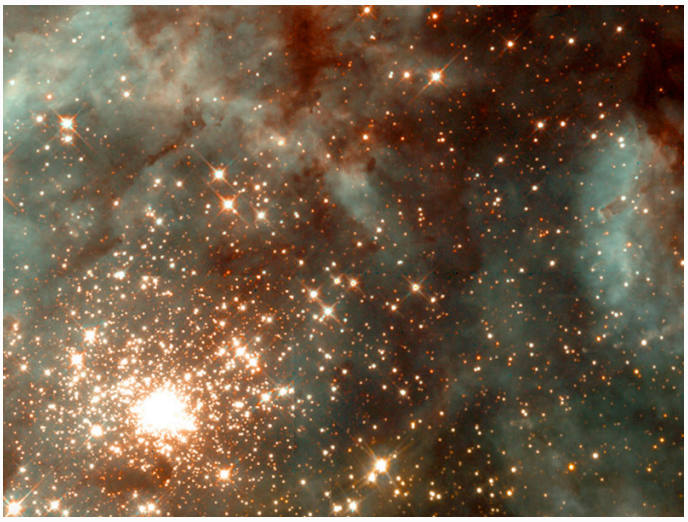

(b) Nearby image of the compact star cluster R136a.

Figure 1.2: The compact star cluster R136a embedded in the center of the Tarantula nebula (Author: ESO).

accretion (Bonnell et al. 1998; Bonnell & Bate 2002; Bonnell et al. 2004; Bate 2009b,a) and the gravo-turbulent model (McKee & Tan 2003) - are referred to in the next section. The starting point of our own research is a high-mass 'starless' core with a diameter of 0.2 pc. The collapse of such a core will force the growth of a low- via an intermediate- up to a high-mass proto-stellar object presumably close to its center, which further accretes material from the high-mass surroundings. Signatures of gravitationally collapsing massive cores have already been found decades ago by e.g. Ho & Haschick (1986), Keto et al. (1987), and Zhang & Ho (1997) as well as in recent observations by e.g. Birkmann et al. (2007). Conservation of initial angular momentum in slowly rotating cores leads to the formation of circumstellar disks. The stability or potential fragmentation of such a massive circumstellar disk will be addressed in detail during the discussion of our three-dimensional pre-stellar core collapse simulation results. Finally, an evolved massive star without further accretion dominates the mass and energy budget at the center of the core.

1.2 The link between low-mass and high-mass star formation

The evolutionary phases described in the last section already indicate a similar formation scenario for high-mass and low-mass stars. Regarding the initial conditions on the large scales, Vázquez-Semadeni et al. (2008) suggest in their preliminary numerical results that high-mass star-forming clumps with a typical scale of 1 pc, harbouring several cores of 0.1 pc and 2-300 $M_{\odot}$, may be in a state of global gravitational collapse rather than in equilibrium supported by strong turbulence. In addition, Hoffmeister et al. (2006) stated that CO absorption is a feature of the early phase in high-mass as well as in low-mass star formation. Although it is difficult to observe the pre-stellar core properties in detail (Beuther et al. 2005a) the main characteristics, given e.g. by Pillai et al. (2007), Beuther & Sridharan (2007), Rathborne et al. (2005, 2006, 2008, 2009), Birkmann et al. (2006), Hennemann et al. (2008, 2009), and Vasyunina et al. (2009) allow us to choose reasonable initial conditions for the collapse phase. The default initial conditions used in our pre-stellar core collapse simulations are described in Sect. 4.1.

At later evolutionary stages the formation of strongly collimated jets and wide-angle bipolar outflows seems to be common through the whole range of stellar masses (e.g. Henning et al. 2000; Zhang et al. 2002, 2007; Wu et al. 2005; Beuther et al. 2005a). Bally (2008) argued that outflows of stars with luminosities less than 10^5 $L_\odot$ are simply scaled-up versions of low-mass ones. Due to the high extinction of the deeply embedded high-mass proto-stars at optical wavelengths, most observations are done in the radio, millimeter and infrared regimes. An

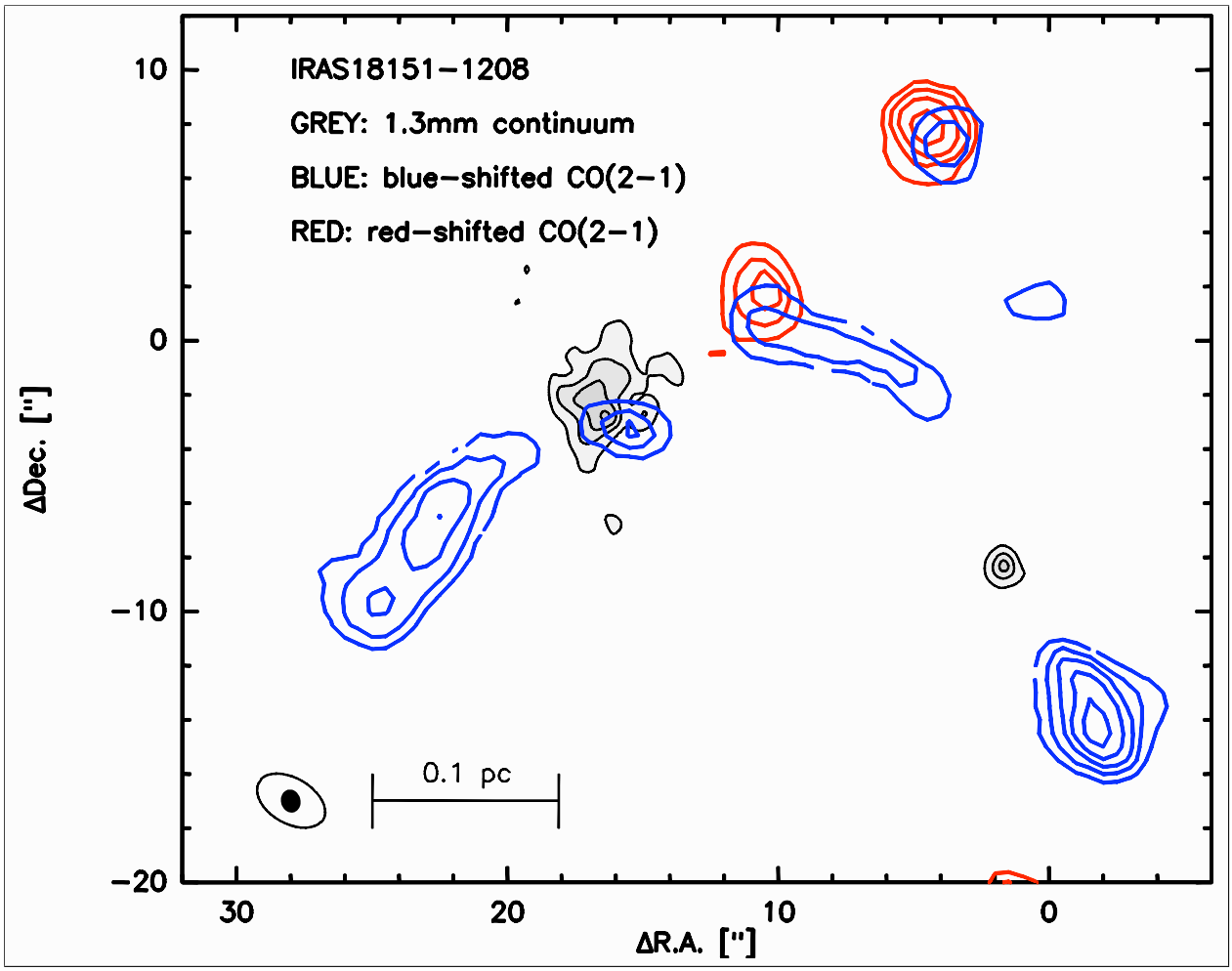

Figure 1.3: 1.3 mm ^{12}CO(2−−1) outflow contours (red and blue) and the 1.3 mm dust continuum contours (gray) of the high-mass proto-stellar object IRAS 18151-1208 (Author: Fallscheer et al., *in prep*).

example of an observed outflow from a high-mass object is shown in Fig. 1.3. The image displays the part of the outflow, which is moving in opposition to the observer (red shifted), the part which is moving towards the observer (blue shifted) as well as the location of the source, seen in the 1.3 mm dust continuum map (gray). A zoom into the central (gray scaled) continuum region reveals a large scale flattened structure of about 10,000 AU in diameter perpendicular to the outflow direction (see Fig. 1.4). The strong collimation of the detected outflows in high-mass star forming regions indicates the presence of circumstellar accretion disks around massive stars. Recent observations using different detection methods further support this presumption. Fitting of the CO first-overtone bandhead emission and K-band spectroscopy (e.g. Bik & Thi 2004; Bik et al. 2005, 2006, 2008), mid-infrared imaging (Chini et al. 2006), near infrared radiative transfer modeling (Steinacker et al. 2006; Nielbock

et al. 2007), and measured velocity gradients perpendicular to the outflow (Beuther et al. 2008) draw a common picture of star formation including circumstellar disks, bipolar jets and outflows as well as radially in-falling envelopes. A reviev on observations of massive accretion disks is given by Zhang (2005). Also Cesaroni et al. (2007) concluded in their review that circumstellar disks are at least common for stars with masses lower than 20 $M_\odot$ (see also Beltrán et al. 2006). The best studied 'proto-types' of such very young, early type high-mass stars surrounded by an accretion disk are IRAS 20126+4104 (Cesaroni et al. 1997; Zhang et al. 1998; Cesaroni et al. 2005) and AFGL 490 (Harvey et al. 1979; Torrelles et al. 1986; Chini et al. 1991; Davis et al. 1998; Lyder et al. 1998; Schreyer et al. 2002, 2006). However IRAS 20126 has a mass of 7 $M_\odot$, and is on the border between intermediate and high mass. Observations towards higher mass stars mostly detect large scale toroids (Beltrán et al. 2004, 2005) or flattened non-keplerian rotating structures (Patel et al. 2005; Beuther et al. 2005b; Beuther & Walsh 2008). A review of observations and theory related to a proposed picture of evolutionary sequences of massive star formation is given in Beuther et al. (2007) and Zinnecker & Yorke (2007). More recently, a review on numerical star formation in general can be found in Klessen et al. (2009).

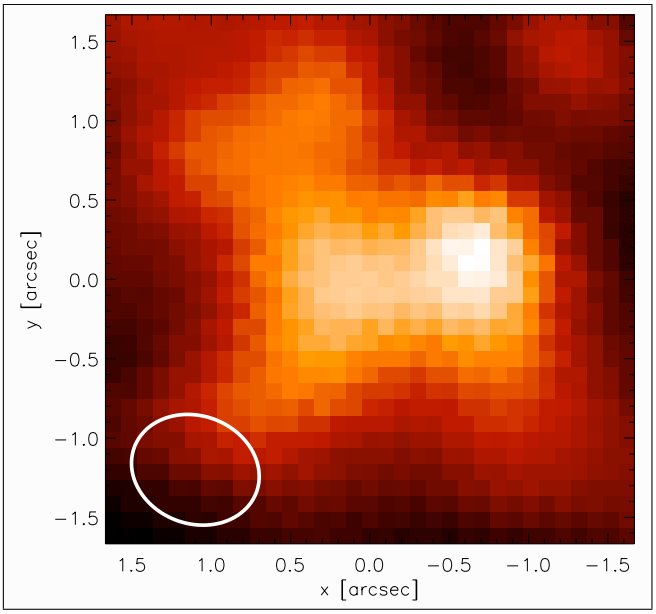

Figure 1.4: Rotated and zoomed-in image of Fig. 1.3 showing 1.3 mm dust continuum of IRAS 18151-1208, a high mass proto-stellar object at a distance of 3000 pc. A single pixel has an edge length of 300 AU. The integrated flux in the area is 0.4 Jy and the peak flux is 41 mJy. The image has linear scaling. The ellipse in the lower left corner is the beam size of the SMA. A large scale flattened structure perpendicular to the outflow direction (here vertically aligned) is revealed. (Author: Fallscheer et al., *in prep*)

The true formation scenario for high-mass stars remains unclear. Massive stars are e.g. generally harboured in a dense cluster environment. Therefore the effect of the so-called competitive accretion (Bonnell et al. 2004) or even merging / coalescence scenarios (Bonnell et al. 1998; Bonnell & Bate 2002) should be considered. In our picture of a monolithic pre-stellar core collapse the effect of competitive accretion in a clustered environment would at least enhance the accretion flow. A comparison between the accretion versus the coalescence scenario, observable consequences as well as observed indications for possible merger examples has been studied in Bally & Zinnecker (2005). The controversial theoretical models of the formation scenario of massive stars are reviewed among other things at great length in Zinnecker & Yorke (2007).

At the moment, observations are not able to distinguish definitely between these competing theoretical models (see e.g. Rodón et al. 2008). Future generations of space telescopes and interferometric systems like the Herschel Space Observatory, the James Webb Space Telescope (JWST) and the Atacama Large Millimeter Array (ALMA) will provide a deeper insight into the mechanisms of in-falling envelopes, bipolar outflows and massive accretion disks. This will definitely put tighter constraints on current theoretical models.

1.3 The radiation pressure problem in the formation of massive stars

In our simulations, we study in detail the accretion flow onto a high-mass star in a monolithic pre-stellar core collapse picture, as recommended by Whitney (2005) and McKee & Ostriker (2007). Under this assumption, the theoretical description of the accretion process onto a massive star has to deal with the interaction between the exerted radiation by the forming star with the accretion flow of gas and dust (Shu et al. 1987). In a perfectly spherically symmetric collapse, this interaction potentially stops the accretion onto the star entirely. In the static limit, radiation pressure overcomes gravity at the so-called generalized Eddington barrier $L_*/M_* = 4\pi Gc/\kappa_*$ (see Sect. 3.4 for a derivation), where L_*, M_* and κ_* denote the stellar luminosity, mass and the dust opacity, G is the gravitational constant and c is the speed of light. But the collapse of a pre-stellar core is far from being a static problem. The momentum transfer from the absorbed photons first has to slow the in-falling accretion flow down. For simplification purposes, we can divide the radiation pressure feedback into two components (see Fig. 1.5). The first exchange of momentum takes place when the irradiation from the massive star is absorbed

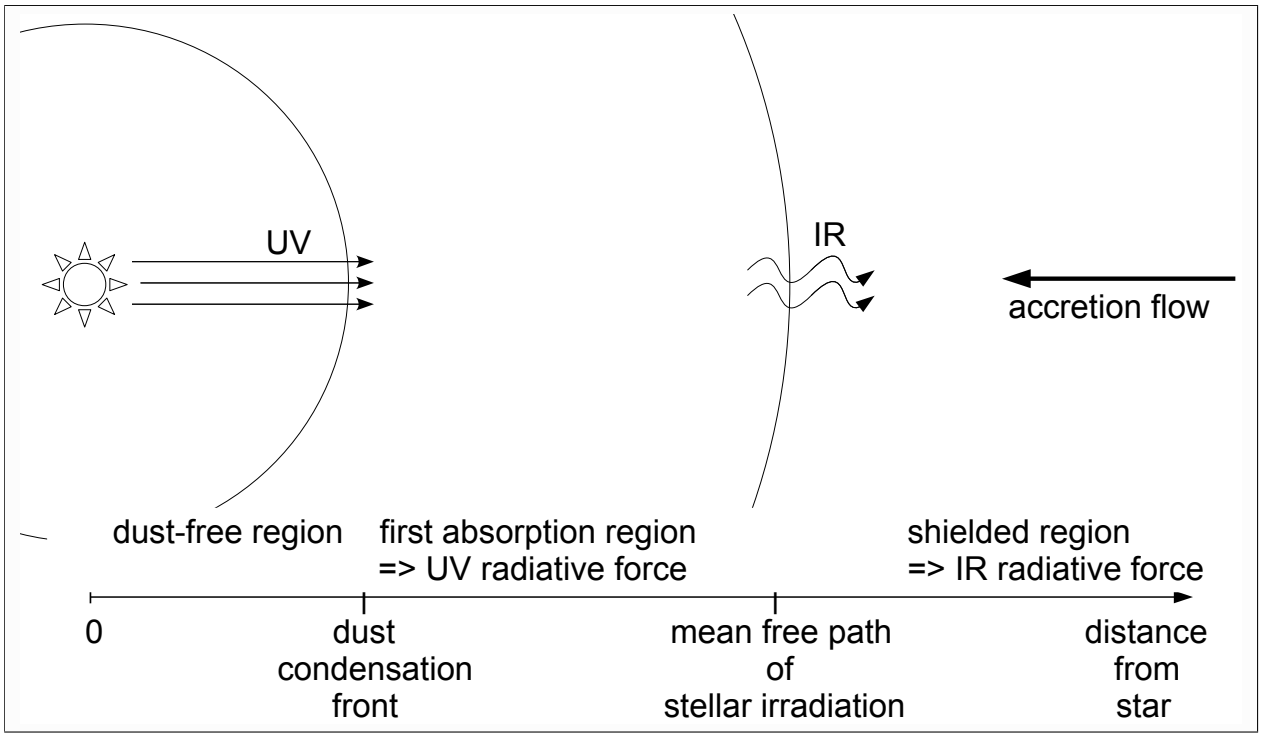

Figure 1.5: Schematic view of radiative forces onto the accretion flow in spherical symmetry. The radiative feedback is divided into direct stellar irradiation and secondary photons.

by the dust grains of the surrounding, i.e. behind the dust condensation radius. The strongest force will thereby be produced by photons with shorter wavelengths, because they have a higher absorption probability and are more energetic. We will call this first interaction 'UV feedback', but the frequency dependence of the broad stellar black body spectrum is clearly not negligible. Afterwards, these heated regions emit photons at the dust temperature (with much longer wavelength). This radiation will be more isotropic and has a longer mean free path. The interaction of this radiation with the enclosed gas and dust is referred to as 'IR feedback'. Our one-dimensional collapse simulations (see Sect. 4.2) confirm the outcome of previous studies that it is essentially

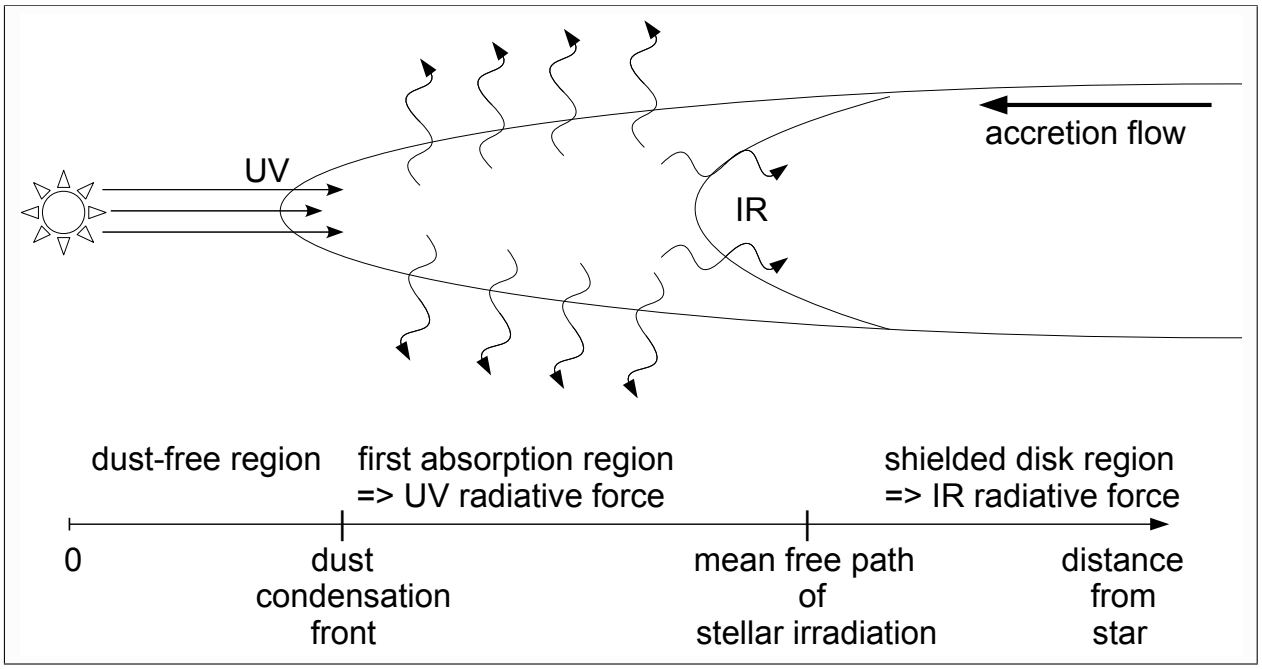

Figure 1.6: Schematic view of the different components of radiation pressure acting in an axially symmetric circumstellar disk geometry.

the IR feedback that stops the accretion flow onto the forming star in spherical symmetry. Although each IR photon transfers less momentum to the dust than the highly energetic stellar UV photons, the spatial length on which the IR flux interacts with the accretion flow is much larger and also further out in regions with less gravity. Different approaches to overcome this barrier for spherically symmetric accretion flows onto massive stars were considered in the past. The generalized Eddington barrier depends only on the stellar evolution (L_*/M_*) and on the dust properties (κ_*). Wolfire & Cassinelli (1987) studied the necessary change of dust properties to enable further accretion, but the restrictions they derived seem to be unrealistic. Also the enhancement of inflow rates has been suggested, but the physical origin of the additional acceleration remains unclear.

Star formation is rarely a perfectly spherically symmetric problem. Initial angular momentum of the collapsing pre-stellar core leads to the formation of a disk as well as polar cavities. This geometry changes the radiation pressure feedback dramatically (see Fig. 1.6). Going from a spherically symmetric in-fall to an axially symmetric disk geometry can help to overcome both - the UV as well as the IR - radiation pressure feedback processes: Developing hydrodynamical (Klahr & Bodenheimer 2003), magneto-rotational (Balbus & Hawley 1991; Hawley & Balbus 1991; Balbus 2003) and self-gravitating instabilities (Yang et al. 1991; Laughlin & Bodenheimer 1994; Bodenheimer 1995) in the accretion disk will transfer angular momentum to outer radii allowing a mass accretion flow radially inward. This additional ram pressure from radiatively shielded parts of the disk will possibly push mass over the thin shell of the UV feedback (Nakano 1989). Secondly, and most important, the irradiated and therefore heated regions of the disk will mainly cool in the vertical direction through the disk's atmosphere, strongly restraining the IR radiation pressure in the radial direction. If the latter process occurs at the innermost part of the disk so that the radiation can escape directly through the bipolar cavity, this

effect is also known as the so-called 'flashlight-effect' (Yorke & Sonnhalter 2002; Krumholz et al. 2005b).

The interaction of the radiation with the accretion flow is very sensitive to the numerical treatment of radiation transport. The Flux Limited Diffusion (hereafter called FLD) approximation, which is a standard technique in modern radiation hydrodynamics codes for astrophysical fluid flows, fails to compute the correct flux between the first transition region from the dust depleted zone around the massive star and the optically thick disk leading to an incorrect temperature distribution in the irradiated regions. Also simplifying the stellar black body spectrum by using frequency averaged Planck mean opacities leads to a thinner shell of the direct stellar irradiation feedback and a stronger heating of the corresponding dust, which afterwards yields a higher IR feedback. Hence, accounting for the frequency dependence of the stellar spectrum seems to be a crucial point. While Krumholz et al. (2005a) claim that the Eddington barrier can be broken via a Rayleigh-Taylor instability, it remains unclear if this instability is the most important one and how this instability will change in the case of realistic frequency dependent radiative feedback instead of the gray (frequency averaged) FLD approximation currently in use. The most violent interaction of the stellar irradiation with the accretion flow takes place at and directly behind the first absorption peak. The location of the first absorption layer is represented by the dust condensation front, where the local dust temperature falls below the evaporation temperature of the dust grains. A systematic study of the radiation pressure feedback on the formation of massive stars therefore implies the need to resolve the ongoing radiation and accretion physics down to the dust condensation front. A formation of massive stars by breaking through the ionization boundary into regions of sublimated dust grains was studied for spherically symmetric accretion flows (Keto 2003) as well as for two-dimensional effects in the so-called small radius limit (Jijina & Adams 1996). Aside from the important contribution of the ongoing physics at the dust condensation front, no previous non-spherically symmetric numerical research has been done so far, presumably due to resolution issues.

1.4 Self-gravitating radiation hydrodynamics in the formation of massive stars

The one-dimensional pre-stellar core collapse problem with stellar radiative feedback has been studied decades ago by Larson & Starrfield (1971), Kahn (1974), Yorke & Krügel (1977) and Wolfire & Cassinelli (1986, 1987). Recent numerical research of Edgar & Clarke (2003, 2004) focused on Bondi-Hoyle accretion (Bondi & Hoyle 1944). As motivated in the last section, the results of these spherically symmetric studies show that the secondary (infrared) radiative flux exceeds the direct stellar feedback easily and eventually limits the final mass of the forming star. Higher mass stars can only be formed by spherically symmetric accretion, if for example, a dramatic change of the corresponding dust properties is assumed (Wolfire & Cassinelli 1987). Therefore, subsequent studies in at least axial symmetry seem to be unavoidable to explain the existence of the most massive stars.

In the monolithic core collapse simulations of Yorke & Sonnhalter (2002) the radiative feedback is treated under the FLD approximation, but computed for several frequency bands. Comparing the outcome of the frequency dependent simulations with their results of corresponding simulations with gray opacities, they conclude that the frequency dependence of the radiative feedback has a major influence on the accretion flow. In fact they found that the use of gray radiation transport results in artificially high radiation pressure and terminates the accretion phase onto the forming massive star much earlier than in the corresponding frequency dependent run. It should be noted, however, that the dust condensation front in their simulations was completely hidden in the huge central sink cell (80 AU radius and 160 AU height of the cylindrical sink cell in the case of a 60 $M_\odot$ core).

The interaction of the radiation with the accretion flow at the dust condensation front is therefore artificially shifted to the radius of the sink cell, where the circumstellar disk would originally be shielded from the direct stellar irradiation. Also, the low resolution in the computational domain (80 AU for the 60 $M_\odot$ and 160 AU for the 120 $M_\odot$ collapse), which was already at the limit to solve the frequency dependent FLD problem in a reasonable amount of time, hampers a detailed study of the radiation hydrodynamics.

Krumholz et al. (2007, 2009a) presented radiation hydrodynamics simulations of a collapsing 100 and 200 $M_\odot$ core focussing on the radiative stellar feedback on the fragmentation of the pre-stellar core. They were tracing the individual regions affected by self-gravity down to a 7.5 and 10 AU scale (in cartesian coordinates) respectively. Despite the significant increase in resolution, it was still not possible to resolve the radiative feedback on the accretion flow, which demands an even higher resolution of the interaction layer. A detailed study of the radiative feedback requires a more precise treatment of the radiation physics as well as the consideration of the frequency dependence of the stellar irradiation spectrum. Both the gray radiation transport approximation and the FLD approximation imply inaccuracies at the interaction zone. Also, Krumholz et al. (2009a) themselves pointed out the relevance of the dust condensation front and stated that it could not be studied on a cartesian AMR grid with the smallest cell size of 10 AU and with a gray FLD approximation. To study the interaction of gravitationally predominant radially in-falling matter with the radially outgoing radiation from a centrally forming massive star we suggest a spherical coordinate system with increasing resolution of the grid towards the center as the natural choice.

Moreover, radiation feedback in non-spherically symmetric hydrodynamics simulations of massive star formation has thus far only been studied under the FLD approximation. The FLD approximation is known to be valid in optically thin as well as in optically thick regions, but yields errors at transition layers (e.g. Yorke & Krügel 1977; Boley et al. 2007). The dust condensation front is such a transition layer. Therefore, a direct ray-tracing method seems to be more appropriate for studying the effects of stellar radiative feedback. However, a full frequency dependent ray-tracing method, e.g. based on a Monte-Carlo routine, would lead to a huge computational overhead related to the hydrodynamics in a three- or even two-dimensional simulation. Therefore, we will introduce in the following our approach to compute the frequency dependent radiative feedback of a forming massive star on the accretion flow with high accuracy, but with as little computational effort as possible.

1.5 The approach to the problem

In our simulations, we study the radiative feedback of a forming massive star on the matter being accreted. Therefore, we have to acquire sufficiently high resolution in the vicinity of the forming star where the radiation interacts with the surrounding gas and dust. Keeping in mind that the dynamical problem includes mostly radially acting forces (gravitationally in-falling matter and stellar irradiation) a grid in spherical coordinates around a centrally forming massive star seems to be the natural choice. The polar and azimuthal resolution of the spherical grid automatically increases towards the center. The usage of a radially increasing resolution towards the center guarantees the possibility to study the radiative feedback in the central core regions with high accuracy by simultaneously saving computational time in the calculation of ongoing physics in the outer core regions far away from the massive star.

Taking the strong influence of the correct treatment of the stellar irradiation into account, we developed a radiation transport module for three-dimensional hydrodynamics simulations which includes a fast gray FLD

solver for the appropriate dust cooling as well as a first order ray-tracing routine for the careful treatment of the stellar irradiation. Furthermore, the splitting of the radiation transport eases the implementation needed to account for the frequency dependence of the stellar irradiation spectrum. Boosted by a modern solver library for large but sparse linear systems of equations, the radiation transport (as well as the self-gravity problem) can be solved quickly and accurately on distributed memory machines. The usage of the well adjusted grid, the speed of our newly developed approximate radiation transport method as well as the efficient parallelization of the corresponding solver allows us to study the dust condensation front around the forming massive star in these kind of collapse simulations down to a sink cell radius of 10 AU with a size of the smallest cells of the spherical grid of about 1.27 AU x 1.04 AU x 1.04 AU.

In the following Chapt. 2, we describe the details of the self-gravitating radiation hydrodynamics code. We show several test problems used to analyze the accuracy and performance of the newly developed modules. Chapt. 3 comprises our analytical estimates of the basic time and length scales of the collapse as well as the most important concepts regarding the radiation pressure problem. In Chapt. 4, we present the results of one-, two-, and three-dimensional radiation hydrodynamics simulations of pre-stellar core collapses focusing on the radiative feedback onto the accretion flow while resolving the dust condensation front. A summary of the results (Sect. 5.1) and a brief outlook on the future direction of this research project (Sect. 5.2) conclude the thesis.

2

Physics of the formation of massive stars

In this chapter, we explain the ingredients and default numerical configuration of the self-gravity radiation hydrodynamics code we are using to model the collapse of massive pre-stellar cores. The first Sect. 2.1 comprises the motivation for our choice of a grid in spherical coordinates and highlights the step forward in resolution we obtain in our simulations compared to previous research. The following two Sects. 2.2 and 2.3 describe the features and the configuration of the hydrodynamics solver including full tensor viscosity, for which we are using the open source MHD code Pluto3 (Mignone et al. 2007). Further sections describe our newly developed modules for self-gravity (Sect. 2.4) and frequency dependent approximate radiation transport (Sect. 2.5).

The importance of the frequency dependence of the stellar spectrum when calculating the radiative feedback of a massive star was already shown in radiation hydrodynamics studies by Yorke & Sonnhalter (2002) and Edgar & Clarke (2003) as well as in purely radiation transport simulations by Krumholz et al. (2005b). On the other hand, no frequency dependent radiation hydrodynamics study related to massive star formation was carried out since the work by Yorke & Sonnhalter (2002) in more than one dimension. To study the radiative feedback of massive stars on their own accretion stream in one-, two-, and three-dimensional simulations we implemented a fast, robust, and accurate frequency dependent radiation transport solver in spherical coordinates into our version of the Pluto code. To achieve a fast solver for the frequency dependent problem we split the radiation field into the stellar irradiation and thermal dust emission. The robustness of the solver was realized by using a modern Krylov subspace solver for sparse linear matrix equations provided by the scientific open source library called 'PETSc' (Balay et al. 2001, 2004). The accuracy of the final radiation transport module was tested in detail against the standard radiation benchmark test by Pascucci et al. (2004) for Monte-Carlo or ray-tracing radiative transfer solvers. Despite the complex radiation physics considered in our simulations, the choice of the static spherical coordinate system and the speed and parallel performance of the modern solving algorithm allows us to study the radiative feedback problem in much higher resolution, for much longer evolutionary time, and for a larger fraction of the parameter space than ever before. We close this chapter with the description of the tabulated dust (Sect. 2.6) and stellar evolution (Sect. 2.7) model used in the simulations.

2.1 Discretization of the computational domain

In our simulations, we are using a time independent grid in spherical coordinates with logarithmically increasing radial resolution towards the center. Two examples of a two-dimensional grid, which also represent a r-θ-slice of the corresponding three-dimensional grid, are displayed in Figs. 2.1 and 2.2. This type of grid is well adapted for the analysis of the interaction of an accretion flow onto a massive star along with the stellar irradiation it generates, because the stellar gravity as well as the stellar radiative force are aligned with the radial coordinate axis. In contrast to e.g. cartesian coordinates, the usage of spherical coordinates guarantees a strict angular momentum conservation. The polar and azimuthal resolution of the spherical grid automatically increases towards the regions of interest around the centrally forming star, where high resolution is desired. We chose a non-uniform logarithmically increasing radial resolution of the grid to even enhance this focus on the inner parts of the core and saving computational effort in the outer parts far away from the dust radiation interaction layer. Thus the non-adaptive grid setup impeded the study of possible core fragmentation in the outer regions. The polar discretization of the two- and three-dimensional grid is uniformly fixed and covers an angle of $\pi/2$ from the top polar axis to the forming disk midplane, assuming midplane symmetry as in Yorke & Sonnhalter (2002). The azimuthal extent of the cells of the three-dimensional grid is chosen to be equal to the polar extent. The radial resolution Δr at a radius r of a computational domain with N_r grid cells in the radial direction is given by

Authors	Resolution in AU in regions of	
	lowest resolution	highest resolution
Yorke & Sonnhalter (2002)	320^2	80^2
Krumholz et al. (2007)	966^3	7.5^3
Krumholz et al. (2009a)	645^3	10^3
Kuiper et al. 1D	1540	0.08
Kuiper et al. 2D	2319 x 1911	1.27 x 1.04
Kuiper et al. 3D	2319 x 1911 x 1911	1.27 x 1.04 x 1.04

Table 2.1: Resolution of different radiation hydrodynamics simulations of a collapse of a slowly rotating massive pre-stellar core. The simulations of Yorke & Sonnhalter (2002) were performed on a non-adaptive two-dimensional grid in cylindrical coordinates with three nested levels. The given resolution (Δr x Δz) of Yorke & Sonnhalter (2002) represents the case of a $M_{\rm core} = 60\,{\rm M}_\odot$ pre-stellar core. The resolution for the lower mass $M_{\rm core} = 30\,{\rm M}_\odot$ collapse was a factor of two better. The resolution for the higher mass $M_{\rm core} = 120\,{\rm M}_\odot$ collapse was a factor of two worse. The simulations of Krumholz et al. (2007, 2009a) were performed on a three-dimensional cartesian adaptive mesh refinement (AMR) grid. The given resolution (Δx x Δy x Δz) represents the lowest and highest resolution during the simulation. The resolution of our own grids in spherical coordinates is given in units of arc length (Δr x ($r\ \Delta\theta$) x ($r\ \sin(\theta)\ \Delta\phi$)) in the midplane.

$$\Delta r(r) = r * \left(10^f - 1\right) \tag{2.1}$$

with $f = \log(r_{\rm max}/r_{\rm min})/N_r$, where $r_{\rm min}$ and $r_{\rm max}$ represent the inner and outer radius of the computational domain. A comparison of our achieved resolution to previous massive pre-stellar core collapse simulations by Yorke & Sonnhalter (2002) and Krumholz et al. (2007, 2009a) is given in table 2.1.

The forming high-mass proto-stellar object is represented by a dedicated stellar evolution model (presented in Sect. 2.7) inside the central sink cell with radius $r_{\rm min}$ at the origin of the coordinate system using pre-calculated stellar evolutionary tracks for accreting massive proto-stars (Hosokawa & Omukai 2008).

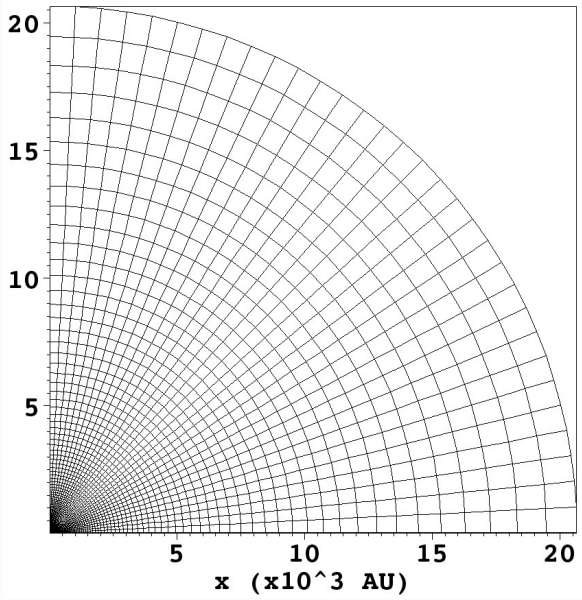

(a) Global image of the total computational domain up to the outer radius of r_{max} = 0.1 pc.

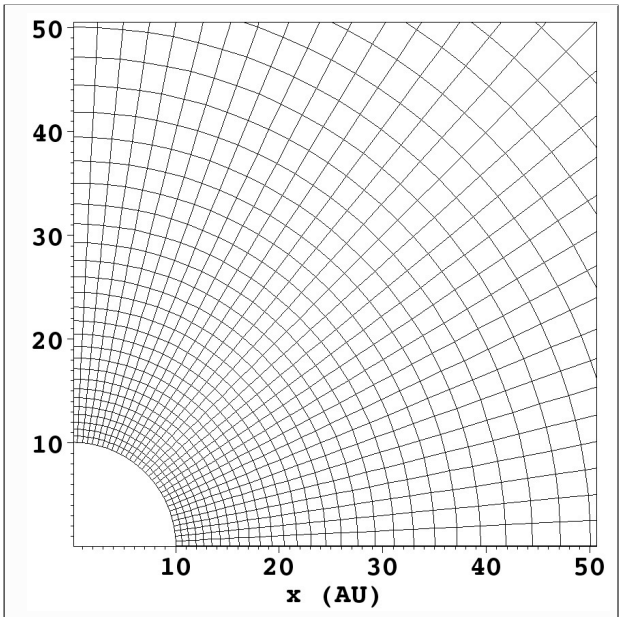

(b) Zoomed-in image of the central 50 AU x 50 AU.
The innermost cells have a resolution of 0.61 AU x 0.51 AU.

Figure 2.1: Two-dimensional grid (128 x 32) in spherical coordinates with logarithmically increasing radial resolution, a central sink cell of radius r_{min} = 10 AU and an outer boundary at r_{max} = 0.1 pc.

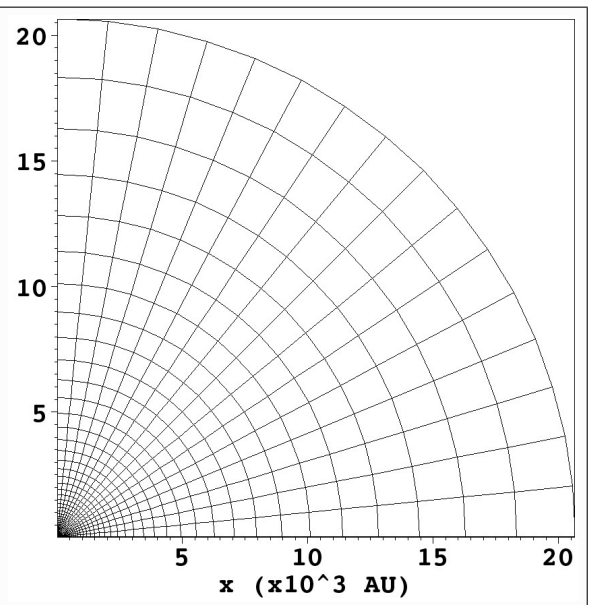

(a) Global image of the total computational domain up to the outer radius of r_{max} = 0.1 pc.

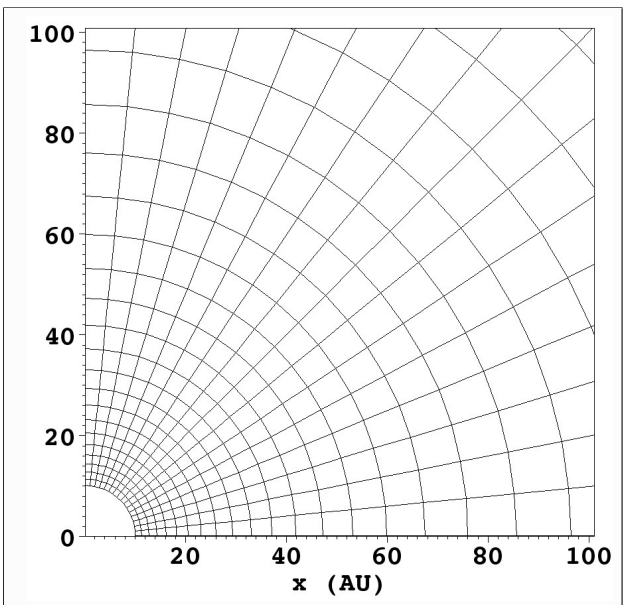

(b) Zoomed-in image of the central 100 AU x 100 AU.
The innermost cells have a resolution of 1.27 AU x 1.04 AU.

Figure 2.2: Two-dimensional grid (64 x 16) in spherical coordinates with logarithmically increasing radial resolution, a central sink cell of radius r_{min} = 10 AU and an outer boundary at r_{max} = 0.1 pc. In three-dimensional simulations the resolution of this grid is retained and expanded in the azimuthal direction with the same angular resolution as in the polar direction.

2.2 Hydrodynamics

To follow the motion of the gas, we solve the equations of compressible hydrodynamics in conservative form

$$\begin{aligned} \partial_t \rho + \vec{\nabla} \cdot (\rho \vec{u}) &= 0 && (2.2) \\ \partial_t (\rho \vec{u}) + \vec{\nabla} (\rho \vec{u} \vec{u}) &= -\vec{\nabla} p + \rho \vec{a} && (2.3) \\ \partial_t E + \vec{\nabla} \cdot ((E + p) \vec{u}) &= \rho \vec{u} \cdot \vec{a} && (2.4) \end{aligned}$$

with the acceleration source term $\vec{a} = \sum_i \vec{a}_i$, which includes the additionally considered physics to the equations of gas dynamics (Euler equations) such as shear viscosity ($\vec{a}_1$), central gravity of the forming star ($\vec{a}_2$), self-gravity ($\vec{a}_3$), and radiation transport and stellar feedback ($\vec{a}_4$). These additional components are described in the following subsections. The evolution of the gas density ρ, velocity $\vec{u}$, pressure p and total energy density E is computed using the open source MHD code Pluto3 (Mignone et al. 2007).

We use an ideal gas equation of state

$$p = (\gamma - 1) E_{\rm int}, \quad (2.5)$$

which relates the gas pressure to the internal energy $E_{\rm int} = E - 0.5 \rho u^2$ and therefore closes the system of Eqs. 2.2 to 2.4. The adiabatic index γ is set to $5/3$.

Pluto is a high-order Godunov solver code, i.e. it uses a shock capturing Riemann solver within a conservative finite volume scheme. The numerical configuration of our simulations makes use of a Strang operator splitting scheme for the different dimensions (Strang 1968). Our default configuration consists further of a Harten-Lax-Van Leer (hll) Riemann solver and a so-called 'minmod' flux limiter using piecewise linear interpolation (plm) and a Runge-Kutta 2 (RK2) time integration, also known as the predictor-corrector-method, compare van Leer (1979). Therefore the total difference scheme is accurate to $2^{\rm nd}$ order in time and space.

To limit the range of densities, the so-called floor value of the density is chosen to be $\rho_0 = 10^{-21}$ g cm^{-3}. This floor value occurs during the simulations only in regions where the radiation pressure driven outflow is depleting the density of the corresponding grid cells in the outward radial direction. Thus, the choice of the floor value does not influence the level of accretion onto the newly forming star we are investigating. To cross-link the energy conservation law with simultaneously acting radiation transport, the energy Eq. 2.4 is not used to directly update the temperature or pressure distribution of the current iteration, but is rather treated as a source term in the Flux Limited Diffusion equation. Further details about this procedure are given in Sect. 2.5 on the radiation physics.

The various sources of additional acceleration $\vec{a} = \sum_i \vec{a}_i$ that enter the equations of hydrodynamics are discussed in the following sections and include viscosity, gravity of the central star as well as self-gravity of the core and radiative feedback.

2.3 Viscosity

In two-dimensional simulations we consider physical shear viscosity of the circumstellar disk medium to mimic the effect of angular momentum transport (via e.g. the magneto-rotational instability, spiral arms, disk winds and jets). Two-dimensional axially symmetric simulation runs without any shear viscosity yield the formation of ring instabilities in the circumstellar disk. The rings would be unstable if non-axially symmetric modes were allowed, leading to the formation of spiral arms and therefore to angular momentum transport as discussed by Yorke et al. (1995).

Full physical tensor viscosity is included in the current version of Pluto3. Viscosity enters the equations of hydrodynamics 2.3 - 2.4 as an additional source of acceleration

$$\boxed{\vec{a}_1 = \vec{\nabla}\Pi.} \qquad (2.6)$$

The components of the viscous stress tensor Π are given (in cartesian coordinates) by

$$\boxed{\Pi_{ij} = \eta\left(\partial_j u_i + \partial_i u_j - \frac{2}{3}\delta_{ij}\partial_k u_k\right) + \eta_\mathrm{b}\delta_{ij}\partial_k u_k} \qquad (2.7)$$

with the Kronecker symbol δ_{ij}. Further details on the analytical treatment of viscosity can e.g. be found in Landau & Lifshitz (1987). In our simulations we do not use any bulk viscosity ($\eta_\mathrm{b} = 0$).
The shear viscosity

$$\boxed{\eta = \rho\,\nu} \qquad (2.8)$$

is described via the so-called α-parameterization of Shakura & Sunyaev (1973), in which the dynamical viscosity ν is set proportional to the product of a typical velocity and length scale of the system under investigation, here the local sound speed c_s and pressure scale height H:

$$\nu = \alpha\, c_\mathrm{s}\, H \qquad (2.9)$$

We further approximate the local pressure scale height H by

$$H = c_\mathrm{s}/\Omega_\mathrm{K}(r) \qquad (2.10)$$

with the keplerian angular velocity

$$\Omega_\mathrm{K}(r) = \sqrt{\frac{GM(r)}{r^3}} \qquad (2.11)$$

derived from the equilibrium between gravity and the centrifugal force. The mass inside the radius r $M(r)$ is calculated by the spatial integral of the density distribution plus the central stellar mass M_* inside the sink cell:

$$M(r) = M_* + \int_0^r dr \int_0^\pi d\theta \int_0^{2\pi} d\phi\, \rho(r,\theta,\phi) r^2 \sin(\theta). \qquad (2.12)$$

Using the relation 2.9 we substitute the local sound speed in Eq. 2.8 yielding

$$\nu = \alpha\, \Omega_\mathrm{K}(r)\, H^2. \qquad (2.13)$$

Introducing the dimensionless parameter H/R, the aspect ratio of the circumstellar disk, leads to

$$\boxed{\nu = \alpha\, \Omega_\mathrm{K}(r)\, R^2 \left(\frac{H}{R}\right)^2} \qquad (2.14)$$

with the cylindrical radius $R = r\,\sin(\theta)$. Both unit-free parameters $(H/R)^2 = 0.1$ and $\alpha = 0.03$ are fixed constants in time and space for the majority of our simulation runs. Results for varying normalization values of the dynamical viscosity are presented in Sect. 4.3.2.

2.4 Gravity

2.4.1 Central gravity and Poisson equation

The calculation of the gravitational potential Φ is split into the gravity of the central star in the sink cell Φ_* and the self-gravity of the mass in the computational domain $\Phi_{\rm sg}$:

$$\Phi = \Phi_* + \Phi_{\rm sg} \qquad (2.15)$$

The acceleration vector $\vec{a}_2$ of the gravity of the central star, which enters the conservation laws of hydrodynamics 2.3 and 2.4, is given analytically by

$$\vec{a}_2 = -\vec{\nabla}\,\Phi_* = \vec{\nabla}\,\frac{G\,M_*}{r} = \partial_r\,\frac{G\,M_*}{r}\vec{e}_r = -\frac{G\,M_*}{r^2}\vec{e}_r. \qquad (2.16)$$

Such external gravity (from point sources) is supported in Pluto3 by defining the gravitational potential Φ_* or the resulting acceleration vector $\vec{a}_2$.
The acceleration $\vec{a}_3$ due to self-gravity is given by

$$\vec{a}_3 = -\vec{\nabla}\Phi_{\rm sg}, \qquad (2.17)$$

in which the gravitational potential $\Phi_{\rm sg}$ is determined via Poisson's equation:

$$\vec{\nabla}^2\Phi_{\rm sg} = 4\pi\,G\,\rho. \qquad (2.18)$$

We implemented a solver of Poisson's equation into our version of the Pluto code in a modular fashion. The module solves the equation via a diffusion ansatz. The discretization of Eq. 2.18 yields the vector equation

$$A\vec{\Phi} = 4\pi\,G\,\vec{\rho}. \qquad (2.19)$$

For a one-dimensional cartesian grid with a uniform grid spacing Δx, where the $i^{\rm th}$ component of the vectors $\vec{\Phi}$ and $\vec{\rho}$ represent the gravitational potential and density of the i^{th} grid point, the matrix A would be of the form

$$A = \begin{pmatrix} \dots & \dots & \dots & \dots & \dots & \dots & \dots \\ \dots & 1 & -2 & 1 & 0 & \dots & \dots \\ \dots & 0 & 1 & -2 & 1 & 0 & \dots \\ \dots & \dots & \dots & \dots & \dots & \dots & \dots \end{pmatrix} \frac{1}{(\Delta x)^2}, \qquad (2.20)$$

representing the discretization stencil $(\Phi_{i-1} - 2\Phi_i + \Phi_{i+1})/(\Delta x)^2$. The desired approximate matrix inversion for solving Eq. 2.19 is done using the so-called GMRES method, which is also used for the FLD equation (see Sect. 2.5). Parallel performance tests of this solver according to the FLD equation are presented in Sect. 2.5.3.

The outer radial boundary values of the gravitational potential are calculated via a Taylor expansion of the density distribution, as previously done, for example, by Black & Bodenheimer (1975). Several tests we performed indicate that it is sufficient to just account for the monopole solution of the Taylor expansion, i.e. the total mass of the core. The mass distribution is perfectly spherically symmetric at the beginning of the simulation and afterwards becomes highly concentrated in the inner region of the computational domain far away from the outer boundary, both yielding analytically to the monopole solution at the outer boundary. To control the resolution, which is necessary to resolve the physics of self-gravity correctly, e.g. preventing artificial fragmentation of a collapsing pre-stellar core, we monitor the so-called Truelove criterium, derived in Truelove et al. (1997). The criterium requires to resolve the Jeans length $\lambda_{\rm J}$

$$\lambda_{\mathrm{J}} = \sqrt{\frac{\pi\, c_{\mathrm{s}}^2}{G\,\rho}} \qquad (2.21)$$

at least by a priorily defined number of grid cells. The inverse of the number of necessary grid cells per Jeans length is the so-called Jeans number

$$J = \frac{\Delta x}{\lambda_{\mathrm{J}}}. \qquad (2.22)$$

Truelove et al. (1997) suggest at least a Jeans number of $J \leq 0.25$ or below.

We tested the Poisson solver in several standard tests which we present in detail in the following subsection. The accelerations $\vec{a}_2 + \vec{a}_3$ enter the hydrodynamics as a source term for momentum and energy in Eqs. 2.3 and 2.4. This coupling to the hydrodynamics was cross-checked in dynamical collapse tests. In all simulations performed, the accuracy of the Poisson solver was chosen to 0.001% relative accuracy of the gravitational potential $\left(\Delta\Phi_{\mathrm{sg}}/\Phi_{\mathrm{sg}} \leq 10^{-5}\right)$.

2.4.2 Tests of the Poisson solver

In the following, we present a suite of test problems we used to check the correct implementation and the performance of the newly developed Poisson solver. All test results were compared to known analytic solutions. Poisson's equation implies no time dependence and can be tested in calculating the static gravitational potential from a given density distribution. The accuracy of the GMRES solver was chosen to a relative accuracy of $\Delta\Phi/\Phi \leq 10^{-5}$ in all test cases.

2.4.2.1 Static one-dimensional test

In this first test, the density distribution is given by an iso-density sphere of radius r_2 with an inner hole of radius r_1, displayed in Fig. 2.3. The analytic solution can be split into the three different regimes: inside the inner cavity $r < r_1$, inside the density distribution $r_1 < r < r_2$ and outside of the sphere ($r > r_2$). In the mass free regions ($\rho_{1,3} = 0$), the Poisson equation (Eq. 2.18) simplifies to the Laplace equation

$$\vec{\nabla}^2\Phi_{1,3} = 0. \qquad (2.23)$$

The solution in the three regions is given by

$$\Phi_1 = -2\pi\, G\rho_0 \left(r_2^2 - r_1^2\right) \qquad (2.24)$$

$$\Phi_2 = \frac{2\pi}{3} G\rho_0 \left(r^2 + 2\frac{r_1^3}{r} - 3r_2^2\right) \qquad (2.25)$$

$$\Phi_3 = -\frac{4\pi}{3} G\rho_0 \left(r_2^3 - r_1^3\right) \qquad (2.26)$$

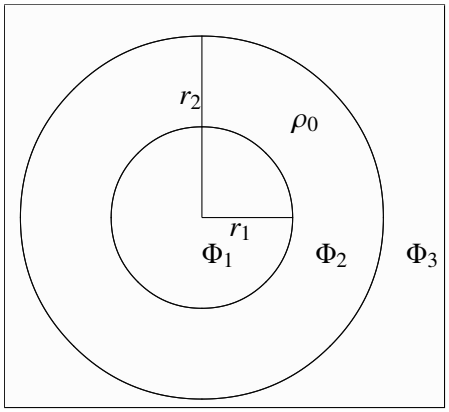

Figure 2.3: Schematic setup of the one-dimensional self-gravity test: A sphere of iso-density ρ_0 with an outer radius r_2 and an empty inner hole of radius r_1.

The iso-density in the test case is chosen to be $\rho_0 = 10^{-10}$ g cm^{-3}, the inner radius to be $r_1 = 1$ AU and the outer radius to be $r_2 = 100$ AU. The computational domain ranges from 0.5 up to 200 AU and is divided into 256 grid cells. The grid size of each cell grows about 2% radially. The resulting gravitational potential and the deviation of the numerical solution from the analytic one is displayed in Fig. 2.4. As required, the outer boundary condition yields the exact analytical result. When approaching the

discontinuity in density at the outer radius r_2, the deviation from the analytic solution grows to its maximum. Afterwards the deviations shrink again. Inside the cavity no gravitational force is acting and the gradient of the potential is zero.

2.4.2.2 Static two-dimensional test

The density distribution of the two-dimensional static test case for the Poisson solver is given by an iso-density oblate spheroid with semiaxes $a = b > c$ in the x, y and z direction respectively (see Fig. 2.5). The interior points of the spheroid fulfill the relation

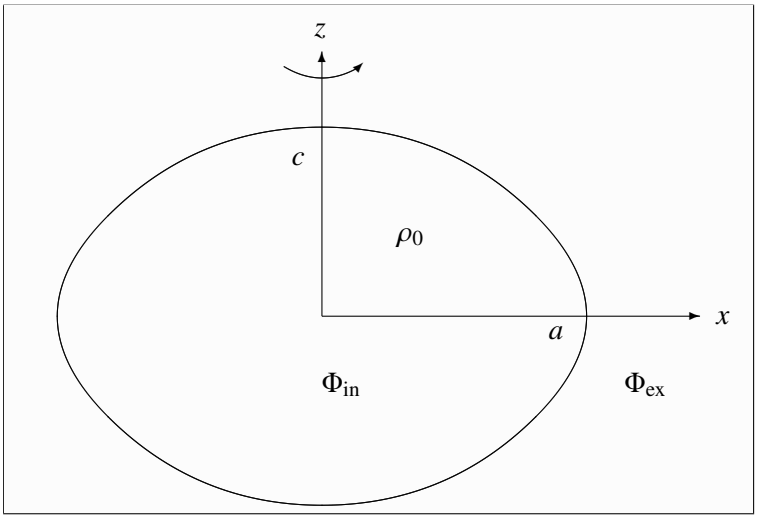

Figure 2.5: Schematic setup of the two-dimensional static self-gravity test: An oblate (disk-like) spheroid with semiaxes $a = b > c$ in the x, y, and z direction respectively.

$$\frac{x^2}{a^2} + \frac{y^2}{b^2} + \frac{z^2}{c^2} \leq 1. \tag{2.27}$$

On the discretized spherical grid, we set the density of grid cells for which the center fulfills this relation to the iso-density value of ρ_0, otherwise to zero. No smoothing or averaging is applied. That means the surface of the discretized ellipsoid follows the grid coordinates rather than an ellipsoid. Therefore the mass of the ellipsoid for the analytic solution is calculated from the integral over the numerical density distribution to avoid discretization errors in the determination of the total mass and hence the gravitational potential at the outer radial boundary. The analytic solution for the interior (Ramsey 1961) and exterior (Kellogg 1929) of such an oblate spheroid is given by

$$\begin{aligned}\Phi_{\rm in}(x,y,z) &= -\pi\, G\rho_0 \frac{2a^2c}{\sqrt{a^2-c^2}}\left(1 - \frac{x^2+y^2-2z^2}{2\left(a^2-c^2\right)}\right)\arcsin\left(\sqrt{1-\frac{c^2}{a^2}}\right) \\ &\quad -\pi\, G\rho_0 \frac{1}{a^2-c^2}\left(c^2x^2 + c^2y^2 - 2a^2z^2\right) \end{aligned} \tag{2.28}$$

$$\Phi_{\rm ex}(x,y,z) = -8\pi\, G\rho_0 \frac{a^2c}{f^2}\left(\frac{4z^2-2r^2+f^2}{2f}\arcsin\left(\frac{f}{s}\right) + \frac{s^2\left(r^2-2z^2\right) - f^2r^2}{s^2\sqrt{s^2-f^2}}\right) \tag{2.29}$$

where r is the cylindrical radius, s is the sum of the focal radii to the specified point (x, y, z) and f is the distance between the foci of a meridian section:

$$r = \sqrt{x^2+y^2} \tag{2.30}$$

$$s = 2\sqrt{a^2+\lambda} \tag{2.31}$$

$$f = 2\sqrt{a^2-c^2} \tag{2.32}$$

where λ is the largest positive root of the equation for confocal ellipsoids:

$$\frac{x^2}{a^2+\lambda} + \frac{y^2}{b^2+\lambda} + \frac{z^2}{c^2+\lambda} = 1 \tag{2.33}$$

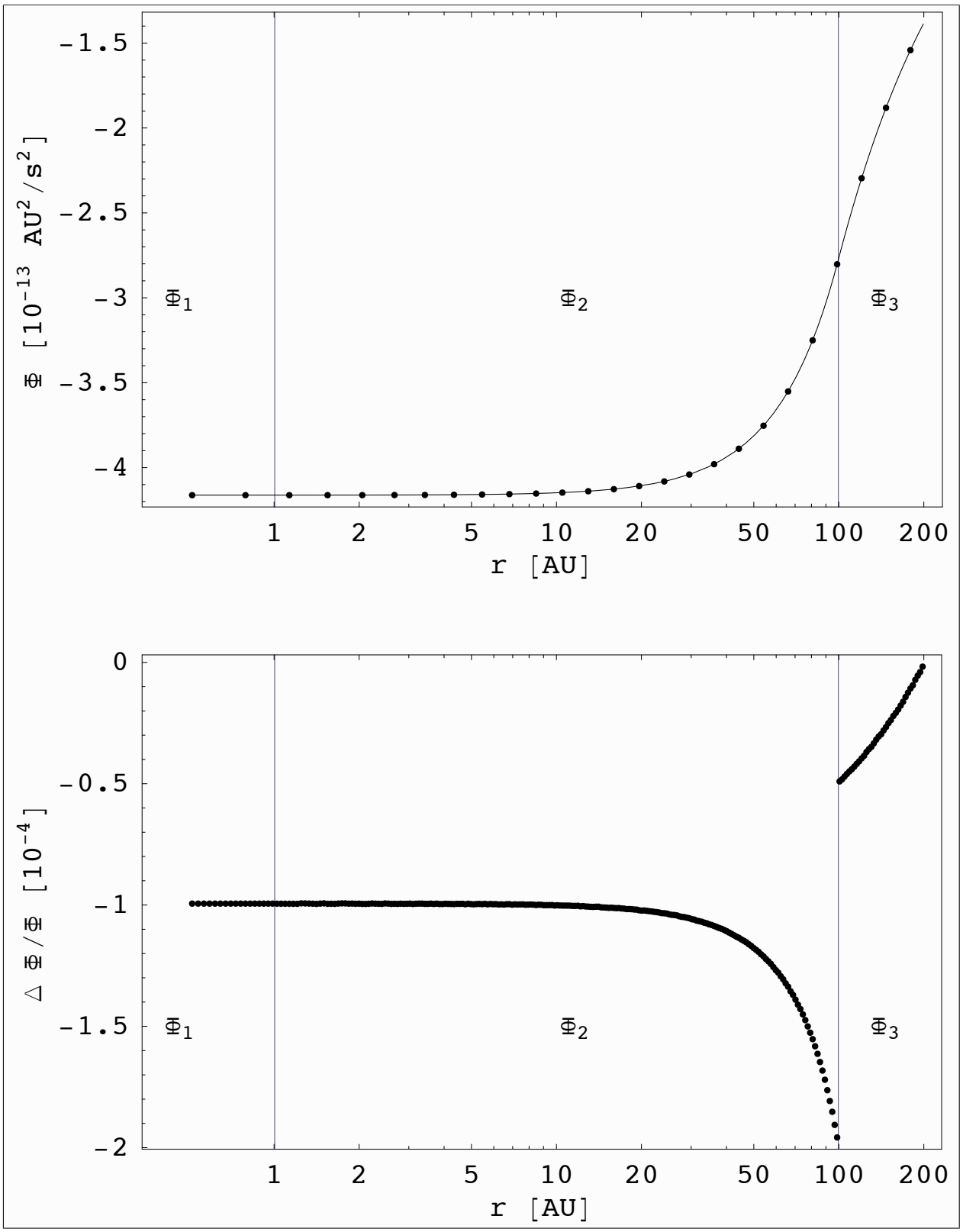

Figure 2.4: Static one-dimensional test results. Vertical lines mark the inner and outer sphere radii. Upper panel: Resulting numerical (dots) and analytical solution (solid line) of the gravitational potential. Lower panel: Deviation of the numerical solution from the analytic one.

An overview of different analytic solution techniques is, for example, given in Wang (1988, 1989). The long and short semiaxes are chosen to be 100 AU and 50 AU respectively. The iso-density in the test case is chosen to be $\rho_0 = 10^{-10}$g cm^{-3}. The computational domain ranges from 0.5 up to 2000 AU radially and covers the full polar angle of 180°.

Remark: The outer boundary is chosen to be a factor of 20 larger than the spheroid. Compared to the collapse simulations performed later on, where the outer boundary is at 0.1 pc, this ratio corresponds to a concentration of the majority of the mass inside the inner 1000 AU during the collapse. The circumstellar disk, which is formed during the collapse, attains 'only' an extent of several 100 AU.

The computational domain is divided into $N^2 = 128^2$, 256^2, or 512^2 grid cells. The radial grid size of each cell grows proportional to the radius. Due to the fact that the elliptical border of the spheroid cannot be reflected exactly on a spherical grid, discretization errors will show up in this setup. Also, the total mass inside the discretized computational domain does not correspond to the analytically given mass of the spheroid. In order to compare the numerical and the analytical solution, the analytic solution is multiplied by the ratio of numerical to analytical given mass inside the spheroid. Further discretization errors should vanish for infinitely high grid resolution. Therefore we performed several runs on different grids with increasing resolution. The resulting gravitational potentials along the long and short axes as well as the deviation of the numerical solution from the analytic one are displayed in Fig. 2.6 and Fig. 2.7. As expected, the deviation of the numerical to the analytical result shrinks with higher and higher resolution.

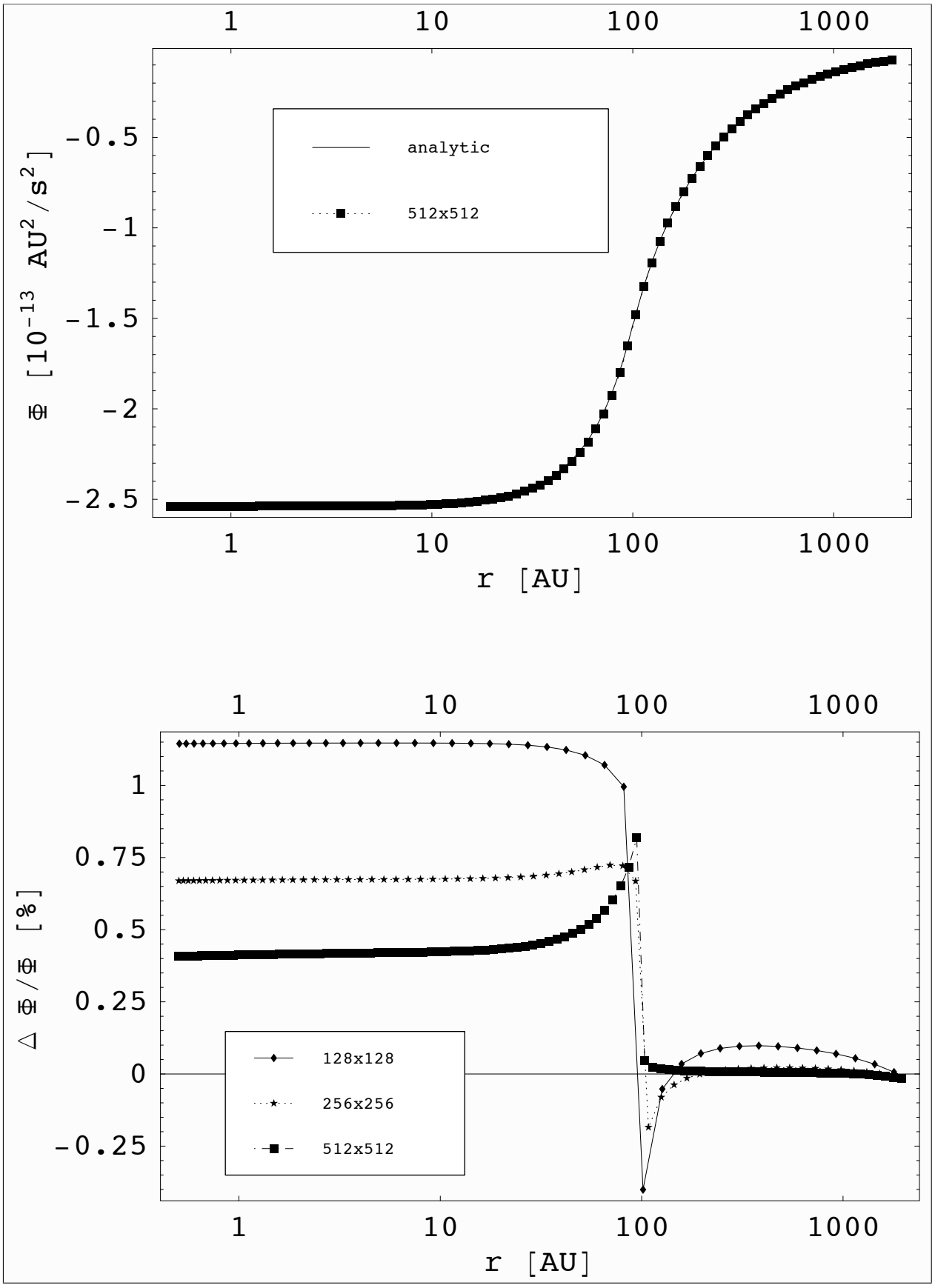

Figure 2.6: Static two-dimensional test results along the long semiaxis in the *x*-*y* plane. The surface of the spheroid is reached at 100 AU.

Upper panel: Numerical (dots) and analytical solution (solid line) of the gravitational potential for the highest resolution run.

Lower panel: Deviation of the numerical solution from the analytic one at different resolutions.

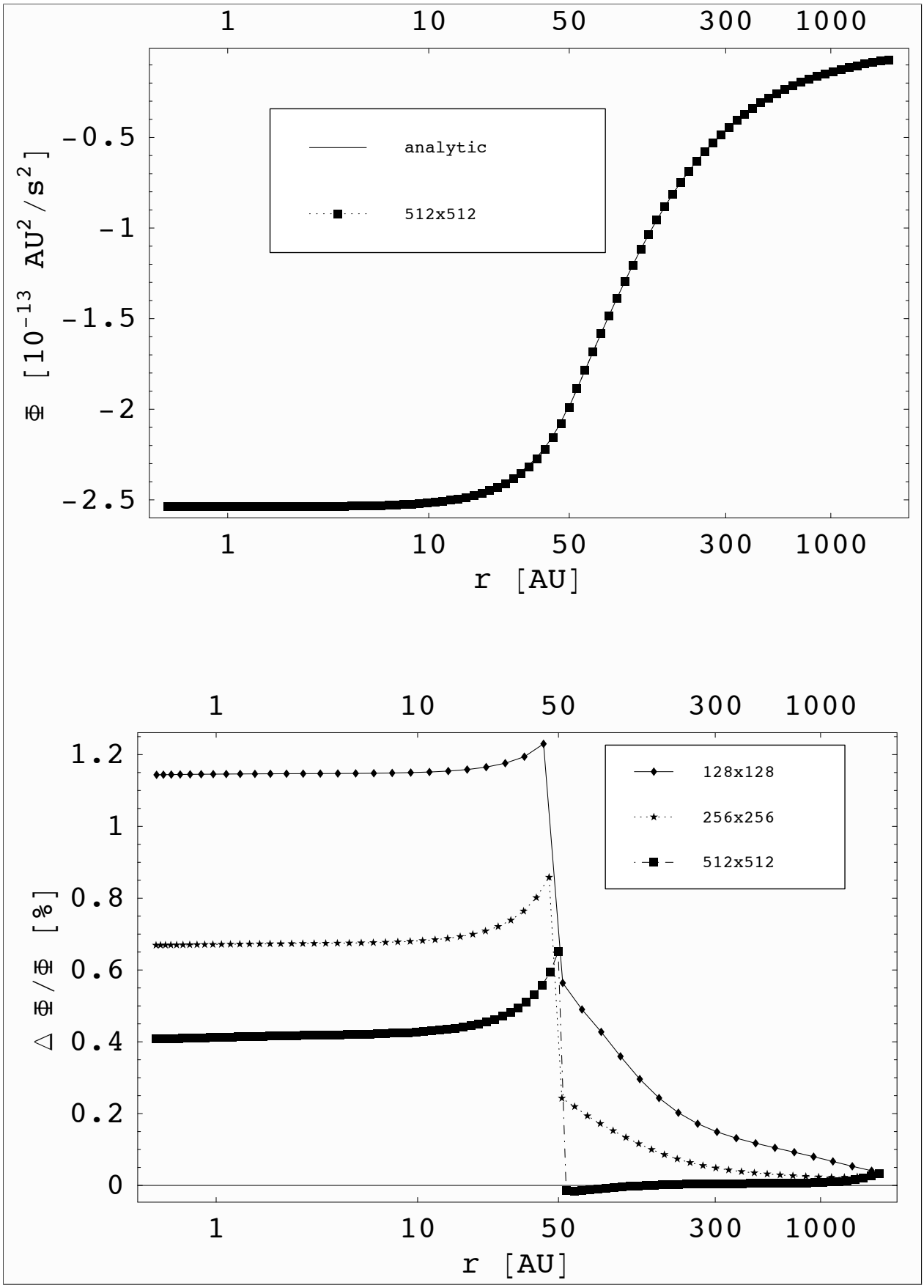

Figure 2.7: Static two-dimensional test results along the short symmetry semiaxis in the z direction. The surface of the spheroid is reached at 50 AU.
Upper panel: Numerical (dots) and analytical solution (solid line) of the gravitational potential for the highest resolution run.
Lower panel: Deviation of the numerical solution from the analytic one at different resolutions.

2.4.2.3 Static three-dimensional test

The density distribution of the three-dimensional test is defined by an iso-density ellipsoid with semiaxes of length $a > b > c$ in the x, y and z direction respectively. The shape of an ellipsoid is given by the fact that its interior points fulfill the relation

$$\frac{x^2}{a^2} + \frac{y^2}{b^2} + \frac{z^2}{c^2} \leq 1. \tag{2.34}$$

On the discretized spherical grid, we set the density of grid cells for which the center fulfills this relation to the iso-density value of ρ_0, otherwise to zero. No smoothing or averaging is applied at the surface of the discretized ellipsoid. The analytic solution in the interior (Ramsey 1961) of an ellipsoid is given by

$$\Phi(x, y, z) = \pi G \rho_0 abc \left(Ax^2 + By^2 + Cz^2 - D \right) \tag{2.35}$$

with the abbreviations

$$A = \int_0^\infty \sqrt{\left(a^2 + \alpha^2\right)^3 \left(b^2 + \alpha^2\right) \left(c^2 + \alpha^2\right)}\, d\alpha \tag{2.36}$$

$$B = \int_0^\infty \sqrt{\left(a^2 + \alpha^2\right) \left(b^2 + \alpha^2\right)^3 \left(c^2 + \alpha^2\right)}\, d\alpha \tag{2.37}$$

$$C = \int_0^\infty \sqrt{\left(a^2 + \alpha^2\right) \left(b^2 + \alpha^2\right) \left(c^2 + \alpha^2\right)^3}\, d\alpha \tag{2.38}$$

$$D = \int_0^\infty \sqrt{\left(a^2 + \alpha^2\right) \left(b^2 + \alpha^2\right) \left(c^2 + \alpha^2\right)}\, d\alpha \tag{2.39}$$

These integrals depend only on the lengths of the three different semiaxes a, b and c and can quickly be solved numerically for the specified case. The semiaxes are chosen to be 100 AU, 50 AU and 25 AU respectively. The iso-density in the test case is chosen to be $\rho_0 = 10^{-10}\mathrm{g\ cm^{-3}}$. The computational domain ranges from 0.5 to 2000 AU radially and covers the full polar (180°) and azimuthal angle (360°). The computational domain is divided into $N^3 = 16^3, 32^3$ or 64^3 grid cells. The radial grid size of each cell grows proportional to the radius. The resulting gravitational potential along the cartesian x, y, and z axes as well as the deviation of the numerical solution from the analytic one is displayed in Figs. 2.8 to 2.10. As expected, the numerical result monotonically approaches the analytic one with increasing resolution.

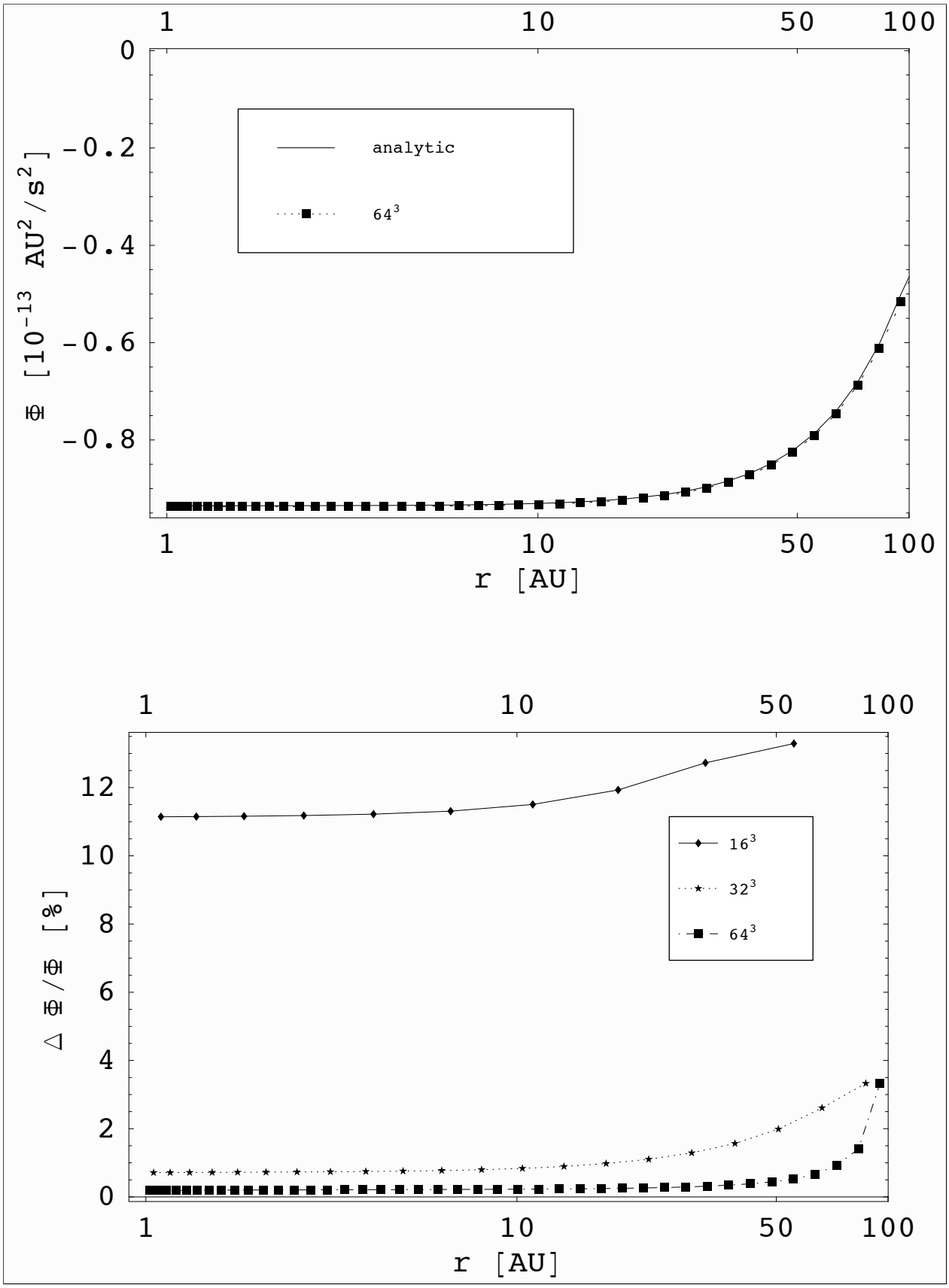

Figure 2.8: Static three-dimensional test results along the x axis (100 AU).
Upper panel: Resulting numerical (dots) and analytical solution (solid line) of the gravitational potential for the highest resolution run.
Lower panel: Deviation of the numerical solution from the analytic one at different resolutions.

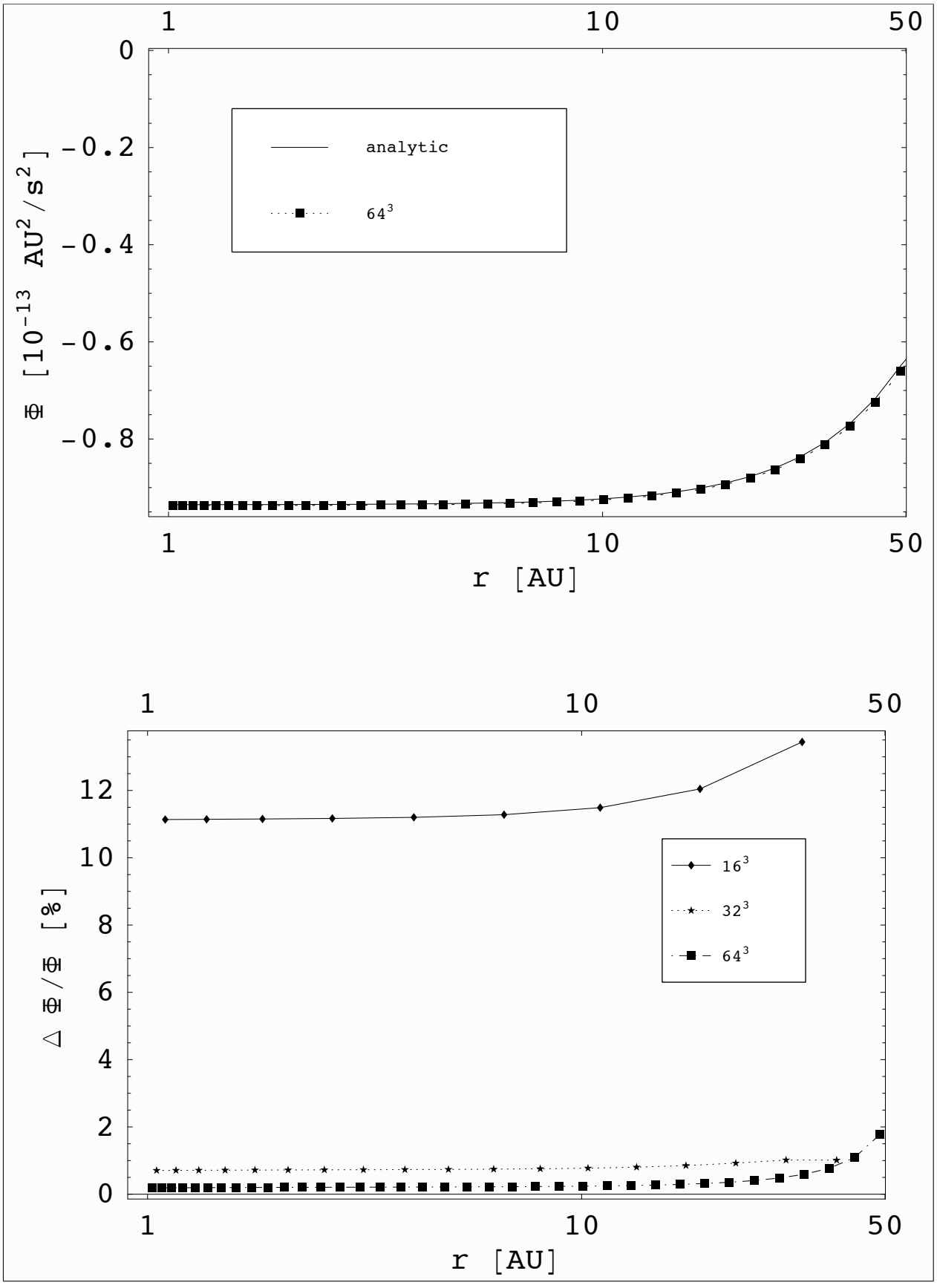

Figure 2.9: Static three-dimensional test results along the *y* axis (50 AU).
Upper panel: Resulting numerical (dots) and analytical solution (solid line) of the gravitational potential for the highest resolution run.
Lower panel: Deviation of the numerical solution from the analytic one at different resolutions.

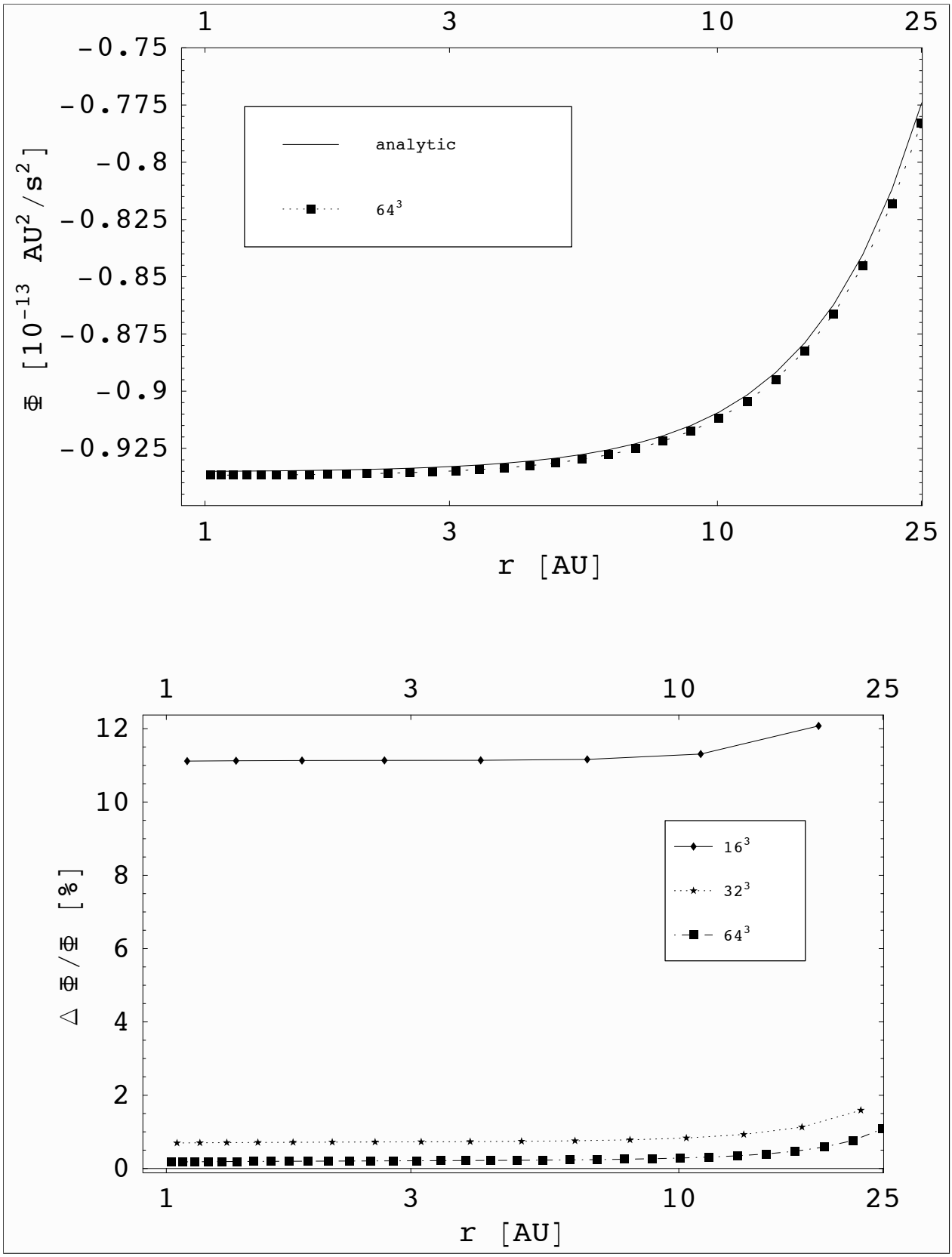

Figure 2.10: Static three-dimensional test results along the z axis (25 AU).
Upper panel: Resulting numerical (dots) and analytical solution (solid line) of the gravitational potential for the highest resolution run.
Lower panel: Deviation of the numerical solution from the analytic one at different resolutions.

2.5 Radiation transport

The most accurate description of the physics proceeding during the collapse of a pre-stellar core would include a frequency dependent radiation transport step after each hydrodynamic timestep using a modern Monte-Carlo based or ray-tracing radiative transfer method. The CPU time needed to solve one single hydrodynamic timestep is generally orders of magnitude lower than the time for a frequency dependent radiative transfer step, especially in complex geometries. This approach is not feasible with current computing technology for a large number of grid cells in more than one dimension due to the large amount of computational time needed for each radiation transport step. A more desired radiation hydrodynamics scheme should roughly spend the same CPU time on the radiation physics as on the hydrodynamics part. Sensible approximations are thus necessary to speed up the radiative transfer in such hydrodynamics studies.

A first approach for fast two-dimensional axially symmetric radiative transfer is, for example, the gray diffusion approximation studied by Tscharnuter & Boss (1993), which is only applicable in the optically thick limit. Ray-tracing based methods (such as Efstathiou & Rowan-Robinson 1990) show high accuracy, but as already mentioned also require much CPU time, which yields low efficiency in combination with hydrodynamics solvers. Another common approach for the description of radiative processes in circumstellar disks is the gray FLD approximation (e.g. Kley 1989; Bodenheimer et al. 1990; Klahr et al. 1999; Klahr & Kley 2006). It provides a fast method to determine the temperature evolution in the optically thick (diffusion) as well as in the optically thin (free-floating) limit, but shows stronger deviations in transition regions (cp. Boley et al. 2007). In the case of gray FLD, which is still the default method in modern radiation hydrodynamics codes, this method suffers strongly from the lack of frequency dependence, when compared to the accuracy of modern Monte-Carlo based codes.

The important role of frequency dependent radiation transport in the formation of massive stars was already shown in Yorke & Sonnhalter (2002), but due to the huge computational overhead of the frequency dependent FLD routine it was neither possible to study a large number of different initial conditions (to scan the parameter space), nor to perform high-resolution simulations of the accretion process. Murray et al. (1994) introduced a splitting of the radiation field into an irradiated and a diffuse part in their hydrostatic disk atmosphere computations. Wolfire & Cassinelli (1987) used such a splitting to study the radiation feedback of massive stars, which has been shown to be a valid approach in one-dimensional simulations by Edgar & Clarke (2003). In this part of the project, we expand the method to higher dimensions and show its validity in an axially symmetric setup, consisting of a star, a flared circumstellar disk and an envelope (Pascucci et al. 2004). We found that it is necessary to consider the frequency dependence of the stellar irradiation feedback to reconstruct a reasonable approximation to the spatial temperature distribution.

We present our results in combining the advantage of the gray FLD approximation (speed) with the accuracy of frequency dependent ray-tracing. The approximation described here results in a large reduction in computing time compared to Monte-Carlo based radiative transfer. This allows us to implement this particular code in the framework of three-dimensional (magneto-) hydrodynamics simulations of circumstellar disks and in-falling envelopes on a parallel decomposed (spherical) grid. The following subsections contain a brief theoretical derivation (Sect. 2.5.1), a comparison study with a standard full frequency dependent Monte-Carlo based radiative transfer code (Sect. 2.5.2), parallel performance tests of the underlying solving algorithm (Sect. 2.5.3), as well as standard radiative hydrodynamic shock tests (Sect. 2.5.4).

2.5.1 Theory and numerics of the approximate radiation transport scheme

In the following, we recapitulate the general ideas, the basic equations and methods of the frequency dependent approximate radiation transport scheme. This section should allow the reader to follow our motivation for the newly implemented three-dimensional radiative transfer module. Every implemented formula and numerical detail is given.

The general idea of the method is to split the radiation field as well as the transport into two components (Wolfire & Cassinelli 1987; Murray et al. 1994; Edgar & Clarke 2003). Stellar radiative forces will mostly act on the surrounding gas and dust mixture in the first transition region from optically thin (e.g. where the dust is evaporated) to optically thick (e.g. a massive accretion disk). This is exactly the region, where the FLD approximation is incorrect (e.g. Boley et al. 2007). To avoid this disadvantage of the FLD approximation, we first calculate the stellar radiative flux through the environment including its absorption in a corresponding first order ray-tracing routine. First order means that the spatial distribution of the radiative flux from the stellar irradiation is calculated according to the frequency dependent optical depth, but re-emission of photons is shifted to a gray FLD solver. Sources for the thermal dust emission are the absorbed energy from the prior stellar irradiation step and potentially additional heating from the hydrodynamics, e.g. due to compression of the gas, accretion luminosity of sink cells, or viscous heating. In other words, this means that instead of solving the whole radiation transfer problem either in the FLD approximation or with a ray-tracing technique, we just extract the first (most important) absorption event of the stellar irradiation from the FLD solver and calculate the appropriate flux in an accurate ray-tracing manner. This splitting method allows us to consider the frequency dependence of the stellar spectrum in a very efficient manner.

In the first subsection, we recapitulate the FLD equation for thermal dust emission. In the following two subsections, we explain how this FLD solver can simply be combined with a first order ray-tracing routine (either gray or frequency dependent) to include irradiation feedback from a single central object. Due to the fact that these rays are aligned with the radial axis in spherical coordinates, this kind of coordinate system is highly favored, but not required, to solve the ray-tracing step. In the last subsection, we comment on the so-called generalized minimal residual method (GMRES), our default implicit solver algorithm for the FLD equation.

2.5.1.1 Flux Limited Diffusion

The thermal dust emission is solved in the FLD approximation based on a diffusion equation for the thermal radiation energy density E_R. Within a given spatial density $\rho(\vec{x})$ and temperature $T(\vec{x})$ distribution, we start from the time evolution of the internal energy density E_int and thermal radiation energy E_R:

$$\partial_t E_\mathrm{int} + \vec{\nabla}\cdot(\vec{u}E_\mathrm{int}) = -p\vec{\nabla}\cdot\vec{u} + \Lambda \tag{2.40}$$

$$\partial_t E_\mathrm{R} + \vec{\nabla}\cdot(\vec{u}E_\mathrm{R}) = -\vec{\nabla}\cdot\vec{F} - \Lambda \tag{2.41}$$

with the corresponding thermal pressure p, dynamical velocity $\vec{u}$ and flux of radiation energy density $\vec{F}$. The radiative heating and cooling of the gas is covered in $\Lambda = \rho c \kappa_\mathrm{R}(aT^4 - E_\mathrm{R})$, where c is the speed of light, κ_R the Rosseland mean opacity and a the radiation constant. Gas and dust temperatures are assumed to be the same ($T_{gas} = T_{dust} = T$).

We add up the Eqs. 2.40 and 2.41 and solve the transport term $\vec{\nabla}(\vec{u}E_\mathrm{R})$ separately, if necessary, in the dynamical problem. If we consider the transport of the internal energy $\vec{\nabla}\cdot(\vec{u}E_\mathrm{int})$ already during the corresponding

hydrodynamics step (operator splitting) the remaining terms yields

$$\partial_t(E_{\text{int}} + E_{\text{R}}) = -\vec{\nabla} \cdot \vec{F} + Q^+, \tag{2.42}$$

where the source term $Q^+ = -p\vec{\nabla} \cdot \vec{u}$ depends on the physics included and can contain additional source terms such as accretion luminosity from sink cells or viscous heating.

In the following, we use the assumption that the gas and radiation temperature are in equilibrium (also called one-temperature radiation transport), which is a widely used approach in radiation hydrodynamics simulations of circumstellar disks. In a purely FLD radiation transport method, this assumption is justified for optically thick regions (e.g. deeply inside an accretion disk). The usage of our split radiation scheme guarantees the correct gas temperature in regions of dominating stellar irradiation (like an optically thin envelope or disk atmosphere). In residual regions (shielded from the irradiation behind the optically thick circumstellar disk) the gas and radiation temperature will differ only for very strong shocks. Otherwise, the gas and radiation temperature of these cold regions will be in equilibrium. In this special case of a strong shock in a shielded, optically thin region, the one-temperature approach yields the correct temperature of the shocked gas, but results in a steeper temperature gradient than a two-temperature radiation transport method in the upstream direction of the radiation flux (see also radiative hydrodynamics shock tests described in Sect. 2.5.4). Consideration of such small effects at outer regions of the domain goes beyond the scope of this research project, which focuses on the details of stellar radiative feedback on the accretion flow onto a massive star. In the end, we will benefit from the speedup of the radiation transport solver by cutting the number of unknown variables in half. Moreover, the stiffness of the set of equations is much less if the above local equilibrium assumption is made.

Expressing both energies on the left hand side of Eq. 2.42 in terms of temperature allows us to derive a relation between the time derivatives of the energies. The radiation energy density in absence of irradiation (see following subsection for the case including irradiation) is given by

$$\boxed{E_{\text{R}} = aT^4.} \tag{2.43}$$

This expression plus the internal energy density $E_{\text{int}} = c_{\text{V}}\rho T$ with the specific heat capacity c_{V} yield

$$\partial_t E_{\text{int}} = c_{\text{V}}\rho\partial_t T = \frac{c_{\text{V}}\rho}{4aT^3}\partial_t E_{\text{R}}. \tag{2.44}$$

With this relation, the problem 2.42 reduces to a standard diffusion equation

$$\boxed{\partial_t E_{\text{R}} = f_c\left(-\vec{\nabla} \cdot \vec{F} + Q^+\right)} \tag{2.45}$$

with $f_c = \left(c_{\text{V}}\rho/4aT^3 + 1\right)^{-1}$, depending only on the ratio of internal to radiation energy. The flux $\vec{F}$ of radiation energy density is determined in the FLD approximation via

$$\vec{F} = -D\vec{\nabla}E_{\text{R}} \tag{2.46}$$

with the diffusion coefficient $D = \lambda c/\kappa_R\rho$. The flux limiter λ is chosen according to Levermore & Pomraning (1981). Scattering is neglected. In the most extreme limits, the flux becomes either $\vec{F} = -cE_{\text{R}}\vec{\nabla}E_{\text{R}}/|\vec{\nabla}E_{\text{R}}|$ for highly optically thin regions (free-streaming limit) or $\vec{F} = -c\vec{\nabla}E_{\text{R}}/3\kappa_{\text{R}}\rho$ for highly optically thick regions (diffusion limit).

2.5.1.2 Irradiation

When including stellar irradiation, some of the equations have to be modified. The irradiation from a central object is treated as an additional flux $\vec{F}_*$, released along radially outward rays. E_R is the energy density of the radiation emitted by the circumstellar material, and does not include the stellar irradiation. The additional radiation power $-\vec{\nabla}\cdot\vec{F}_*$ from this irradiation is therefore added to the diffusion Eq. 2.45 as a source term

$$\partial_t E_\mathrm{R} = -f_c(\vec{\nabla}\cdot\vec{F} + \vec{\nabla}\cdot\vec{F}_* - Q^+) \qquad (2.47)$$

and has to be added to the left hand side of Eq. 2.43, which is used to calculate either the thermal radiation density or the corresponding dust temperature T under the assumption that the dust is in equilibrium with the combined stellar and diffuse radiation field:

$$aT^4 = E_\mathrm{R} + \frac{\kappa_P(T_*)}{\kappa_P(T)}\frac{|\vec{F}_*|}{c}. \qquad (2.48)$$

Here $\kappa_P(T)$ represents the Planck mean opacity at a given temperature T and T_* is the star's effective temperature.

Since the opacity $\kappa_\mathrm{P}(T)$ depends on the temperature the right hand side of Eq. 2.48 also depends on the solution of T. This makes an iterative procedure based on the Newton-Raphson method necessary to find the solution. The ratio of opacities $\kappa_\mathrm{P}(T_*)/\kappa_\mathrm{P}(T)$ corresponds to the relation of emission from and absorption by dust.

The stellar radiative flux as a function of distance r from the central object is calculated by

$$\vec{F}_*(r) = \vec{F}_*(R_*)\left(\frac{R_*}{r}\right)^2 e^{-\tau(r)} \qquad (2.49)$$

The (boundary) flux at the stellar surface $\vec{F}_*(R_*)$ can be calculated from the Stefan-Boltzmann law

$$|\vec{F}_*(R_*)| = \sigma_\mathrm{SB}\, T_*^4 \qquad (2.50)$$

with the Stefan-Boltzmann constant $\sigma_\mathrm{SB} = a\,c/4$. The optical depth τ is, in the case of gray irradiation (see following subsection for specific changes due to frequency dependent irradiation), calculated along radial rays through the spherical grid via

$$\tau_\mathrm{P}(r) = \int_{R_*}^{r} \kappa_\mathrm{P}(T_*)\,\rho(r)\,dr. \qquad (2.51)$$

The optical depth between the stellar surface and the inner boundary of the spherical computational domain is assumed to be negligible.

A flow chart of the radiation module described so far is shown for a static problem such as the benchmark test of Sect. 2.5.2 in Fig. 2.11.

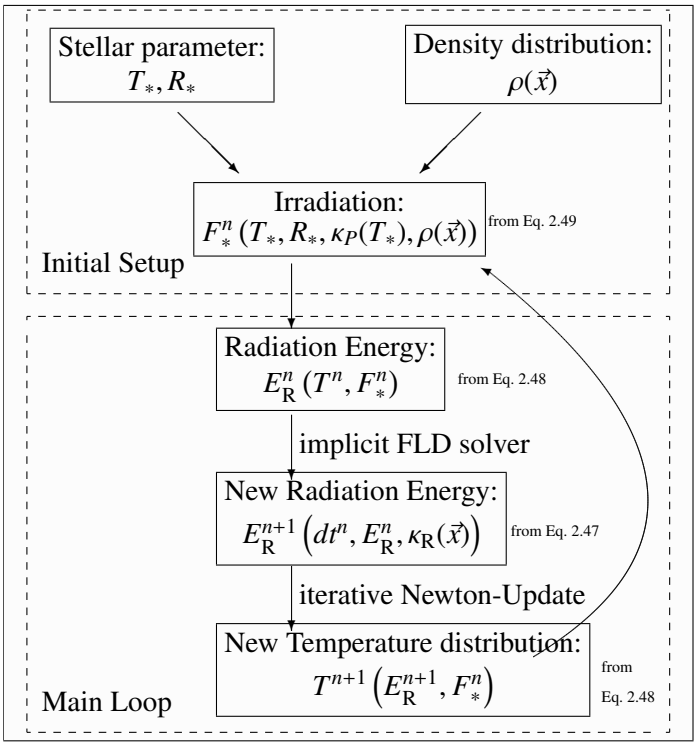

Figure 2.11: Schematic flow chart of the radiation module for a static problem. Exponents declare the timestep number n. The timestep used is denoted by $dt^n = t^n - t^{n-1}$.

2.5.1.3 Frequency dependent irradiation

Taking into account the frequency dependence of the stellar flux, we consider a fixed number of frequency bins, characterized by their mid-frequency ν_i, instead of the gray irradiation. For the radiation benchmark test (Sect. 2.5.2) we use the opacity tables of Draine & Lee (1984), including 61 frequency bins (see Fig. 2.19 on p. 57). For the pre-stellar core collapse simulations (Chapt. 4) we use the opacity tables of Laor & Draine (1993), including 79 frequency bins (see Fig. 2.12). Each dot in Fig. 2.12 represents the mid-frequency of the corresponding frequency bin. Including the frequency dependence, we have to replace the Planck mean opacity $\kappa_P(T_*)$ in Eqs. 2.48 and 2.51 with the frequency dependent opacity $\kappa(\nu)$ and the stellar flux $\vec{F}_*$ in Eqs. 2.47 and 2.48 with the corresponding sum over the frequency dependent fluxes $\vec{F}_*(\nu)$, each calculated via Eq. 2.49.

The boundary condition, given by Eq. 2.50, is now determined for each frequency bin by the integral over the corresponding part of the stellar black body Planck function $B_\nu(\nu, T_*)$ in the frequency dependent interval:

$$|\vec{F}_*(R_*, \nu_i)| = \frac{c}{4} \int_{(\nu_{i-1}+\nu_i)/2}^{(\nu_i+\nu_{i+1})/2} B_\nu(\nu, T_*)\, d\nu \tag{2.52}$$

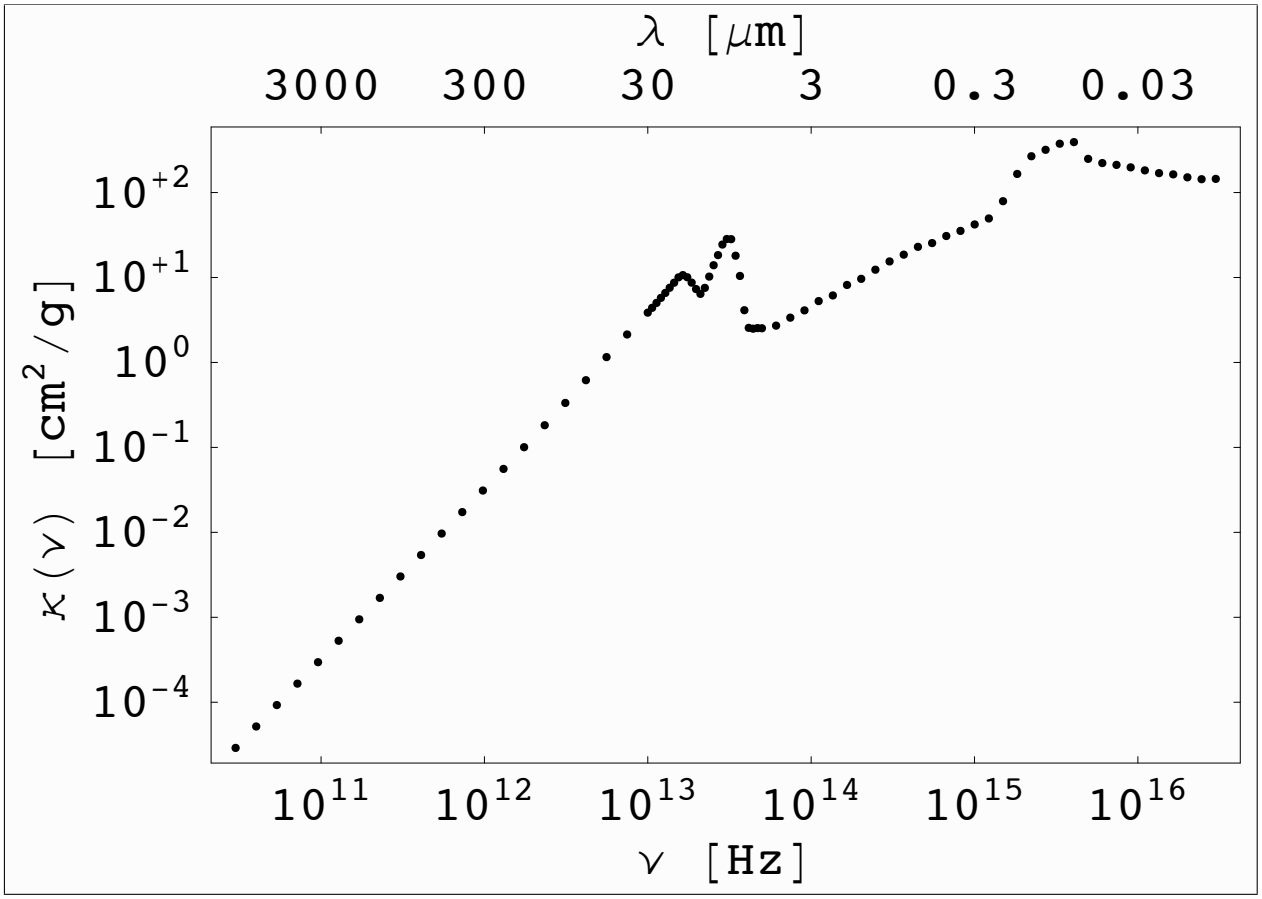

Figure 2.12: Frequency dependent opacities $\kappa(\nu)$ in tabulated form from Laor & Draine (1993).

2.5.1.4 Radiative force

Stellar radiative feedback onto the dynamics of the environment plays a crucial role in the formation of massive stars. The heating will probably prevent further fragmentation of the cloud by enhancing the Jeans mass (e.g. Krumholz et al. 2007). Furthermore the dusty environment feels the radiative force when absorbing the radiation due to momentum conservation, which potentially stops the accretion process for highly luminous massive stars. Therefore, it is necessary to compute the correct radiative flux (and its derivative, the radiative force) in addition to the temperature distribution in such simulations.

The radiative force density is, accordingly to Mihalas & Mihalas (1984), given by

$$\vec{f}_{\rm rad} = \rho\kappa\frac{\vec{F}_{\rm tot}}{c}. \qquad (2.53)$$

In our split radiation transport the total radiative flux $\vec{F}_{\rm tot}$ is given by the sum of the irradiated stellar flux $\vec{F}_*$ from the ray-tracing routine and the diffuse component $\vec{F}$ from the FLD solver. The flux calculated in the FLD approximation is $\vec{F} = -D\vec{\nabla}E_{\rm R}$ (see Sect. 2.1).

In discretized space the opacity and density are constant over a single grid cell and the irradiated stellar radiative flux $\vec{F}_*$ is calculated at the cell interfaces. To calculate the mean radiative force inside this cell it is necessary to integrate the radiative force over the cell volume (e.g. a simple ansatz of averaging only the stored fluxes at the interfaces towards the cell center would lead to unphysically high radiative forces for $\tau >> 1$, i.e. for the case that most of the flux is absorbed on a length scale much smaller than the grid size). Integrating the above formula Eq. 2.53 over space (for simplicity here: an one-dimensional cartesian grid with an uniform grid spacing of Δx) leads to:

$$\vec{f}_* = \frac{1}{\Delta x}\int_0^{\Delta x}\rho\kappa\frac{\vec{F}_*}{c}dx \qquad (2.54)$$

$$= \frac{1}{c\Delta x}\rho\kappa\int_0^{\Delta x}\vec{F}_* dx \qquad (2.55)$$

The flux at position x inside the grid cell is given by the flux $\vec{F}_*^i$ entering the cell at the interface i and the absorption of this flux along the length x:

$$\vec{F}_*(x) = \vec{F}_*^i e^{-\tau} \qquad (2.56)$$

with the optical depth $\tau = \kappa\rho x$. The remaining integral yields:

$$\vec{f}_* = \frac{1}{c\Delta x}\rho\kappa\vec{F}_*^i\int_0^{\Delta x}e^{-\kappa\rho x}dx \qquad (2.57)$$

$$= -\frac{1}{c\Delta x}\vec{F}_*^i\,(e^{-\kappa\rho\Delta x} - 1). \qquad (2.58)$$

Finally the mean radiative force is therefore given by the spatial derivative of the radiative flux:

$$\vec{f}_* = -\frac{1}{c}\frac{\vec{F}_*^{i+1} - \vec{F}_*^i}{\Delta x} \qquad (2.59)$$

$$= -\frac{1}{c}\partial_x\vec{F}_* \qquad (2.60)$$

Eqs. 2.53 and 2.59 reflect the fact that without emission the radiative flux is given by the differential equation

$$\partial_x \vec{F}_* = -\rho\kappa\vec{F}_*. \qquad (2.61)$$

In other words, this relationship shows that the original Eq. 2.53 and the derived Eq. 2.59 are indeed identical (in continuous physical space), whereas the left hand side of Eq. 2.61 gives the expression easily available in discretized space.

In our code we use a grid in spherical coordinates, thus the derivative of the stellar irradiation is given by

$$\vec{f_*} = -\frac{1}{cr^2}\partial_r(r^2\vec{F}_*). \qquad (2.62)$$

So the purely geometrical dilution of the flux in the radially outward direction $\left(\vec{F}_*(r) \propto r^{-2}\right)$ does of course not contribute to the radiative force.

Summing up, the radiative force feedback entering the conservation laws of hydrodynamics 2.3 and 2.4 via the acceleration vector $\vec{a}_4$ is

$$\vec{a}_4 = -\frac{\vec{\nabla}\cdot\vec{F_*}}{\rho c}\vec{e}_r - \kappa_{\mathrm{R}}\frac{D\vec{\nabla}E_{\mathrm{R}}}{c}. \qquad (2.63)$$

2.5.1.5 The generalized minimal residual method

The FLD Eq. 2.45 or 2.47 are solved in our newly implemented approximate radiation transport module for hydrodynamics in an implicit fashion via a generalized minimal residual (GMRES) solver. The GMRES solver is a Krylov subspace (KSP) method for solving a system of linear equations $A\vec{x} = \vec{b}$ via an approximate inversion of the large but sparse matrix A and is an advancement of the minimal residual (MinRes) method. The GMRES method was developed in 1986 and is described in Saad & Schultz (1986). This method is much better than the conjugate gradient (CG) or successive over-relaxation (SOR) method, which was used in prior versions of the radiation transport scheme, and at least as good as the well-known improved stabilized Bi-Conjugate Gradient (BiCGstab) method used, e.g., in Yorke & Sonnhalter (2002).

The general idea of minimal residual solvers based on the KSP method is the following: The i^{th} KSP is defined as $K_i = \mathrm{span}\{\vec{b}, A\vec{b}, A^2\vec{b}, ..., A^{i-1}\vec{b}\}$. In each solver iteration i the GMRES method increments the used subspace K_i with an additional basis vector $A^{i-1}\vec{b}$ and approximates the solution of the system of linear equations by the vector $\vec{x}_i$ which minimizes the norm of the residual $r = |A\vec{x}_i - \vec{b}|$. This method converges monotonically and theoretically reaches the exact solution after performing as many iterations as the column number of the matrix A (which equals the number of grid cells). Of course, in practice the iteration is already stopped after reaching a specified relative or absolute tolerance of the residual, which normally takes only a small number of iterations. The computation of each iteration grows like $O(i^2)$. In the current implementation, we use the so-called 'GMRES restarted' by default. GMRES restarted never performs all the iterations to reach the exact solution. After a priorily fixed number of internal iterations n, the solver starts a second time in the first subspace K_1 but with the last approximate solution $\vec{x_n}$. Due to the growing computational effort with $O(i^2)$ this approach generally results in a speedup of the computation.

The radiation transport module is parallelized for distributed memory machines, using the message passing interface (MPI) language. The results of a detailed parallel performance test of the whole radiation transport module, including this GMRES solver is presented in Sect. 2.5.3.

2.5.2 Frequency dependent test of the approximate radiation transport

The approximate radiative transfer introduced in the previous section can now be tested for realistic dust opacities in a standard benchmark test for irradiated circumstellar disk models. The setup of the following comparison was adopted from Pascucci et al. (2004) and includes a central solar-type star, an irradiated flared disk and an envelope. We had to choose a low-mass central star because no benchmark for high-mass stars has been performed so far. However, the tests should not depend on the actual size and luminosity of the central star. For comparison, we chose a standard full frequency dependent Monte-Carlo based radiation transport code. The comparison was done for two different (low and high) optical depths taken from the original radiation benchmark test. To test each of the components (gray and frequency dependent irradiation as well as Flux Limited Diffusion) of the proposed approximate radiative transfer separately, we performed several test runs with and without the different physical processes (absorption and re-emission) with both the approximate (see table 2.3) and the Monte-Carlo based (see table 2.2) radiative transfer code.

2.5.2.1 Setup

Physical setup of the star, the disk and the envelope The stellar parameters are solar-like: The effective temperature of the star is 5800 K and the stellar radius is fixed to 1 solar radius. The disk ranges from $r_{\min} = 1$ AU up to $r_{\max} = 1000$ AU.
Although the numerical setup of the gas density is done in spherical coordinates, the analytic setup of the gas density, as described in the original benchmark test, is given in cylindrical coordinates:

$$\rho(r,z) = \rho_0 \, f_1(r) \, f_2(r,z) \tag{2.64}$$

with the radially and vertically dependent functions

$$f_1(r) = \frac{r_d}{r}$$
$$f_2(r,z) = \exp\left(-\frac{\pi}{4}\left(\frac{z}{h(r)}\right)^2\right)$$

making use of the following abbreviations

$$\begin{aligned} h(r) &= z_d \left(\frac{r}{r_d}\right)^{1.125} \\ r_d &= \frac{r_{\max}}{2} = 500AU \\ z_d &= \frac{r_{\max}}{8} = 125 \text{ AU} \end{aligned}$$

The lowest density is limited to a relative factor of 10^{-100} compared to the highest density (at $r_{\min}$ in the midplane) to avoid divisions by zero (e.g. in the calculation of the diffusion coefficients). The normalization ρ_0 of the density setup is chosen to define different optical depths $\tau_{550\text{nm}}$ through the midplane of the corresponding circumstellar disk (at a visual wavelength of 550 nm):

$\tau_{550\text{nm}}$	ρ_0 [g cm^{-3}]	M_{tot} of gas [M$_\odot$]
0.1	$8.321 * 10^{-21}$	$1.1 * 10^{-5}$
100	$8.321 * 10^{-18}$	$1.1 * 10^{-2}$

The opacity tables used are the same as in the original benchmark test (Pascucci et al. 2004) taken from Draine & Lee (1984). They are displayed in Fig. 2.19.

Numerical setup of the approximate radiative transfer code The runs of the approximate radiative transfer code were performed on a radially stretched, polar uniform, spherical, two-dimensional grid. The chosen grid consists of 60 cells in the radial direction by 61 cells in the polar direction (plus additional cells for storage of boundary conditions). The polar range covers the full spatial setup of 180°. Stretching of the radial grid dimension by an additional 10% from one cell to the next was applied. The implicit diffusion Eq. 2.47 was solved via the GMRES method (see prior section) after parallel/global Block-Jacobian and serial/local ILU preconditioning in the framework of the version 2.3.3 of the open source parallel solver library PETSc (Portable, Extensible Toolkit for Scientific Computation). More detailed information about this solver library can be found in Balay et al. (2001, 2004).

The gradient of the radiation energy is zero at the inner radial and both polar boundaries $\left(\vec{\nabla} E_{\mathrm{R}} = 0\right)$, i.e. radiative flux over these boundaries is prohibited. The radial outer boundary is defined as a constant Dirichlet boundary corresponding to $T_0 = 14.7$ K $\left(E_{\mathrm{R}} = aT_0^4\right)$.

The timestep used for the FLD solver was 10^4 s. The main iteration (circle of irradiation and FLD steps) was stopped when the relative change of the temperature in each cell was smaller than 0.01%, leading to 3 main iterations in the purely absorption run and more than 600 main iterations in the irradiation plus FLD runs.

Numerical setup of the Monte-Carlo based comparison code RADMC For comparison we used the Monte-Carlo based radiative transfer code RADMC described in Dullemond & Turolla (2000) and Dullemond & Dominik (2004). The general solver method of the code is based on Bjorkman & Wood (2001). The Monte-Carlo runs were performed on a 60 x 31 grid assuming symmetry to the disk midplane. The grid was stretched in both directions. One million photons were used.

Scattering can be handled by this code, but was simply switched off as it is neglected in the radiation transport module described here. Scattering would increase the temperature in the irradiated parts (up to an optical depth of about unity) by about 2% in the optically thin envelope up to a maximum of 19% in the optically thick inner rim of the disks midplane due to higher extinction. The more effectively shielded outer regions of the disk would be about 10% cooler. For more massive and luminous stars the effect of scattering would decrease due to stronger forward scattering, which is included in our ray-tracing routine per definition.

2.5.2.2 Configurations of runs performed

The following comparison of the results is divided into three parts (each of the proposed components of the theoretical Sects. 2.5.1.1 - 2.5.1.3 were tested independently): First, we study a pure absorption scenario without diffusion in the optically thin and thick case. Afterwards we include diffusion effects. Therefore, we performed three different runs of the Monte-Carlo based code: a full run for the optically thin case $\tau_{550\mathrm{nm}} = 0.1$, a full run for the optically thick case $\tau_{550\mathrm{nm}} = 100$, and an additional run for the optically thick case $\tau_{550\mathrm{nm}} = 100$ with excluded re-emission of the photons (to achieve a pure absorption scenario for comparison with our first order ray-tracing routine), hereafter called the "one-photon-limit". An overview of these three comparison runs is given in table 2.2.

The resulting temperature distributions of these Monte-Carlo runs are compared with the results of the approximate radiative transfer runs including different components of our module: We discuss five different configurations for the optically thin and thick setup including gray and frequency dependent irradiation plus potential diffusion. An overview of the physics applied and the resulting deviations of these runs from the comparison data is given in table 2.3. All of these results are discussed in detail in the following subsections.

Run	MC0.1-full	MC100-A	MC100-full
Optical depth $\tau_{550\text{nm}}$	0.1	100	100
RADMC - Configuration	"full"	"one-photon-limit"	"full"
Frequency dependence	yes	yes	yes
Comparison Sect.	2.5.2.3	2.5.2.4	2.5.2.5 & 2.5.2.6

Table 2.2: Monte-Carlo comparison runs: The overview table of the comparison runs performed with the Monte-Carlo based code RADMC contains the corresponding optical depth of the test case and the configuration of the Monte-Carlo code used.

Run	G0.1	G100	F100	GD100	FD100
Optical depth $\tau_{550\text{nm}}$	0.1	100	100	100	100
Comparison run	MC0.1-full	MC100-A	MC100-A	MC100-full	MC100-full
Ray-tracing Irradiation	gray	gray	freq. dep.	gray	freq. dep.
Flux Limited Diffusion	no	no	no	yes	yes
Comparison Sect.	2.5.2.3	2.5.2.4	2.5.2.4	2.5.2.5	2.5.2.5 & 2.5.2.6
Deviation $\Delta T/T$ [%]	< +2.0	+10.9 → -57.2	+5.0 → -0.6	+5.0 → -38.4	+9.3 → -11.1

Table 2.3: Overview of runs using the proposed approximate radiation transport: The table contains the corresponding optical depth of the test case and the Monte-Carlo run, which is used for comparison (see also table 2.2 and the corresponding comparison Sects.). Furthermore the applied radiative modules (gray or frequency dependent absorption as well as possible diffusion) of our proposed approximate radiation transport method and the corresponding sections, in which these modules and the final results are discussed, are given. The deviations in the resulting temperature slopes of the approximate radiation transport from the corresponding Monte-Carlo comparison run are shown in the lower row.

2.5.2.3 Gray absorption in an optically thin disk

In the most optically thin case ($\tau_{550\mathrm{nm}} = 0.1$), diffusion effects should be negligible. Therefore, we can test the validity of the routines described in Sect. 2.5.1.2 without running the diffusion routine. Compared to the full Monte-Carlo simulation from RADMC also the deviation in the most "difficult" region of the midplane (due to having the highest absorption) stays below 2% (see Fig. 2.13).

In this optically thin limit, the diffusion effects are indeed negligible: An additionally performed full run of the approximate radiation transfer module with frequency dependent irradiation plus Flux Limited Diffusion shows a variation in the radial temperature slope from the pure gray irradiation run below 1%.

2.5.2.4 Gray and frequency dependent absorption in an optically thick disk

In the most optically thick case ($\tau_{550\mathrm{nm}} = 100$), we tested a pure absorption case to distinguish the deviations introduced by the FLD approximation in the full run from the deviations introduced by the irradiation component of our module. Therefore, we ran the Monte-Carlo code only until every initial photon was absorbed, neglecting re-emission or scattering events. In this scenario, we are able to probe the absorption routines of Sects. 2.5.1.2 and 2.5.1.3 in detail and determine the improvement by considering the frequency dependence of the stellar irradiation. Indeed we found that in order to limit the deviation in the absorption part of the radiation module to less than 5% it is essential to account for the frequency dependence of the stellar irradiation. That is due to the fact that the infrared part of the stellar spectrum has a lower optical depth than the UV part. Neglecting the frequency dependence results roughly in a 57% cooler disk at large radii and a 10% hotter inner rim compared to the Monte-Carlo based radiative transfer code. The resulting temperature profiles through the midplane for both simulations and the corresponding deviation from the Monte-Carlo comparison run are shown in Fig. 2.14.

2.5.2.5 Gray and frequency dependent absorption plus diffusion in an optically thick disk (the complete problem)

In this and the following section, we show the comparison results between the complete approximate radiation transport method with the combination of (gray or frequency dependent) irradiation and Flux Limited Diffusion and the corresponding Monte-Carlo simulation in the most optically thick case ($\tau_{550\mathrm{nm}} = 100$).

Also in this case, we found that the frequency dependent irradiation is necessary to achieve the accuracy needed for realistic radiative feedback in hydrodynamics studies (e.g. in massive star formation or in irradiated accretion disks). Gray irradiation combined with the FLD approximation leads to deviations up to 38.4% in the resulting temperature profile (see Fig. 2.15). Including frequency dependent irradiation and Flux Limited Diffusion the radial temperature profiles agree within 0.7% at the inner boundary up to a maximum deviation of 11.1% at roughly 200 AU. The comparison between the complete radiation scheme and the corresponding Monte-Carlo run is shown in radial and polar temperature profiles in Figs. 2.15 and 2.16. The turnover point (at a polar angle from the midplane of $\theta \approx 19°$) from the optically thin envelope to the optically thick disk region is reproduced very well.

Further remarks and discussion of these results are given in the last Subsect. 2.5.2.7 at the end of the comparison section.

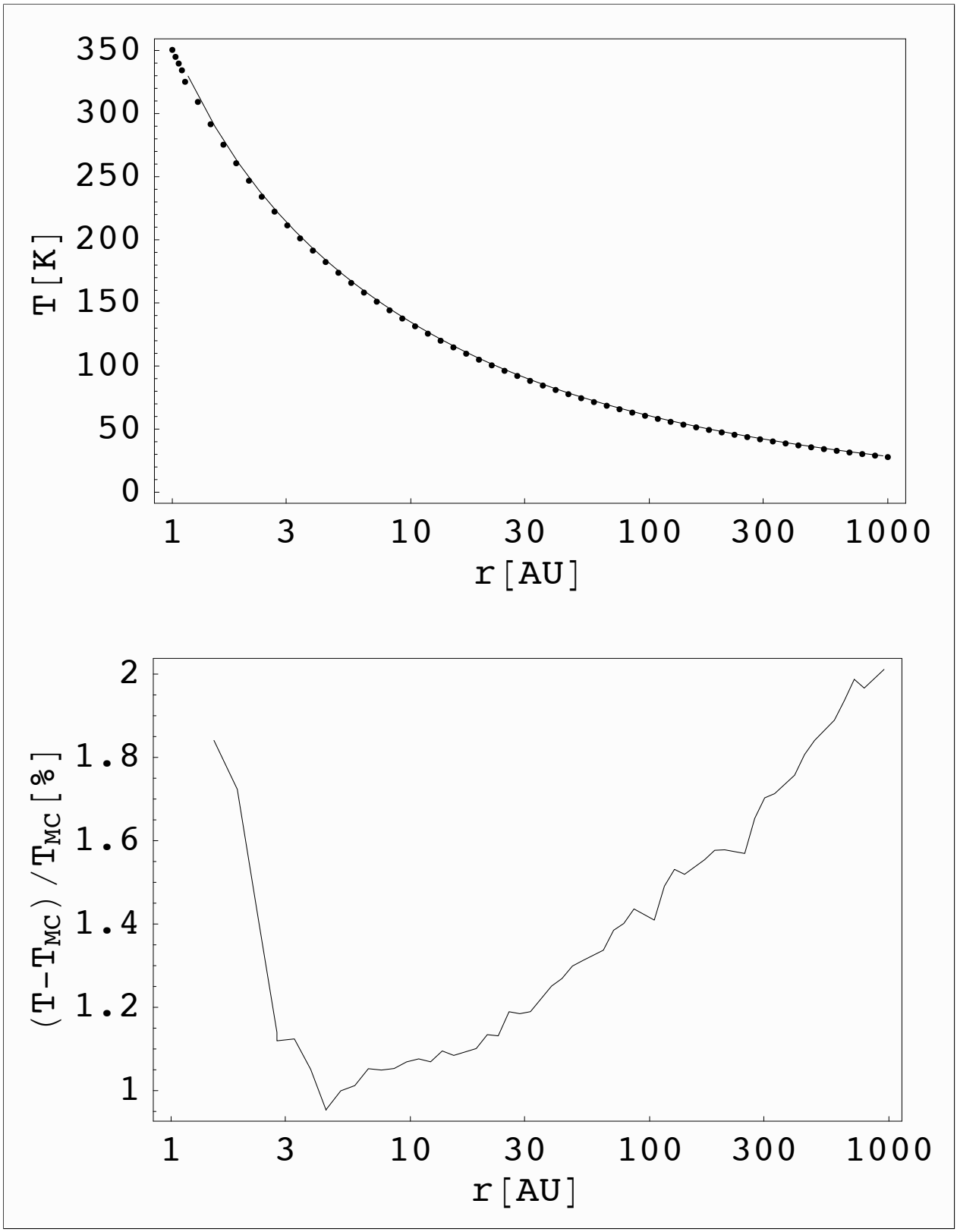

Figure 2.13: Radial cut through the temperature profile in the midplane in the most optically thin case ($\tau_{550\mathrm{nm}} = 0.1$).
Upper panel: Radial temperature slope of the gray irradiation routine (solid line) and the Monte-Carlo based comparison code (dots).
Lower panel: Differences between the two codes in percent.

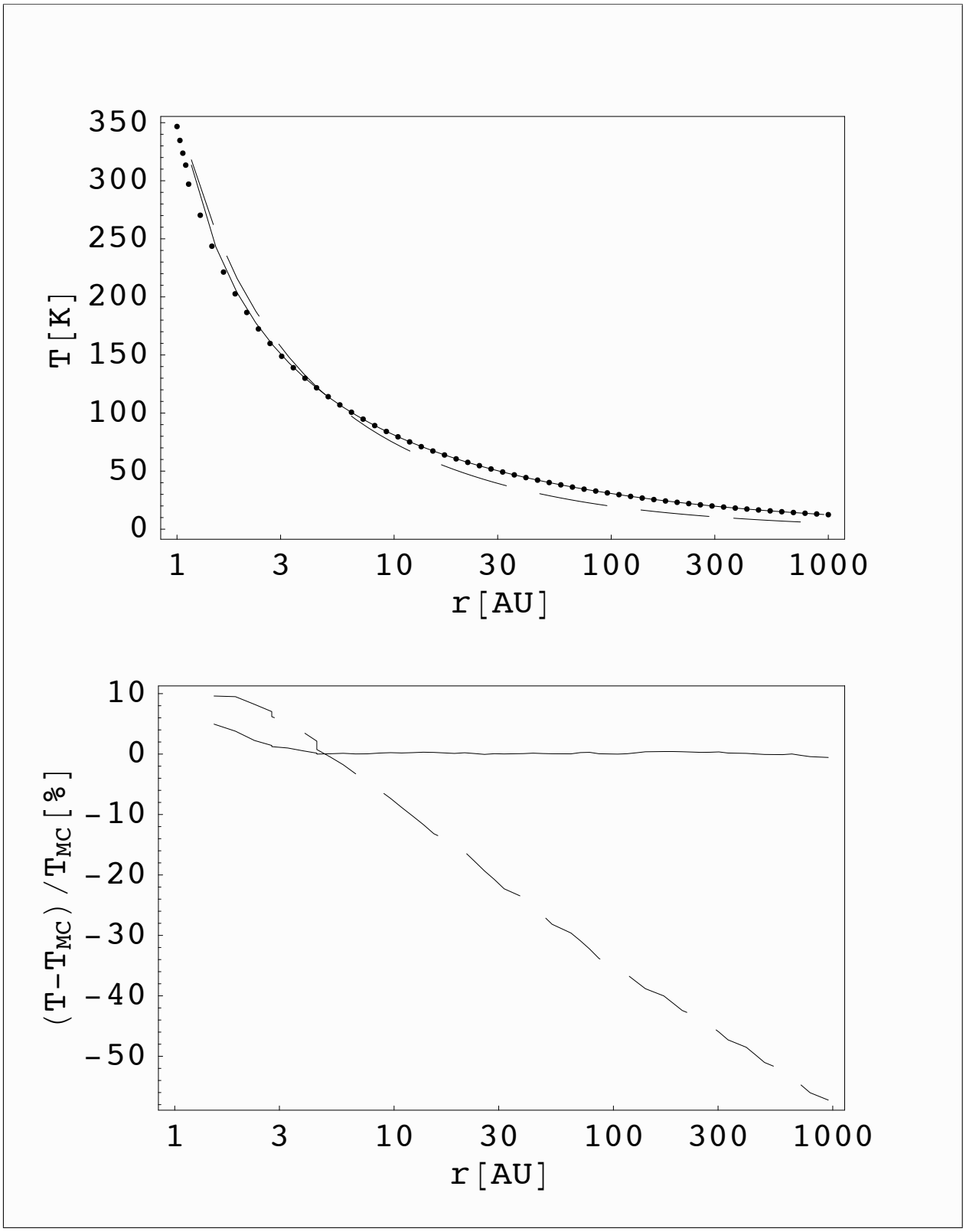

Figure 2.14: Radial cut through the temperature profile in the midplane in the most optically thick case ($\tau_{550\text{nm}} = 100$) without diffusion.
Upper panel: Radial temperature slope of gray irradiation (dashed line), frequency dependent irradiation (solid line) and the Monte-Carlo routine in the "one-photon-limit" (dots).
Lower panel: Deviations of the gray (dashed line) and frequency dependent (solid line) method from the Monte-Carlo code in percent.

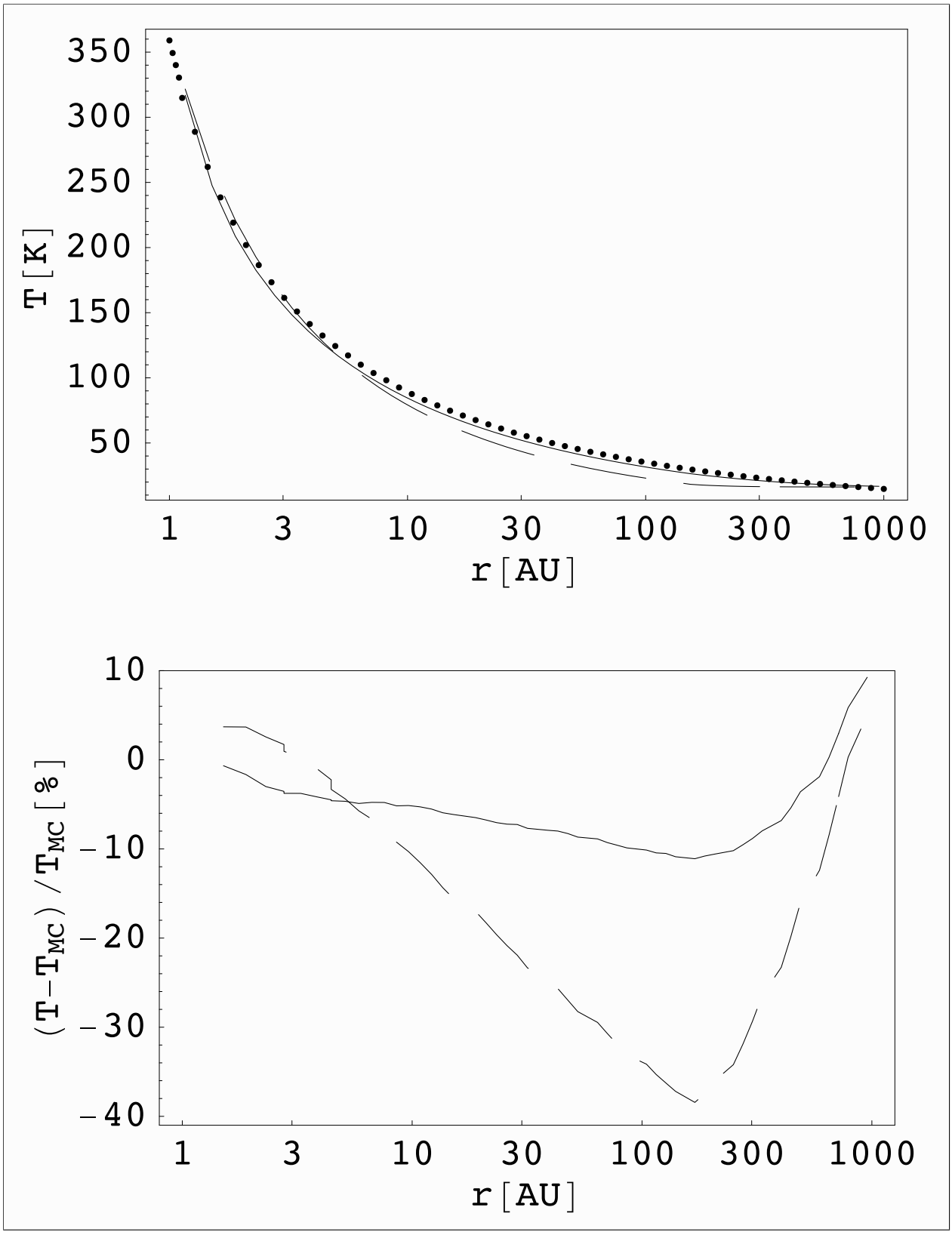

Figure 2.15: Radial cut through the temperature profile in the midplane in the most optically thick case ($\tau_{550\mathrm{nm}} = 100$) including irradiation and Flux Limited Diffusion.
Upper panel: Radial temperature profile of gray irradiation plus Flux Limited Diffusion (dashed line), frequency dependent irradiation plus Flux Limited Diffusion (solid line) and the corresponding Monte-Carlo routine (dots).
Lower panel: Deviations of the gray (dashed line) and frequency dependent run (solid line) from the Monte-Carlo code in percent.

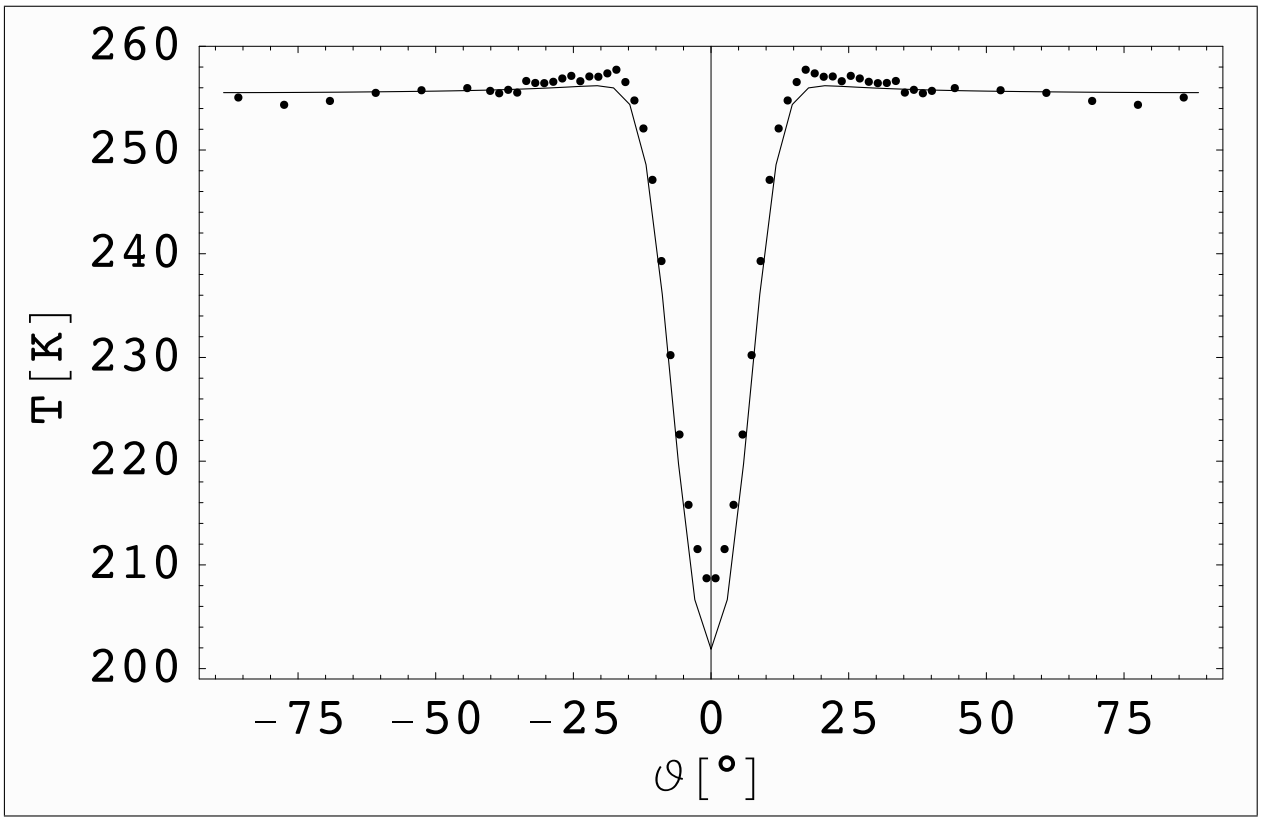

Figure 2.16: Polar cut through the temperature profile at $r = 2$ AU of the frequency dependent irradiation plus FLD run for the most optically thick case ($\tau_{550\mathrm{nm}} = 100$), reproducing the turnover point at a polar angle of $\theta \approx 19°$ above the midplane from the optically thin envelope to the optically thick disk region.
Solid line: Frequency dependent irradiation plus Flux Limited Diffusion.
Dots: Data from the corresponding Monte-Carlo comparison run.
The vertical axis covers only a small temperature range from 200 to 260 Kelvin to better visualize the small deviations.

2.5.2.6 Radiative forces in an optically thick disk

We compute the radiative force with gray and frequency dependent irradiation as well as the thermal radiative force for the most optically thick setup of Pascucci et al. (2004) and compare our results with the corresponding Monte-Carlo based run. The result is visualized in Fig. 2.17. The peak position is reproduced very well. The absolute value of the peak is underestimated by 3-4%. Behind the absorption peak the radiative force smoothly drops down and the relative deviations grow radially outwards, but stay below 10%. The fraction of the radiative force, resulting from the thermal flux, is relatively small and is most important at and directly after the absorption peak (where most of the thermal radiation is emitted). This fraction will presumably be higher in denser environments. At larger radii (> 300 AU) where the disk becomes highly optically thin to its own thermal radiation, the radiative force resulting from the thermal flux is negligible (see Figs. 2.18 and 2.17).

The gray approximation and the corresponding frequency dependent run show only small deviations (< 5%) at the outer part of the disk for radii roughly larger than 200 AU (after the absorption of the stellar irradiation). With the setup of Pascucci et al. (2004) the gray approximation leads to a higher radiative force than the frequency dependent ones, but in general the difference of both methods depends strongly on the stellar luminosity. The black body spectrum of more luminous stars shifts to higher frequencies (see Fig. 2.19).

Further remarks, explanations, and detailed discussion of the resulting radiative force and temperature profiles are given in the following subsection.

2.5.2.7 Remarks and Analysis

The Monte-Carlo comparison code For comparison and interpretation of the results, we should mention that in the original radiation benchmark test (Pascucci et al. 2004) the different Monte-Carlo codes themselves differ in the radial temperature slope through the midplane of the disk in the most optically thick case ($\tau_{550\mathrm{nm}} = 100$) by 5% in most of the region between 1.2 to 200 AU and up to 15% towards the outer border of the computational domain in the radial direction. This means that the deviations in the optically thin case (Fig. 2.13) as well as the frequency dependent ray-tracing part of the optically thick case (Fig. 2.14) stay beneath the discrepancy of the different Monte-Carlo solutions. As expected, the direct stellar irradiation is determined highly accurately, when considering the frequency dependence. Therefore, the errors introduced by using an FLD approximation can be limited in the test throughout the irradiated regions.

The influence of the so-called photon noise in the Monte-Carlo method is illustrated in the highly optically thin regions ($|\theta| > 30°$ from the midplane) in Fig. 2.16, where the temperature should actually be independent for large polar angles (as displayed by the solid line).

The FLD approximation A special feature of the setup of the original benchmark test (Pascucci et al. 2004) is the fact that even in the most optically thick case ($\tau_{550\mathrm{nm}} = 100$), which is defined for a wavelength of 550 nm, the pre-described disk is locally optically thin for the radiation from thermal dust emission. Integrating the corresponding local optical depth $\tau_R(r) = \kappa_\mathrm{R}(T)\,\rho(r)\,\Delta r$ from the outer edge of the disk through the midplane yields a final optical depth of $\tau_R \approx 0.5$ (see Fig. 2.18). The FLD approximation is known to be valid in the most optically thin (free-streaming) limit as well as for the most optically thick (diffusion) regions only. The apparent yet surprisingly good agreement between the Monte-Carlo based runs and our radiation transport module in the intermediate region of the flared disk atmosphere (see Fig. 2.16) is due to the newly implemented direct irradiation routine which yields the correct flux and depth of penetration for the different frequency bins

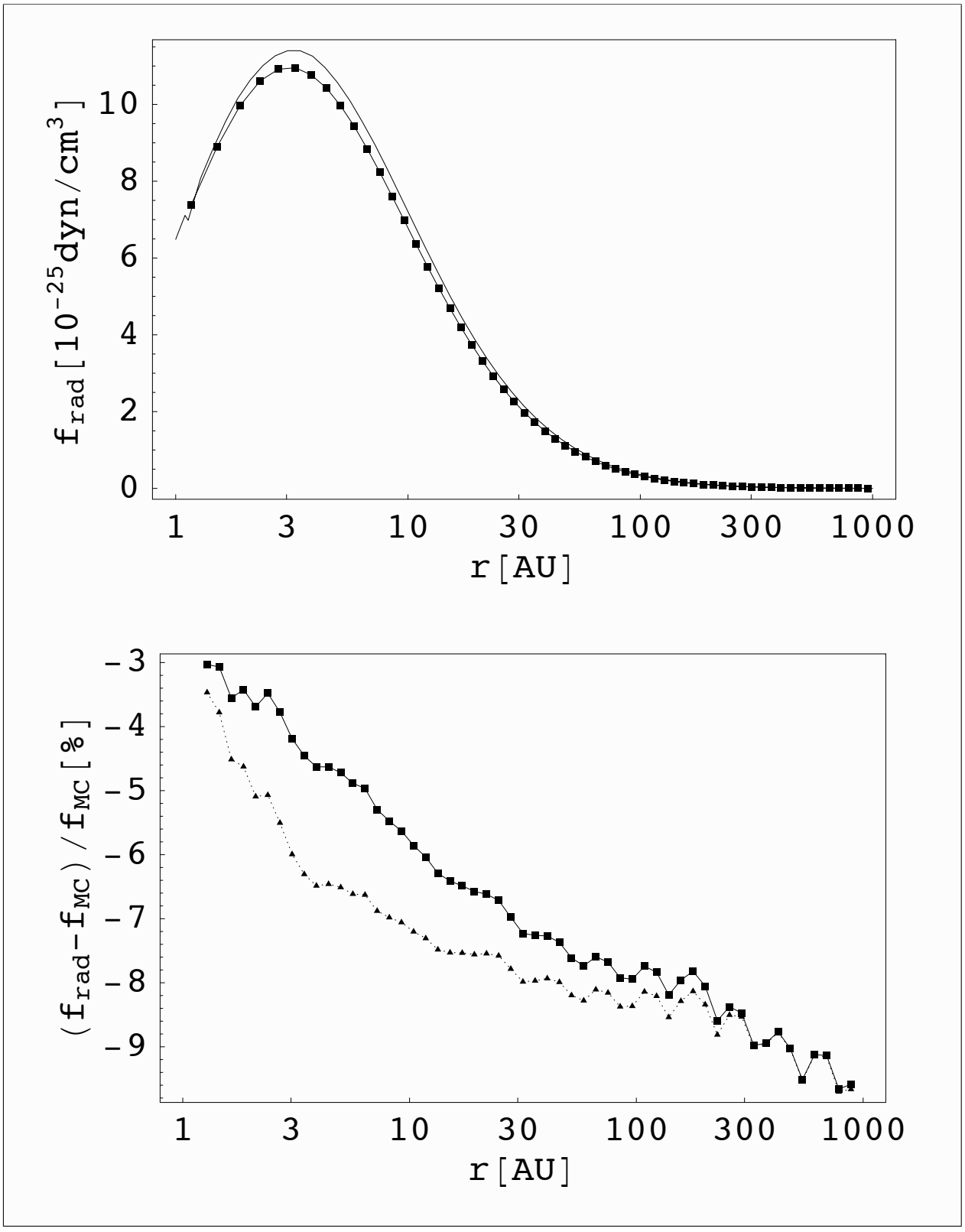

Figure 2.17: Radial cut through the radiative force profile at a polar angle of $\theta \approx 27°$ from the midplane (to display the onset of the radiative force at the transition from the optically thin envelope to the optically thick disk) in the most optically thick case ($\tau_{550\mathrm{nm}} = 100$):
Upper panel: Radial radiative force profile of frequency dependent irradiation plus FLD (solid line with squares) as well as the results from the Monte-Carlo routine (solid line).
Lower panel: Deviations of purely stellar (dotted line with triangles) and stellar plus thermal radiative force (solid line with squares) from the Monte-Carlo run in percent.

of the stellar irradiation spectrum (see Sect. 2.5.2.4). The slight underestimation of the temperature at $r \approx 200$ AU (see Fig. 2.15) in the disk midplane in the most optically thick case is most likely a result of an intermediate region (transition from optically thick to optically thin) in the outward radial direction, which is shielded from the direct irradiation and is not in good agreement with the FLD approximation.

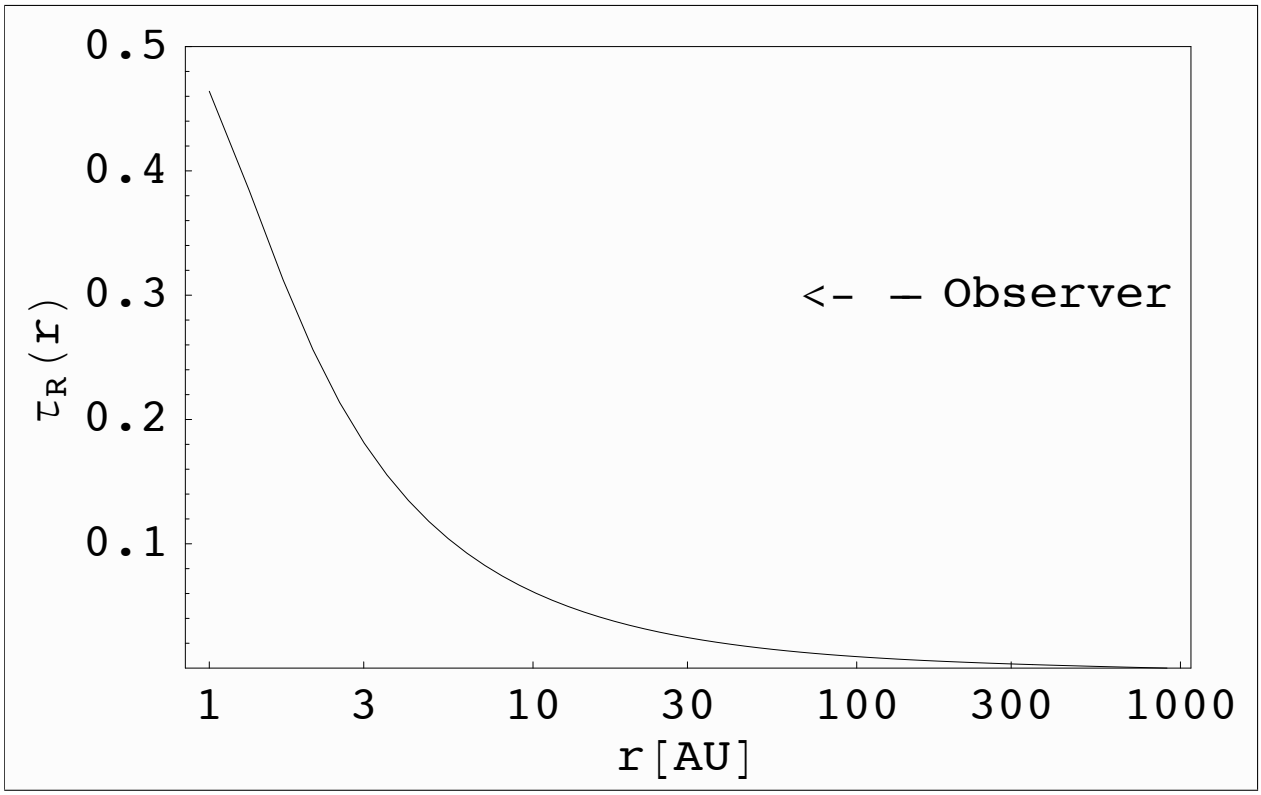

Figure 2.18: Radial profile of the optical depth τ_R through the midplane in the most optically thick case ($\tau_{550\mathrm{nm}} = 100$). The optical depth $\tau_R(r) = \kappa_\mathrm{R}(T)\,\rho(r)\,\Delta r$ as a function of the Rosseland mean opacity is integrated from the outer edge of the disk towards the center. The plot clearly shows the low optical depth for the thermal component of the radiation field especially in the outer part of the disk, which results in an underestimation of the temperature in the transition region at roughly 200 AU due to the FLD approximation.

The frequency dependence Approximating the frequency dependence of the stellar spectrum by gray Planck mean opacities results in an underestimation of absorption in the ultraviolet part of the spectrum, which is most important for the radiative force onto dust grains, and an overestimation of absorption in the infrared part of the spectrum, which is most important for the temperature estimation at larger radii which are shielded from the UV radiation (see Fig. 2.19). Due to the steep decay of the stellar black body spectrum at high frequencies, the difference of the gray and frequency dependent radiative force turns out to be very small in this specific setup. On the other hand, consideration of the frequency dependence is essential to limit the deviations in the resulting temperature profile to less than 11.1% (compared to 38.4% for gray irradiation plus FLD, see Fig. 2.15). These

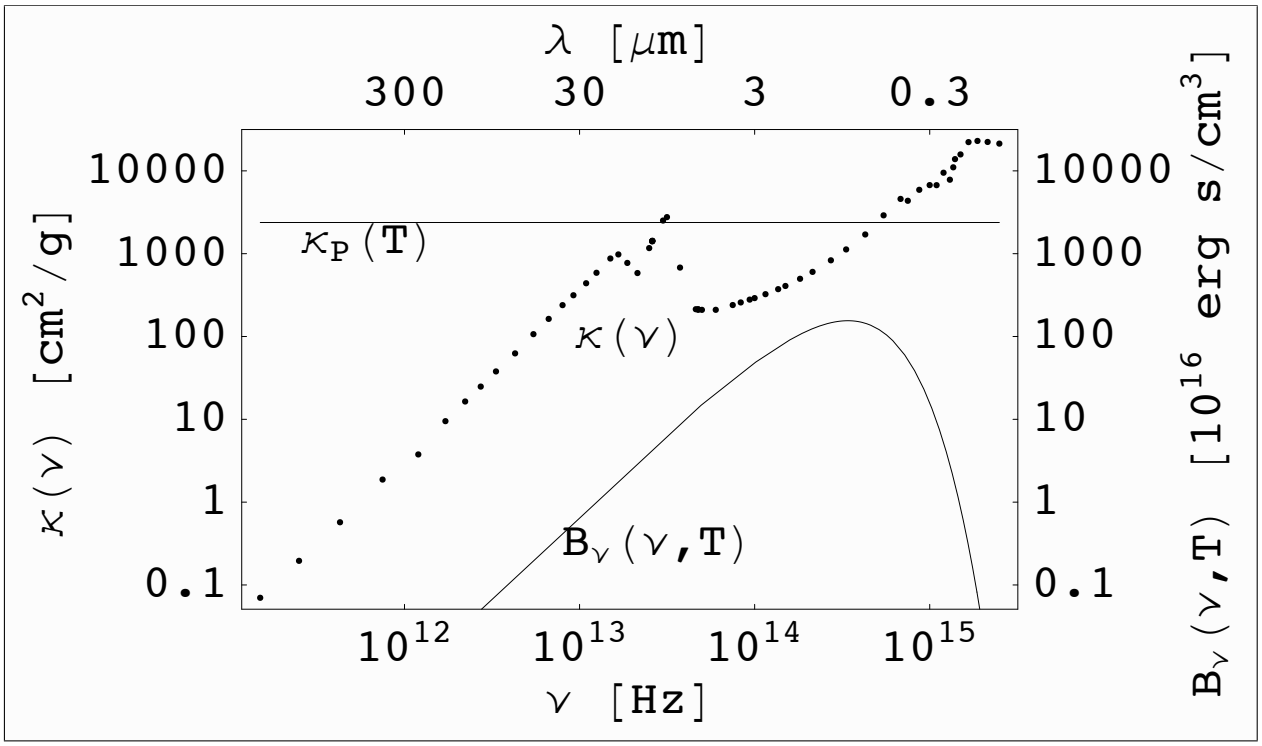

Figure 2.19: Regarding the frequency dependence of stellar irradiation feedback: frequency dependent opacities $\kappa(\nu)$ from Draine & Lee (1984), Planck mean opacities $\kappa_P(T_*)$ and stellar black body spectrum $B_\nu(\nu, T_*)$ as functions of frequency ν. The usage of gray (frequency averaged) opacities results in an overestimation of the optical depth in the infrared part and an underestimation of the absorption in the ultraviolet part of the stellar spectrum.

issues are well illustrated in Fig. 2.19. The figure shows the frequency dependent opacities of Draine & Lee (1984), the approximated frequency averaged value of the Planck mean opacity regarding the stellar effective surface temperature as well as the black body spectrum of the central star (to visualize the amount of radiative flux which is emitted per frequency bin). Each dot in the figure marks the mid-frequency of the correspondingly chosen frequency bin. The effects on the resulting temperature profile and radiative force cannot be generalized easily. They depend on the underlying dust model and strongly on the properties of the central star, which yield a shift of the peak position of the black body spectrum in Fig. 2.19 according to Wiens displacement law $\nu_{peak} \propto T$. In the specific setup of Pascucci et al. (2004) the Planck mean opacity at the black body peak position is higher than in the frequency dependent ones, leading to a slightly higher radiative force. The strong overestimation of the opacity in the infrared regime leads to the huge discrepancy of the gray approximation in the radial temperature profile through the disk.

2.5.3 Parallel performance tests of the approximate radiation transport module

The parallelization of the radiation transport scheme and the GMRES solver are taken care of by the PETSc library (Portable, Extensible Toolkit for Scientific computation, see also Balay et al. (1997)). To test the parallel speedup of the implemented radiation transport module we performed two tests with an extended version of the circumstellar disk setup introduced in Sect. 2.5.2.1.

We adopt the most optically thick setup for $\tau_{550\mathrm{nm}} = 100$ and expand it to 3D assuming axial symmetry. All runs include frequency dependent irradiation and gray Flux Limited Diffusion. The tests run for 10 main iterations, which consume the main computational effort for the approximate solver (later on, near equilibrium, the internal iterations needed decrease strongly). The number of internal iterations of the approximate implicit solver (see Sect. 2.5.1.5 for details of how the solver works) is fixed to 100 to guarantee the same amount of computation in all runs during this benchmark test. Due to the parallel Block-Jacobian pre-conditioner, the number of internal iterations needed (for a specified accuracy) normally increases with increasing number of processors. The precise value for the increase is strongly problem dependent (B. F. Smith, developer of the PETSc library, private communication).

The parallel domain (the linear system of equations) is only split in the azimuthal and polar direction, which insures good speedup and efficiency. Decomposing the domain in the radial direction would decrease the parallel performance due to the fact that in the ray-tracing routine it is necessary to compute and therefore communicate the flux from the central sink cell to the outer boundary from the inside outward. Since the knowledge of the flux at the inner cell interface is needed to compute the flux at the outer interface, this method is hardly parallelizable as a domain decomposition.

The measured times t_2 to t_n (n is the number of processors) represent the wall clock time per main iteration per grid cell without the non-recurring initialization and finalization of the code. We performed runs with 2 up to 64 processors due to the fact that single job submission is not available on the cluster we used. Cases, in which the local cache size would exceed the parallel decomposed problem size, are not taken into account, i.e. no misleading super linear speedup for a high number of processors used is shown here. The speedup S is calculated as the ratio of the 'serial' run time compared to the wall clock time used by the parallel run: $S = t_2/t_n$. The efficiency E is determined via $E = t_2/(t_n n) = S/n$. Each run for a specific grid and a specific number of processors is performed three times and averaged afterwards, but the differences of the resulting run times are negligible.

All tests were performed on a 64-Bit Opteron cluster consisting of 80 nodes with 2 CPUs each.

2.5.3.1 The constant grid test

The runs during this test are performed on a grid consisting of 64 x 64 x 256 grid cells. Each processor covers therefore a (64 x 64 x 256)/n subdomain, depending on the number of processors used. This test shows the speedup one can gain when running a fixed problem on more and more processors. Therefore, the parallel efficiency declines stronger than in the following growing grid test due to the fact that with the usage of an increasing number of processors you lower the amount of computation and increase the amount of communication per single CPU. This means that the granularity (ratio of computation to communication) of the parallel problem drops strongly with an increasing number of processors. The resulting speedup factors and efficiencies of this test are shown in Fig. 2.20.

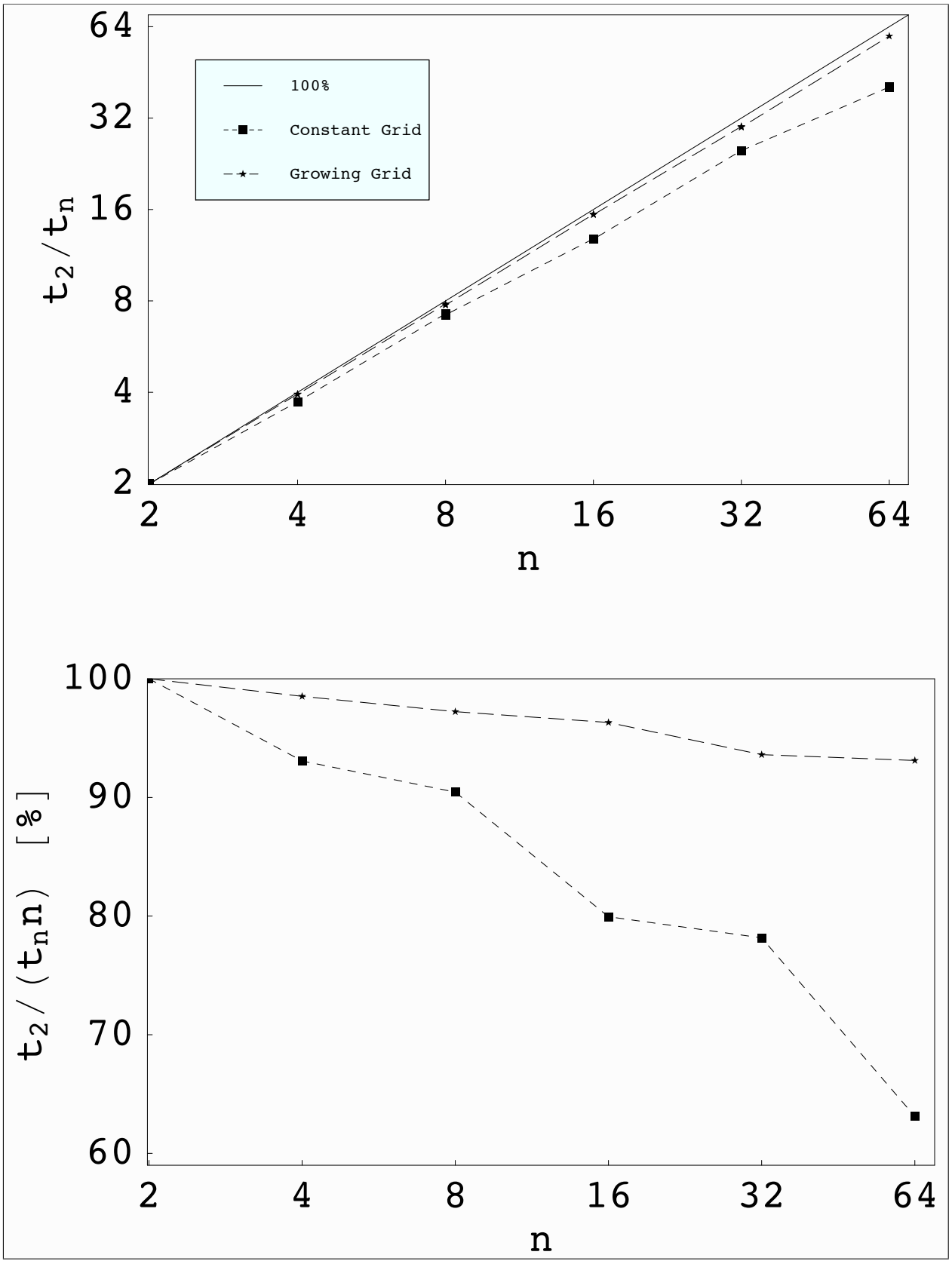

Figure 2.20: Measured speedup factors $S = t_2/t_n$ and efficiencies $E = t_2/(t_n n) = S/n$ for a fixed (squares) and a growing (stars) problem size.

2.5.3.2 The growing grid test

The runs during this test are performed on a grid consisting of 32,768 grid cells times the number n of processors used (e.g. a 64 x 64 x 8n grid). Each processor covers therefore a subdomain containing 32,768 grid cells respectively during all runs, independent of the number of processors used. This test shows the efficiency achievable when using more processors to run a bigger problem. This is a realistic setup for our three-dimensional radiative hydrodynamics studies of collapsing massive pre-stellar cores, which are at the current limit of our available clusters. The resulting speedup factors and efficiencies are shown in Fig. 2.20.

2.5.3.3 Parallel performance results

The constant grid test shows a clear speedup for the fixed problem, so it is simply possible to compute a fixed problem faster by using more processors. The growing grid case shows a high efficiency of more than 95% during all runs. This speedup seems to be higher than the speedup of any actual freely available three-dimensional hydrodynamics code for spherical grids (well known in the astrophysical community, e.g. Pluto2, Flash2.5 and Zeus-MP1.5), which we tested during the summer of 2007 in an accretion disk setup in hydrostatic equilibrium. In this sense, the resulting parallel speedup is high enough for the integration of this radiation transfer module into a (magneto-) hydrodynamics framework.

Finally, we can recommend the usage of such an implicit modern KSP solver method leading to a fast convergence of the radiative diffusion problem (at least for the setup discussed) while simultaneously offering high parallel efficiency. Admittedly, attention should be paid to the general fact that such an approximate solver method strongly depends on the physical problem at hand as well as on the specified accuracy or abort criterion.

2.5.4 Radiative hydrodynamics shock tests

To test the approximate radiation transport scheme also in a dynamical interaction with a streaming fluid, we performed two standard radiative shock tests. We adopted the setup of the supercritical and subcritical radiative shock tests for the VISPHOT code in Ensman (1994). These radiative shock tests were already repeated in tests of the TITAN code (Sincell et al. 1999a,b), ZEUS-2D (Turner & Stone 2001) as well as ZEUS-MP (Hayes et al. 2006). Analytic approximations for this kind of problem were given by Zel'Dovich & Raizer (1967).

The test setup describes a piston moving with supersonic velocity through an initially uniform, cold gas. The one-dimensional domain covers a distance of length $l_0 = 7 * 10^{10}$ cm. The iso-density in the domain is fixed to $\rho_0 = 7.78 * 10^{-10}$ g cm^{-3}. For testing purposes, the gas is set to be completely ionized, thus the mean molecular weight is $\mu = 0.5$. An ideal gas equation of state is used with $\gamma = 5/3$. The opacity is fixed to a constant value of $\kappa = 0.4$ cm^2 g^{-1}. The initial temperature drops down linearly from 85 K at the starting position of the piston to 10 K at the outer boundary. The velocity $u_0 > c_s$ of the piston is used to determine the strength of the shock. While the piston moves through the domain the radiative energy from the shocked gas will stream upwards leading to a preheating, preacceleration as well as precompression of the gas directly in front of the shock. If the temperature in this preheated region stays below the temperature of the shocked gas, it is called a subcritical radiative shock. If the temperature in the preheated region equals the temperature of the shocked gas it is called a supercritical radiative shock. The smallest piston velocity leading to a supercritical shock defines the critical velocity u_c.

Ensman (1994) used a Lagrangian grid moving with the piston velocity. This setup was translated into an Eulerian grid by setting the initial velocity in the whole domain as well as the permanent velocity at the outer

boundary to the negative of the piston velocity u_0, compressing the gas at the inner reflective boundary, which represents the moving piston. In the visualization of our results (see Fig. 2.21 and 2.22) the spatial axes are retranslated into the non-moving frame used in the visualization by Ensman (1994) to alleviate the comparison. The spherical coordinate system used at large radii (to achieve a planar geometry) by Ensman (1994) was translated into cartesian coordinates. We used 512 uniform grid cells to cover the spatial extent of the grid. These grid adjustments were also used in the test of the ZEUS-MP code (Hayes et al. 2006).

In this radiative shock test setup we are able to check the dynamical behaviour of the radiation module and the hydrodynamics. On the other hand it implies a much easier treatment of radiation transport (due to the fact that the optical depth in front of the shock is practically constant) than the prior static but frequency dependent benchmark test of Pascucci et al. (2004). Therefore only the FLD routine is needed to run the test.

We studied this shock scenario in purely adiabatic as well as radiative hydrodynamics simulations.

2.5.4.1 Radiative supercritical shock

Higher velocity of the piston results in a stronger preheating of the gas directly in front of the shocked gas. When a piston velocity higher than the critical velocity u_c is used, the peak temperature of the preheated region (which is equal to the temperature of the shocked gas) will not increase any more, but the enlargement of the preheated region will extend further out. The gas temperature of the preheated region will presumably be in equilibrium with the radiative ones for a majority of the domain. At one point of the sloping tail of the temperature distribution in the upstream direction both temperatures will differ. In an equilibrium diffusion (also called one-temperature diffusion) code like ours the temperature will decline at this point sharply (see also Fig. 15 in Ensman (1994), which compares an adiabatic, an equilibrium, a non-equilibrium and a full radiation transport method for this setup). The reason for this sharp decline is (according to Ensman (1994)) that the radiation can only penetrate through the cold environment, if it heats this environment up to the equilibrium temperature. Once the radiation energy is absorbed, the radiative flux is zero. In a non-equilibrium radiation transport method the radiation energy can penetrate further into the environment simply by heating it to less than the equilibrium temperature.

We chose the piston velocity to be the one used originally by Ensman (1994), $u_0 = 20\,\mathrm{km\,s^{-1}}$. In some of the subsequent tests mentioned above a slightly lower piston velocity ($u_0 = 16\,\mathrm{km\,s^{-1}}$) for the supercritical radiative shock was used by the authors. Fig. 2.21 displays the resulting density, pressure, velocity and temperature distributions for four different times (same as Fig. 10 - 12 in Ensman (1994)) as well as the initial setup. The analytic limit of a maximum jump in density by four in adiabatic shocks is reproduced. The effect of preheating, preacceleration and precompression is clearly visible. The position of the peak temperature fits the one by Ensman (1994). Although the non-equilibrium gas temperature spike cannot be reproduced with an equilibrium radiation transport method (the width of this gas temperature spike would always be less than a mean free path across), the value of the peak temperature is in very good agreement with the radiation temperature of the corresponding non-equilibrium run by Ensman (1994) aside from minor geometrical effects of the modified coordinate system as already discussed in Hayes et al. (2006). Furthermore the equilibrium temperature distribution resembles the temperature distribution of the non-equilibrium run by Ensman (1994) in all regions, where the gas temperature equals the radiation temperature (which is the most part of the domain in a supercritical shock). As expected, our temperature distributions sharply decline at the boundary with the non-equilibrium region as predicted by Ensman (1994).

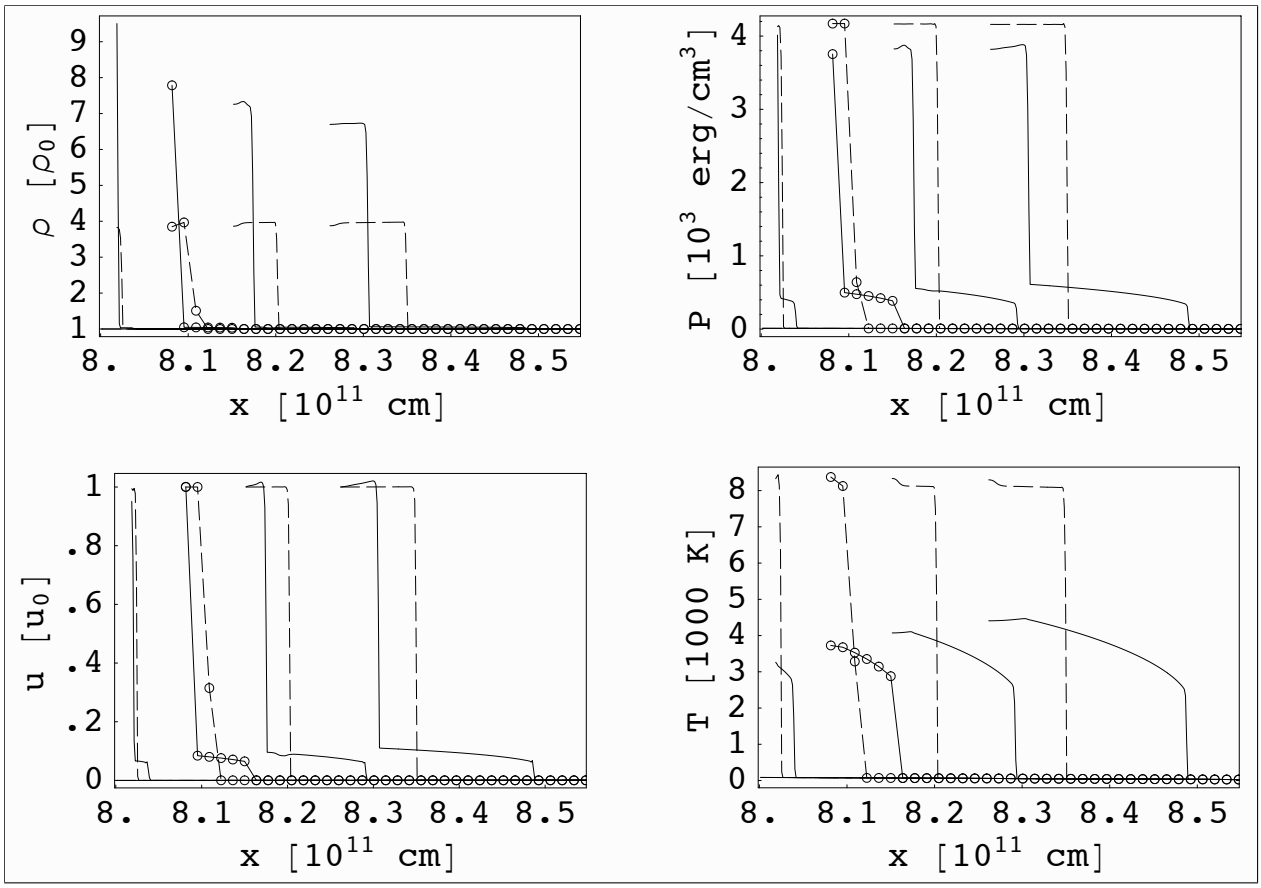

Figure 2.21: Radiative supercritical shock: Resulting density, pressure, velocity and temperature distributions at four different snapshots in time. Dashed lines represent the adiabatic runs, solid lines the radiative ones. The time snapshots are taken (from left to right) at 860 s, 4,000 s, 7,500 s, and 13,000 s after launching. Mostly horizontal lines at the lower border of the graphics refer to the initial setup. The snapshots at 4000 s are additionally marked by circles for every 10^{th} grid cell to illustrate the resolution used. The spatial axes are retranslated into the non-moving frame used in the visualization by Ensman (1994) for the sake of comparison.

2.5.4.2 Radiative subcritical shock

In a radiative subcritical shock ($c_s < u_0 < u_c$), the gas in front of the shock region is only heated to a temperature lower than the temperature of the shocked gas region. In a non-equilibrium radiation transport method, the gas temperature sharply drops down (after the narrow temperature spike similar to the supercritical shock), whereas the radiation energy penetrates the cold unshocked gas region and declines more smoothly (see also Fig. 8 in Ensman (1994)). An equilibrium radiation transport is expected to first ignore the narrow gas temperature spike. Secondly, it drops down sharply when arriving the region, where the gas and radiation temperature are out of equilibrium. In other words , the equilibrium radiation transport resembles the decline of the gas temperature distribution.

We chose the piston velocity to be the one used originally by Ensman (1994), $u_0 = 6\,\mathrm{km\,s^{-1}}$. Fig. 2.22 displays the resulting density, pressure, velocity and temperature distributions for five different times (same

as Fig.8 in Ensman (1994)). Given the constraints of the equilibrium radiation transport discussed above, the resulting distributions fully satisfy the predictions.

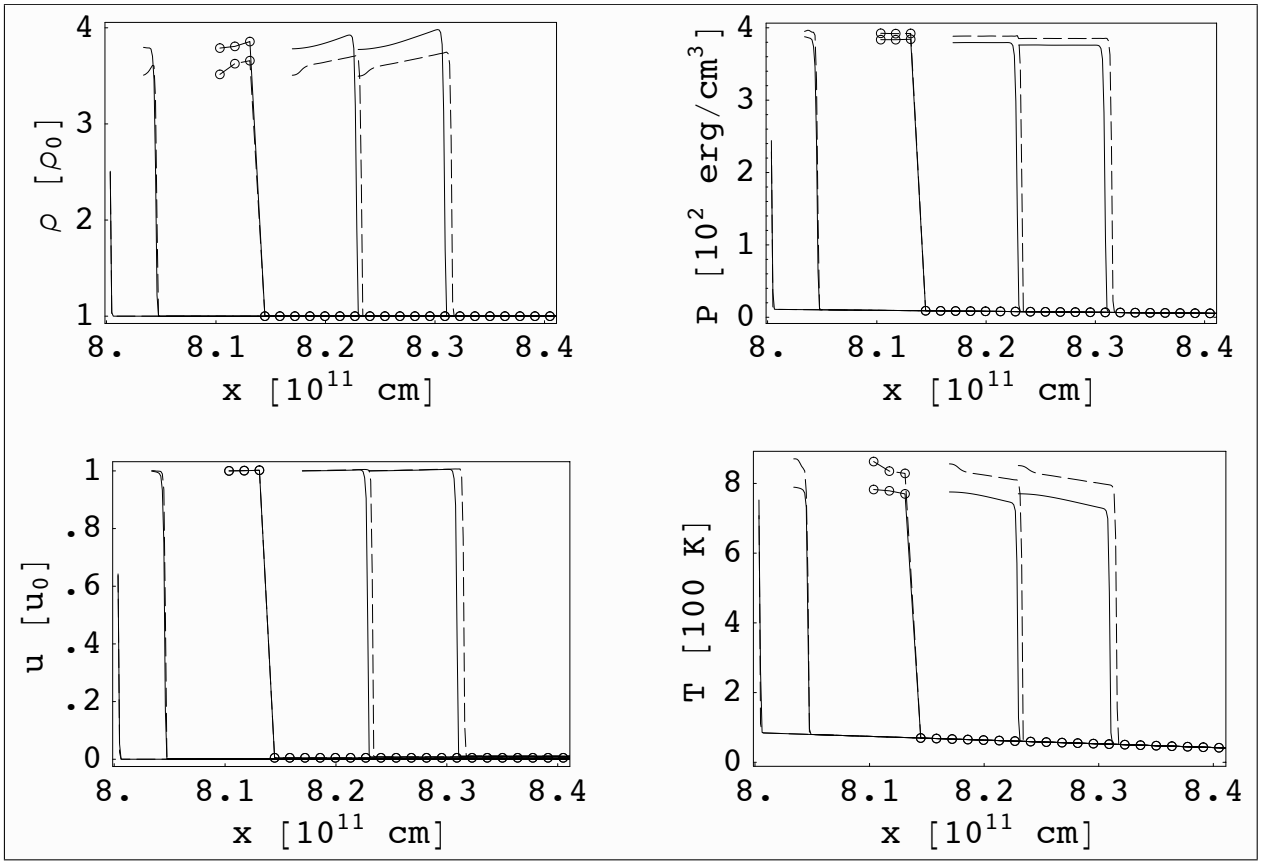

Figure 2.22: Radiative subcritical shock: Resulting density, pressure, velocity and temperature distributions at five different snapshots in time. Dashed lines represent the adiabatic runs, solid lines the radiative ones. The time snapshots are taken (from left to right) at 350 s, 5,400 s, 17,000 s, 28,000 s, and 38,000 s after launching. The snapshot at 350 s shows approximately the initial setup. The snapshots at 4000 s are additionally marked by circles for every 10^{th} grid cell to illustrate the resolution used. The spatial axes are retranslated into the non-moving frame used in the visualization by Ensman (1994) for the sake of comparison.

2.6 Dust model

For the implementation of realistic dust opacities for the frequency dependent radiation transport module, we use an opacity table of Laor & Draine (1993) for the pre-stellar core collapse simulations. The opacity table covers the full frequency range from infrared radiation up to x-rays. It describes a mixture of dust grains in the size range between 0.005 to 10.0 μm. The grains are taken to be spherical and consist out of amorphous silicate with a composition like that of olivine. As shown in Fig. 2.12 on p. 43 this dust grain mixture takes into account the strong absorption/emission features at 9.7 μm and 18 μm observed in the interstellar medium. Each of the 79 dots in Fig. 2.12 marks the mid-frequency of the corresponding frequency bin. The resulting frequency averaged Planck- and Rosseland mean opacities are shown in Fig. 2.23 as a function of temperature.

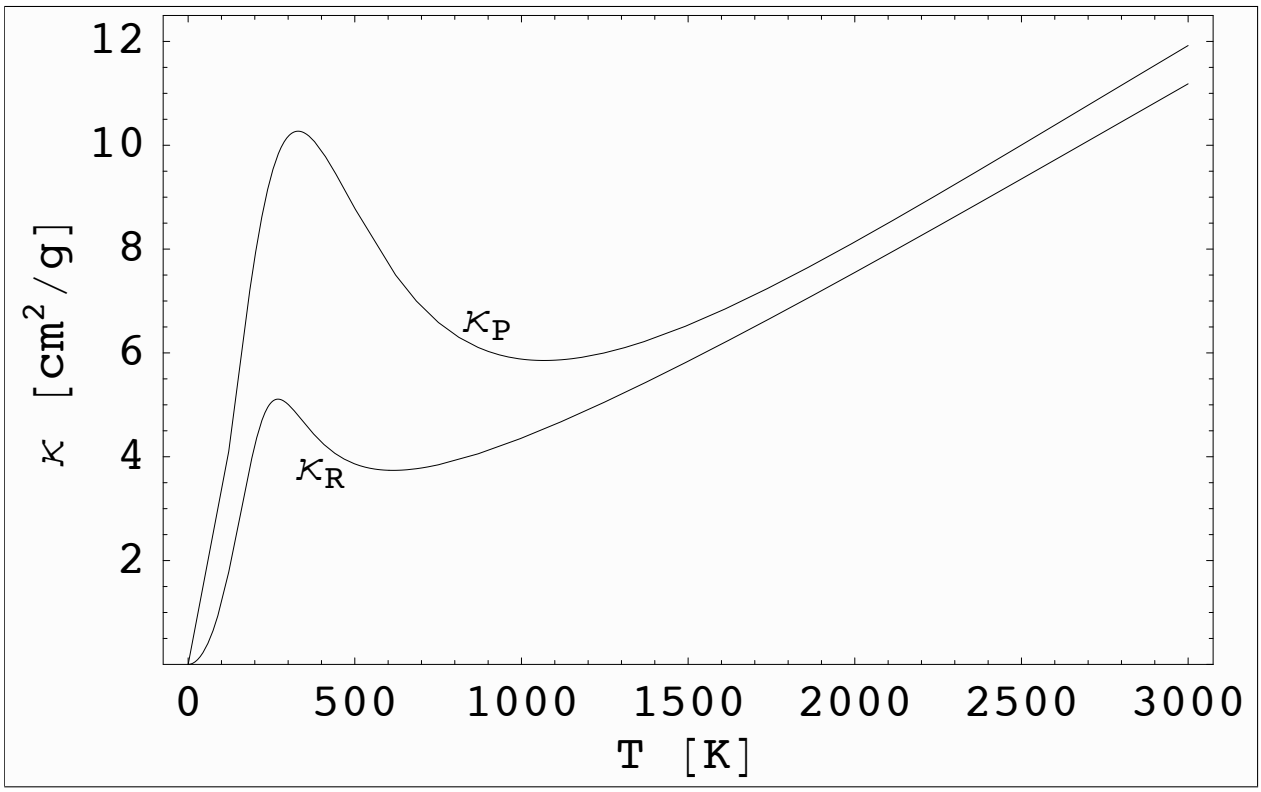

Figure 2.23: Calculated Rosseland κ_R and Planck κ_P mean opacities as a function of temperature. The possible evaporation of dust grains at high temperatures (and/or low densities) is considered in the dust to gas mass ratio M_{dust}/M_{gas} of each grid cell, see also Fig. 2.24.

Aside from the dust opacities, the opacity of a given grid cell depends also linearly on the local dust to gas mass ratio. The initial dust to gas mass ratio $\left(M_{dust}/M_{gas}\right)_0$ is fixed to 1%. Gas and dust is treated as a single fluid, so the dust to gas mass ratio only shrinks due to possible evaporation of the dust grains in hot regions (around the central massive star). The local evaporation temperature of the dust grains is calculated by using the formula of Isella & Natta (2005)

$$T_{evap} = g\,\rho^{\beta} \tag{2.65}$$

with $g = 2000$ K, $\beta = 0.0195$, and the gas density ρ given in g cm^{-3}. The formula describes a power-law approximation to the evaporation temperatures T_{evap} determined by Pollack et al. (1994). A smooth spatial and time dependent transition of the associated dust to gas mass ratio between completely evaporated and condensated regions is achieved via the transition function

$$\frac{M_{\mathrm{dust}}}{M_{\mathrm{gas}}}(\vec{x}) = \left(\frac{M_{\mathrm{dust}}}{M_{\mathrm{gas}}}\right)_0 \left(0.5 - \frac{1}{\pi}\arctan\left(\frac{T(\vec{x}) - T_{\mathrm{evap}}(\vec{x})}{100}\right)\right). \tag{2.66}$$

The transition slope is displayed in Fig. 2.24 as a function of the temperature for a gas density of $\rho = 10^{-10}$g cm^{-3} as well as for the floor value of the density $\rho_0 = 10^{-21}$g cm^{-3}.

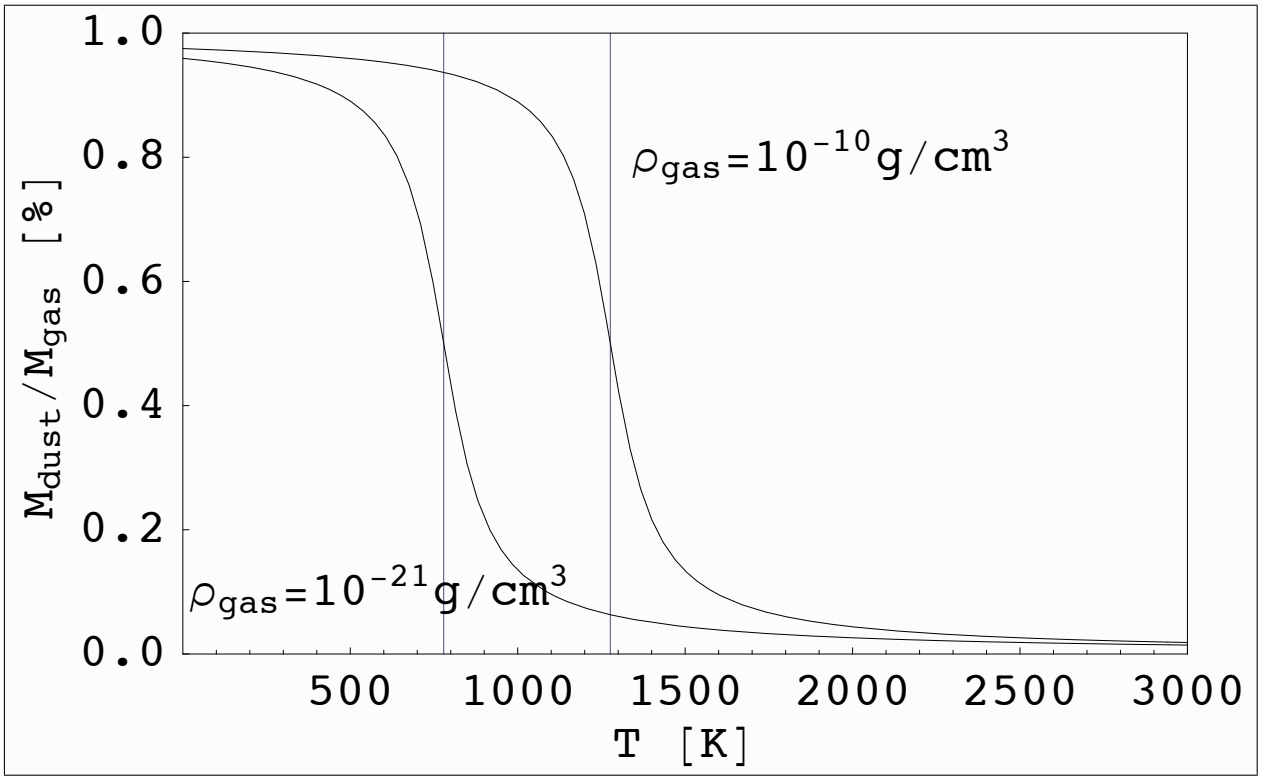

Figure 2.24: Transition slope of the local dust to gas mass ratio as a function of temperature due to evaporation of dust grains for two different gas densities.

2.7 Stellar evolution model

The evolution of the central star, described by a central sink cell, is coupled to the hydrodynamics of the pre-stellar core by measuring the mass flux into the sink cell. The initial mass of the star at the beginning of the simulation is simply given by the integral over the initial density distribution up to the radius $r_{\rm min}$ of the sink cell and is therefore in all cases less than a few percent of 1 $M_\odot$. The mass, which enters the sink cell during the hydrodynamics is assumed to be accreted onto the central star. From the mass flux $\rho\vec{u}$ into the sink cell during the timestep Δt we calculate the accretion rate $\dot{M}$ onto the central star via

$$\dot{M} = \int_0^{2\pi} d\phi \int_0^{\pi} d\theta\, \rho\vec{u} \cdot \vec{e}_r r_{\rm min}^2 \sin\theta. \tag{2.67}$$

Integrating the accretion rate $\dot{M}$ over the time yields the growth of the stellar mass M_*:

$$M_*(t + \Delta t) = M_*(t) + \int_t^{t+\Delta t} \dot{M} dt = M_*(t) + \dot{M}\Delta t. \tag{2.68}$$

The total luminosity L_* of the star is given by the sum of the luminosity from accretion $L_{\rm acc}$ and nuclear fusion $L_{\rm nuc}$:

$$L_*(t) = L_{\rm acc}(t) + L_{\rm nuc}(t). \tag{2.69}$$

The accretion luminosity is directly calculated from the hydrodynamics simulation via

$$L_{\rm acc} = \frac{GM_*}{R_*}\dot{M} \tag{2.70}$$

with the stellar radius R_*. The nuclear fusion luminosity and the stellar radius are obtained via fits to the pre-calculated evolutionary tracks by Hosokawa & Omukai (2008). These evolutionary tracks of massive stars depend on the stellar mass as well as on the actual accretion rate. We use polynomial fits to the mass relation up to $10^{\rm th}$ order for separated mass ranges (an example of these fits is shown in Fig. 2.25) and linear regression for the dependency on the accretion rate. For stellar masses below the accessible data (0.05 $M_\odot$ in the worst case) the nuclear fusion of the star is assumed to be negligible and the stellar radius is assumed to be constant up to the first data point. An even more realistic approach would be to directly include a stellar evolution code such as Hosokawa & Omukai (2008) to calculate the ongoing stellar physics in the sink cell consistently.

Given the stellar radius and total luminosity, the stellar effective temperature T_* is calculated from

$$L_* = 4\pi\, \sigma_{\rm SB}\, R_*^2\, T_*^4 \tag{2.71}$$

with the Stefan-Boltzmann constant $\sigma_{\rm SB}$.

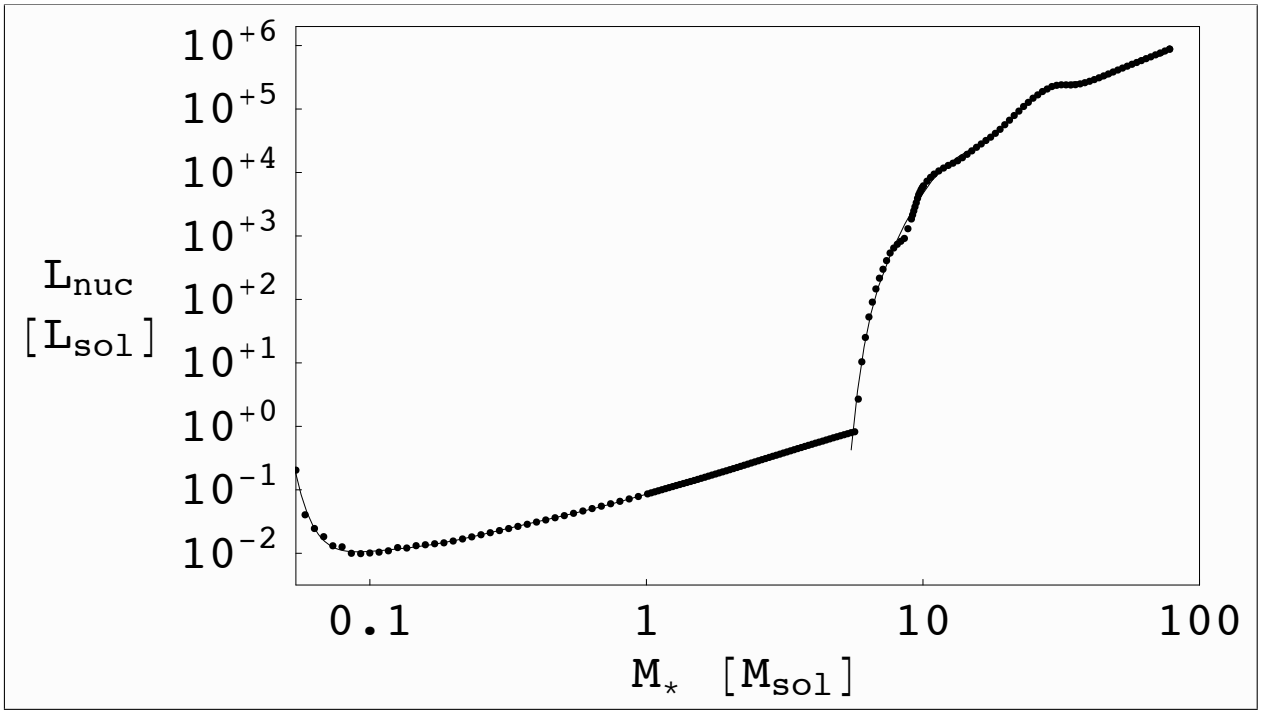

Figure 2.25: Polynomial fits to the nuclear fusion luminosity as a function of the stellar mass as calculated by Hosokawa & Omukai (2008). The data points represent an evolving massive star with an accretion rate of 10^{-3} $M_\odot$ yr^{-1}. The mass range was split into two regimes above and below 5.5 $M_\odot$ (at the sharp bend) and each part is fitted by a polynomial up to 10^{th} order (solid lines).

3

Basic analytical solutions and concepts

In this chapter, we present the basic concepts to solve specific problems of the collapse of a pre-stellar core analytically. We show the derivations of formulae and rough estimates, which we use either to determine the correct numerical setup for our simulations or to analyze the numerical data in a post processing step. We start with the analytical derivation of the classical keplerian orbit (Sect. 3.1.1), which will be used several times subsequently. Afterwards we will estimate the importance of the thermal pressure in a massive accretion disk relative to the gravity and the centrifugal force (Sect. 3.1.2) and discuss the equilibrium of forces in the vertical direction (Sect. 3.1.3). In Sect. 3.2 and 3.3 we derive the free fall time and the mean centrifugal radius for the kind of massive pre-stellar cores, we study in our simulations. The free fall time and the mean centrifugal radius determine useful typical time and length scales of the general collapse problem respectively. These derivations can also be found in standard text books of theoretical mechanics and astronomy or in part in the open source online encyclopedia 'wikipedia' as well. A good review on classical accretion disk physics has given by Lodato (2008).

Additionally, we estimate two important quantities related to the radiation hydrodynamics interaction and depending on the specific stellar evolution and dust model assumed. The so-called generalized Eddington limit (Sect. 3.4) allows us to derive the importance of the radiation pressure force on the stellar environment relative to the gravity, both depending on the actual stellar mass. In the last section of this chapter (Sect. 3.5), we estimate the dust condensation radius of a massive star. The dust condensation radius marks the transition region from the dust-free optically thin vicinity of the massive star to its optically thick envelope or disk region. Its location plays an important role for the stellar radiative feedback on its environment. The simulation series in Sect. 4.2.2 and 4.3.2 for non-rotating and rotating cores respectively show that it is unavoidable to include this critical transition region into the computational domain of the numerical simulation. The dust condensation radius and the generalized Eddington limit therefore strictly constrains the choice of the size of the sink cell which represents the forming massive star in such simulations.

3.1 Circumstellar disks in equilibrium

The in-fall of gravitationally accelerated mass during the collapse of a rotating pre-stellar core involves an increase of the rotation speed due to the conservation of angular momentum and an increase in pressure due to compression. The resulting centrifugal and thermal pressure forces in the outward direction grow until the sum of both compensate the gravitational force. While the gravitational force of the central star is directed spherically radially inwards, the thermal pressure force acts in the opposite direction of the pressure gradient and the centrifugal force introduces an acceleration in the outwards direction perpendicular to the axis of rotation. Fig. 3.1 displays schematically the equilibrium state of these forces split in the directions of an associated cylindrical coordinate system.

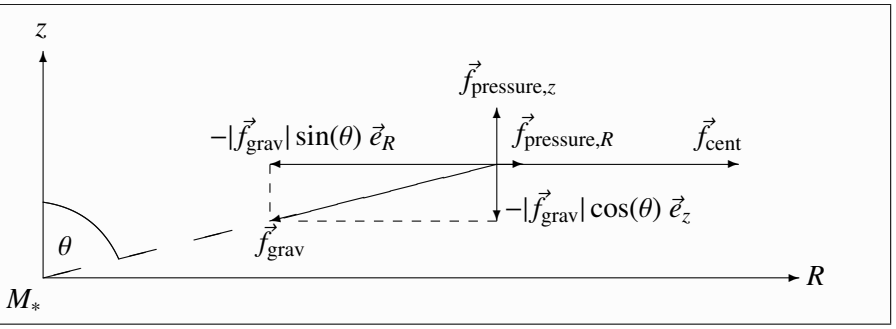

Figure 3.1: Equilibrium state of the stellar gravitational $\vec{f}_{\text{grav}}$, the thermal pressure $\vec{f}_{\text{pressure}}$, and the centrifugal $\vec{f}_{\text{cent}}$ force acting in a circumstellar disk perpendicular to the azimuthal direction.

The figure shows a slice (of the axially symmetric setup) perpendicular to the azimuthal direction. The cylindrical coordinate system of the disk is given by the disk height or distance z from the midplane and the cylindrical radius or distance R from the axis of rotation. The spherical coordinate system is defined by the spherical radius or the distance r from the central star of mass M_* and the polar angle θ between the given radial point vector and the axis of rotation. The transformation of the spherical coordinates into the cylindrical ones is given by:

$$R = r\,\sin(\theta) \tag{3.1}$$

$$z = r\,\cos(\theta) \tag{3.2}$$

The stellar gravitational, the thermal pressure, and the centrifugal force density expressed in cylindrical coordinates are

$$\vec{f}_{\text{grav}} = -\rho\frac{GM_*}{r^2}\,\vec{e}_r = -\rho\frac{GM_*}{r^2}\,(\sin\theta\,\vec{e}_R + \cos\theta\,\vec{e}_z) \tag{3.3}$$

$$\vec{f}_{\text{pressure}} = -\vec{\nabla}p = -\partial_R p\,\vec{e}_R - \partial_z p\,\vec{e}_z \tag{3.4}$$

$$\vec{f}_{\text{cent}} = +\rho\frac{u_\phi^2}{R}\,\vec{e}_R \tag{3.5}$$

with the density ρ, the gravitational constant G, the stellar mass M_*, the thermal pressure p and the velocity u_ϕ in the azimuthal direction. In the following subsections, we derive the profiles of the angular velocity and density of the circumstellar disk from the equilibrium of these components of the acting forces.

3.1.1 Classical keplerian motion

In a first step, we neglect the thermal pressure. In the following subsection we estimate its relative importance compared to the gravitational and the centrifugal force. The equilibrium of the gravitational and the centrifugal force acting perpendicular to the axis of rotation (in the cylindrical radial direction) is illustrated in Fig. 3.1 and the expressions of the force components are given in Eqs. 3.3 and 3.5. The equilibrium state yields:

$$-|\vec{f}_{\text{grav}}| \sin(\theta)\, \vec{e}_R + \vec{f}_{\text{cent}} = 0 \tag{3.6}$$

$$\Rightarrow \quad -\frac{G\, M_*}{r^2} \sin(\theta) + \frac{u_\phi^2}{R} = 0 \tag{3.7}$$

Solving this equation for the velocity in the azimuthal direction allows us to derive the radial slope of the rotation speed, the so-called classical keplerian orbital velocity Ω_{K}:

$$\boxed{\Omega_{\text{K}} = \frac{u_\phi}{R} = \sqrt{\frac{G\, M_*}{r^3}}} \tag{3.8}$$

In the following subsection we derive the more general expression for the orbital angular velocity Ω_ϕ including the thermal pressure force.

3.1.2 Orbital motion in 'hot' disks

Now we add the effect of the internal gas pressure to the keplerian motion derived in the previous subsection. During the formation of the circumstellar disk the gas is strongly compressed and the resulting pressure gradient acts against gravity. Hence this will minimize the centrifugal force required to compensate the gravity. Due to the fact that the thermal pressure p grows proportional to the local temperature T of the disk, this effect is much more important in 'hot' disks or especially in irradiated parts of the circumstellar disk, in particular the inner rim and the disk's atmosphere. The equilibrium of the gravity, the centrifugal, and the thermal pressure force acting in the cylindrically radial direction is illustrated in Fig. 3.1 and the expressions of the force components are given in Eqs. 3.3 to 3.5. The equilibrium state yields:

$$-|\vec{f}_{\text{grav}}| \sin(\theta)\, \vec{e}_R + \vec{f}_{\text{cent}} + \vec{f}_{\text{pressure},R} = 0 \tag{3.9}$$

$$\Rightarrow \quad -\rho\frac{G\, M_*}{r^2} \sin(\theta) + \rho\frac{u_\phi^2}{R} - \partial_R p = 0 \tag{3.10}$$

Solving for the equilibrium orbital velocity Ω_ϕ gives:

$$\boxed{\Omega_\phi = \frac{u_\phi}{R} = \sqrt{\frac{G\, M_*}{r^3} + \frac{\partial_R p}{\rho\, R}}} \tag{3.11}$$

To calculate the next step we need an appropriate expression for the spatial derivative of the internal gas pressure. Therefore we use its relation to the local sound speed c_{s} and the density ρ of the disk

$$p = \frac{1}{\gamma} c_{\text{s}}^2\, \rho \tag{3.12}$$

with the adiabatic index γ. The local sound speed further depends on the local temperature T and on the mean molecular weight μ

$$c_{\text{s}}^2 = \gamma \frac{R\, T}{\mu} \tag{3.13}$$

with the universal gas constant R. If we assume an arbitrary power-law of the density slope $\rho \propto R^{-\beta_\rho}$ as well as of the temperature slope $T \propto R^{-\beta_T}$, we get:

$$\partial_R p = \frac{1}{\gamma}\,\partial_R\, c_\mathrm{s}^2\,\rho = -\frac{1}{\gamma}\,(\beta_\rho + \beta_T)\,\frac{c_\mathrm{s}^2\,\rho}{R} \tag{3.14}$$

Inserting this result in Eq. 3.11 leads to an orbital angular velocity of:

$$\Omega_\phi = \sqrt{\frac{G\,M_*}{r^3} - \frac{1}{\gamma}\,(\beta_\rho + \beta_T)\,\left(\frac{c_\mathrm{s}}{R}\right)^2} \tag{3.15}$$

Compared to the pressure-less classical keplerian motion (Eq. 3.8) this gives a 'correction' factor of:

$$\boxed{\frac{\Omega_\phi}{\Omega_\mathrm{K}} = \sqrt{1 - \frac{\beta_\rho + \beta_T}{\gamma}\,\left(\frac{c_\mathrm{s}}{u_\mathrm{K}}\right)^2}} \tag{3.16}$$

with the keplerian velocity $u_\mathrm{K} = \Omega_\mathrm{K} R$. The importance of the thermal pressure force grows with the ratio of the thermal sound speed to the keplerian velocity $c_\mathrm{s}/u_\mathrm{K}$, so it increases for slowly rotating or hotter disks. In standard disk theory the so-called thickness H of the disk is introduced as the ratio of the thermal sound speed to the keplerian angular velocity $H = c_\mathrm{s}/\Omega_\mathrm{K}$. That means the ratio $c_\mathrm{s}/u_\mathrm{K}$ is directly related to the aspect ratio H/R of the circumstellar disk

$$\frac{H}{R} = \frac{c_\mathrm{s}}{u_\mathrm{K}}. \tag{3.17}$$

A higher mass star leads to higher gravity, but on the other hand the strongly growing luminosity heats up the circumstellar disk to higher temperatures. To estimate the maximum influence of the thermal pressure gradient in hot accretion disks around massive stars, we calculate the relative change in orbital velocity for one specific example: For a given temperature of 6000 K at 10 AU, declining in the radial direction with $\beta_T = 1$, a density slope with $\beta_\rho = 1.5$, an adiabatic index of $\gamma = 5/3$, a mean molecular weight of a mixture of hydrogen and helium of $\mu = 2.343\mathrm{g\ mol}^{-1}$, and a stellar mass of $M_* = 20\ \mathrm{M}_\odot$ we get for the midplane of the disk:

$$\frac{\Omega_\phi}{\Omega_K} \sim 0.985 \tag{3.18}$$

As initially assumed, the internal gas pressure of the accretion disk determines only a small fraction of the acting forces compared to gravity and centrifugal force, at most a maximum of a few percent. In the last subsection we analyze the state of equilibrium in the vertical direction.

3.1.3 Vertical stratification

Centrifugal forces can prevent the mass from falling further inwards onto the star, but the vertical component of the gravity will lead to a settling of the mass down to the midplane. This increases the thermal gas pressure in the midplane layer until both forces compensate each other. We neglect the effect of self-gravity of the circumstellar disk during this derivation. The solution of the vertical hydrostatic balance of accretion disks including self-gravity can be found in Spitzer (1942). The equilibrium of the gravity and the thermal pressure force acting in the vertical direction is illustrated in Fig. 3.1 and the expressions for the force components are given in Eqs. 3.3 and 3.4. The equilibrium state yields:

$$-|\vec{f}_\mathrm{grav}|\cos(\theta)\,\vec{e}_z + \vec{f}_{\mathrm{pressure},z} = 0 \tag{3.19}$$

Therefore the pressure gradient of the disk is determined by

$$\partial_z P = \rho \frac{G\, M_*}{r^2} \cos(\theta) \qquad (3.20)$$

In regions, where the assumption of an isothermal sound speed (involving no temperature stratification) is valid, the density stratification in the vertical direction of the accretion disk can be derived analytically from this equilibrium. The pressure gradient yields under this assumption

$$\partial_z P = c_\mathrm{s}^2\, \partial_z\, \rho \qquad (3.21)$$

and the gravity in the vertical direction can be expressed as

$$\frac{G\, M_*}{r^2} \cos(\theta) = \frac{G\, M_*}{r^3} z = \Omega_\mathrm{K}^2\, z \qquad (3.22)$$

Inserting Eqs. 3.21 and 3.22 in the equilibrium Eq. 3.20 results in a Gaussian profile for the density stratification

$$\rho(z) = \rho(0)\ \exp\left(-\frac{z^2}{2H^2}\right) \qquad (3.23)$$

with the previously introduced thickness $H = c_\mathrm{s}/\Omega_\mathrm{K}$ of the circumstellar disk.

3.2 Free fall time

After the review of circumstellar disk physics we focus on the analysis of the global pre-stellar core collapse. A typical time scale, on which a collapse of a pre-stellar core occurs, is the so-called free fall time scale. The free fall time t_ff is defined as the time the outermost shell of the core needs to arrive at the center of the core. Thereby all forces with the exception of the gravity are neglected. This simplifies the problem: In such a collapsing body no shell of radius r will overtake any other with a smaller radius. That means, each shell with its specific starting radius r feels the gravity of the time independent included mass $M(r)$ of the core as it would be a point mass $M \equiv M(r)$ at the origin. The most elegant way to derive the free fall time in this picture is to use Kepler's law of orbiting bodies around a dominating central mass, illustrated in Fig. 3.2. The orbit of the body is an ellipse $s_{ellipse}$ with the center of mass M in one focus. The time t_orbit for one single orbit is given by

$$t_\mathrm{orbit}(a) = \frac{2\pi}{\Omega_\mathrm{K}} = \frac{2\pi\, a^{3/2}}{\sqrt{G\, M}}, \qquad (3.24)$$

with the semi-major axis a of the ellipse. Given the eccentricity e of the elliptical orbit, the point r of the farthest destination from the point mass and the semi-major axis a fulfill the relation $a = r/(1+e)$. For example, an eccentricity of zero yields $a = r$ and describes the circular orbit s_{circle} drawn in Fig. 3.2. The orbital time results in

$$t_\mathrm{orbit}(r, e) = \frac{2\pi\ (r/(1+e))^{3/2}}{\sqrt{G\, M}}. \qquad (3.25)$$

The fact that the body arrives at the same distance r from the central mass again and again means that the integrated gravitational force matches the integrated centrifugal force along any

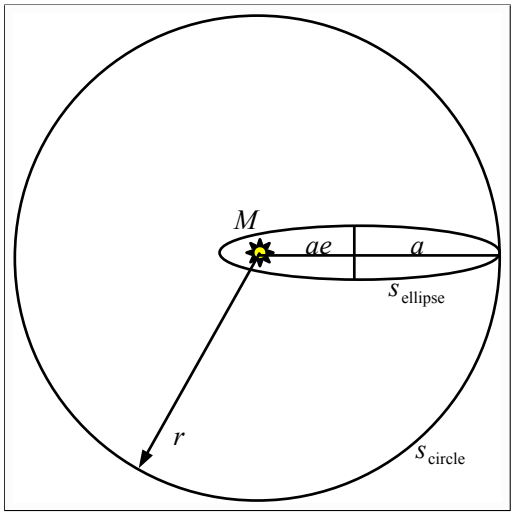

Figure 3.2: Derivation of the free fall time from Kepler's law of orbiting planets.

of the trajectories. After one orbit the gravity has acted on the body in the same amount than the centrifugal force. Furthermore, if the eccentricity of the ellipse tends to unity, the orbit describes a straight line from the outer point to the center and back. Therefore a rotating body at distance r from the center feels along half a single orbit the same acting gravity than an along the radius r free falling body. Hence, the free fall time $t_{\rm ff}$ is just half an orbital period with the eccentricity $e = 1$:

$$t_{\rm ff} = \frac{t_{\rm orbit}(r, 1)}{2} = \frac{\pi\, r^{3/2}}{\sqrt{8\, G\, M}} \tag{3.26}$$

The free fall time associated with a pre-stellar core can now be calculated by inserting the outer core radius $r = r_{\rm max}$ and its total mass $M = M_{\rm core}$. Furthermore, we can make this equation also a little bit more accessible for our specific application by expressing the time in years, the total core mass $M_{\rm core}$ in units of solar mass $\mathrm{M}_\odot$, and the outer core radius $r_{\rm max}$ in AU. With Eq. 3.24 we can directly express a year in these units (in one year the earth moves around the sun with a mass of $M = 1\ \mathrm{M}_\odot$ on an orbit with the farthest destination of $r = 1$ AU):

$$1\mathrm{yr} = \frac{2\pi\ \mathrm{AU}^{3/2}}{\sqrt{G\ \mathrm{M}_\odot}} \tag{3.27}$$

Inserting Eq. 3.27 in Eq. 3.26 yields a handy expression for the free fall time of a pre-stellar core:

$$t_{\rm ff}[\mathrm{yr}] = \sqrt{\frac{(r_{\rm max}[\mathrm{AU}])^3}{32\ M_{\rm core}[\mathrm{M}_\odot]}} \tag{3.28}$$

The numerically analyzed pre-stellar cores, introduced and discussed in Chapt. 4, have an outermost radius of $r_{\rm max} = 0.1$ pc $= 20626.5$ AU and initial core masses of $M_{\rm core} = 60$, 120, 240, and 480 $\mathrm{M}_\odot$. This corresponds to free fall times of the massive pre-stellar cores of $t_{\rm ff} \approx 67.6$, 47.8, 33.8, and 23.9 kyr respectively.

3.3 Centrifugal radius

A typical length scale of the dynamics of a rotating pre-stellar core is given by its so-called mean centrifugal radius. We start the following derivation with an initially slowly rotating spherically symmetric collapsing pre-stellar core. Due to the conservation of angular momentum a specific fluid volume will speed up its rotation while falling further inwards. The in-fall motion will be subsequently decreased until the fluid volume arrives at its keplerian orbit in the disk midplane, where the gravitational force inwards is balanced by the centrifugal force in the outward direction. Any other force is neglected during the derivation of the definition of the centrifugal radius. The final orbital radius of the fluid volume is called the centrifugal radius $r_{\rm cent}$. It can be derived from the angular momentum conservation during the in-fall phase and the force balance of the final state. The specific angular momentum $\vec{j}$ of the rotating fluid volume with the density ρ with respect to the core center at the origin is given by:

$$\vec{j}(\vec{x}) = \rho\ \vec{u} \times \vec{x} \tag{3.29}$$

The position vector $\vec{x}$ is simply given by the actual radius $\vec{x} = r\vec{e_r}$ and the velocity $\vec{u}$ in the initial as well as in the final state is fixed in azimuthal direction $\vec{u} = u_\phi \vec{e_\phi}$:

$$\vec{j}(\vec{x}) = \rho\ u_\phi \vec{e_\phi} \times r\vec{e_r} \tag{3.30}$$

With the angular velocity $\Omega = u_\phi / R$ and the cylindrical radius $R = r\sin(\theta)$ the absolute value of the angular momentum results in:

$$j(r,\theta) = \rho\ u_\phi\ r = \rho\ \Omega\ r^2 \sin(\theta) \tag{3.31}$$

The angular momentum conservation from the arbitrary initial starting point (r_i, θ_i) inside the pre-stellar core to the final location $(r_{\rm cent}, \theta = 90°)$ in the midplane yields:

$$j(r_i,\theta_i) = j(r_{\rm cent}, 90°) \tag{3.32}$$

$$\Omega_i\ r_i^2 \sin(\theta_i) = \Omega_f\ r_{\rm cent}^2 \tag{3.33}$$

Secondly, we use the knowledge about the final angular velocity Ω_f, which is a result of the balance of the centrifugal and the gravitational force in the forming circumstellar disk. The final angular velocity Ω_f is given by the keplerian orbital motion around a point mass at the origin, which is equal to the included mass $M(r_{\rm cent}, t_f)$. Repeating the argument of the free fall case, discussed in the previous section, that no in-falling shell will overtake any other shell during the collapse the finally and initially included mass are equivalent $M(r_i, t_i) = M(r_{\rm cent}, t_f) \equiv M(r_i)$ and the angular velocity of the final keplerian orbit is therefore:

$$\Omega_f = \sqrt{\frac{G\ M(r_i)}{r_{\rm cent}^3}} \tag{3.34}$$

Combining Eqs. 3.32 and 3.34 finally yields the demanded expression for the centrifugal radius:

$$\boxed{r_{\rm cent} = \frac{\Omega_i^2\ r_i^4}{G\ M(r_i)} \sin^2(\theta_i)} \tag{3.35}$$

Furthermore, we would like to derive a simple scalar property of pre-stellar cores, which defines the location, where in the mean the most mass of the collapsing core will end up. This quantity is called the mean centrifugal radius $\bar{r}_{\rm cent}$. To achieve this property of a pre-stellar core we average the centrifugal radius $r_{\rm cent}(\vec{x})$ (Eq. 3.35) weighted by the initial density distribution $\rho(\vec{x})$:

$$\bar{r}_{\rm cent} = \frac{1}{M_{\rm core}} \int \rho\left(\vec{x}\right)\ r_{\rm cent}\left(\vec{x}\right)\ dV \tag{3.36}$$

The later on studied pre-stellar cores (Sect. 4) have an initial density distribution, which drops with r^{-2} up to a maximum radius of $r_{\rm max}$, a total mass of $M_{\rm core}$, and start in rigid rotation Ω. For this specific setup, the mean centrifugal radius is determined by:

$$\bar{r}_{\rm cent} = \frac{1}{M_{\rm core}} 2\pi \int_0^{r_{\rm max}} dr \int_0^{\pi} d\theta\, \rho(r)\, \frac{\Omega^2\ r^4\ \sin^2(\theta)}{G\ M(r)}\ r^2 \sin(\theta) \tag{3.37}$$

The integral over the polar dependent parts of Eq. 3.37 yield:

$$\int_0^{\pi} \sin^3(\theta)\ d\theta = \left[-\frac{3}{4}\cos(\theta) + \frac{1}{12}\cos(3\theta)\right]_0^{\pi} = \frac{4}{3} \tag{3.38}$$

The included mass $M(r)$ for the specified initial density distribution can be expressed as:

$$\begin{aligned} M(r) &= \int \rho(\vec{x})\ dV && (3.39)\\ &= 4\pi \int_0^r \rho_0\ (r'/r_0)^{-2}\ r'^2\ dr' && (3.40)\\ &= 4\pi\ \rho_0\ r_0^2 \int_0^r 1\ dr' && (3.41)\\ &= 4\pi\ \rho_0\ r_0^2\ r && (3.42) \end{aligned}$$

Inserting the resulting Eqs. 3.38 and 3.39 as well as $\rho(r) = \rho_0\ (r/r_0)^{-2}$ in Eq. 3.37 gives

$$\bar{r}_{\rm cent} = \frac{2\ \Omega^2}{3\ G\ M_{\rm core}} \int_0^{r_{\rm max}} r^3\ dr, \tag{3.43}$$

which allows us to compute the mean centrifugal radius finally as

$$\boxed{\bar{r}_{\rm cent} = \frac{\Omega^2\ r_{\rm max}^4}{6\ G\ M_{\rm core}}} \tag{3.44}$$

We calculate the mean centrifugal radius for the given setup of the pre-stellar cores we investigate in Chapt. 4: The default values of the physical initial conditions (see Sect. 4.1) are a rigid rotation of $\Omega = 5 * 10^{-13}$ Hz, an outer core radius of $r_{\rm max} = 0.1$ pc, and varying core masses of $M_{\rm core} = 60$, 120, 240, as well as 480 $M_\odot$. The corresponding mean centrifugal radii are approximately $\bar{r}_{\rm cent} \approx 3200$, 1600, 800, and 400 AU respectively.

3.4 Generalized Eddington limit

Originally the so-called classical Eddington limit, also referred to as the Eddington luminosity, defines the equilibrium of the gravity inside a spherically symmetric star in hydrostatic equilibrium and the radiative force introduced by the electron (Thomson-) scattering. The so-called generalized Eddington limit in the context of massive star formation describes the (maximum) luminosity L_* of a star of given mass M_*, at which the radiative force onto the stellar environment compensates the stellar gravity.

$$|\vec{f}_{\text{radiative}}| = |\vec{f}_{\text{grav}}| \tag{3.45}$$

That means a previously resting mass cannot accrete onto the stellar surface anymore. Inserting the expression for the corresponding forces yields

$$\rho\kappa_* \frac{F(r)}{c} = \rho \frac{G\,M_*}{r^2} \tag{3.46}$$

with the stellar radiative flux $F(r) = L_*/(4\pi r^2)$. Due to the fact that this stellar radiative flux as well as the stellar gravity declines with r^{-2} the radial dependence drops out and solving for the luminosity to mass ratio of the massive star finally gives:

$$\boxed{\frac{L_*}{M_*} = \frac{4\pi\, G\, c}{\kappa_*}} \tag{3.47}$$

But the derived ratio is far from being a strict limit for the formation scenario of a massive star. For instance, the assumption of previously resting material is clearly not fulfilled inside a collapsing pre-stellar core. On the other hand, the relation gives an easily accessible method to determine the importance of radiative feedback for a specific setup. In our models we make use of the pre-calculated stellar evolutionary tracks of Hosokawa & Omukai (2008) and calculate the dust opacities from the frequency dependent opacity tables of Laor & Draine (1993). Fig. 3.3 displays the result of the criterion given by Eq. 3.47 for an evolving massive star with a constant accretion rate of $\dot{M}_* = 10^{-3}\ \mathrm{M_\odot\ yr^{-1}}$ as well as $\dot{M}_* = 10^{-5}\ \mathrm{M_\odot\ yr^{-1}}$, taking the stellar evolution data for L_*/M_* and the corresponding stellar radius R_* from Hosokawa & Omukai (2008), and calculating the opacities κ_* as the Planck mean opacities derived from Laor & Draine (1993).

It is clearly visible in the lower panel that radiative forces onto the environment of a low-mass star with accretion rates below $\dot{M}_* = 10^{-5}\ \mathrm{M_\odot\ yr^{-1}}$ are orders of magnitude lower than the acting stellar gravity. But for higher accretion rates above $\dot{M}_* = 10^{-3}\ \mathrm{M_\odot\ yr^{-1}}$ (cp. upper panel in Fig. 3.3) the radiative force becomes as strong as the stellar gravity of the new born star with a mass up to approximately $10\ \mathrm{M_\odot}$. But we also detect that a factor of 100 in the accretion rate (lower panel versus upper panel) does only result in a factor of about 15 when comparing the ratio of the radiative force to the gravity. The reason for this is that the high accretion rate yields to a swelling of the forming star and this increase of the stellar radius implies a decrease of the stellar effective surface temperature. That means the star radiates at lower frequencies, where the radiative force strongly shrinks due to the corresponding lower opacities κ_*.

When the star grows further in time up to $30\ \mathrm{M_\odot}$, the luminosity of the massive star is dominated by nuclear fusion (solid line in Fig. 3.3) and the radiative force rises even further. From the point in time at which the massive star enters the super Eddington regime $L_*/M_* > 4\pi\, G\, c/\kappa_*$, the previous in-fall of the pre-stellar core will be slowed down and the mass flux onto the forming star will potentially be reverted when the nuclear fusion luminosity gets dominant.

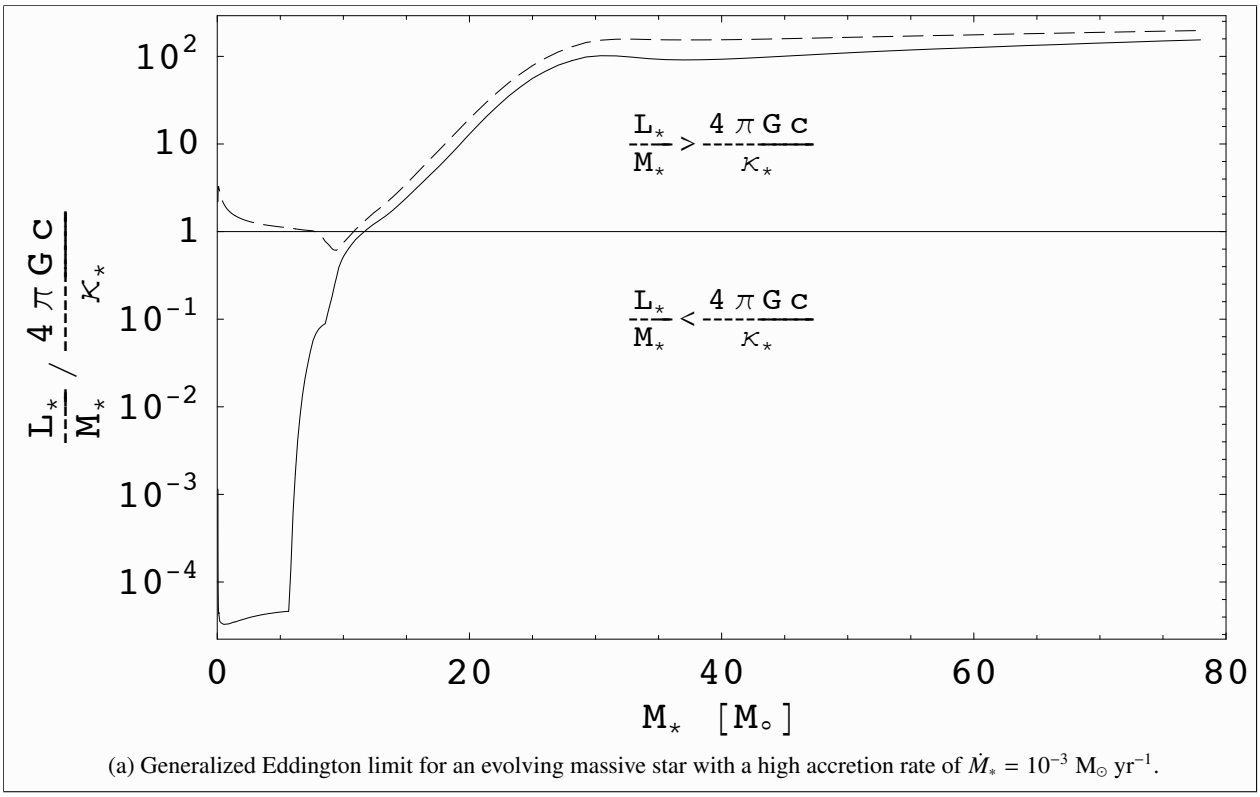

(a) Generalized Eddington limit for an evolving massive star with a high accretion rate of $\dot{M}_* = 10^{-3}$ $M_\odot$ yr^{-1}.

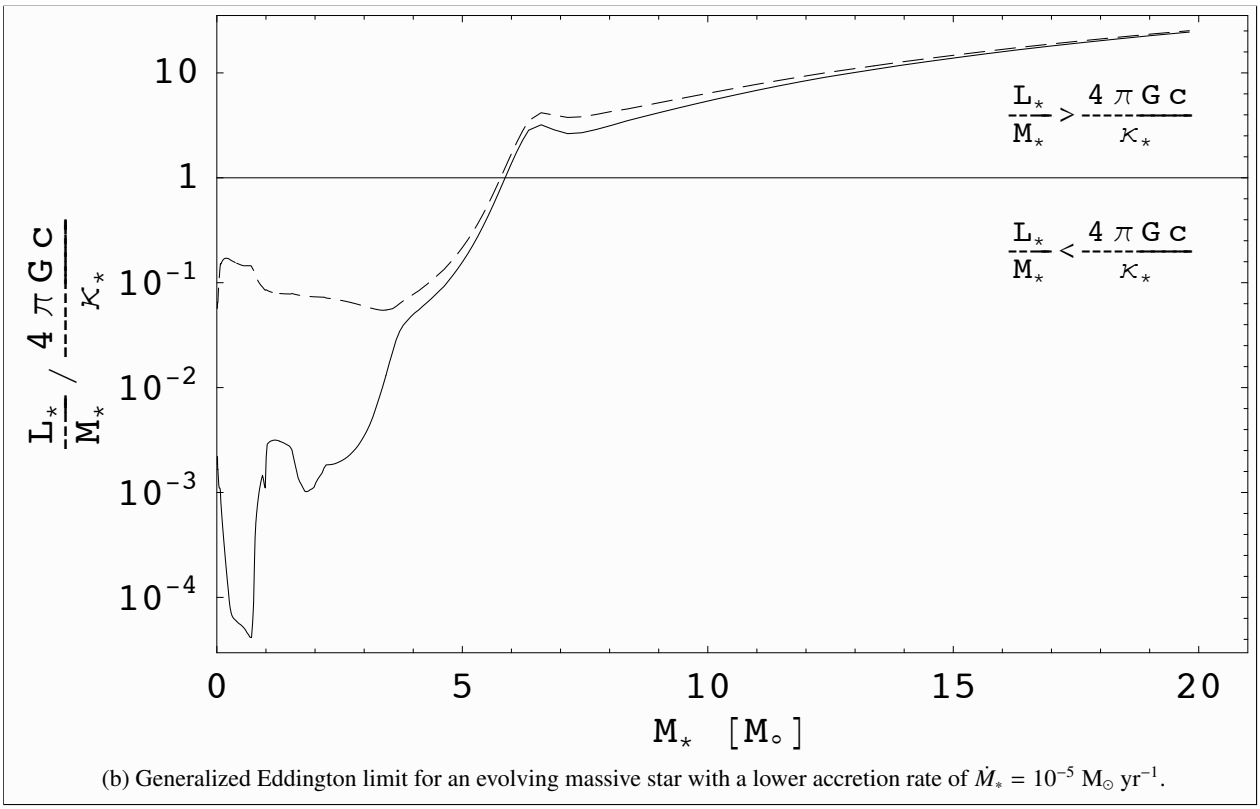

(b) Generalized Eddington limit for an evolving massive star with a lower accretion rate of $\dot{M}_* = 10^{-5}$ $M_\odot$ yr^{-1}.

Figure 3.3: Sub-Eddington and Super-Eddington regimes for a massive star with a constant accretion rate of $\dot{M}_* = 10^{-3}$ $M_\odot$ yr^{-1} and $\dot{M}_* = 10^{-5}$ $M_\odot$ yr^{-1} respectively. The solid line marks the result if only the nuclear fusion luminosity of the forming star is taken into account. The dashed line identifies the result for the total luminosity (nuclear fusion plus accretion luminosity).

3.5 Dust condensation radius

The close neighborhood of a newly forming massive star is strongly heated by the stellar irradiation. When the local temperature T of the surroundings exceeds the evaporation temperature $T_{\rm evap}$ of the dust grains the dust in the corresponding region melts. In this subsection, we want to estimate the extent of the dust free region around a massive star of a given luminosity L_*. This extent is hereafter called the dust condensation radius $r_{\rm cond}$ and plays an important role for the numerical setup of the later on studied collapse problem (see Sects. 4.2.2 and 4.3.2). Besides the stellar irradiation any other heating (or cooling) process of the pre-stellar envelope is neglected during the derivation. The optical depth between the stellar surface R_* and the dust condensation radius $r_{\rm cond}$ is assumed to be negligible. That means the expelled stellar luminosity

$$L_* = 4\pi\,\sigma_{\rm SB}\,R_*^2\,T_*^4 \tag{3.48}$$

with the Stefan-Boltzmann constant $\sigma_{\rm SB}$ is constant up to the first absorption of stellar light at $r_{\rm cond}$. The corresponding local temperature $T(r)$ of the optically thin region declines from the stellar surface temperature $T(R_*) = T_*$ proportional to the square root of the radius

$$T(r) = T_*\,\sqrt{\frac{R_*}{r}}. \tag{3.49}$$

Combining Eqs. 3.48 and 3.49 and solving for the dust condensation radius gives

$$r_{\rm cond} = R_*\left(\frac{T_*}{T_{\rm evap}}\right)^2 = \sqrt{\frac{L_*}{\pi\,\sigma_{\rm SB}}}\,\frac{1}{T_{\rm evap}^2} \tag{3.50}$$

Analogously to the dust model used in the collapse simulations and presented in Sect. 2.6, we relate the dust evaporation temperature T_e to the corresponding gas density ρ at the radius $r_{\rm cond}$ by using the formula of Isella & Natta (2005)

$$T_{\rm evap} = g\,\rho^{\,\beta} \tag{3.51}$$

with $g = 2000$ K, $\beta = 0.0195$ and ρ given in g cm^{-3}. The formula describes a power-law approximation to the evaporation temperatures determined by Pollack et al. (1994). The dust condensation radius finally yields:

$$\boxed{r_{\rm cond} = \sqrt{\frac{L_*}{\pi\,\sigma_{\rm SB}}}\,\frac{1}{(g\,\rho^{\,\beta})^2}} \tag{3.52}$$

Fig. 3.4 displays the resulting dust condensation radius of a massive star depending on its luminosity L_* for a high value of the gas density of the stellar environment of $\rho = 10^{-10}$ g cm^{-3} as well as for the floor value of the gas density $\rho = 10^{-21}$ g cm^{-3} of the numerical hydrodynamics simulations. The given mass of the massive star at the upper axis is estimated from the stellar evolutionary track from Hosokawa & Omukai (2008) for a constant accretion rate of $\dot{M}_* = 10^{-3}$ M$_\odot$ yr^{-1}.

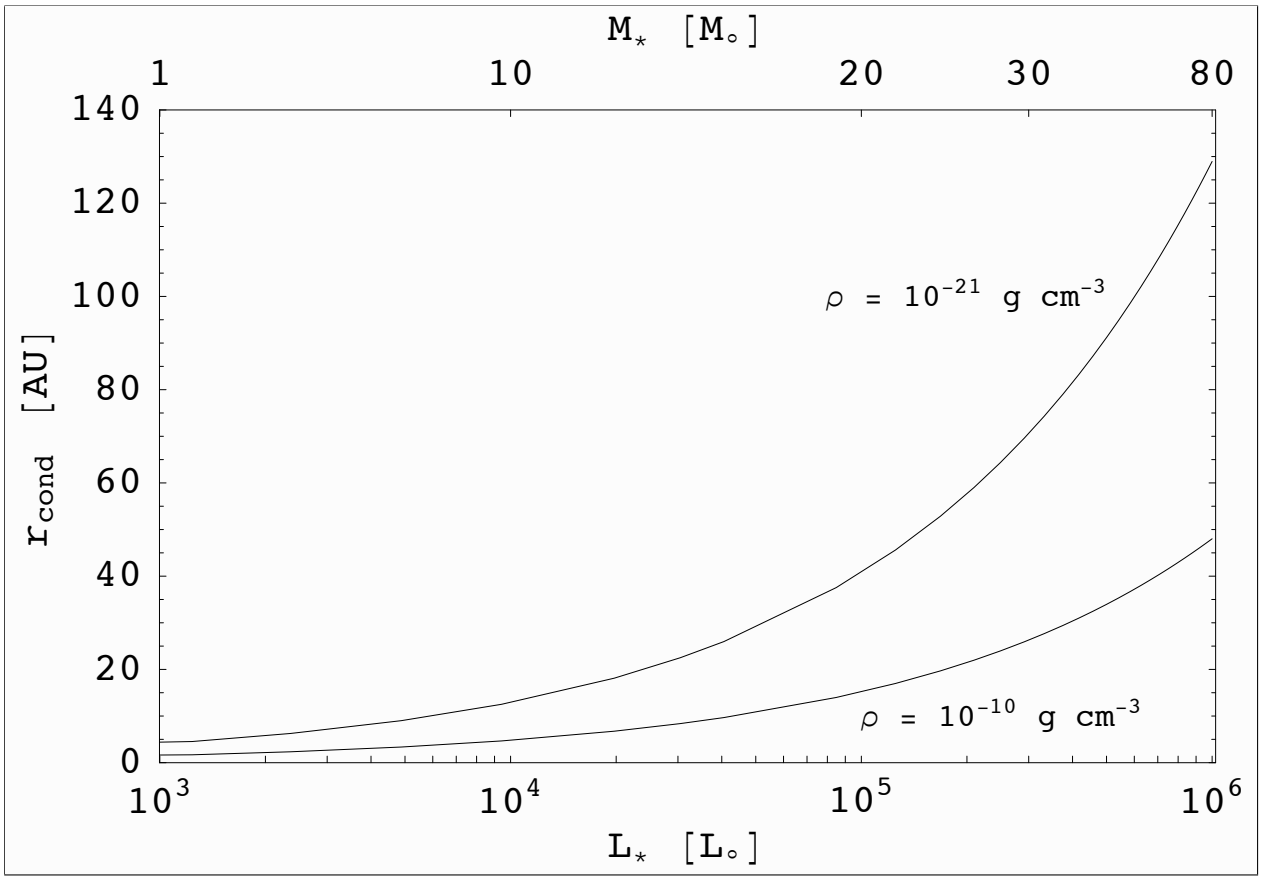

Figure 3.4: Dust condensation radius $r_{\rm cond}$ of a massive star as a function of the stellar luminosity for a high as well as a low value of the corresponding gas density of the stellar environment respectively. Stellar irradiation is the only heating process which is taken into account for the estimation of the dust condensation radius. The corresponding mass of the star at the upper axis is taken from the stellar evolutionary tracks by Hosokawa & Omukai (2008) for a forming star with a constant accretion rate of $\dot{M}_* = 10^{-3}$ M$_\odot$ yr^{-1}.

4

Simulations of the formation of massive stars

Using the newly developed modules of the self-gravitating radiation hydrodynamics code presented in Chapt. 2, we perform multiple simulations of collapsing massive pre-stellar cores. We study in particular the radiative feedback on the hydrodynamics as it depends on the dimension or symmetry of the system. In one-dimensional simulations, we verify qualitatively the upper mass limit for spherically symmetric accretion flows onto a massive star found in previous research studies. Quantitatively we determine the stellar mass to stay below 40 $M_\odot$ for an initially steep density profile of the pre-stellar core of $\rho \propto r^{-2}$, recently computed stellar evolutionary tracks for accreting high-mass stars (Hosokawa & Omukai 2008), and the frequency dependent dust opacities taken from Laor & Draine (1993). We show that the spherical coordinate system used is suited perfectly to follow the ongoing radiation accretion physics in one-, two-, and three-dimensional simulations. This leads to a numerically converging result even for a low number of grid cells in the polar direction. Thus we save computational time and are able to resolve the dust condensation front

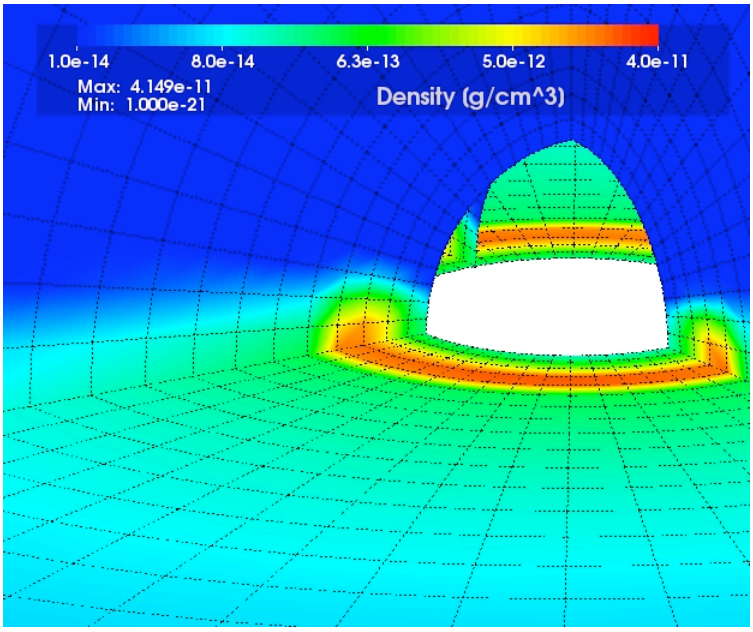

Figure 4.1: The formation of a self-gravitating ring instability in the massive accretion disk. The snapshot is taken at 7,820 yr of evolution of a collapsing pre-stellar core of 120 $M_\odot$. The radius of the ring is roughly 15 AU. The numerical grid is highlighted by dashed lines. The central sink cell is treated as transparent.

with $(1.27\ \mathrm{AU})^3$ and below even in three-dimensional simulations. Additionally, this gain in CPU time offers the possibility to study the collapse of the pre-stellar core and the evolution of the circumstellar disk as well as its large-scale envelope up to several hundreds of kyr, ten times longer than ever studied before. We demonstrate the need to include the dust condensation front in the computational domain to reproduce the radiative feedback on the accretion flow correctly. Especially, we argue in a code comparison with the simulations of Yorke & Sonnhalter (2002) that neglecting this first absorption region leads to artificially high radiative feedback and therefore limits the stellar mass reached in their simulations dramatically. We verify the results of analytical estimates by Vaidya et al. (2009) about the viscous regime of stable massive accretion disks around massive stars. When applying the α-parametrization by Shakura & Sunyaev (1973) the viscous regime of stable disks lies roughly between $\alpha = 0.1$ and $\alpha = 0.01$. In axially symmetric two-dimensional simulations of rotating core collapses, we found that the accretion onto the massive star is not stopped at the upper mass limit, previously determined in spherical symmetry. The radiative flux is bypassed through the disk's atmosphere perpendicular to the accretion flow. We analyze in detail the dynamics of the system consisting of the forming star, the circumstellar disk and the envelope, which lead to this clear breakthrough. We categorize the evolution of the rotating and non-rotating collapsing pre-stellar cores into distinguishable epochs. This proposed classification is based on major events shaping the morphology of the pre-stellar cores such as the formation of a circumstellar disk and the launching of a bipolar outflow. In three-dimensional, high-resolution simulations of the collapse of massive pre-stellar cores, we study the evolution of the dust condensation front and the associated blowout of the radiation pressure driven outflow. We reveal the onset of a close-by gravitational instability in the resulting accretion disk. The accretion rate induced by this instability is in good agreement with the two-dimensional α-viscosity models. In general, most of the simulations were performed either to scan the huge numerical parameter space of the setup to guarantee significant results or to explore individual physical initial conditions. An overview of the simulations evaluated is presented in table 4.1 on p. 83 and following. The table also contains the simulation specific parameters, which are not already part of the default configuration described in Sect. 4.1. Each subsequent section covers the results of simulations performed in a specific dimension from spherically symmetric one-dimensional (Sect. 4.2) through axially and midplane symmetric two-dimensional (Sect. 4.3) up to three-dimensional runs (Sect. 4.4).

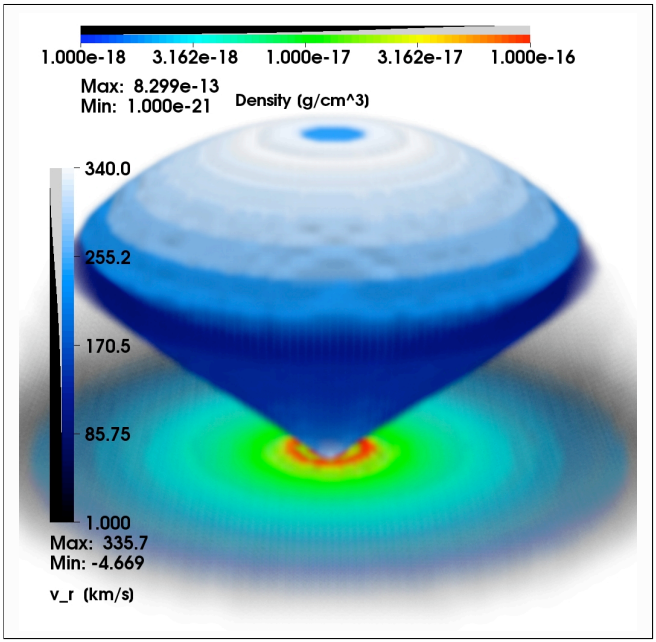

Figure 4.2: Volume rendering of an axially symmetric pre-stellar core of $120\,\mathrm{M}_\odot$ at 10 kyr after the start of the collapse. The image shows the entire computational domain with a radius of 0.1 pc. The gas density is rendered in a logarithmic scale from 10^{-18} g cm^{-3} up the maximum value. The low-density gas $\left(\rho < 10^{-18}\ \mathrm{g\ cm^{-3}}\right)$ of the envelope is visualized in black. The positive radial velocity highlighting the radiation pressure driven outflow is rendered in a linear scale from dark blue to light blue and white.

Label	Dimension	Grid cells	Resolution [AU]	$r_{\rm min}$ [AU]	α	$M_{\rm core}$ [$M_\odot$]	$t_{\rm ff}$ [kyr]	$t_{\rm end}$ [kyr]
1D Convergence runs		Sect. 4.2.1						
1D-rmin80AU-Convergence16	1D	16	33.2	80	-	60	67.6	200
1D-rmin80AU-Convergence32	1D	32	15.2	80	-	60	67.6	200
1D-rmin80AU-Convergence64	1D	64	7.25	80	-	60	67.6	200
1D-rmin80AU-Convergence128	1D	128	3.55	80	-	60	67.6	300*
1D-rmin80AU-Convergence256	1D	256	1.75	80	-	60	67.6	200
1D-rmin1AU-Convergence32	1D	32	0.36	1	-	60	67.6	120
1D-rmin1AU-Convergence64	1D	64	0.17	1	-	60	67.6	120
1D-rmin1AU-Convergence128	see '1D-Mcore60Msol'							
1D-rmin1AU-Convergence256	1D	256	0.04	1	-	60	67.6	56
1D rmin runs		Sect. 4.2.2						
1D-rmin1AU	1D	99 + 128	1.0	1	-	60	67.6	200
1D-rmin5AU	1D	95 + 128	1.0	5	-	60	67.6	300*
1D-rmin10AU	1D	90 + 128	1.0	10	-	60	67.6	300*
1D-rmin80AU	1D	20 + 128	1.0	80	-	60	67.6	300*
1D Mcore runs		Sect. 4.2.3						
1D-Mcore-60Msol	1D	128	0.08	1.0	-	60	67.6	328*
1D-Mcore-120Msol	1D	128	0.08	1.0	-	120	47.8	55*
1D-Mcore-240Msol	1D	128	0.08	1.0	-	240	33.8	60*
1D-Mcore-480Msol	1D	128	0.08	1.0	-	480	23.9	11*

Table 4.1: Overview of massive pre-stellar core collapse simulations presented. The table is structured in blocks of topics and their corresponding sections. For each run the label, the dimension, the number of used grid cells, the resolution of the best resolved regions in the midplane $(\Delta r \text{ x } r\ \Delta\theta \text{ x } r\ \sin(\theta)\ \Delta\phi)_{\rm min}$, the size of the central sink cell $r_{\rm min}$ (the location of the inner boundary of the computational domain), the strength of the so-called α-viscosity if applied (cp. Sect. 2.3), the initial mass of the pre-stellar core $M_{\rm core}$, its corresponding free fall time $t_{\rm ff}$ (cp. Sect. 3.2), and the period of evolution simulated $t_{\rm end}$ are given. If results of a single run are used in several sections, only a link to the final evaluation is given. Simulations, which were at least performed until the accretion rate onto the central star has dropped to zero, are marked by an additional '$*$' in the $t_{\rm end}$ column; most of these runs contain no mass in the computational domain anymore. Simulations, which are still running, are marked by an additional '+' in the $t_{\rm end}$ column.

Label	Dimension	Grid cells	Resolution [AU]	$r_{\rm min}$ [AU]	α	$M_{\rm core}$ [$M_\odot$]	$t_{\rm ff}$ [kyr]	$t_{\rm end}$ [kyr]
2D Convergence runs		Sect. 4.3.1						
2D-Convergence-32x16	2D	32 x 16	2.69 x 1.11	10	0.03	60	67.6	62
2D-Convergence-64x4	2D	64 x 4	1.27 x 4.18	10	0.03	60	67.6	93
2D-Convergence-64x8	2D	64 x 8	1.27 x 2.09	10	0.03	60	67.6	737*
2D-Convergence-64x16	see '2D-Mcore60Msol'							
2D-Convergence-128x32	2D	128 x 32	0.61 x 0.51	10	0.03	60	67.6	33+
2D rmin runs		Sect. 4.3.2						
2D-Mcore60Msol-rmin80AU	2D	64 x 16	7.25 x 8.21	80	0.03	60	67.6	293*
2D-Mcore60Msol-rmin10AU	see '2D-Mcore60Msol'							
2D-Mcore60Msol-rmin5AU	2D	64 x 16	0.69 x 0.52	5	0.03	60	67.6	140+
2D-Mcore60Msol-rmin1AU	2D	64 x 16	0.17 x 0.11	1	0.03	60	67.6	57+
2D-Mcore120Msol-rmin160AU	2D	64 x 16	12.62 x 16.33	160	0.03	120	47.8	450*
2D-Mcore120Msol-rmin80AU	2D	64 x 16	7.25 x 8.21	80	0.03	120	47.8	260+
2D-Mcore120Msol-rmin10AU	see '2D-Mcore120Msol'							
2D-Mcore120Msol-rmin5AU	2D	64 x 16	0.69 x 0.52	5	0.03	120	47.8	13+
2D alpha runs		Sect. 4.3.3						
2D-alpha0	2D	64 x 16	1.27 x 1.04	10	0	60	67.6	33
2D-alpha1e-3	2D	64 x 16	1.27 x 1.04	10	0.001	60	67.6	56
2D-alpha1e-2	2D	64 x 16	1.27 x 1.04	10	0.01	60	67.6	1,000
2D-alpha3e-2	see '2D-Mcore60Msol'							
2D-alpha1e-1	2D	64 x 16	1.27 x 1.04	10	0.1	60	67.6	107+
2D-alpha1	2D	64 x 16	1.27 x 1.04	10	1	60	67.6	37
2D Mcore runs		Sect. 4.3.5						
2D-Mcore60Msol	2D	64 x 16	1.27 x 1.04	10	0.03	60	67.6	550+
2D-Mcore120Msol	2D	64 x 16	1.27 x 1.04	10	0.03	120	47.8	454*+
2D-Mcore240Msol	2D	64 x 16	1.27 x 1.04	10	0.03	240	33.8	201*+
2D-Mcore480Msol	2D	64 x 16	1.27 x 1.04	10	0.03	480	23.9	24+

Table 4.1: Continuation of table 4.1 on p. 83.

Label	Dimension	Grid cells	Resolution [AU]	r_{min} [AU]	α	M_{core} [$\mathrm{M}_{\odot}$]	t_{ff} [kyr]	t_{end} [kyr]
3D Mcore runs		Sect. 4.4						
3D-Mcore120Msol	3D	64 x 16 x 64	1.27 x 1.04 x 1.04	10	-	120	47.8	8.232^{+}
3D-Mcore240Msol	3D	64 x 16 x 64	1.27 x 1.04 x 1.04	10	-	240	33.8	3.416^{+}

Table 4.1: Continuation of table 4.1 on p. 83f.

4.1 Default initial conditions of the massive pre-stellar cores

In the following sections we discuss the results of 37 simulations of the collapse of a massive pre-stellar core. Aside from varying the configuration, most of the initial conditions and the physics considered in the simulations stay the same. The default initial condition is very similar to the one used by Yorke & Sonnhalter (2002). We start from a cold (T_0 = 20 K) pre-stellar core of gas and dust. The initial dust to gas mass ratio is chosen to be $M_{\rm dust}/M_{\rm gas}$ = 1%. The model describes a so-called quiescent collapse scenario without turbulent motion ($\vec{u}_r = \vec{u}_\theta = 0$). In non-spherically symmetric two- or three-dimensional runs the core is initially in slow rigid rotation $\left(|\vec{u}_\phi|/R = \Omega_0 = 5 * 10^{-13}\text{Hz}\right)$. The rotation speed of Ω_0 results roughly in an equilibrium between gravity and centrifugal force at the outer core radius $r_{\rm max}$ in the case of the lowest mass core of $M_{\rm core}$ = 60 $M_\odot$. The outer radius of the core is fixed to $r_{\rm max}$ = 0.1 pc and the total mass of the core $M_{\rm core}$ varies in the different simulations from 60 up to 480 $M_\odot$. The initial density slope drops with r^{-2}. A brief overview of these physical initial conditions of the massive pre-stellar cores studied is given in table 4.2.

Symbol	Value	Quantity
T_0	20 K	temperature of the pre-stellar core
$M_{\rm dust}/M_{\rm gas}$	1%	dust to gas mass ratio
$\|\vec{u}_r\|$	0	radial velocity
$\|\vec{u}_\theta\|$	0	polar velocity
$\Omega_0 = \|\vec{u}_\phi\|/r$	$5 * 10^{-13}$ Hz	azimuthal angular velocity in 2D and 3D
$r_{\rm max}$	0.1 pc	outer radius of the pre-stellar core
$\rho(r)$	r^{-2}	density slope of the pre-stellar core
$M_{\rm core}$	60 to 480 $M_\odot$	mass of the pre-stellar core

Table 4.2: Overview of default physical initial conditions used in the collapse simulations of massive pre-stellar cores.

In axial symmetric (two-dimensional) runs, physical shear viscosity is used to maintain the accretion flow through the growing circumstellar disk. Therefore, we adopted the well-known α-parametrization model for shear viscosity of standard disk theory (Shakura & Sunyaev 1973). We performed several simulations with varying normalization values for the physical α-viscosity and compare our results to high-resolution simulations of angular momentum transport by the magneto-rotational instability as well as analytic stability analysis of massive accretion disks. Please see Sect. 2.3 for details of the treatment of physical shear viscosity and Sect. 4.3.3 for the results of the simulations with different strength of viscosity. Apart from the runs included in the parameter scan the normalization was fixed to α = 0.03.

The simulations were performed on a time independent grid in spherical coordinates (see Sect. 2.1). The radially inner boundary of the computational domain is a semi-permeable wall towards the forming star, i.e. the gas can enter the central sink cell, but it cannot leave. The outer radial boundary is a semi-permeable wall as well. The mass can be pushed out of the computational domain (by radiative forces) but no mass is allowed to enter the computational domain. This limits the extent of the mass reservoir to the initially fixed mass of the pre-stellar core $M_{\rm core}$. The semi-permeable outer boundary implies the assumption that the collapsing core is mostly isolated from its environment. While we started the first simulations with a radius of the inner sink cell

of $r_{\rm min}$ = 80 AU as in the case of 'F60' in Yorke & Sonnhalter (2002) we experienced that it is necessary to shrink the sink cell down to $r_{\rm min}$ = 10 AU to guarantee that the dust condensation front of the forming massive star is included in the computational domain at least after the initial free fall phase. Most of the one-dimensional simulations have an inner sink cell radius of $r_{\rm min}$ = 1 AU. The resolution of the computational domain, which is necessary to follow the radiation and fluid physics as well as its interactions, is determined in several so-called convergence runs, see Sect. 4.2.1 and 4.3.1 for non-rotating and rotating cores respectively.

In previous test runs we studied several non-radiative and radiative physics. We performed isothermal and adiabatic collapse simulations as well as gray and frequency dependent radiation transport with and without radiation pressure feedback from the star or the diffuse radiation field. Here we confine ourselves to present only the most realistic runs including frequency dependent radiation transport as well as full radiative feedback.

4.2 Non-rotating spherically symmetric pre-stellar cores (one-dimensional simulations)

We start the discussion of the simulation results with the analysis of one-dimensional runs performed in spherical symmetry. As described in Sect. 1.3, spherically symmetric accretion onto a massive star is potentially stopped by the growing radiation pressure. Previous radiation hydrodynamics studies (introduced in Sect. 1.4) with diverse radiation transport methods agree on the issue that the effect of the infrared radiative force by photons from thermal dust emission dominates over the radiative feedback from direct absorption of the stellar irradiation. In these simulations, the upper mass limit $M_*^{\rm 1D}(t \rightarrow \infty)$ of the forming massive star for spherically symmetric accretion was found to lie between 30 and 40 $\rm M_\odot$. The exact value strongly depends on the dust and stellar evolution physics, which is also shown in the derivation of the Eddington limit in Sect. 3.1.5.

In the following two subsections, we present our results of one-dimensional simulations used to fix the numerical parameters of the setup, namely, the resolution and the size of the inner sink cell. Afterwards, we performed simulations with varying initial core masses $M_{\rm core}$ to determine the upper mass limit, if such a limit exists, for our specific model (the chosen dust and stellar evolution model, the configuration of the hydrodynamics solver as well as the treatment of radiation transport). To re-perform these one-dimensional simulations on our own allows us to directly compare the results with subsequent simulation results in higher dimensions.

4.2.1 Convergence simulations

Numerical hydrodynamics simulations involve a discretization of the underlying equations of hydrodynamics given in continuous space (cp. Eqs. 2.2-2.4). This causes a discretization error, which in general vanishes for infinitely high resolution of the numerical solver method. To compute a specific quantity, such as the accretion history, with a specific accuracy therefore needs a specific resolution, which is necessary to damp the discretization errors down to the requested accuracy. To fix the number of grid cells, which are necessary for a correct representation of the radiation fluid interactions, we performed several simulations with varying resolution. Focusing on the inner regions of the pre-stellar core, the radial cell sizes of the grid thereby grow logarithmically from inside out as described in Sect. 2.1. The initial conditions and numerical parameters of these convergence runs are described in Sect. 4.1. The simulations were performed for an initial core mass of $M_{\rm core}$ = 60 $\rm M_\odot$ and with an inner sink cell radius of $r_{\rm min}$ = 80 AU and $r_{\rm min}$ = 1 AU. We followed the long-

term evolution of the pre-stellar cores for at least 200 kyr and 60 kyr, representing 5.9 and 1.8 free fall times respectively. The resulting mass growth of the centrally forming star is displayed in Figs. 4.3 and 4.4.

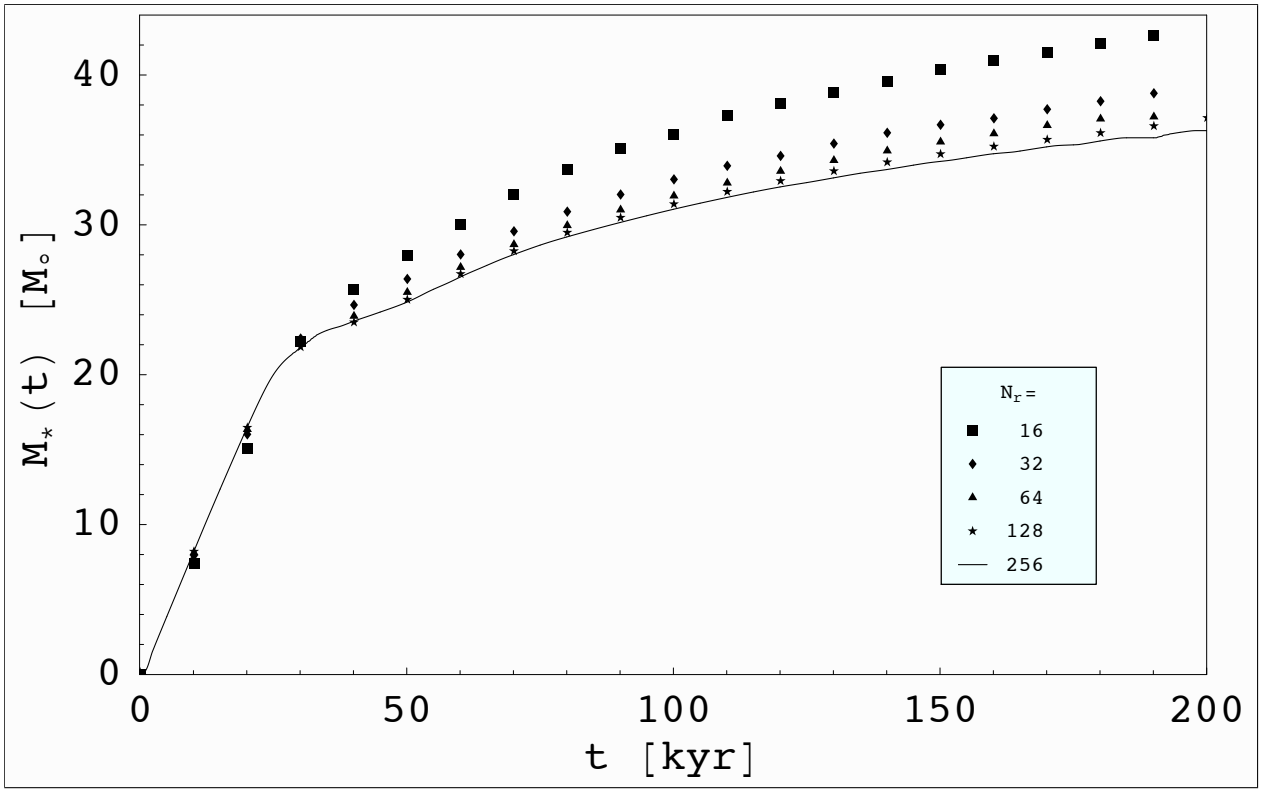

Figure 4.3: Stellar mass M_* as a function of time for five different resolutions of the spherically symmetric pre-stellar core collapse simulations with an inner sink cell radius of $r_{\min}$ = 80 AU. The number of grid cells N_r varies from 16 to 256, corresponding to a size of the smallest grid cell of $(\Delta r)_{\min}$ = 33.2 AU down to 1.75 AU respectively.

The lowest resolution run of both cases fail to compute the correct amount of accretion already during the mostly isothermal initial free fall phase (up to 25 kyr). For higher resolution runs at least with 64 grid cells, the mass growth of the forming star is identical during this phase. At a later evolutionary epoch, when radiative feedback becomes important, simulations with higher resolution lead generally to a slower mass growth and the deviations of the different runs shrink with higher resolution. So the code fulfills the requirement of a monotonic convergence towards higher resolution. Subsequent one-dimensional simulations with varying initial core masses (Sect. 4.2.3) will use 128 grid cells in radial direction and an inner radial boundary at $r_{\min}$ = 1 AU corresponding to a grid size of $(\Delta r)_{\min}$ = 0.08 AU for the innermost grid cell.

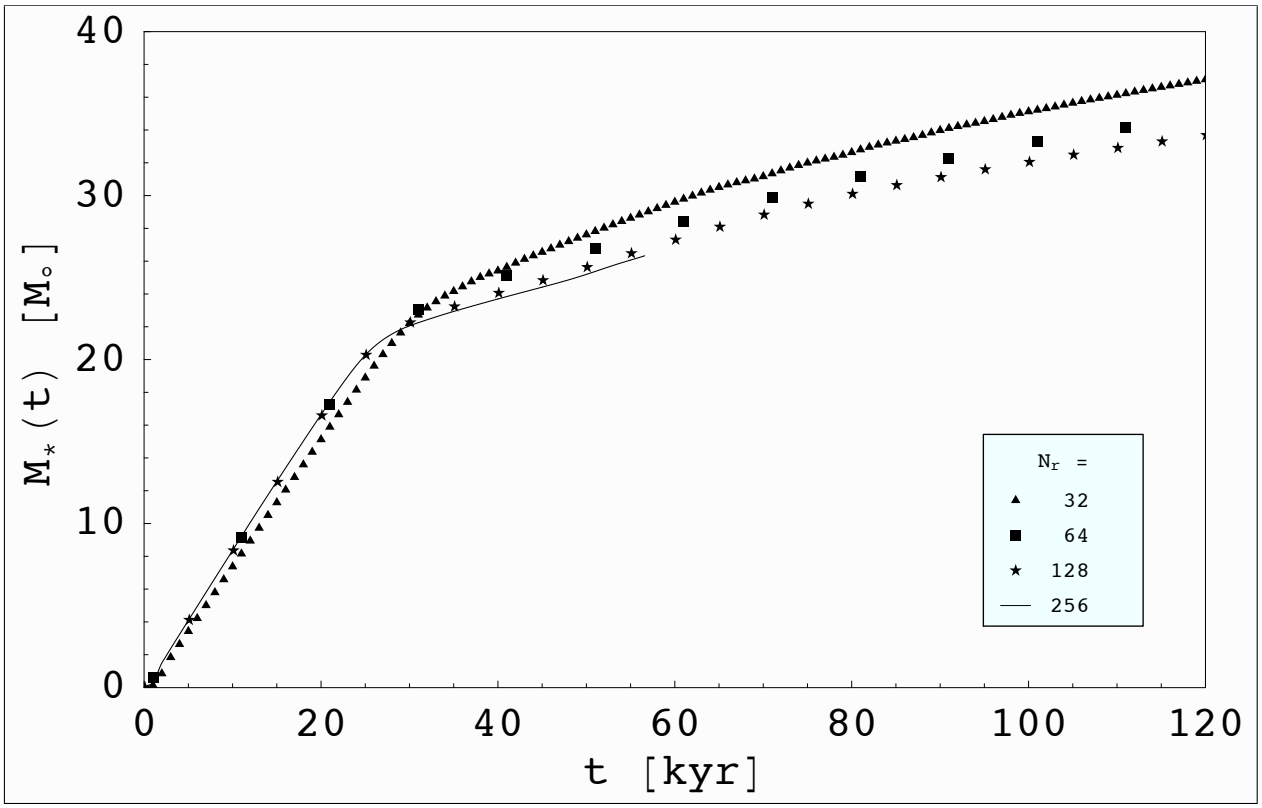

Figure 4.4: Stellar mass M_* as a function of time for four different resolutions of the spherically symmetric pre-stellar core collapse simulations with an inner sink cell radius of $r_{\rm min}$ = 1 AU. The number of grid cells N_r varies from 32 to 256, corresponding to a size of the smallest grid cell of $(\Delta r)_{\rm min}$ = 0.36 AU down to 0.04 AU respectively.

4.2.2 The influence of the size of the sink cell

In order to limit the run time of the simulations to an adequate amount, the formation and evolution of the central proto-star cannot be included in the computational domain. In fact, the radially inner computational boundary defines the radius of a so-called sink cell. The mass flux into this sink cell defines the accretion rate onto the proto-star, which is assumed to form in the center of the pre-stellar core. Inside of this sink cell the stellar properties such as luminosity and radius are taken from pre-calculated stellar evolutionary tracks. We use therefore recent results for the evolution of accreting high-mass stars (Hosokawa & Omukai 2008). In the following, we study the influence of the size of this inner boundary on the radiative feedback on the resulting accretion rate onto the evolving massive star.

The first absorption of stellar irradiation takes place directly behind the dust condensation radius $r_{\rm cond}$. If the radius of the central sink cell $r_{\rm min}$ exceeds this dust condensation radius, this interaction is artificially shifted to $r_{\rm min}$. Due to the fact that the Eddington limit is independent of the radius (stellar gravity and stellar luminosity both drop with r^{-2}), the shift of this first transfer of momentum from the stellar irradiation to the dust flow should be independent of the radius of the sink cell. Secondly, the absorption of stellar irradiation heats up the region behind the dust condensation radius respectively. The thermal radiative flux from this region

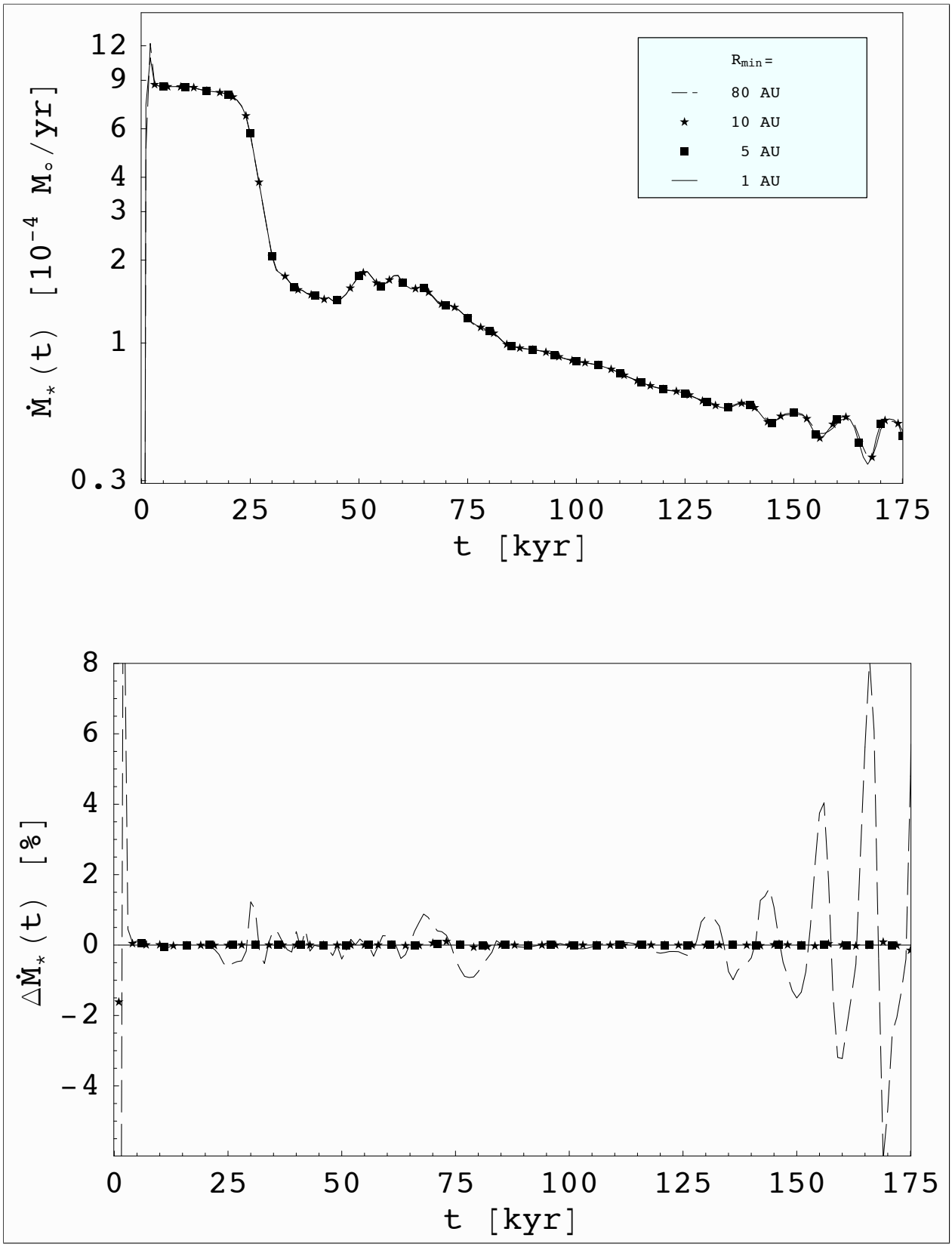

Figure 4.5: Accretion rate (upper panel) and deviations of the accretion rates from the simulation run with the smallest sink cell radius of $r_{\rm min}$ = 1 AU (lower panel) as a function of time for four different sizes of the spherical sink cell. The resolution of the grid is fixed to Δr = 1 AU up to a radius of r = 100 AU and decreases logarithmically afterwards in all simulations performed.

outwards slows down the gravitationally in-falling accretion flow. In general, this interaction depends on the radius, which defines the temperature of the heated region, the velocity of the accretion flow and the opacity of the corresponding dust. We checked this dependency in four simulations with a radius of the inner sink cell of $r_{\rm min}$ = 1, 5, 10, and 80 AU. To decouple the results from the dependence on resolution (see previous section) the size of the grid cells was fixed (Δr = 1 AU) up to a radius of 100 AU. So the different simulations use 99, 95, 90, and 20 grid cells up to 100 AU respectively. Afterwards, the grid resolution decreases logarithmically throughout additional 128 grid cells from 100 AU up to 0.1 pc. The initial conditions and numerical parameters of these runs are described in Sect. 4.1 and the simulations were performed for an initial core mass of $M_{\rm core}$ = 60 $M_\odot$. We followed the long-term evolution of the runs for at least 200 kyr, representing 3.0 free fall times. The resulting accretion flow onto the forming star as well as the deviations of the simulations from the run with $r_{\rm min}$ = 1 AU are displayed in Fig. 4.5.

In the plot of the resulting accretion rates (Fig. 4.5, upper panel) only slight deviations of the run with the largest sink cell radius $r_{\rm min}$ = 80 AU are visible during the initial and final epoch. Both other runs look identical. The lower panel of Fig. 4.5 shows in more detail the deviations of the simulations from the run with $r_{\rm min}$ = 1 AU. Apart from the beginning of the simulation, the runs with $r_{\rm min}$ = 10, 5, and 1 AU stay identical. Presumably this is due to the fact that in these simulations the dust condensation radius of the forming massive star is included in the computational domain before the onset of radiation pressure occurs at roughly 25 kyr. On the other hand, the largest sink cell of $r_{\rm min}$ = 80 AU exceeds the dust condensation radius $r_{\rm cond}$, which can be roughly estimated to 20 to 30 AU for a corresponding 20 to 30 $M_\odot$ star. The resulting accretion rate of the corresponding run oscillates around the results from the more precise simulations with a maximum deviation of 10% mostly at the end of the simulation, when the radiation pressure starts to revert the accretion flow throughout the whole domain. Due to the oscillation of these deviations and the fact that the strongest deviations occur at the end of the simulation where the accretion rate is already an order of magnitude lower than at the beginning, the four simulations yield the same final mass of the proto-star. Subsequent one-dimensional simulations presented make use of a radius of the central sink cell of $r_{\rm min}$ = 1 AU.

4.2.3 Parameter scan of the initial pre-stellar core mass: The upper mass limit of spherically symmetric accretion

The simulations presented in the previous sections were performed to fix the remaining free numerical parameters, namely the grid resolution and the size of the central sink cell. We now study the collapse of massive pre-stellar cores of different initial core masses $M_{\rm core}$ in this fixed setup. The initial conditions and numerical parameters for these runs are described in Sect. 4.1. The simulations were performed with an inner boundary of the computational domain of $r_{\rm min}$ = 1 AU and 128 grid cells with logarithmically increasing resolution towards the center. The size of the innermost grid cell of the computational domain is $(\Delta r)_{\rm min}$ = 0.08 AU.

With growing mass and luminosity of the centrally forming massive star, the radiation pressure of the direct stellar irradiation as well as from the thermal infrared dust emission will increase. Therefore, the accretion rate will potentially drop down and the massive star has grown to its final mass. The actual luminosity of the star in the sink cell is determined by the nuclear fusion luminosity from pre-calculated stellar evolutionary tracks from Hosokawa & Omukai (2008) in addition to the accretion luminosity, which is directly calculated from the mass flux into the sink cell.

Both kinds of radiative feedback (direct stellar irradiation and subsequent thermal re-emission by dust grains) are considered in the collapse simulations. We followed the evolution of the system practically until the

end of the simulation when no initial mass is left in the computational domain. Part of this mass was accreted onto the central massive star and part was expelled over the outer boundary by radiative forces. We performed spherically symmetric collapse simulations with initial pre-stellar core masses ranging from $M_{\rm core} = 60\ {\rm M}_\odot$ up to 480 $\rm M_\odot$. The resulting accretion histories are displayed in Fig. 4.6 as a function of the actual star mass.

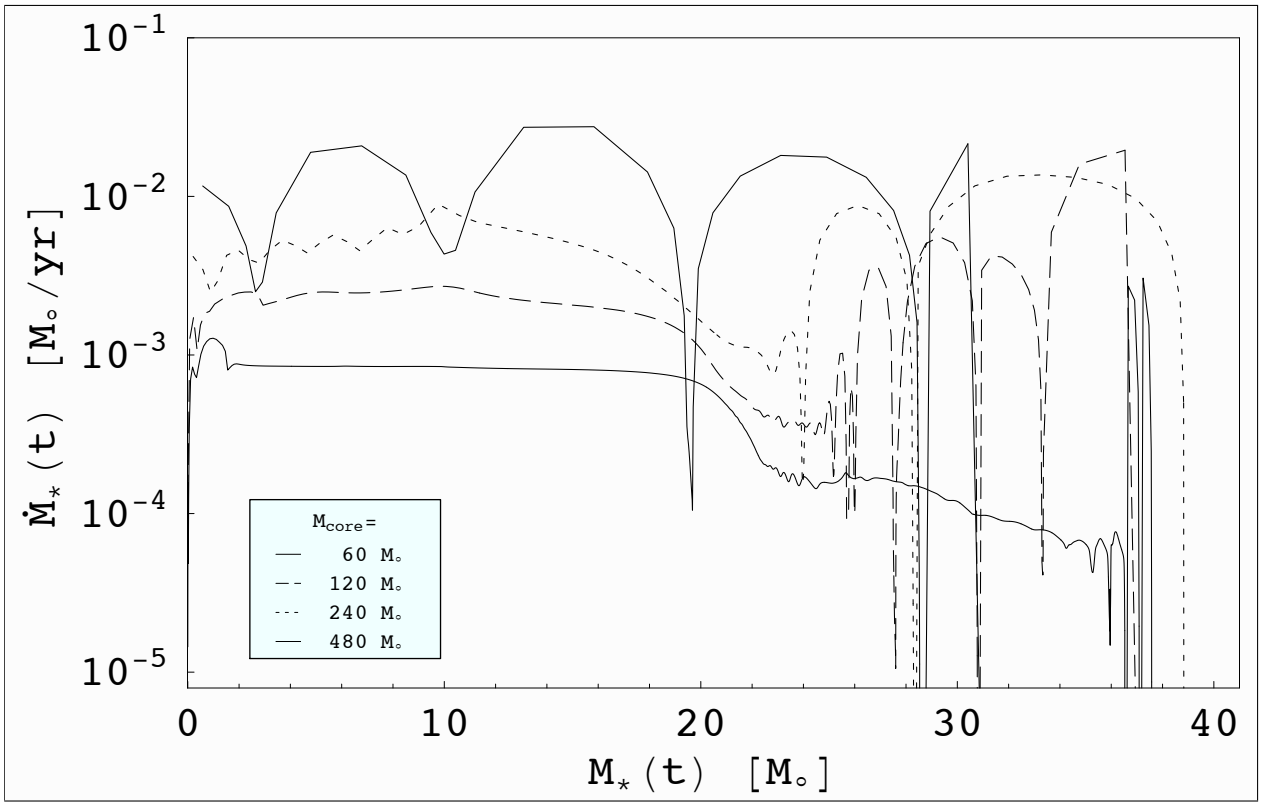

Figure 4.6: Accretion rate $\dot{M}$ as a function of the actual stellar mass M_* for four different initial pre-stellar core masses of $M_{\rm core} = 60\ {\rm M}_\odot$ up to 480 $\rm M_\odot$. The spherically symmetric accretion models yield an upper mass limit of the final star of $M_*^{\rm 1D} \leq 40\ {\rm M}_\odot$.

By increasing the initial mass of the pre-stellar core, the value of the accretion rate and therefore the accretion luminosity increases as well. Due to the resulting stronger radiative force, the increase of accretion luminosity leads to a deacceleration of the accretion flow, which results in a reduction of the corresponding accretion luminosity. This negative feedback yields a highly episodic accretion history for more massive collapsing cores, where the accretion luminosity has the same order of magnitude or even higher than the nuclear fusion luminosity. The final star does not reach a mass higher than 40 $\rm M_\odot$ in any of the simulations. The individual force densities as as function of the radius through the spherically symmetric pre-stellar core are displayed in Fig. 4.7. The limit found in this parameter scan is in good agreement with previous numerical studies, e.g. the formation of a 36 $\rm M_\odot$ star from a 150 $\rm M_\odot$ core in Yorke & Krügel (1977). The fact that the final mass of the star in the most massive case $M_{\rm core} = 480\ {\rm M}_\odot$ is lower ($M_* \approx 31\ {\rm M}_\odot$) than for the mass cores that initially had less mass, should be taken with care: In such highly episodical simulations, the influence of the underlying stellar evolution model increases strongly. To follow this time dependent interaction of the stellar evolution

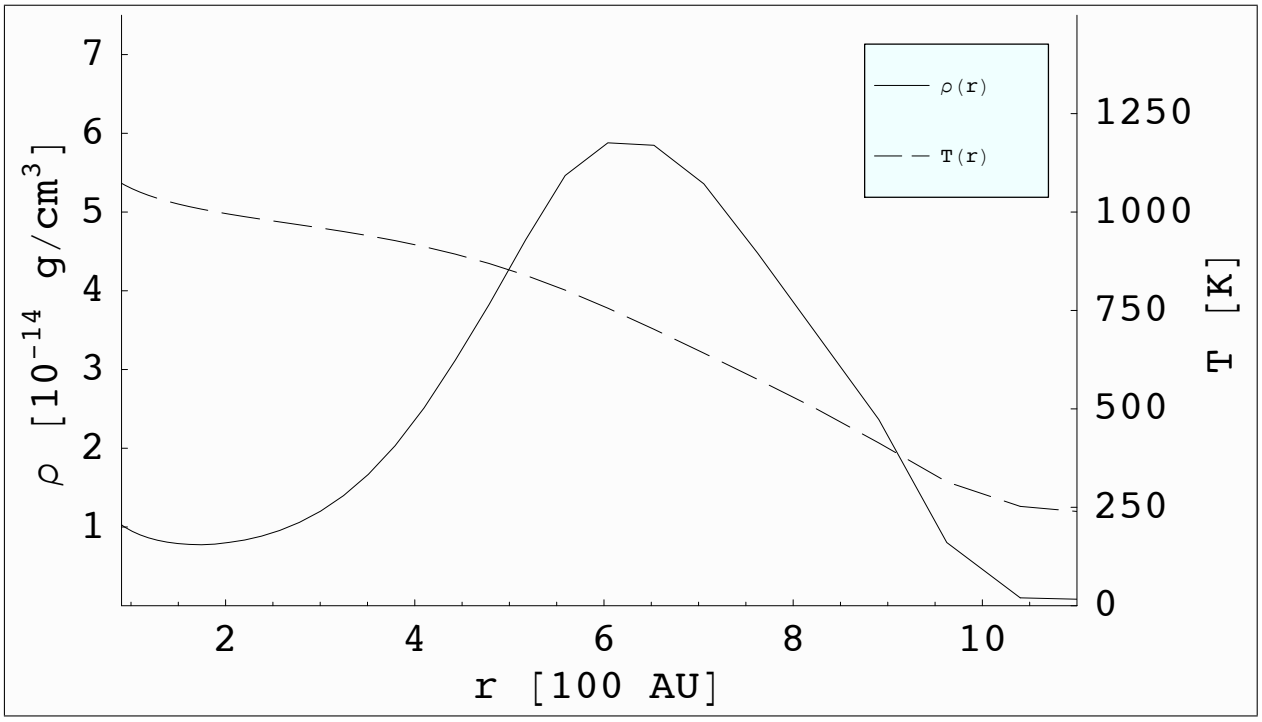

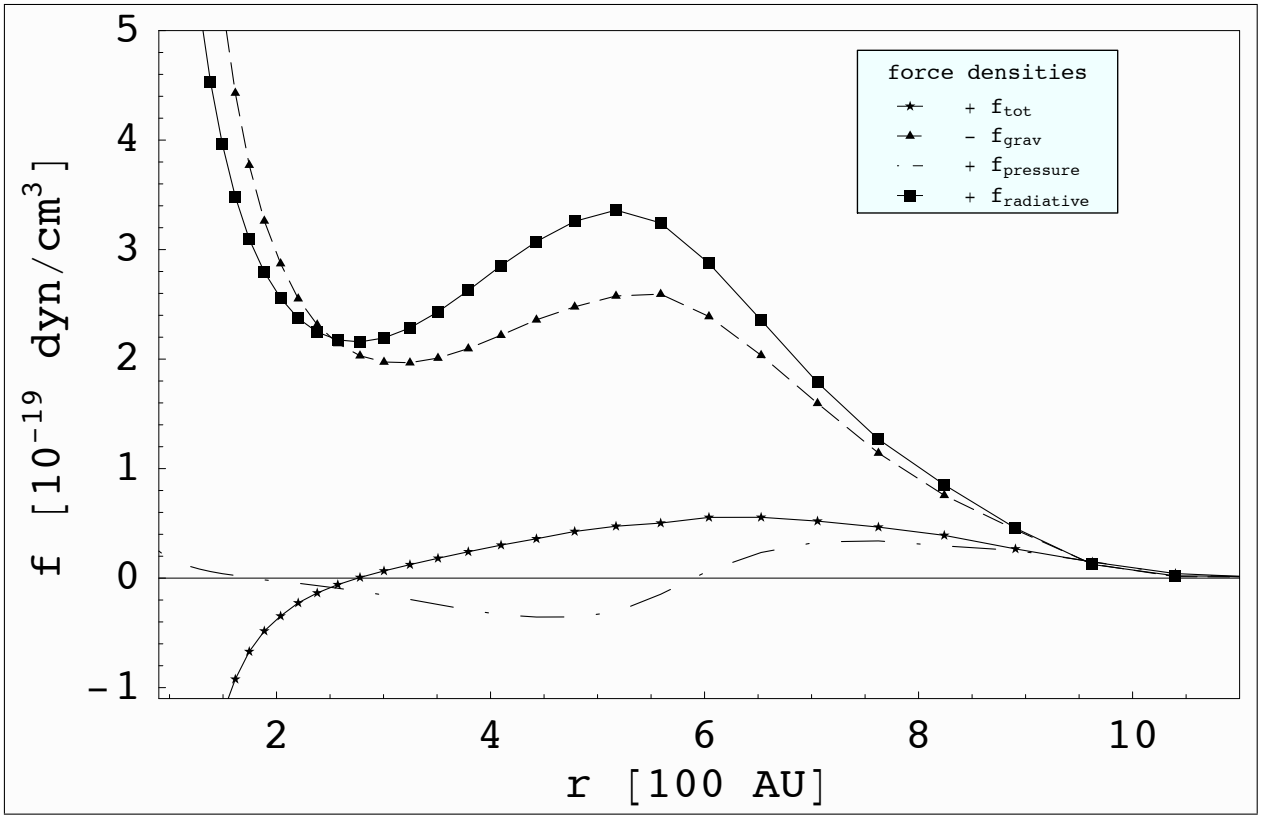

Figure 4.7: Snapshot of radial force densities in the innermost core region taken from the collapse simulation of a $M_{\rm core} = 120\,{\rm M}_\odot$ pre-stellar core at 20 kyr corresponding to a proto-stellar mass of about $M_* = 25\,{\rm M}_\odot$. Due to the superior radiative force the spherically symmetric accretion models yield an upper mass limit of the final star of $M_*^{\rm 1D} \leq 40\,{\rm M}_\odot$.

and the accretion flow, a more sophisticated treatment of stellar evolution than pre-calculated tracks should be considered. We encourage the direct implementation of a stellar evolution code like the one by Hosokawa & Omukai (2008) for such high-mass pre-stellar core collapse simulations to achieve a self-consistent evolution of the proto-star and its environment.

In the following section we analyze the data obtained from these simulations in more detail.

4.2.4 Epochs and dynamics of the collapse of spherically symmetric pre-stellar cores

To analyze and depict the physics as it proceeds through the pre-stellar core collapse in more detail, we distinguish its development in time into a sequence of epochs. The transitions between these epochs are thereby characterized by a change of the global potential $E_{\rm pot}$, kinetic $E_{{\rm kin},r}$, or thermal $E_{\rm thermal}$ energy of the core. Therefore, the energies are integrated over the computational domain

$$E_{\rm pot} = 4\pi \int_{r_{\rm min}}^{r_{\rm max}} \rho \Phi r^2 dr \tag{4.1}$$

$$E_{{\rm kin},r} = 4\pi \int_{r_{\rm min}}^{r_{\rm max}} \rho u^2 r^2 dr \tag{4.2}$$

$$E_{\rm thermal} = 4\pi \int_{r_{\rm min}}^{r_{\rm max}} c_{\rm V} \rho T r^2 dr. \tag{4.3}$$

The evolution of these global energies are depicted in Fig. 4.8 for the collapse of a 60 $M_\odot$ pre-stellar core. Of all cases studied, the 60 $M_\odot$ core yields the longest free fall time and hence the slowest evolution and is

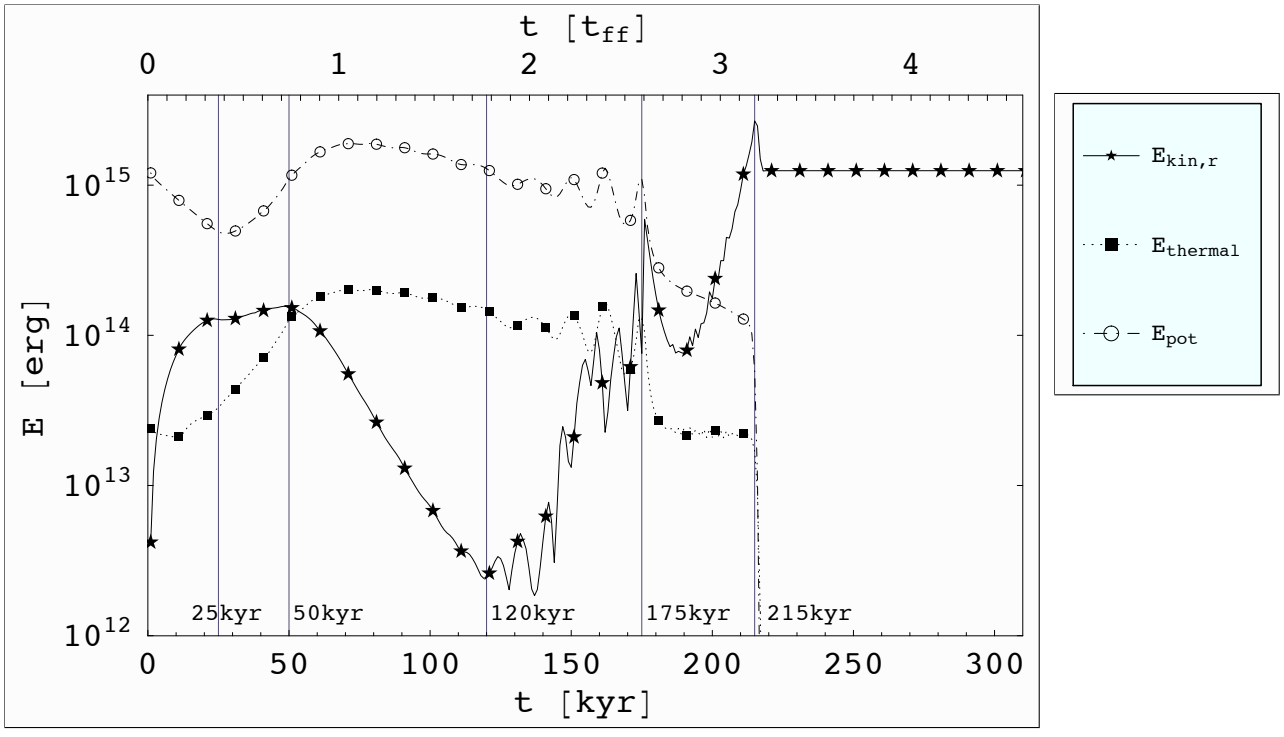

Figure 4.8: Integrated global potential, kinetic, and thermal energy as a function of time. Vertical lines identify transitions between different evolutionary epochs of the pre-stellar core collapse.

therefore best suited to separate the evolution of the large scale morphology of the proto-stellar environment

into distinguishable phases. Higher mass cores evolve on a shorter time scale and the different epochs described below are more strongly overlapped. Due to the fact that the computational domain does not represent a closed system, the total energy is not conserved. Mass, carrying momentum and energy, leaves the domain over the semi-permeable inner and outer boundaries. Accretion and nuclear fusion luminosity enters the computational domain at the inner radius and radiation energy streams over the outer boundary.

In Fig. 4.8, the abrupt changes in at least one of the displayed global energies are identified by vertical lines at 25, 50, 120, 175, and 215 kyr, which mark a local minimum or maximum of the corresponding energies. In the following, we go through these characterized epochs step by step and describe the physics as it proceeds highlighting special features of each epoch. The sub-figures of Fig. 4.9 illustrate the actual states of the pre-stellar core during the different epochs in selected examples more clearly. Although the change-overs from one epoch to the next are mostly smooth transitions, the classification of the evolution of the pre-stellar core collapse into several epochs allows us to categorize the dominant proceeding physics at each evolutionary stage in a more vivid way.

0 - 25 kyr ($M_* = 0$ - $20\,\mathrm{M}_\odot$): At the beginning of the simulation, the dynamics of the pre-stellar core are dominated by gravity. Up to a proto-stellar mass of roughly $20\,\mathrm{M}_\odot$ the evolution of the core resembles free fall, resulting in a constant accretion rate (see also Fig. 4.6). Correspondingly, Fig. 4.9a displays a typical density profile of r^{-2} and a monotonically decreasing velocity in the outward direction. Energetically, this epoch is dominated by the conversion of potential energy into kinetic energy (Fig. 4.8). This epoch ends with the onset of radiation pressure at roughly 25 kyr. The radiative force triggered by the stellar luminosity attains the same order of magnitude as the previously dominant gravity at a proto-stellar mass M_* of about $20\,\mathrm{M}_\odot$ mostly independent of the initial core mass (cp. Fig. 4.6).

25 - 50 kyr ($M_* = 20$ - $25\,\mathrm{M}_\odot$): During this second epoch, the thermal radiative force counterbalances the gravitational force directly behind the innermost heated region. As a consequence, the velocity in this region drops and the density increases and is augmented by the accretion flow from the outermost part of the core. The resulting strong temperature gradient through this denser shell even enhances the radiative feedback. Fig. 4.9b displays the actual state at 36 kyr. The relative importance of the gravitational, radiative, and thermal pressure force is shown in Fig. 4.7. The force densities are calculated from the collapse of a $120\,\mathrm{M}_\odot$ pre-stellar core at an actual star mass of about $M_* = 25\,\mathrm{M}_\odot$. The resulting forces are compared with the results from the rotating $120\,\mathrm{M}_\odot$ core collapse simulation performed in axial symmetry in Sect. 4.3.6. At the end of this epoch the enhancement of mass relative to the prior r^{-2}-profile covers the whole region between 30 and 1000 AU. Energetically, this second epoch is dominated by the boost of thermal energy (Fig. 4.8). The shift of mass to larger radii also results in an increase of potential energy. Meanwhile, the inner parts of the pre-stellar core are still in an in-fall motion and the central star grows to $25\,\mathrm{M}_\odot$. The accretion rate during this phase is fairly constant but strongly reduced.

50 - 120 kyr ($M_* = 25$ - $34\,\mathrm{M}_\odot$): This long epoch of roughly one free fall time is dominated by the uniform decrease of kinetic energy (Fig. 4.8). Steadily, the mass flux from the outer region enlarges the dense cocoon formed during the previous epoch and depletes the outer core region. Also, the accretion rate onto the massive star continuously decreases during this phase (see Fig. 4.6). The depletion of the outermost parts (see Fig. 4.9c) of the pre-stellar core as well as the kinetic energy loss over the inner boundary leads to the slow decrease of the kinetic energy inside of the computational domain.

120 - 175 kyr ($M_* = 34$ - $38\,\mathrm{M}_\odot$): Fig. 4.9d and 4.9e both represent an example of the actual state of the pre-stellar core during this fourth epoch. The remnant mass of the outer core region is now expelled by the radiative

force in the outward direction. Meanwhile, the previously accumulated cocoon region oscillates stronger and stronger leading to an oscillating accretion rate (see Fig. 4.6). The acceleration of the outer core region results in a sharp rise of the kinetic energy during this epoch (cp. Fig. 4.8). The oscillations are clearly visible in the kinetic, the potential, as well as the thermal energy. This oscillating phase ends when the radiative force resulting from the nuclear fusion plus the oscillating accretion luminosity is able to reject the remaining mass from the computational domain.

175 - 215 kyr ($M_* = 38\ \mathrm{M}_\odot = \text{const.}$): From 175 kyr on, the radiative force dominates the stellar environment throughout the whole computational domain. The remnant mass is expelled in the outward direction (Fig. 4.9f) and the accretion rate sharply drops (Fig. 4.6). The star has reached its final mass of about $M_* = 38\ \mathrm{M}_\odot$. Independent of the initial core mass, no spherically symmetric simulation yields a final stellar mass of more than $40\ \mathrm{M}_\odot$. Due to the mass loss at the outer boundary, the thermal and the potential energy drop sharply at the end of this epoch, whereas the high velocity leads to a rise of the kinetic energy.

215 kyr and later on ($M_* = 38\ \mathrm{M}_\odot = \text{const.}$): The final state of the simulation is displayed in Fig. 4.9g. The computational domain of the simulation is mostly depleted. The majority of the grid cells contain only the chosen floor value of the density ($\rho_0 = 10^{-21}\ \mathrm{g\ cm^{-3}}$), so the simulation was stopped here.

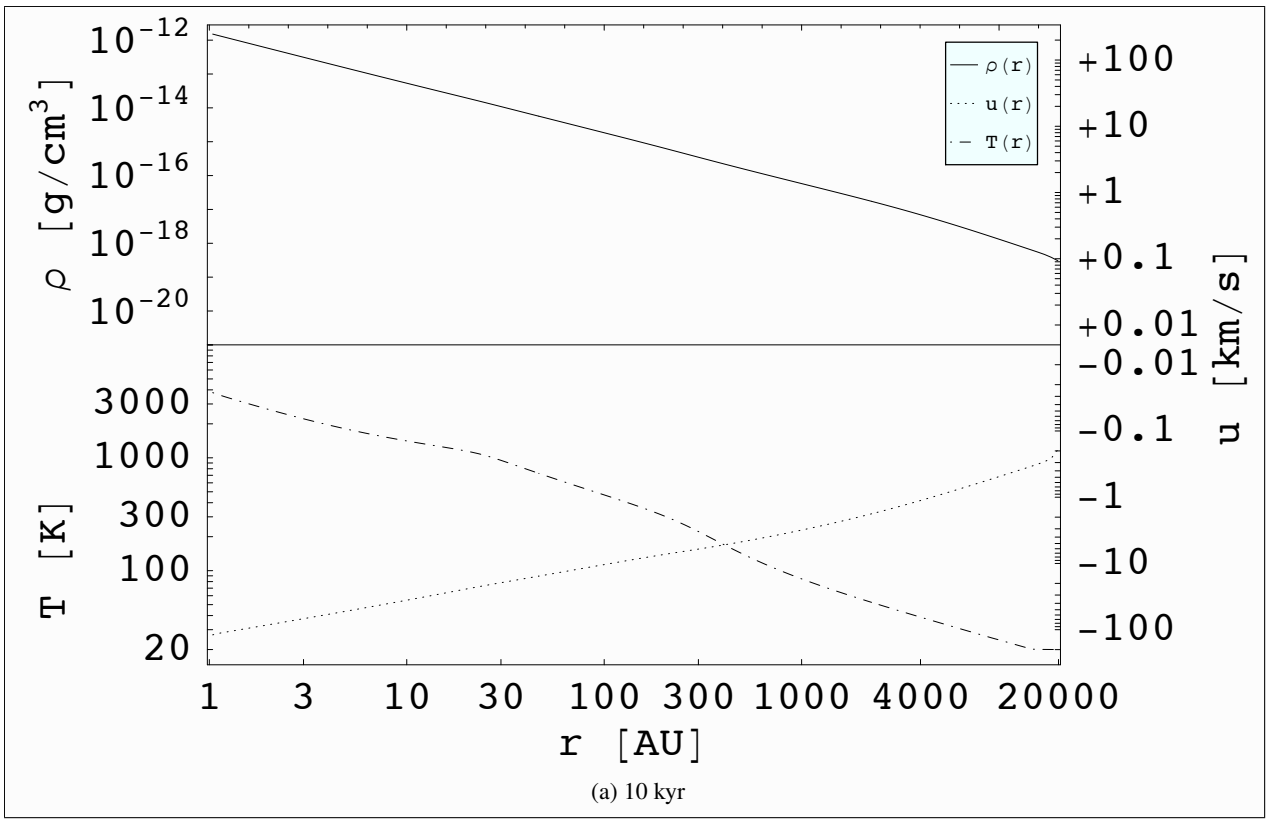

(a) 10 kyr

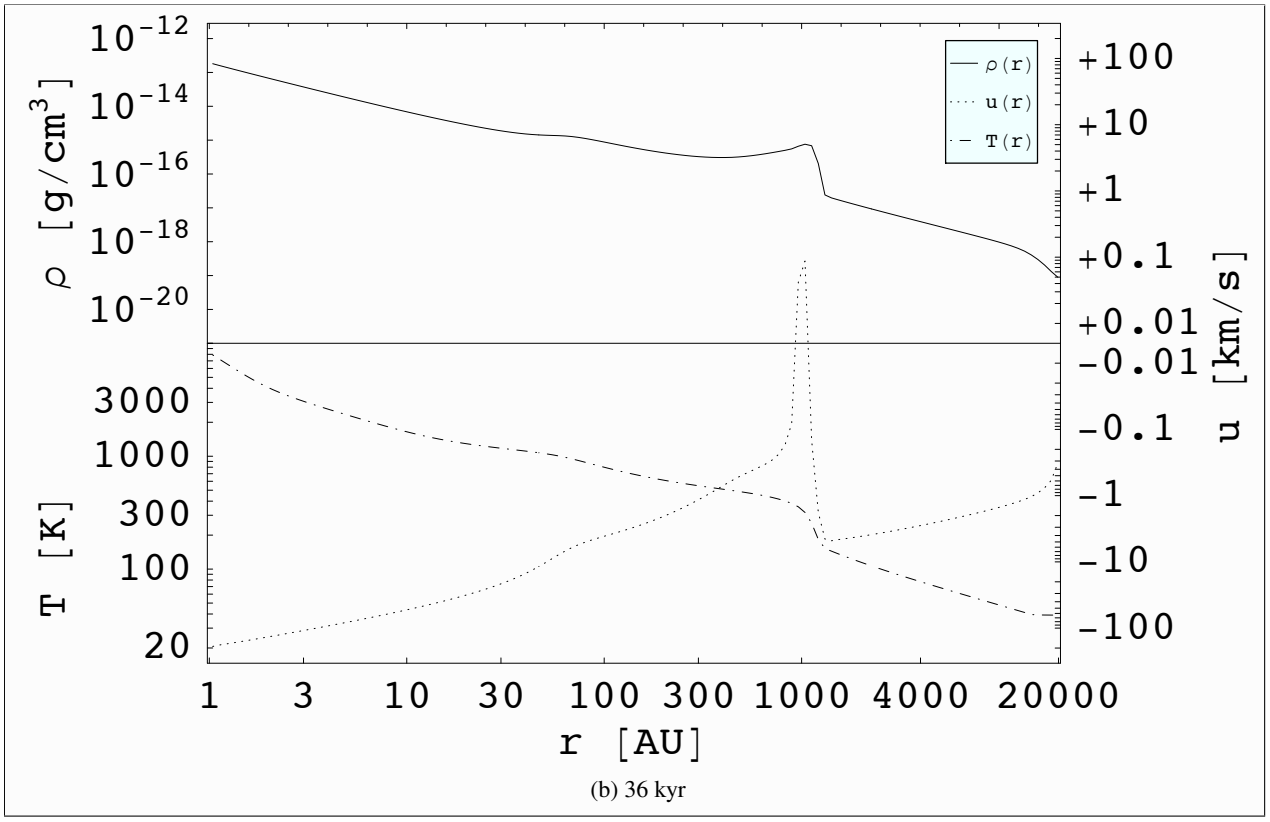

(b) 36 kyr

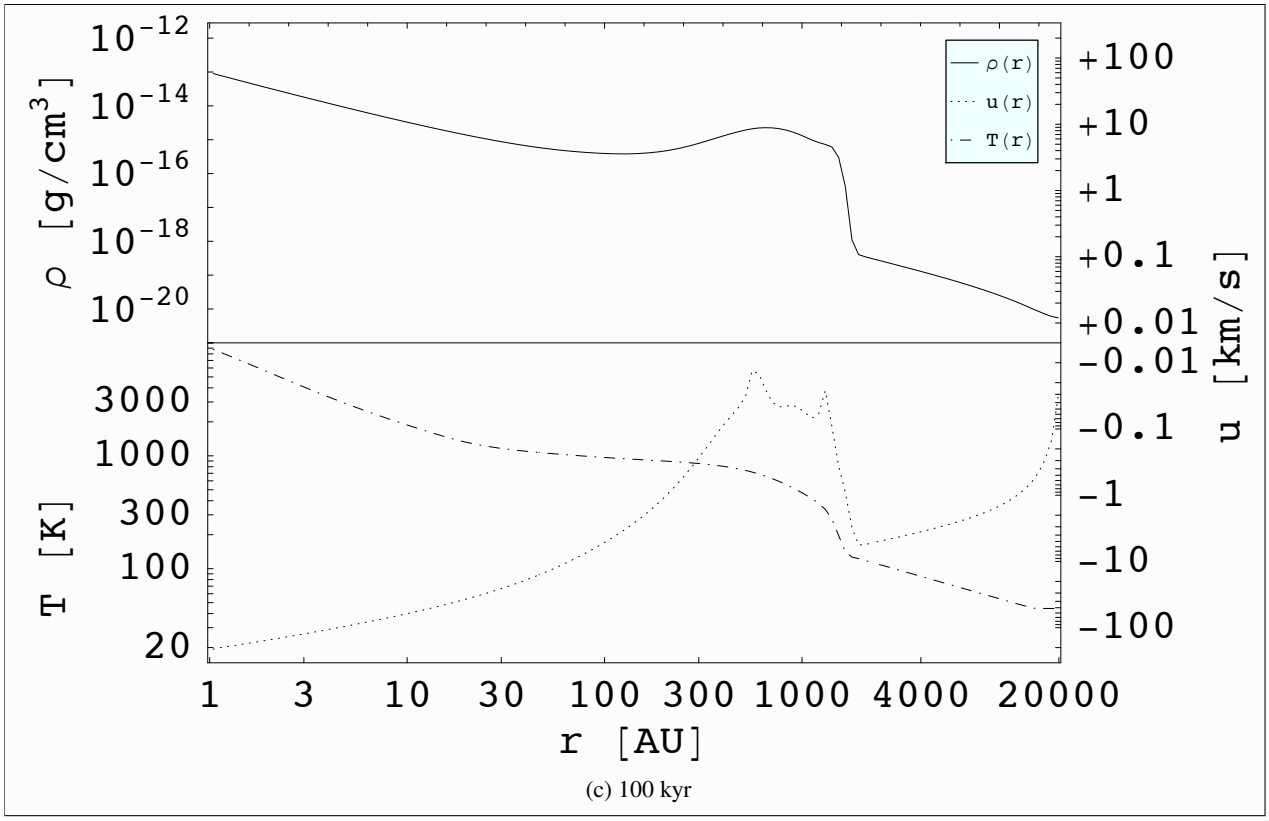

(c) 100 kyr

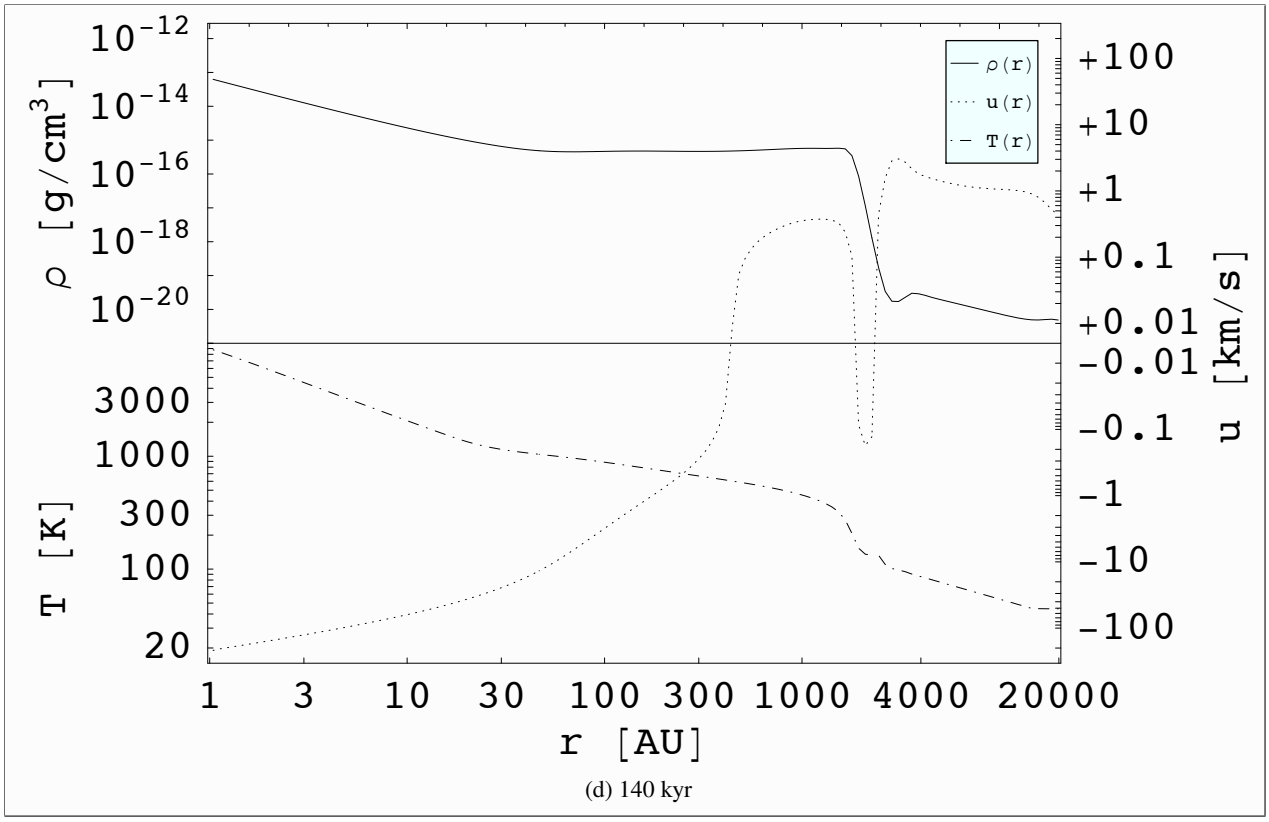

(d) 140 kyr

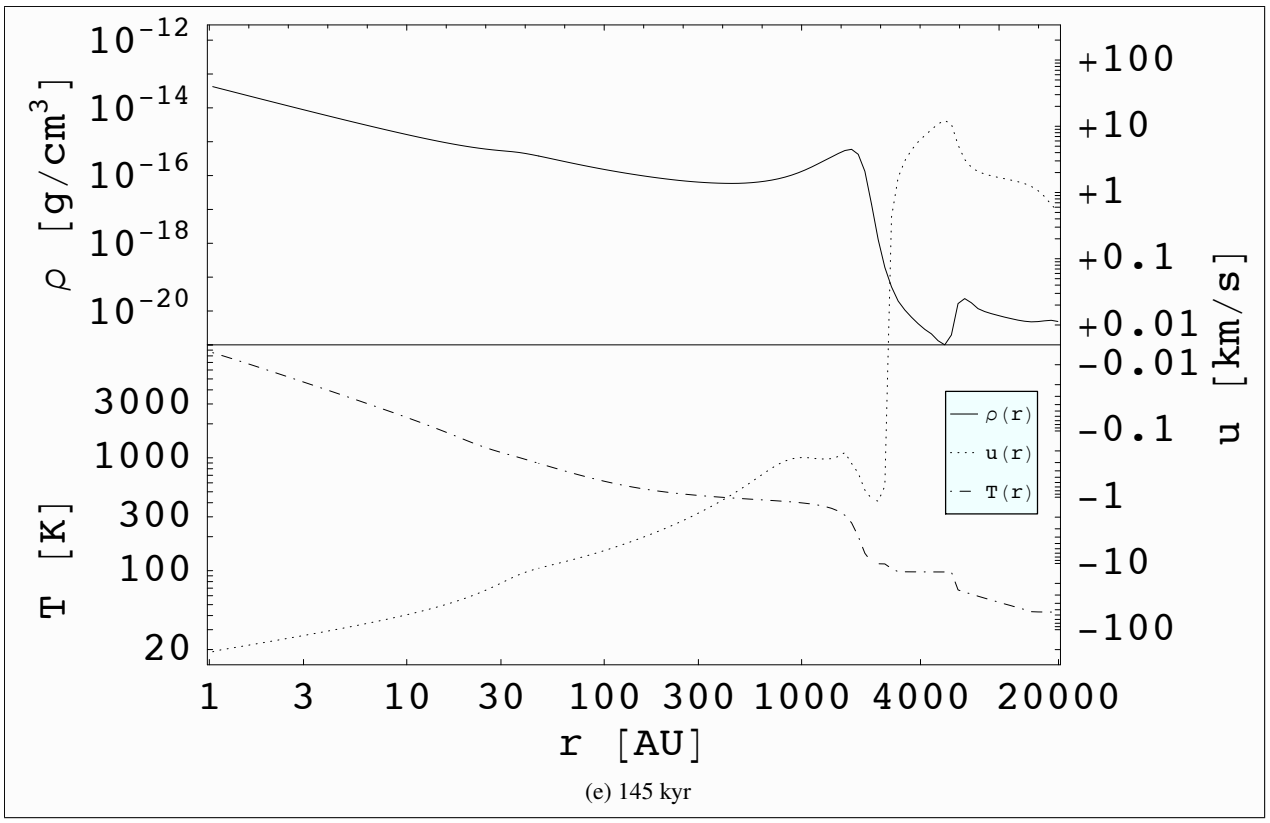

(e) 145 kyr

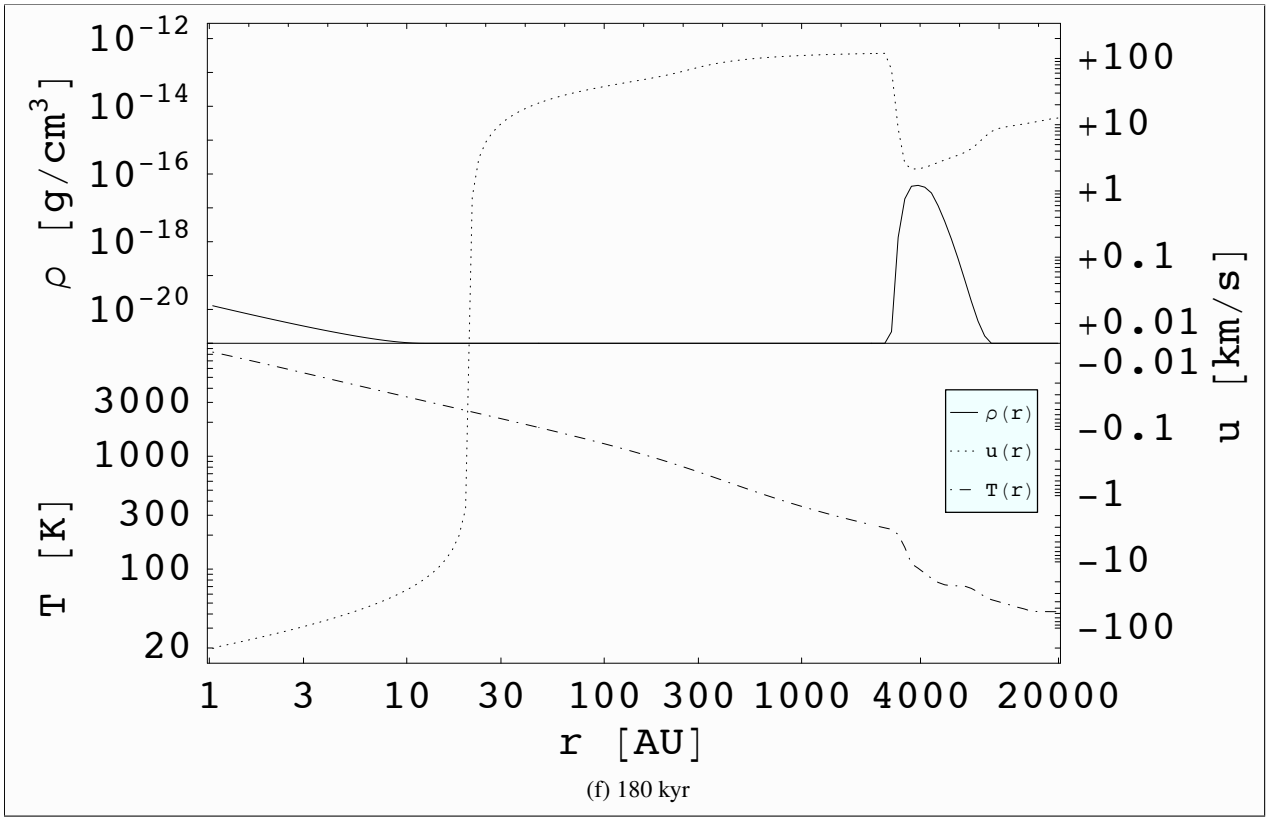

(f) 180 kyr

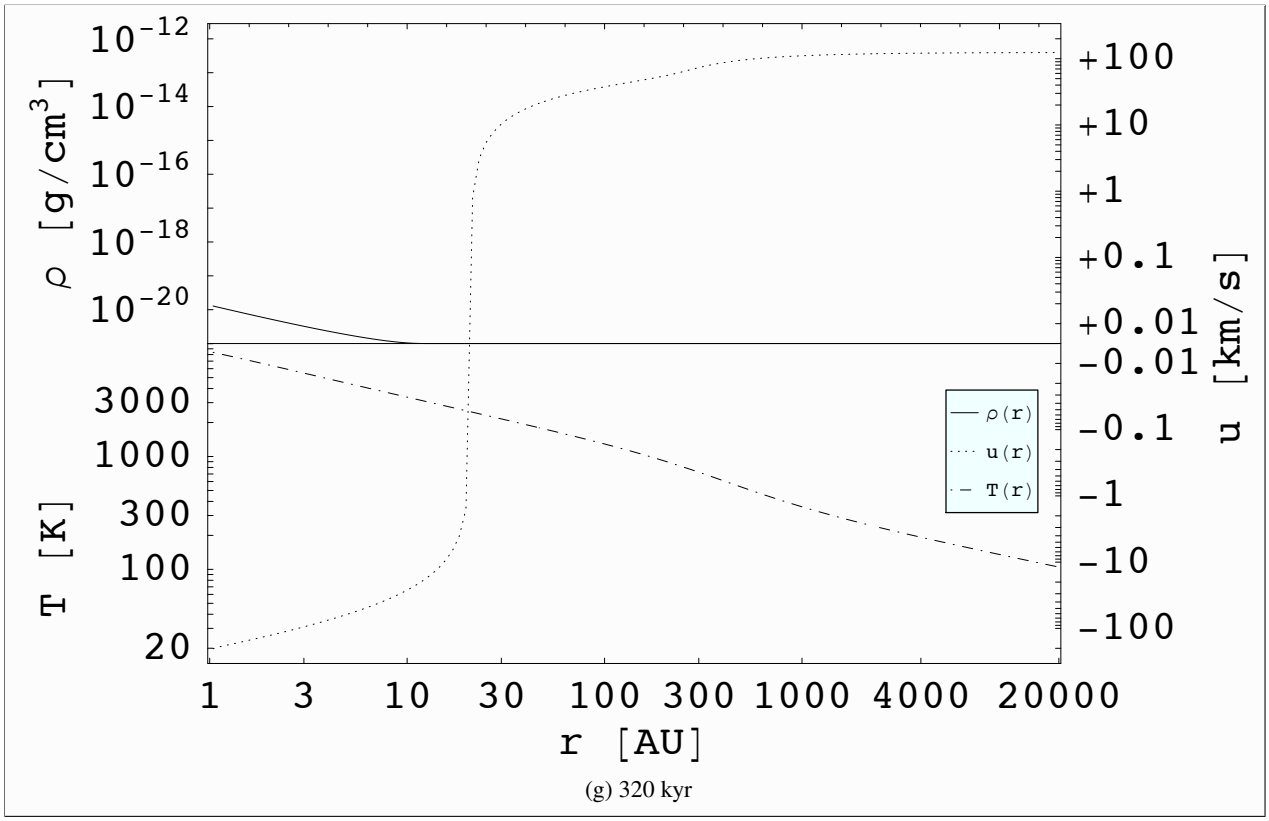

(g) 320 kyr

Figure 4.9: Density $\rho(r)$, velocity $u(r)$ and temperature $T(r)$ as a function of radius r for the case of a 60 $M_\odot$ pre-stellar core collapse at seven snapshots in time, representing distinguishable epochs of the evolution of the one-dimensional collapse.

4.3 The collapse of rotating axially and midplane symmetric pre-stellar cores (two-dimensional simulations)

The most massive stars known cannot be formed by spherically symmetric accretion. As shown in the last section, the radiative forces in a spherically symmetric envelope lead to a cut-off of the accretion rate. For a massive star of about 40 $M_\odot$, the high luminosity heats the region in its vicinity to such a high temperature that the resulting thermal radiation pressure overcomes the gravitational force. The radiation pressure stops, and finally reverses the accretion flow. Besides this theoretical issue, observations indicate the presence of angular momentum in all epochs of star formation, starting with the rotation of pre-stellar cores and finally resulting in rotating flattened circumstellar structures. Leaving perfectly spherical symmetry will thereby potentially help to overcome the radiation pressure problem. The presence of higher densities in the forming disk region results in a thinner shell, where the first absorption of stellar photons takes place. This enables an accretion flow to break through this region of direct stellar feedback more easily. The feedback by radiation from dust grains, which actually stops the accretion in the spherically symmetric case, will be strongly reduced, because the majority of the radiative flux from the irradiated inner rim of the disk will escape in the vertical direction through the optically thin disk atmosphere and therefore does not interact with the radially inward-streaming accretion flow. The different kinds of radiative feedback in spherical symmetry as well as in an axially symmetric disk geometry are illustrated in detail in Sect. 1.3.

Analogously to the discussion of the one-dimensional simulations, we present in the following subsections the results of axially and midplane symmetric simulations of the collapse of massive pre-stellar cores. Before being able to scan the parameter space of different initial core masses (Sect. 4.3.5), we determine the required resolution in convergence runs (Sect. 4.3.1) and fix the value of the central sink cell radius $r_{\rm min}$ (Sect. 4.3.2) as well as the strength of the α-viscosity (Sect. 4.3.3) in various simulations. A comparison of the results obtained from our newly developed code with similar simulations performed by Yorke & Sonnhalter (2002) is presented in Sect. 4.3.4. Finally, we analyze the physical processes during the axially and midplane symmetric pre-stellar core collapse in more detail in Sect. 4.3.6.

4.3.1 Convergence simulations

Analogously to the one-dimensional case (see Sect. 4.2.1), we first have to determine the adequate grid resolution for the specific problem. To fix the number of grid cells necessary for computing the correct physics of the radiation fluid interaction, we performed several simulations with varying resolution. Thereby, the radial cell sizes of the grid grow logarithmically from inside out as described in Sect. 2.1. The basic initial conditions and numerical parameter used for these convergence runs are described in Sect. 4.1. The simulations were performed for a core mass of $M_{\rm core}$ = 60 $M_\odot$, the value of the α-viscosity was chosen to be α = 0.03 and the inner boundary of the computational domain is located at $r_{\rm min}$ = 10 AU. We followed the evolution of the collapsing core up to 33 kyr (0.5 free fall times) for the highest resolution case yet and up to several hundred kyr (about 2 to 12 free fall times) for all other individual runs. The simulation with the highest resolution is still running and will be further evaluated in the near future. The accretion history and the corresponding mass growth of the centrally forming star are displayed in Fig. 4.10.

Due to the clear dominance of the motion of gas in the radial direction during the initial ‘free fall’ phase up to roughly 8 kyr the accretion rates of this epoch can be calculated correctly independent of the resolution used

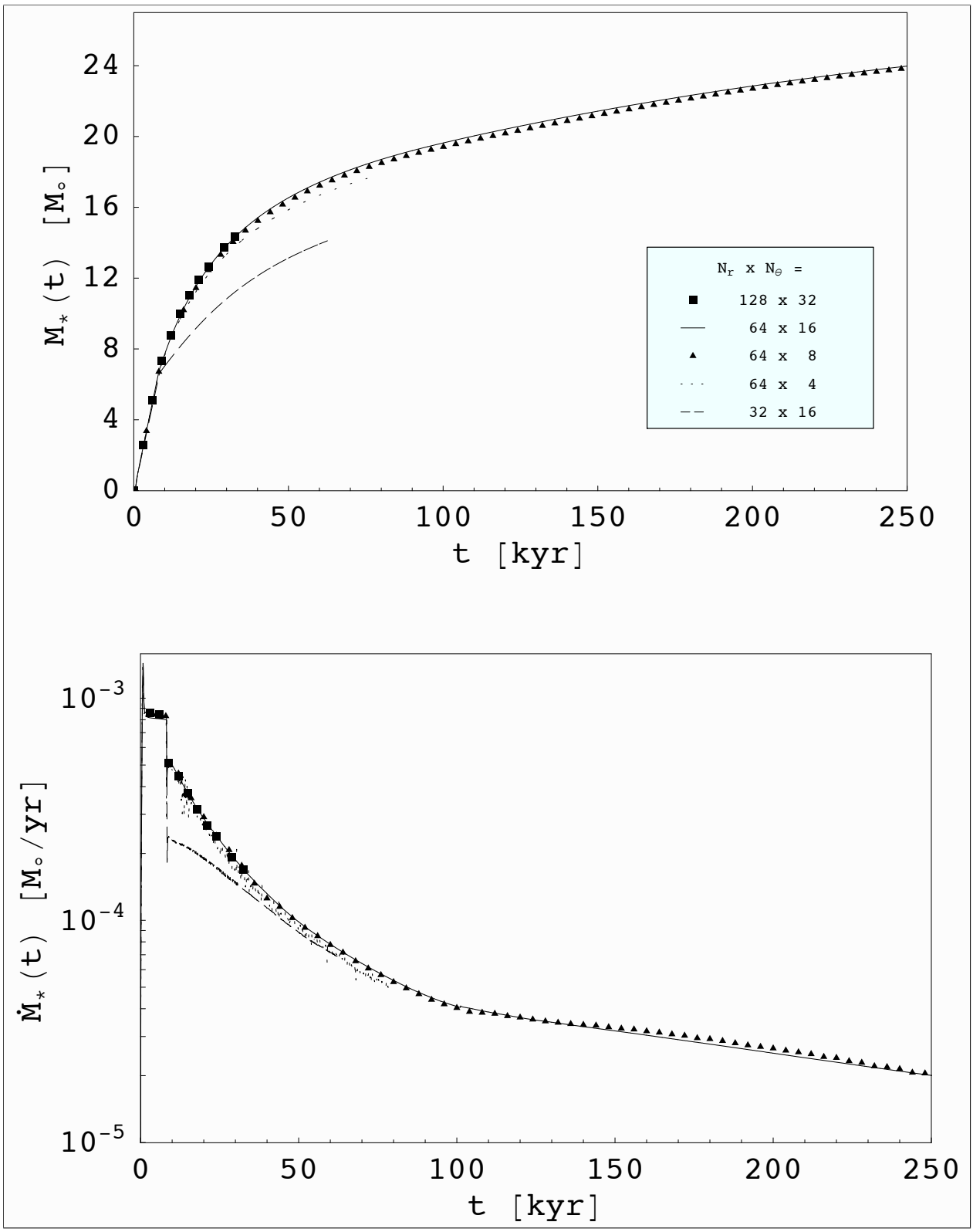

Figure 4.10: Stellar mass M_* (upper panel) and accretion rate $\dot{M}_*$ (lower panel) as a function of time for five different resolution to determine the adequate number of grid cells necessary for the axially and midplane symmetric pre-stellar core collapse simulations.

in the polar direction. In contrast to the purely one-dimensional in-fall (Sect. 4.2.1) the centrifugal forces slow down the radially proceeding dynamics during later epochs, during which the radiative feedback gets important. So the usage of 64 grid cells in the radial direction, corresponding to a radial grid size of the innermost cells of $(\Delta r)_{\rm min}$ = 1.27 AU, yields a converged result for the accretion rate onto the forming high-mass star. The low-resolution run with only 32 grid cells in the radial direction clearly fails to compute the correct onset of disk formation after 8 kyr. The required resolution in the polar direction to compute a converged result also during later epochs remains notably poor, reflecting the fact that the complex radiation hydrodynamics interactions act mostly in the radial direction. This result confirms the expedient choice of spherical coordinates in monolithic core collapse simulations. Higher resolution of the polar stratification of the forming circumstellar disk mostly influences the cooling of the irradiated and viscously heated midplane layer. The usage of only 4 or 8 grid cells in the polar direction therefore results in stronger fluctuations of the accretion flow, which vanish in the higher resolution runs (clearly visible in the lower panel of Fig. 4.10). On the other hand the runs with low resolution in the polar direction underestimate the mass growth of the forming star only slightly (upper panel in Fig. 4.10). The deviations of each run to the next run in higher resolution shrink towards higher resolution, that means the simulation series yields a monotonous convergence.

The runs with 64 x 16 and 128 x 32 grid cells show fully converged results even during the epoch of the most rapid changes at the onset of disk formation. The spike in the accretion rate downwards during this onset represents the short period in time, in which for the first time a fluid package from the outer core region got to the innermost radius $r_{\rm min}$ with high enough angular momentum to compensate the stellar gravity. Quickly hereafter the following mass builds up a circumstellar disk, in which the shear viscosity yields an angular momentum transfer outwards resulting in a steady accretion rate anew. At later evolutionary phases the amplitude of the accretion rate is mostly a result of a quasi-stationary accretion flow inwards and an interactive radiative flux in the outward direction, which smoothly grows proportional to the luminosity of the forming massive star. The deviations of the individual runs during this more evolved and 'less violent' phase shrink again for all resolutions studied. Subsequent two-dimensional simulations presented use 64 x 16 grid cells as the default setup corresponding to a grid size of $(\Delta r \text{ x } r\Delta\theta)_{\rm min}$ = 1.27 AU x 1.04 AU for the innermost grid cells.

4.3.2 The influence of the size of the sink cell: Resolving the dust condensation front

In the spherically symmetric models, we conclude that the numerical results do not depend on the radius $r_{\rm min}$ of the central sink cell unless it is smaller than the dust condensation radius $r_{\rm cond}$ from the point in time at which the radiative force overcomes gravity. These results cannot easily be transferred to the axially symmetric disk configuration. Including centrifugal forces, which compensate the gravity in the disk region, the chosen location $r_{\rm min}$ of the inner boundary of the computational domain influences the resulting accretion rate in two distinguishable effects.

Due to the fact that the circumstellar disk is growing in time from the inside outwards, a smaller sink cell leads to an earlier onset of the disk formation phase during the simulation. In other words, the mass with an initial centrifugal radius $r_{\rm cent}$ (see Sect. 3.1.2 for a derivation of the centrifugal radius) smaller than the sink cell radius $r_{\rm min}$ is accreted onto the forming star during the so-called free fall epoch at the beginning of the simulation. This effect is associated with the gas physics (hydrodynamics) of the pre-stellar core, because the gas represents roughly 99% of the mass of the pre-stellar core. A second important effect depending on the chosen sink cell radius is related to the dust and therefore to the radiation physics. The region in the vicinity of the forming massive star will be heated up to temperatures beyond the dust condensation temperature. Therefore

a gap is formed between the central star and the dust disk. Under the assumption that the absorption by gas in this gap is smaller than the absorption by dust grains behind the dust condensation front the inner rim of the dust disk determines the region of the first stellar radiative feedback onto the accretion flow. Also the most important radiative feedback by dust emission sets in directly behind this irradiated heated region.

Due to the importance of this inner core region for the associated interaction of the radiation with the accretion flow it seems to be unavoidable to include the whole dust disk down to its inner rim in the computational domain. This defines an upper limit of the radius of the central sink cell, which has to be smaller than the dust condensation radius in the midplane from that point in time at which the radiative force has grown to a competetive magnitude compared to the viscous force driving the accretion flow. Otherwise, for an inner sink cell radius $r_{\rm min}$ larger than the dust condensation radius $r_{\rm cond}$ the region of radiative feedback is artificially shifted to higher radii including a strong change in density, opacity, and thickness of the dust disk as well as a change in gravity and viscosity. The resulting strong heating of the disk region behind the radius $r_{\rm min} > r_{\rm cond}$, which 'realistically' would be shielded from the stellar irradiation by the inner parts of the disk, potentially leads to an unphysical result of the simulation performed.

We studied both, the mass and the radiative effect, related to an artificial inner cut-off of the gas and the dust disk respectively, in a series of simulations scanning the parameter space of the sink cell radius $r_{\rm min}$. The resulting accretion rates and the corresponding mass growth of the central star are displayed in Figs. 4.11 and 4.12 for an initial mass of the pre-stellar core of 60 $M_\odot$ and 120 $M_\odot$ respectively.

As expected the duration of the so-called free fall phase shortens with the radius $r_{\rm min}$ of the sink cell. This behaviour can fortunately be estimated analytically given the sink cell radius and the initial conditions of the pre-stellar core to account for the overestimation of the final mass of the forming star, if necessary. Moreover, this effect of the artificial inner rim of the gas disk results on the one hand in an overestimation of the final mass of the central star by approximately 1 $M_\odot$ or below (upper panel of Fig. 4.11), but on the other hand influences the proceeding radiation hydrodynamic interactions in its environment only marginally (lower panel of Figs. 4.11 and 4.12). The corresponding accretion rates after the disk formation are not influenced at all. This result is quite reasonable keeping in mind that the balance of radiative and gravitational forces can be described in first order by the luminosity to mass ratio L_*/M_* of the central massive star, which only changes marginally with another choice of the size of the central sink cell.

The artificial shift of the region of the dust radiation interactions in runs with huge sink cells leads to a completely wrong evolution of the central star, the disk as well as the large scale environment, which morphologies are mostly shaped by the massive star in the center. Therefore it is unavoidable to reduce the size $r_{\rm min}$ of the central sink cell at least down to the estimated dust condensation radius of the forming massive star. Subsequent simulations were performed with an adequate central sink cell radius of $r_{\rm min} = 10$ AU. See also Sect. 3.5 for an analytical estimate of the dust condensation radius $r_{\rm cond}$ of a massive star as well as Figs. 4.25 and 4.26 at p. 124 and 126 in Sect. 4.4.1 and 4.4.2 for the visualization of the numerical result of the evolving dust condensation front in three-dimensional simulations respectively.

The radius of the central sink cell in the simulations of Yorke & Sonnhalter (2002) was 80 AU and 160 AU for a 60 $M_\odot$ and 120 $M_\odot$ pre-stellar core collapse respectively. We strongly believe that the usage of these huge sink cells determine the unphysically abrupt end of the accretion phase they computed, clearly shown in Figs. 4.11 and 4.12.

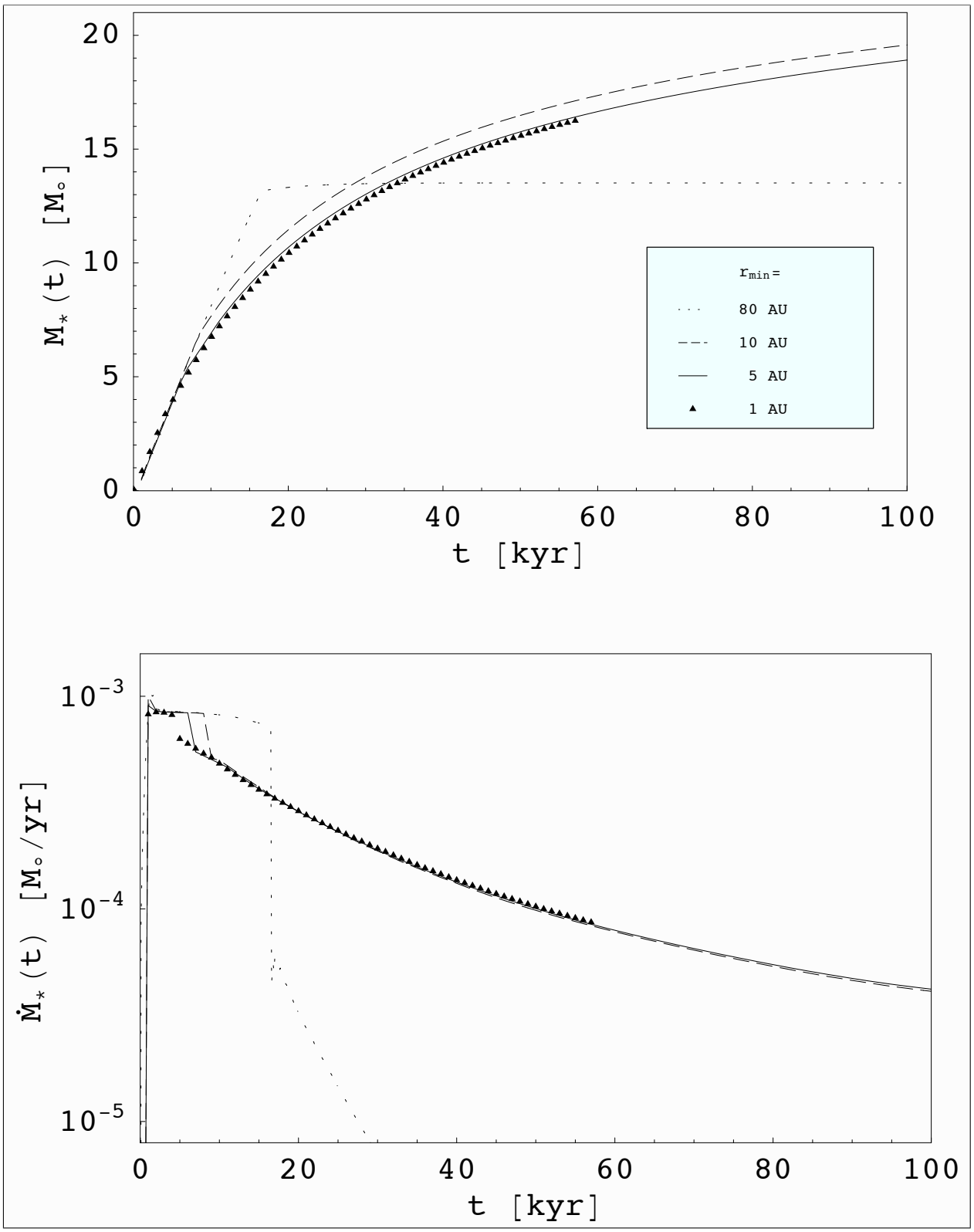

Figure 4.11: Stellar mass M_* (upper panel) and accretion rate $\dot{M}_*$ (lower panel) as a function of time for different radii $r_{\rm min}$ of the central sink cell in the axially and midplane symmetric collapse simulation of a 60 $M_\odot$ pre-stellar core.

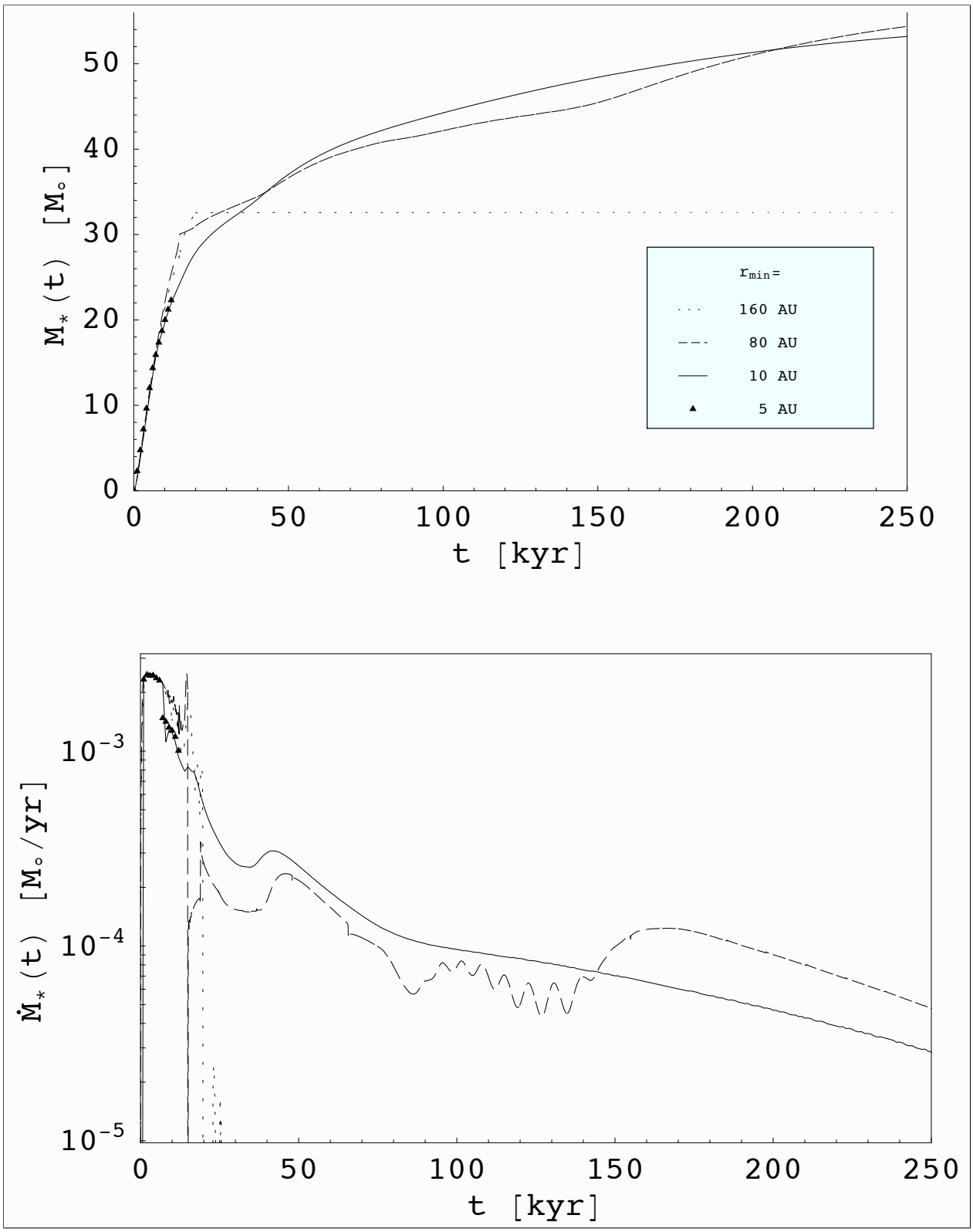

Figure 4.12: Stellar mass M_* (upper panel) and accretion rate $\dot{M}_*$ (lower panel) as a function of time for different radii $r_{\rm min}$ of the central sink cell in the axially and midplane symmetric collapse simulation of a 120 $M_\odot$ pre-stellar core.

4.3.3 Parameter scan of the α-viscosity

In circumstellar disks the gravity is assumed to be compensated by centrifugal forces and thermal pressure. The maintenance of further accretion therefore requires the loss of angular momentum. The main processes, which carry angular momentum, are disk winds, the magneto-rotational instability (MRI) in the most inner part of the disk (Balbus & Hawley 1991; Hawley & Balbus 1991; Balbus 2003), and unstable regions of the disk due to its own gravity (Yang et al. 1991; Laughlin & Bodenheimer 1994; Bodenheimer 1995). Also the interaction of self-gravity and the MRI has been studied (Fromang et al. 2004b,a). As far as we are able to incorporate these kind of small scale mechanisms during the large scale collapse of the pre-stellar core in a consistent way, we have to mimic the global effect of these 'micro' physics by adding physical shear viscosity to the disk system.

The usage of the α-parametrization (Shakura & Sunyaev 1973) of the viscosity, described in Sect. 2.3, still requires to fix the strength of this angular momentum transport (a priori). If no or too less shear viscosity is added to the system the collapse will yield the formation of ring instabilities with unstable non-axially symmetric modes leading to the formation of spiral arms and angular momentum transport in three-dimensional simulations as discussed by Yorke et al. (1995). This sets a lower limit on the α-value representing this angular momentum transport in subsequent two-dimensional collapse simulations including the formation of an accretion disk. On the other hand, a higher α-value implies a shorter cooling time of the circumstellar disk material, finally resulting in the fragmentation of the disk and the potential formation of a binary star. The probability of binary formation will be further addressed in the discussion of the results of the three-dimensional simulations (Sect. 4.4). In the case of axially symmetric disk simulations the resulting reduction of the cooling time sets therefore an upper limit of the according α-value. The limits of angular momentum transport in stable massive accretion disks is also studied analytically in Vaidya et al. (2009). To determine the range of the amount of viscosity, which allows to achieve the formation of a stable disk for our configuration, we ran several simulations scanning the value of the α-parameter from $\alpha = 10^{-3}$ up to $\alpha = 1$ in powers of ten. Besides these results, also simulations without any viscosity ($\alpha = 0$) and with $\alpha = 0.03$, a value lying in the middle of the allowed range, are displayed in Fig. 4.13.

As expected the accretion phase ends abruptly for α-values beneath a lower and above a higher. Simulations, which do not yield the formation of a stable accretion disk ($\alpha = 0, \alpha = 10^{-3}, \alpha = 1.0$), were aborted. The determined range of stable disk formation between $\alpha = 10^{-2}$ and $\alpha = 10^{-1}$ agrees completely with the one found in the analytic studies of potential stable circumstellar disks around massive stars (Vaidya et al. 2009). Recent simulations by our colleague M. Flock concerning angular momentum transport in disks due to the magneto-rotational instability using the same code Pluto3 (Mignone et al. 2007) confirm the plausibility of the restrictions found. The deviations between the different runs ($\alpha = 0.1, 0.03,$ and 0.01) leading to the formation of a stable accretion disk will in all probability not affect the qualitative results of the subsequent studies of the ongoing radiation hydrodynamic processes during and after the disk formation. The chosen default value of the α-parameter in subsequent two-dimensional simulations is therefore fixed to a value of $\alpha = 0.03$. After fixing the last outstanding free parameters, namely the grid resolution, the size of the inner sink cell and the value of the α-viscosity, we present in the following subsection a comparison study of our simulations to the one by Yorke & Sonnhalter (2002). Following this comparison, we present the most significant results of our massive pre-stellar core collapse simulations performed so far.

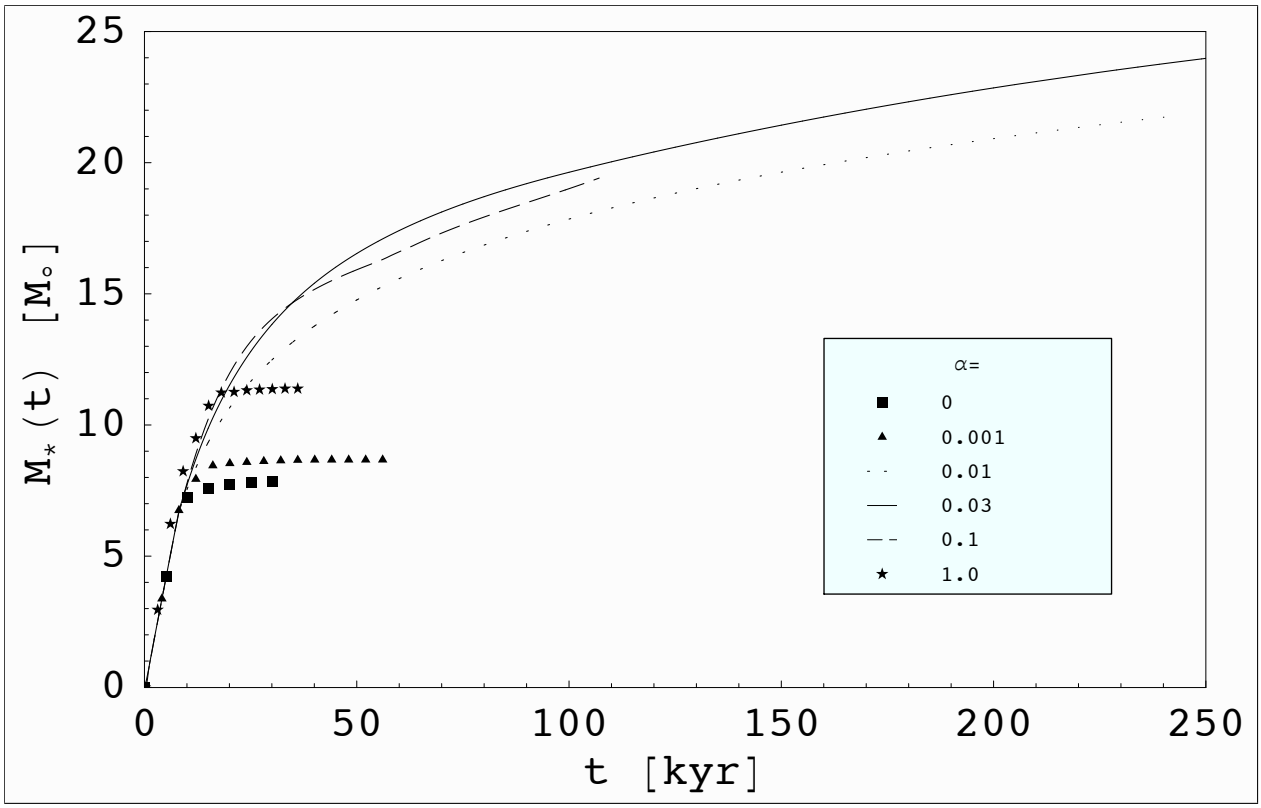

Figure 4.13: Stellar mass M_* as a function of time for six different values of the strength of the α-viscosity in the axially and midplane symmetric pre-stellar core collapse simulations.

4.3.4 Comparison to Yorke & Sonnhalter (2002)

Yorke & Sonnhalter (2002) presented simulations of collapsing pre-stellar cores of $M_{\rm core}$ = 30 $M_\odot$, 60 $M_\odot$ and 120 $M_\odot$. The runs were performed assuming axial and midplane symmetry on nested grids with three levels of refinement in cylindrical coordinates. The radiative feedback was calculated consistently in a frequency dependent way, but under the FLD approximation. The radius of their inner sink cell was chosen proportional to the initial mass of the core to be 40, 80, and 160 AU respectively. As shown in Sect. 4.3.2 such huge sink cells lead to an artificial cut-off of the dust disk and result therefore in unphysically strong radiative feedback. We strongly believe that this yields also the abrupt and early end of the accretion phase in their simulations. We performed a comparison simulation with a similar setup to compare the results from our code with the one obtained in Yorke & Sonnhalter (2002). We ran the simulation labeled with 'F60' in Yorke & Sonnhalter (2002). It describes a collapse of a 60 $M_\odot$ pre-stellar core with an outer radius of $r_{\rm max}$ = 0.1 pc and a central sink cell of 80 AU. Since the original data such as the accretion history obtained in the simulations by Yorke & Sonnhalter (2002) is not available anymore (H. Yorke, private communication), we will compare the resulting accretion history by eye, i.e. we read some data points out of Fig. 7 in Yorke & Sonnhalter (2002) with a ruler and over-plotted the results from our own simulation. The results are displayed in Fig. 4.14. Due to the resulting big discrepancy between both codes and the fact that the original code used in Yorke & Sonnhalter (2002) is not available anymore (H. Yorke, private communication), we tried to double-check the result with another already existing code. Johannes Schönke (ITA Heidelberg) developed during his Ph.D. thesis a two-dimensional hydrodynamics code in spherical coordinates used for low-mass pre-stellar core collapse simulations (Tscharnuter et al. 2009) without radiative feedback (due to the focus on low-mass stars yet). He performed a run with identical initial conditions, which allows us to compare the results up to the onset of radiative feedback. During this initial free fall epoch the accretion rate should certainly be independent of any stellar feedback. Our own, J. Schönke's, and the results presented in Yorke & Sonnhalter (2002) are displayed in Fig. 4.14.

Apparently the resulting accretion rates in our own and the corresponding simulation of Yorke & Sonnhalter (2002) differ roughly by a factor of two. This is especially curious in the first thousand years of evolution, where the physics are dominated by a radial in-fall without any radiative feedback. The calculations done by J. Schönke confirm our results accurately up to the onset of the radiative feedback, which is not included in J. Schönke's code so far. Presumably the presented accretion history in Yorke & Sonnhalter (2002) is not associated with the therein defined initial condition, e.g. the initial accretion rate of the case 'F60' in Yorke & Sonnhalter (2002) lies in between our simulations of a 60 $M_\odot$ and a 120 $M_\odot$ core collapse (but the misleading part of the setup can also be the initial density slope, the outer core radius or the initial rotation speed). The high level of agreement of our results with the independent code of J. Schönke assures the correct behaviour of the by now well established Pluto-code, which we use for the hydrodynamics part of our code. Further detailed tests of our newly developed frequency dependent radiation transport module as well as standard radiative hydrodynamic shock simulations are exposed in Sect. 2.5.

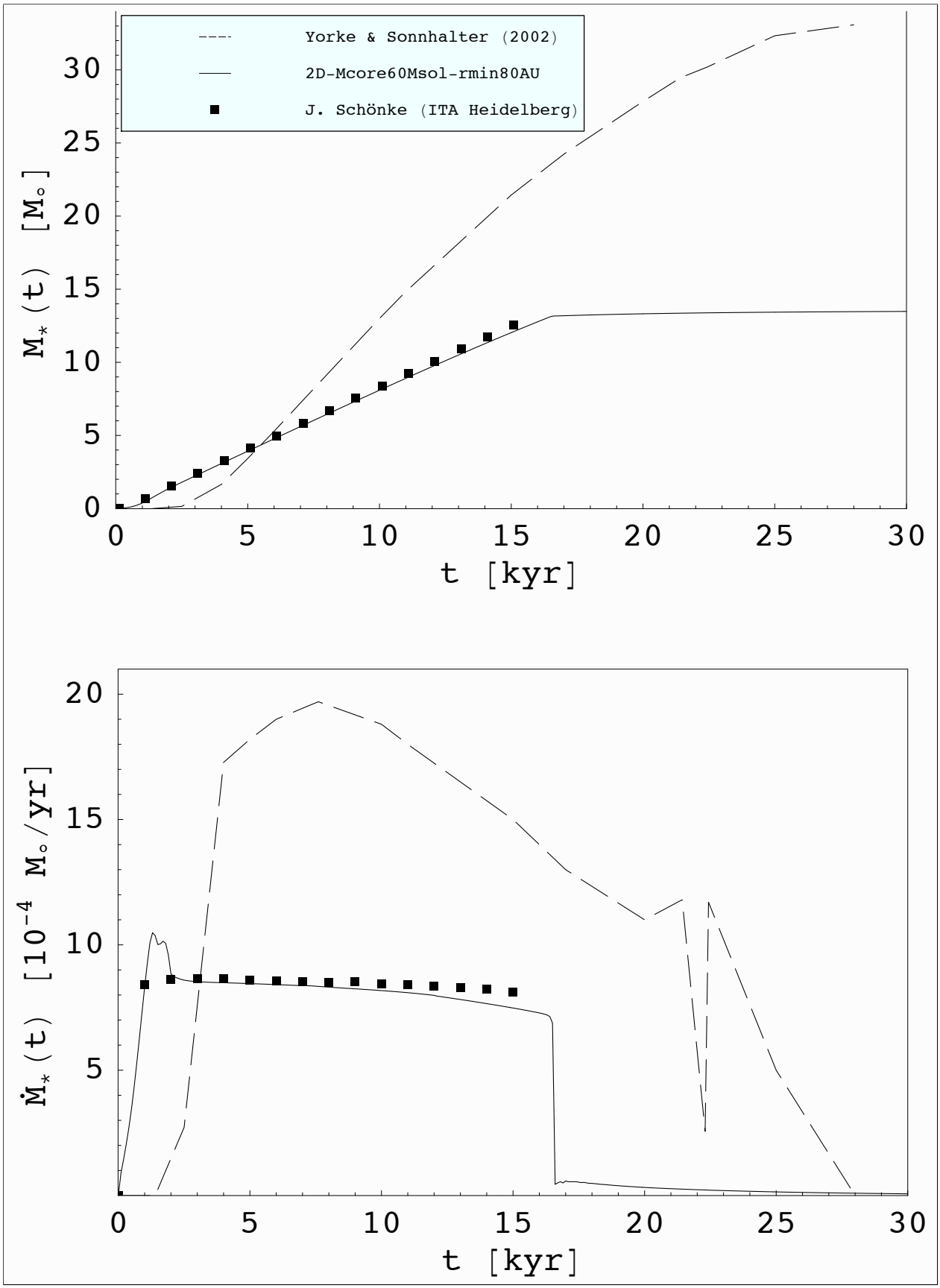

Figure 4.14: The resulting stellar mass M_* (upper panel) and accretion rate $\dot{M}_*$ (lower panel) from a collapse of a 60 $M_\odot$ pre-stellar core with an outer radius of $r_{\rm max}$ = 0.1 pc and an inner sink cell radius of $r_{\rm min}$ = 80 AU using three different codes.

4.3.5 Parameter scan of the initial pre-stellar core mass: Breaking through the upper mass limit of spherically symmetric accretion

In spherically symmetric (one-dimensional) collapse simulations of massive pre-stellar cores the final stellar mass is limited to less than 40 $M_\odot$ independent of the initial core mass $M_{\rm core}$ due to radiative feedback. We attack this radiation pressure barrier in two-dimensional axially and midplane symmetric circumstellar disk geometry now. The implications of this change of geometries are discussed at full length in Sect. 1.3. We performed four simulations with the default initial conditions described in Sect. 4.1 and the fixed numerical parameters presented in Sect. 4.3.1 to 4.3.3. The different initial core masses of $M_{\rm core}$ = 60 $M_\odot$, 120 $M_\odot$, 240 $M_\odot$, and 480 $M_\odot$ were chosen analog to the one-dimensional scan of the initial core mass parameter. The resulting accretion histories as a function of the actual stellar mass are displayed in Fig. 4.15.

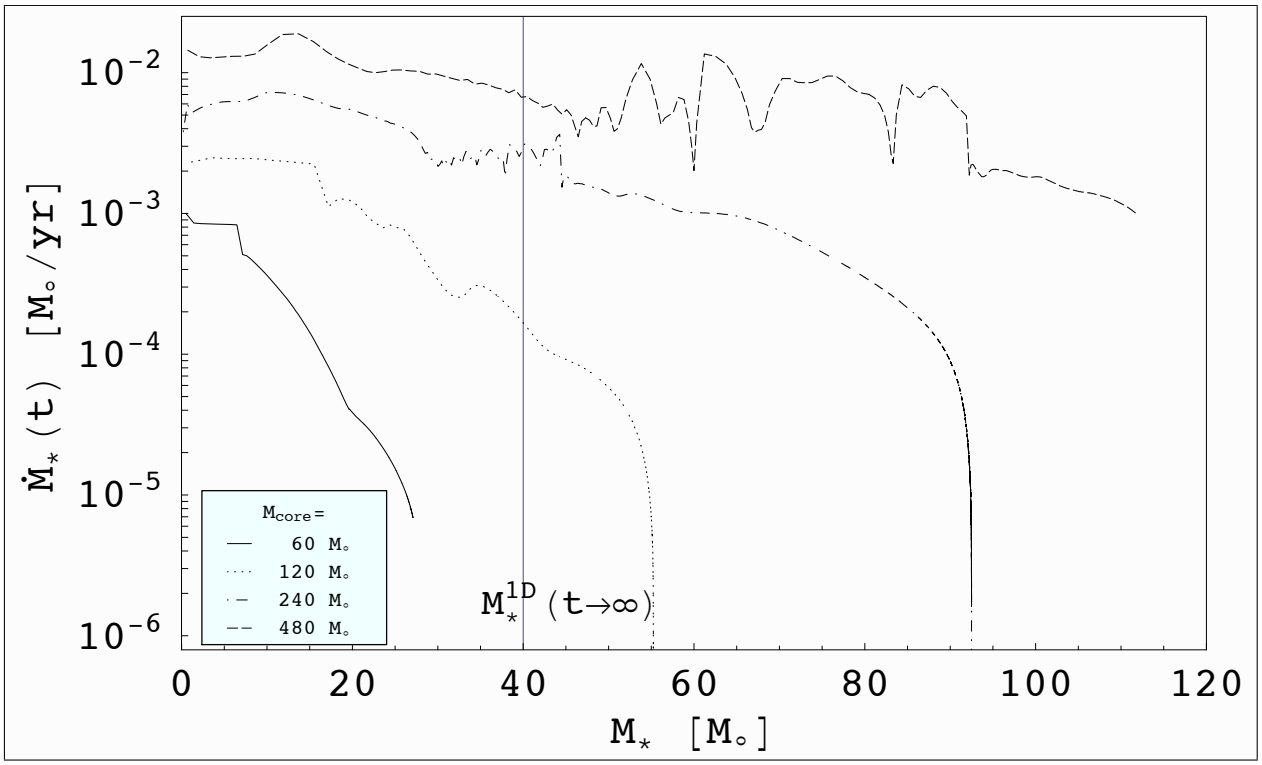

Figure 4.15: Accretion rate $\dot{M}_*$ as a function of actual stellar mass M_* for four different initial core masses $M_{\rm core}$ = 60 $M_\odot$, 120 $M_\odot$, 240 $M_\odot$, and 480 $M_\odot$. The two-dimensional axially and midplane symmetric collapse models of slowly rotating pre-stellar cores clearly break through the upper mass limit of the final star of $M_*^{\rm 1D} \leq 40\ M_\odot$ found in previous spherically symmetric accretion models.

As expected, the lowest mass case of $M_{\rm core}$ = 60 $M_\odot$ results finally in a less massive central star than the corresponding run in spherical symmetry simply due to the fact that the additional angular momentum results in centrifugal forces, which counteracts the accretion flow driven by gravity and viscosity. But for higher mass pre-stellar cores this slowed down accretion flux in the two-dimensional setup breaks easily through the upper mass limit of the final star of $M_*^{\rm 1D} \leq 40\ M_\odot$ found in spherically symmetric accretion models! In these axially and midplane symmetric disk accretion models no upper mass limit of the final star is detected so far.

The reason for that breakthrough can be displayed by a closer look at the driving force densities in the evolved pre-stellar core, plotted in Figs. 4.16 to 4.21. All figures represent a snapshot of the $M_{\rm core} = 120\ {\rm M}_\odot$ case at 60 kyr after start of the simulation. At this point in time, the actual mass of the central massive star is 40 $\rm M_\odot$, representing the spherically symmetric upper mass limit found in previous simulations (Sect. 4.2.3). In contrast to the spherically symmetric models, the geometry of the proto-stellar environment can now be divided into a very dense circumstellar disk and the lower density envelope. We visualized exemplary the actual density, velocity, and the acting forces in the radial direction for both regimes, Figs. 4.16 to 4.18 for the midplane of the accretion disk, Figs. 4.19 to 4.21 for a polar angle of 30° above the midplane. In the midplane the gravity and centrifugal force are one to two orders of magnitude higher than the thermal pressure and up to three orders of magnitude higher than the radiative and viscous force. The upper panel of Fig. 4.16 shows three individual regions of the midplane layer, in between the sign of the total force density changes. The gravity dominates the individual forces for the outer core regions (above 3000 AU) leading to a steady accretion flow onto the inner core region (Figs. 4.16 and 4.17). In the very inner part of the core around the massive star (below 200 AU) the gravity is balanced by the centrifugal force and in small part by the thermal pressure (Fig. 4.17). In this region, which we will refer to as the disk region hereafter, the shear viscosity yields a quasi-stationary accretion flow through the disk, which clearly exceeds the radiative force (Fig. 4.18). In between this disk region and the global in-fall region the mass flux describes transient oscillations, because gravity, centrifugal forces and thermal pressure are not in equilibrium yet, as it is the case for the mass finally arriving the disk region. The viscous force in the accretion disk is able to drive a steady accretion flow towards the evolving massive star of 40 $\rm M_\odot$, because the radiative force is one to two orders of magnitude lower in this dense disk region than in the low density envelope (cp. Figs. 4.18 and 4.21).

At an polar angle of 30° above the midplane this strong radiative force already accelerates the remnant mass in the radially outward direction through mostly the entire pre-stellar core (Fig. 4.20). Only at the outer rim of the core we still see the previous in-fall motion. This distribution of the individual force densities confirms in high detail the assumed procedure presented in Sect. 1.3: Most of the radiative flux from the irradiated inner rim of the disk is bypassed in the vertical direction through the optically thin atmosphere of the circumstellar disk. Meanwhile, the accretion flow is reduced compared to the one-dimensional gravitational in-fall to a steady stream driven by the viscous properties of the accretion disk. In the envelope region of the pre-stellar core the radiative force reverts the in-fall motion and depletes the stellar surrounding similar to the spherically symmetric accretion models (cp. the corresponding density and velocity distribution in Fig. 4.19). The evolution of the accretion disk and the radiatively driven outflow will also be discussed in detail in the following subsection on the epochs of the collapse of rotating cores.

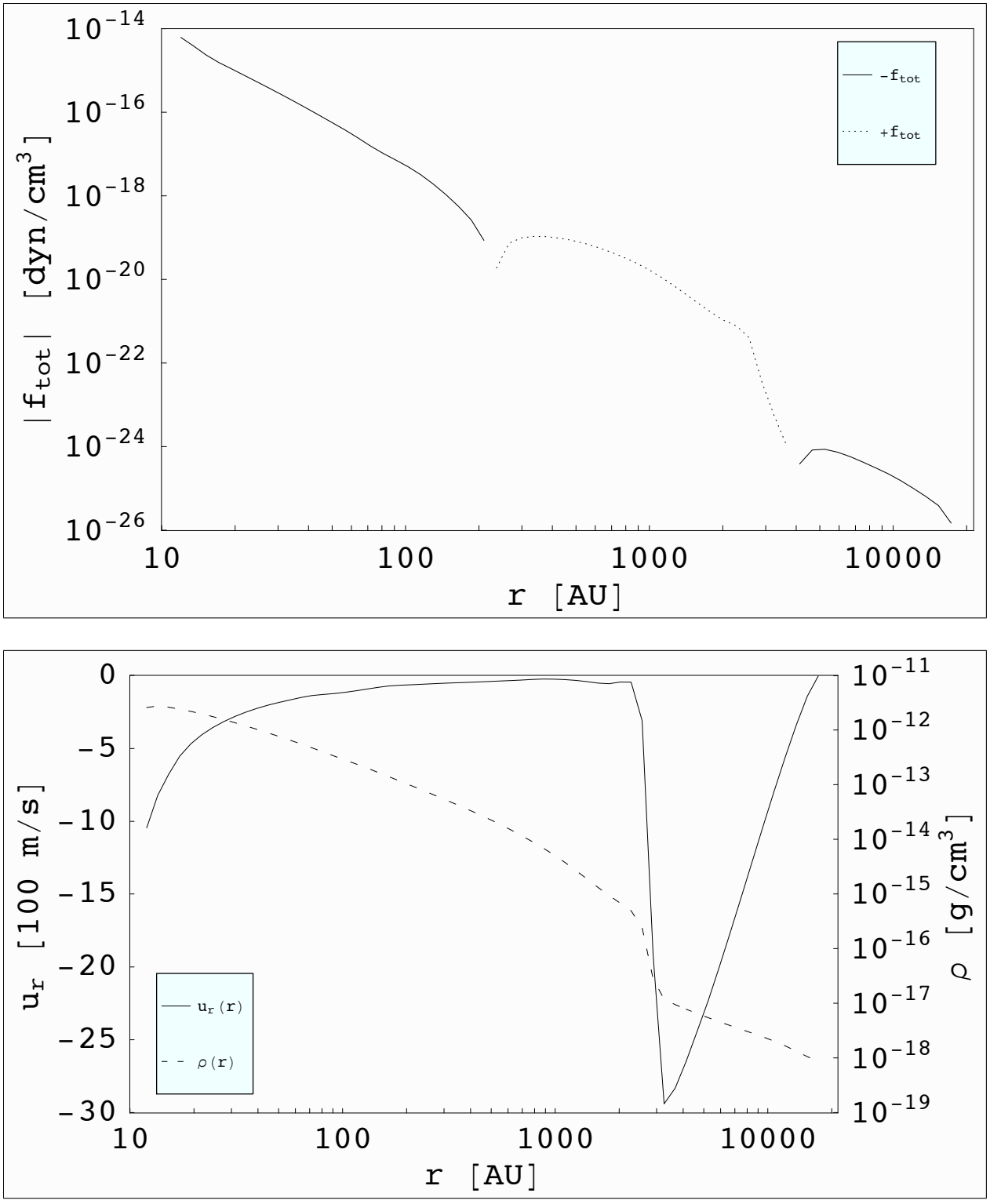

Figure 4.16: Total force density $|f_{tot}(r)|$ (upper panel) as well as density $\rho(r)$ and radial velocity $u_r(r)$ (lower panel) as a function of radius r through the disk's midplane. The snapshot was taken at 60 kyr after start of the simulation, corresponding to a central stellar mass of roughly 40 $M_\odot$. The individual force densities along this line of sight through the total and the inner core region are displayed in Figs. 4.17 and 4.18.

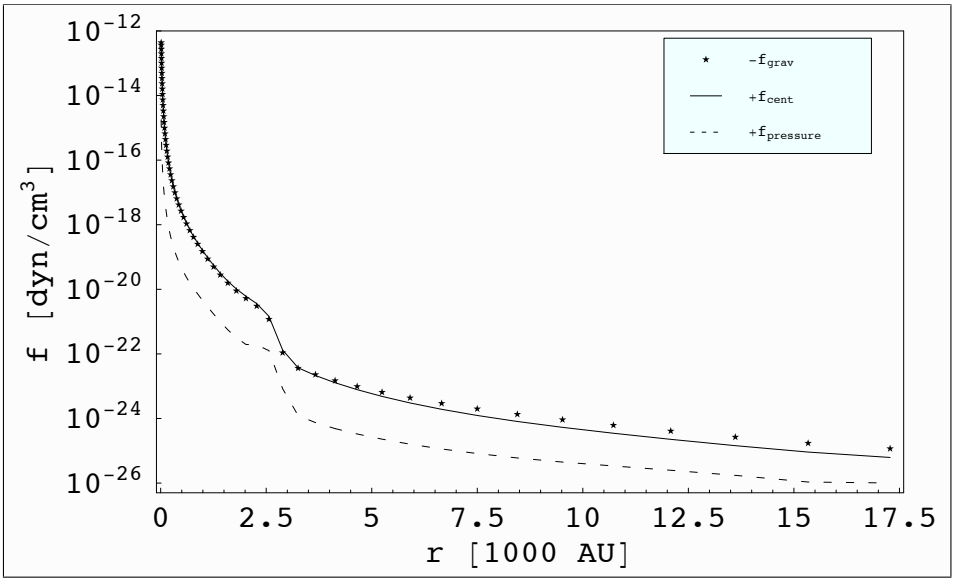

Figure 4.17: Gravity, centrifugal, and thermal pressure force as a function of radius through the disk's midplane. The snapshot was taken at 60 kyr after start of the simulation, corresponding to a central stellar mass of roughly 40 $M_\odot$. The radiative and viscous forces are orders of magnitude smaller than the illustrated ones, but become important in the inner disk region, where the stronger forces are in equilibrium. The radiative and viscous force densities along this line of sight through the inner core region are displayed in Fig. 4.18.

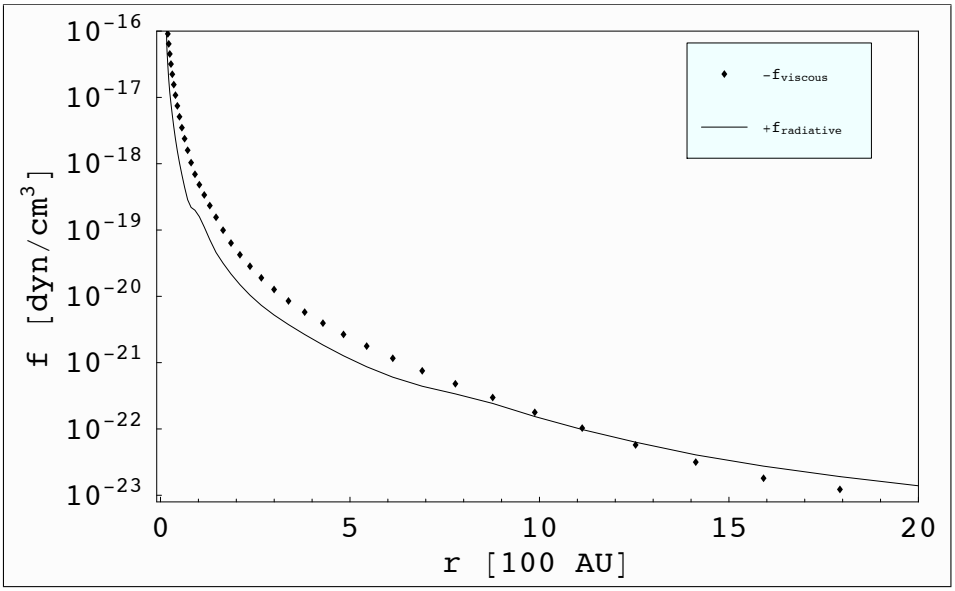

Figure 4.18: Viscous and radiative force density of the inner core region as a function of radius through the disk's midplane. The snapshot was taken at 60 kyr after start of the simulation, corresponding to a central stellar mass of roughly 40 $M_\odot$.

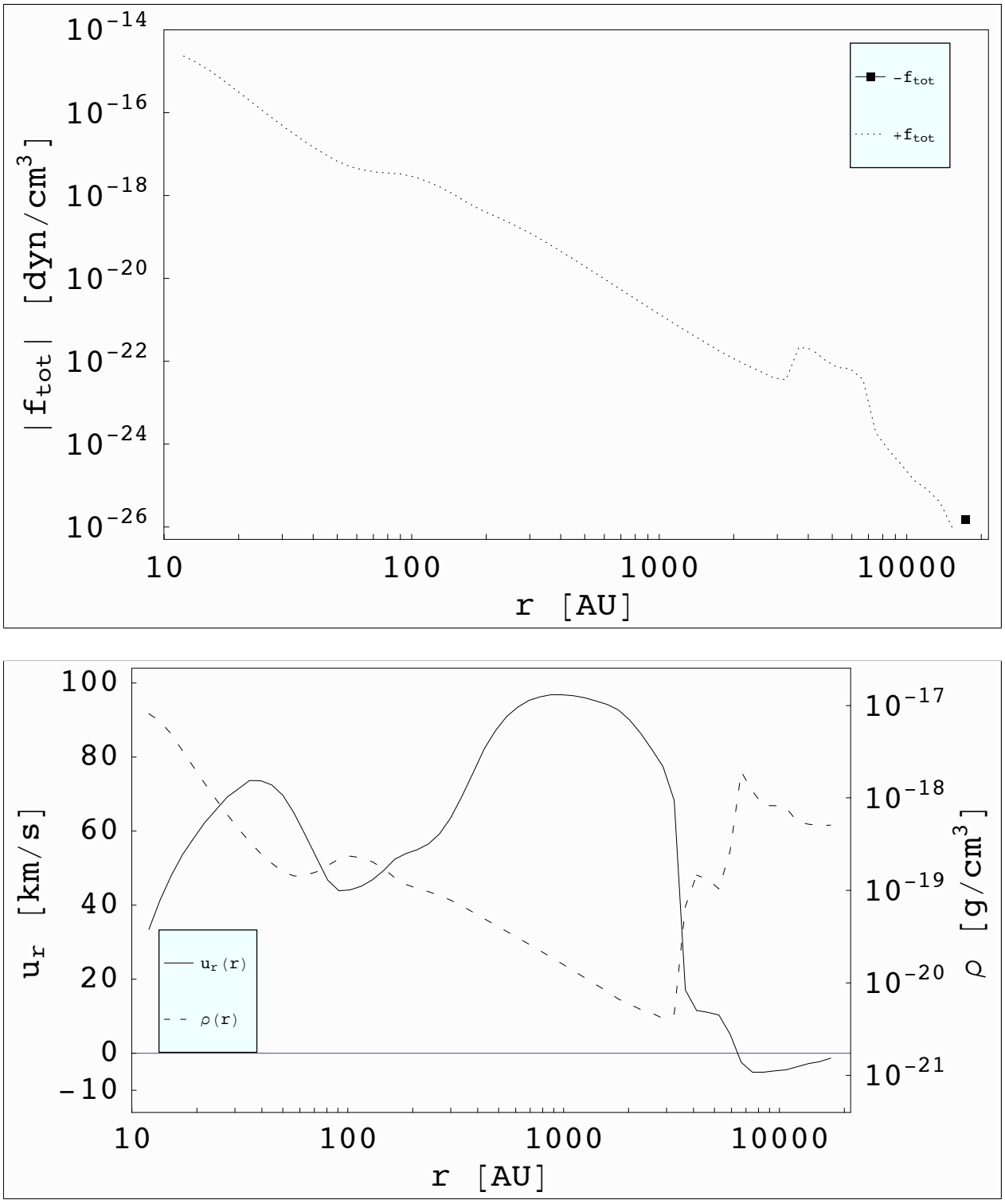

Figure 4.19: Total force density $|f_{tot}(r)|$ (upper panel) as well as density $\rho(r)$ and radial velocity $u_r(r)$ (lower panel) as a function of radius r at 30° above the disk's midplane. The snapshot was taken at 60 kyr after start of the simulation, corresponding to a central stellar mass of roughly 40 $M_\odot$. The individual force densities along this line of sight through the total and the inner core region are displayed in Figs. 4.20 and 4.21.

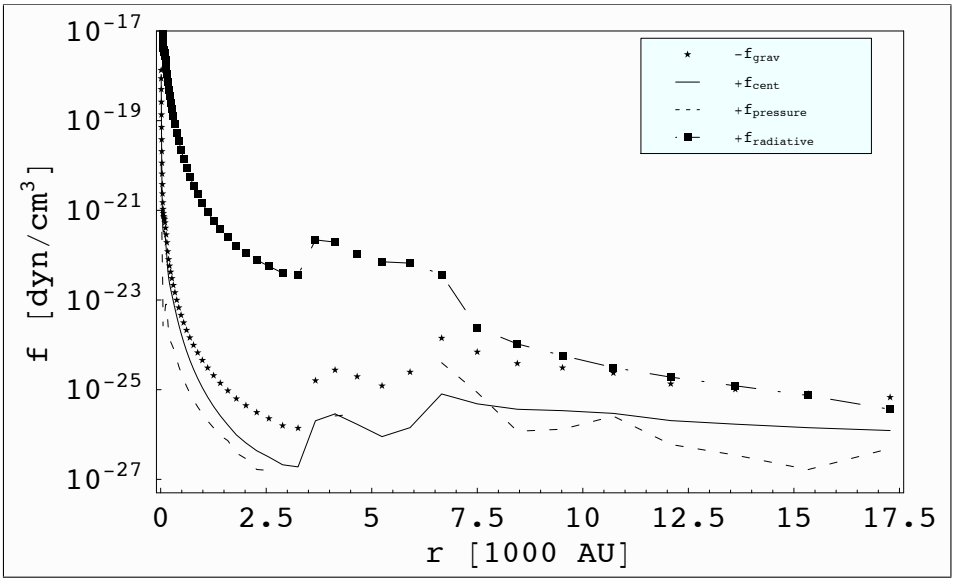

Figure 4.20: Gravity, centrifugal, thermal pressure, and radiative forces as a function of radius at 30° above the disk's midplane. The snapshot was taken at 60 kyr after start of the simulation, corresponding to a central stellar mass of roughly 40 $M_\odot$. The individual force densities along this line of sight through the inner core region are displayed in Fig. 4.21.

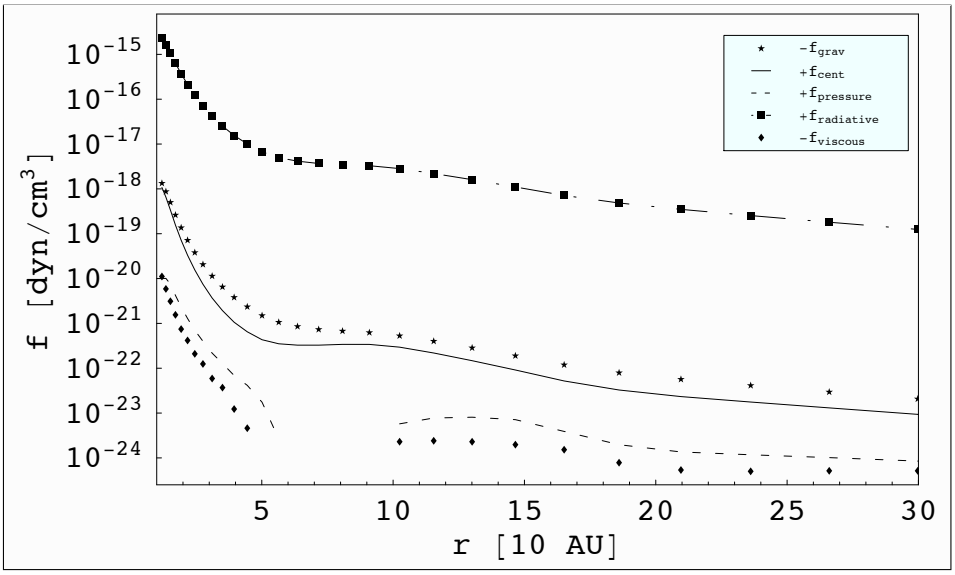

Figure 4.21: Gravity, centrifugal, thermal pressure, radiative, and viscous force density of the inner core region as a function of radius at 30° above the disk's midplane. The snapshot was taken at 60 kyr after start of the simulation, corresponding to a central stellar mass of roughly 40 $M_\odot$.

4.3.6 Epochs and dynamics of the collapse of rotating axially and midplane symmetric pre-stellar cores

As done for the spherically symmetric collapse evolution, we discuss the dominant processes in the evolution of the rotating axially and midplane symmetric pre-stellar cores for different epochs. Major changes in the morphology of the stellar environment such as a formation of the circumstellar disk or the launching of a radiatively driven outflow yield an alteration of the corresponding global energies. Therefore the kinetic, thermal, and potential energy are integrated over the computational domain

$$E_{\rm pot} = 2\pi \int_{r_{\rm min}}^{r_{\rm max}} dr \int_0^{\pi} d\theta\, r^2 \sin\theta\, \rho\Phi \tag{4.4}$$

$$E_{{\rm kin},r} = 2\pi \int_{r_{\rm min}}^{r_{\rm max}} dr \int_0^{\pi} d\theta\, r^2 \sin\theta\, \rho u_r^2 \tag{4.5}$$

$$E_{{\rm kin},\theta} = 2\pi \int_{r_{\rm min}}^{r_{\rm max}} dr \int_0^{\pi} d\theta\, r^2 \sin\theta\, \rho u_\theta^2 \tag{4.6}$$

$$E_{{\rm kin},\phi} = 2\pi \int_{r_{\rm min}}^{r_{\rm max}} dr \int_0^{\pi} d\theta\, r^2 \sin\theta\, \rho u_\phi^2 \tag{4.7}$$

$$E_{\rm thermal} = 2\pi \int_{r_{\rm min}}^{r_{\rm max}} dr \int_0^{\pi} d\theta\, r^2 \sin\theta\, \rho c_{\rm V} T. \tag{4.8}$$

The evolution of these global energies is visualized in Fig. 4.22 for the collapse of a slowly rotating 60 $M_\odot$ pre-stellar core. The vertical lines in the upper panel identify major events during the evolution of the collapsing core. These star formation specific processes such as disk formation and the launching of a large-scale outflow are essential elements in all simulations of rotating pre-stellar core collapses performed. The duration of the epochs or the onset of the transition processes occur on shorter time scales for higher mass cores. We go through the different epochs step by step:

0 - 8 kyr ($M_* = 0$ - $7\,M_\odot$): At the beginning of the simulations the dynamics of the system are strongly dominated by gravity. The centrifugal force of the initially slow rotation of the pre-stellar core has only a marginally influence and the accretion rate during this epoch is almost as high as during the initial free fall phase in the spherically symmetric models without rotation. Due to the conservation of angular momentum the in-falling matter speed up its rotation until the resulting centrifugal force counterbalances the gravity in the midplane layer of the innermost parts of the core. The evolution of the individual energies during this epoch is characterized by the conversion of potential energy into kinetic energy in the radial direction.

8 - 45 kyr ($M_* = 7$ - $16\,M_\odot$): A clear drop in the accretion rate marks the onset of the disk formation phase (see Fig. 4.15). The reason for this sudden decrease of the accretion rate is that the first fluid elements with a centrifugal radius $r_{\rm cent}$ (see Sect. 3.1.2 for a derivation of the centrifugal radius) equal to the radius $r_{\rm min}$ of the central sink cell has arrived at this inner computational boundary and keep on moving on a keplerian orbit. This means that the centrifugal force completely counteracts the gravity and the accretion rate drops down sharply. Directly afterwards the subsequently following mass will build up an accretion disk in which the shear viscosity will transport angular momentum outwards and the accretion rate rises again (but stays below the free fall accretion rate). This drop is very short in time and is superimposed by the proceeding accretion onto the massive star in the bipolar direction. The formation and growth of the circumstellar disk is accompanied by a steep increase of the kinetic energy in the azimuthal direction. Due to the growing centrifugal forces, which counteract on the initial in-fall, the kinetic energy in the radial direction decreases during this epoch.

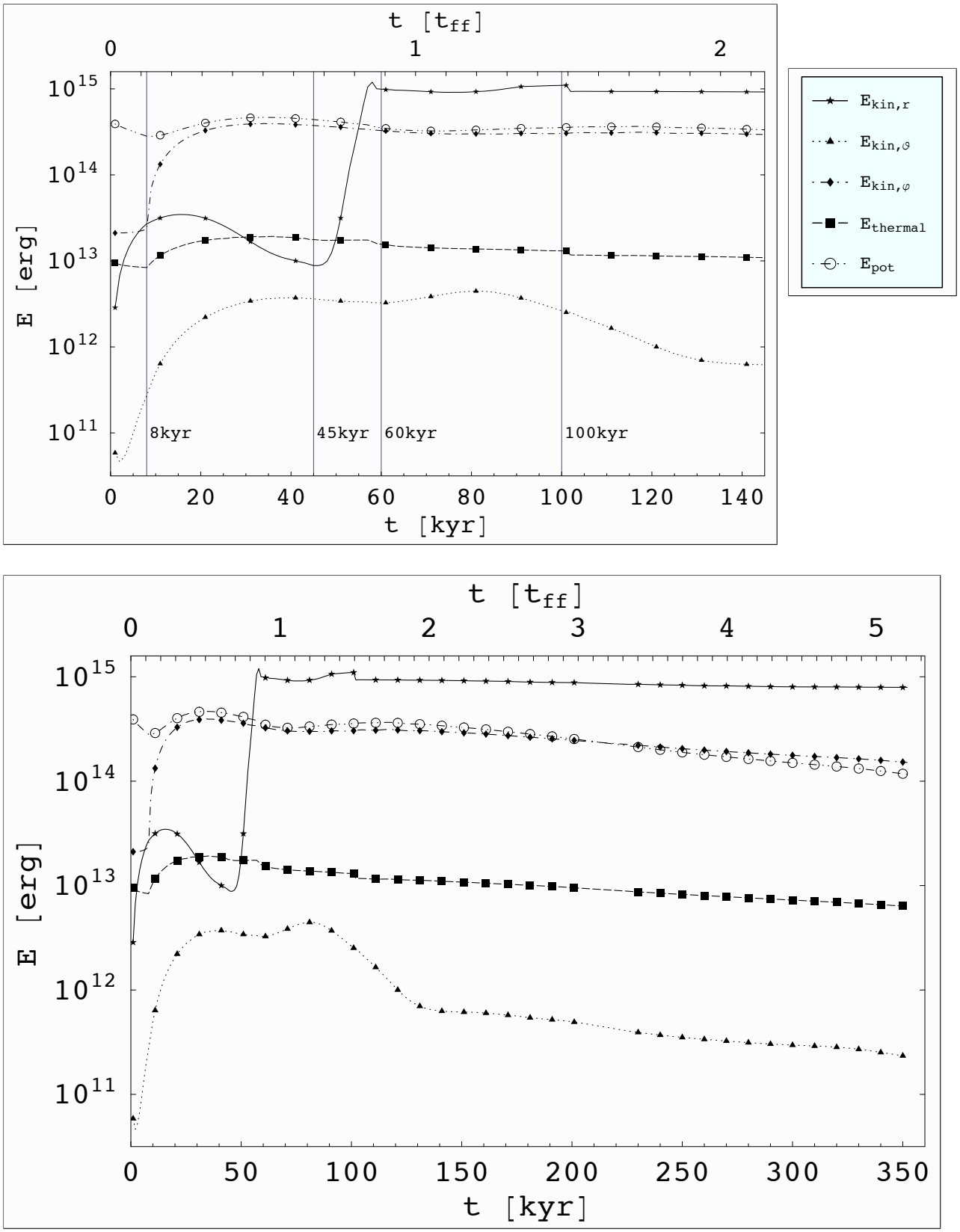

Figure 4.22: Global kinetic, thermal, and potential energy as a function of time for the collapse of a rotating axially and midplane symmetric pre-stellar core of 60 $M_\odot$. Vertical lines in the image of the first two free fall times (upper panel) identify transitions between distinguished evolutionary epochs of the collapse dynamics. The lower panel shows the long-term evolution of the energies up to 5 free fall times.

The dynamics of the most dense part of the pre-stellar core, the accretion disk, are now driven mostly by viscous forces, which are orders of magnitude lower than gravity. The decrease of the kinetic energy is further enhanced by the slow-down of the gravitationally in-falling regions due to growing radiative forces. At roughly 25 kyr the first motion in radially outward direction is detected. With growing mass of the central proto-star the radiative force becomes more and more important. As shown in the previous subsection the midplane layer is strongly shielded against the radiative flux due to the high opacity of the inner part of the disk. In the exact perpendicular direction along the poles the gravity is not reduced by centrifugal forces and the resulting strong flux of in-falling mass first has to be slowed down by radiative forces. Therefore the first region, in which the growing radiative force reveals the onset of an outflow motion, represents the layer directly above and beneath the shielded disk region, where centrifugal forces alleviate the acceleration in the radially outward direction.

45 - 60 kyr ($M_* = 16$ - $18\,M_\odot$): With the beginning of this epoch the radiative forces have stopped the in-fall motion in the bipolar direction and now start to drive an outflow growing in the radial direction. The velocity of this outflow is of the order of 100 km s^{-1} and therefore roughly one order of magnitude higher than the previous accretion flow driven by gravity. The speed of the rotation due to angular momentum conservation is higher than the gravitational in-fall but lower than the radiatively driven outflow motion. The movement in the polar direction is orders of magnitude lower than any other as also displayed in Fig. 4.22 of the kinetic energies in the different directions. This division of the absolute velocities occurring during the collapse allows us to classify the stellar environment into specific regions: Regions, which are dominated by motion in the radial outward direction ($u_r > u_\phi$), are referred to as 'outflow regions'. Fig. 4.23 visualizes the onset and the later on evolution of the launched outflow for the 240 $M_\odot$ case. The outflow regions are thereby identified by the $u_r = u_\phi$ iso-contour. The left panel shows the launching of the outflow in the bipolar direction as well as the previous acceleration of the large scale layer above the rotating disk due to thermal radiation pressure. At the later evolutionary stage (right panel) both regions have merged and shape (by chance) some kind of 'batman-contour'. To visualize the resulting over-density near the top of the polar outflow the color scale of the density plot in the right panel resolves only a maximum density of $2 * 10^{-16}$ g cm^{-3}, roughly five orders of magnitude lower than the actual maximum density in the computational domain. Therefore, no details of the midplane layer are visible up to several 1000 AU. Due to the faster evolution of the illustrated more massive pre-stellar core, the onset of the launching of this outflow happens already after the first 5 kyr, in which the central star has already reached a mass of 28 $M_\odot$. The stellar mass at the more evolved state in the right panel is about twice as massive ($M_* = 56\,M_\odot$). The strong acceleration in the outflow regions yields a steep increase of the radial kinetic energy (Fig. 4.22). Further in time, the kinetic energy in the radial direction grows according to the expansion of the accelerated region. At the end of this epoch the outflow has reached the outer computational boundary.

60 - 100 kyr ($M_* = 18$ - $20\,M_\odot$): With progressing mass flux from the envelope towards the midplane layer the density of the envelope decreases in time until the radiative force dominates the dynamics and the outflow region expands in the polar direction as well. This expansion occurs on a much larger time scale than the previous launching of the outflow in the radial direction. At the end of this epoch, the depletion of the envelope regions adjacent to the accretion disk layer results in a decrease of the kinetic energy in the polar direction.

100 kyr and later on ($M_* > 20\,M_\odot$): From roughly 1.5 free fall times after beginning of the simulation the system reaches a quasi-stationary evolution without further dramatical changes of its morphology. Due to the decrease of density inside the computational domain all energies continuously decline hereafter, shown in the

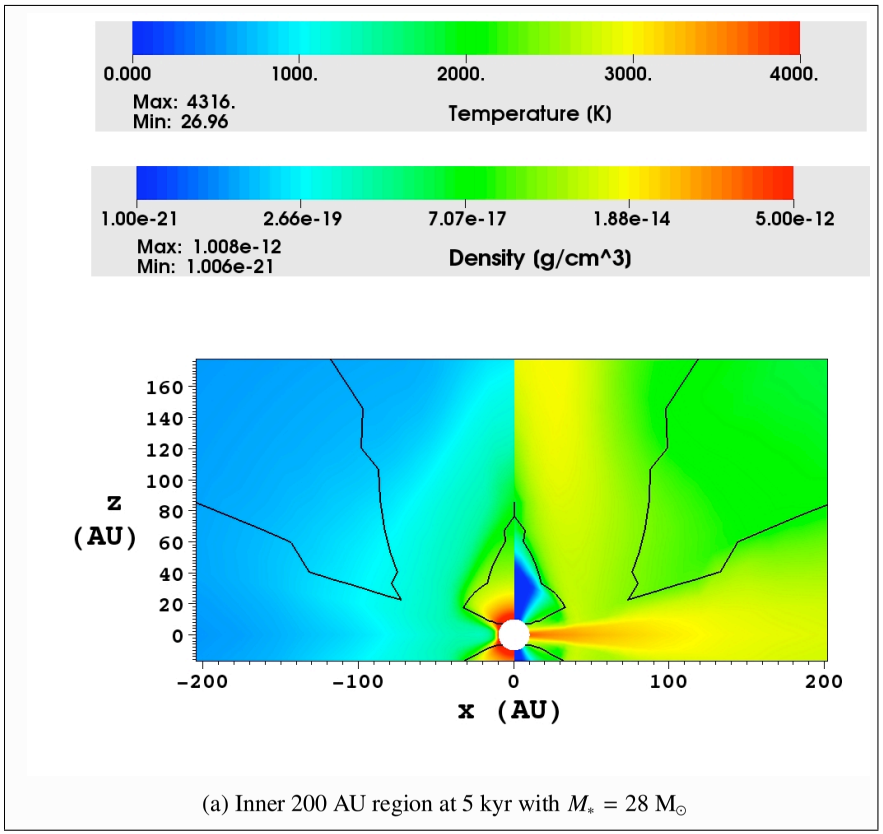

(a) Inner 200 AU region at 5 kyr with $M_* = 28\ M_\odot$

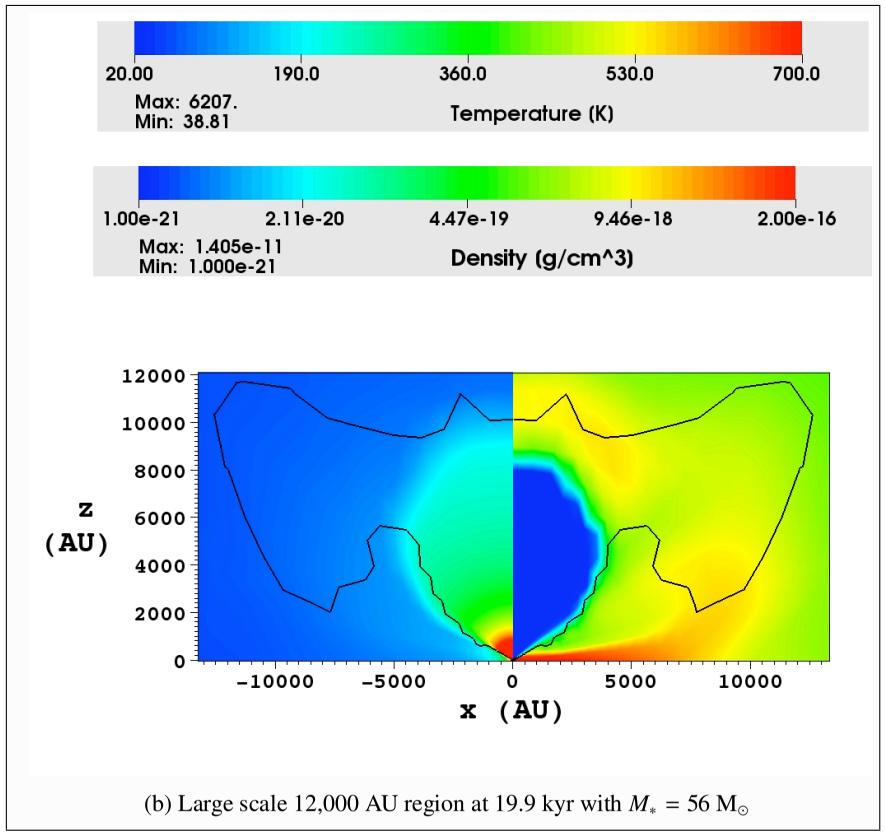

(b) Large scale 12,000 AU region at 19.9 kyr with $M_* = 56\ M_\odot$

Figure 4.23: The onset of the radiation pressure driven bipolar outflow in the vicinity of the massive star (left panel) and its large scale extent at a more evolved state (right panel). The color coding in both panels is divided into the visualization of the temperature (colors on the left) and the density (colors on the right). Due to the different length scale of both panels also the color coding extents over different magnitudes. A separation into rotation and outflow dominated regions is highlighted by the $u_r = u_\phi$ iso-contour. Both images are from an axially and midplane symmetric collapse simulation of a 240 $M_\odot$ pre-stellar core.

long-term evolution of the integrated global energies in the lower panel of Fig. 4.22. The large scale accretion flow during this long-term epoch is still driven by gravity and the corresponding mass flux increases with decreasing radius. The accretion flow in the disk region, where the gravity is balanced by centrifugal forces, is driven by viscosity and is therefore roughly an order of magnitude lower than the large scale accretion onto the disk. Fig. 4.24 on p. 122 visualizes the mass flux on the large scales as well as in the stellar neighborhood. The left panel also shows the huge extent of the depleted region due to the radiation pressure driven outflow during previous epochs.

In the long term, the steady depletion of the core density yields a continuous decrease of the stellar accretion rate. Thus, the corresponding mass growth of the massive star gets negligible, see Fig. 4.15. The simulations are not finished yet as in the one-dimensional case, that means there is still mass inside the computational domain of about 15.2, 15.7, 15.8, and 120 $M_\odot$ for the $M_{\rm core}$ = 60, 120, 240, and 480 $M_\odot$ case respectively. Potentially the circumstellar disk will loose its shielding property at some point in time and the radiative force will eject the remnant disk material into outer space. The final mass of the central star adds up to 27.4, 56.5, and 92.6 $M_\odot$ for the 60, 120, and 240 $M_\odot$ case respectively. No indication of an upper mass limit of the final star due to radiation pressure is found yet, but the star formation efficiency seems to decline for higher mass cores. The evolution of the 480 $M_\odot$ core is simulated up to slightly more than one free fall time so far. The corresponding massive star of more than 112 $M_\odot$ is still gaining mass from its environment with an accretion rate of roughly 10^{-3} $M_\odot$ yr^{-1}.

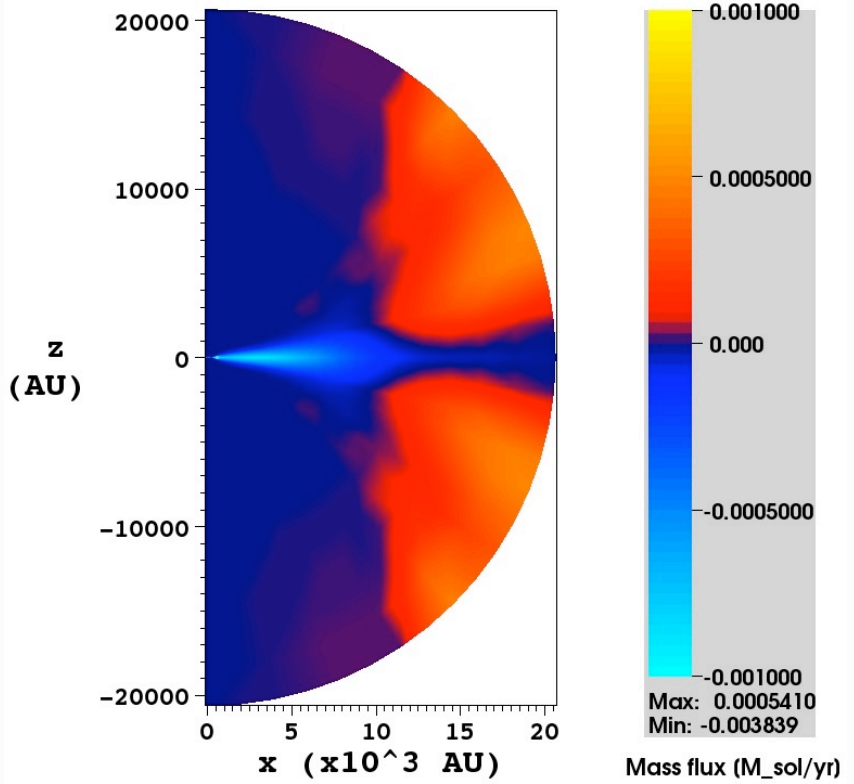

(a) Mass flux in the whole computational domain.

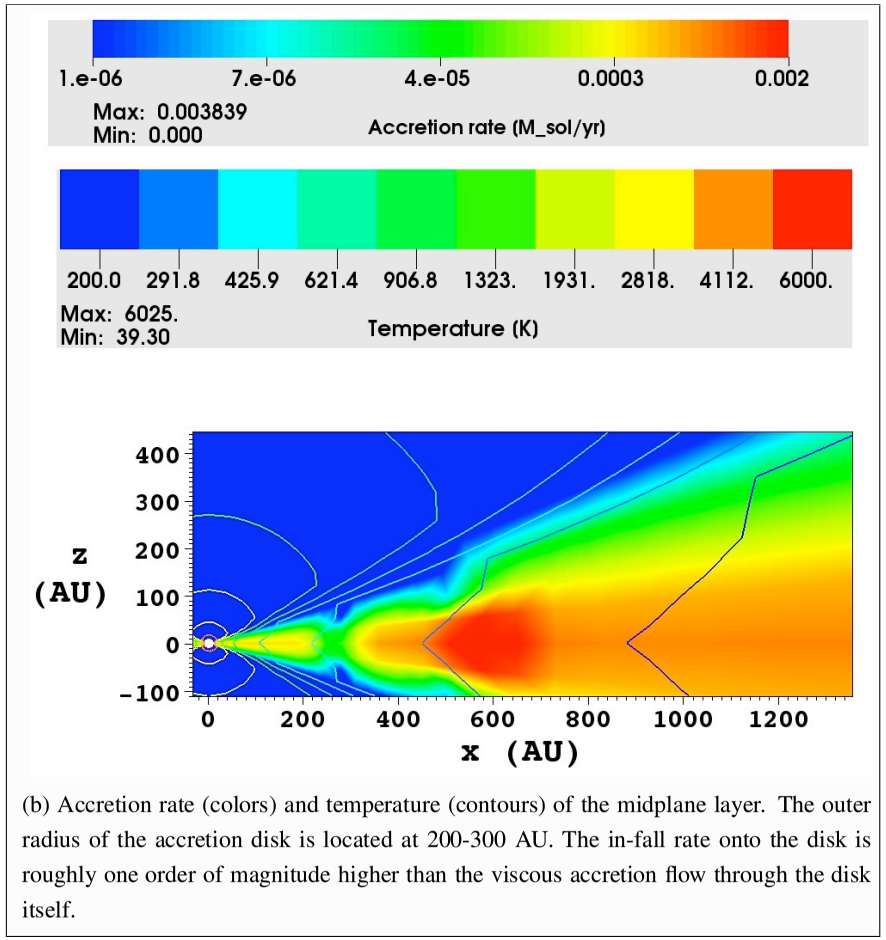

(b) Accretion rate (colors) and temperature (contours) of the midplane layer. The outer radius of the accretion disk is located at 200-300 AU. The in-fall rate onto the disk is roughly one order of magnitude higher than the viscous accretion flow through the disk itself.

Figure 4.24: Mass flux on the large scales (left image) as well as the accretion flow onto the star and the circumstellar disk (right image). The blue colored region on the right panel implies a radial velocity in the outward direction. Both images represent a snapshot of an axially and midplane symmetric collapse simulation of a 240 $M_{\odot}$ pre-stellar core at a highly evolved state at 30 kyr.

4.4 Three-dimensional simulations

As a starting point of our study of non-axially symmetric effects in the formation of massive stars, we performed two three-dimensional simulations of the collapse of slowly rotating pre-stellar cores. We used the same initial conditions as in the axially symmetric runs (see Sect. 4.1) and masses of the pre-stellar cores of $M_{\rm core}$ = 120 $M_\odot$ and $M_{\rm core}$ = 240 $M_\odot$. To save CPU time wherever possible, the runs were performed assuming symmetry to the midplane of the disk. The three-dimensional simulations are very expensive in terms of CPU time and are therefore not finished yet. Nonetheless, the evolution of the system is computed up to a state at which non-axially symmetric effects occur in the circumstellar accretion disk. In this section, we discuss subsequently the resolution of the stellar radiative feedback achieved in the three-dimensional simulations (Sect. 4.4.1), the onset of radiation pressure driven outflows during the early state of massive star formation (Sect. 4.4.2), the fragmentation of massive circumstellar accretion disks and the potential formation of a stellar companion (Sect. 4.4.3), as well as angular momentum transport in self-gravitating unstable disks (Sect. 4.4.4).

4.4.1 Resolving the dust condensation front

In the three-dimensional simulations, we study pre-stellar cores with the same initial conditions and physics applied as in the two-dimensional cases (see Sect. 4.3). We transfer the resolution from the axially symmetric runs expanded to 3D by setting $\Delta\phi = \Delta\theta$. Also the size of central sink cell is chosen accordingly to the restriction found in the two-dimensional simulations. With a radius of the sink cell of $r_{\rm min}$ = 10 AU and a radially growing grid with 64 x 16 x 64 grid cells in the radial, polar, and azimuthal direction respectively we end up at a resolution in units of arc length of $(\Delta r \text{ x } r\,\Delta\theta \text{ x } r\,\sin(\theta)\,\Delta\phi)_{\rm min}$ = 1.27 AU x 1.04 AU x 1.04 AU for the innermost grid cells in the midplane layer. This high resolution in the vicinity of the newly forming massive star guarantees a detailed reconstruction of the radiative feedback on the inner rim of the accretion disk. As an example, Fig. 4.25 on p. 124 shows the dust condensation front resolved at 1,500 yr after beginning of the collapse of a 240 $M_\odot$ pre-stellar core. The image visualizes a zoomed-in snapshot of the inner (25 AU)^2 region perpendicular to the azimuthal axis. At this early point in time, the morphology of the stellar environment shows no deviation from axial symmetry. The transition from the dust free region in the vicinity of the forming proto-star to the dust disk is smoothly resolved over six grid cells. Such a resolution of the region of the first radiative feedback of a forming massive star was not achievable in hydrodynamics simulations of massive star formation so far. The transition from the dust free to dusty regions is thereby very narrow in the most massive midplane of the disk, whereas the transition in the low-density polar direction occurs on a much larger extent. In the bipolar direction, the local temperature exceeds the evaporation temperature of the dust up to approximately 100 AU at this point in time already. As discussed more precisely in the following subsection, Fig. 4.26 on p. 126f. shows the onset of the associated radiative acceleration of a bipolar outflow.

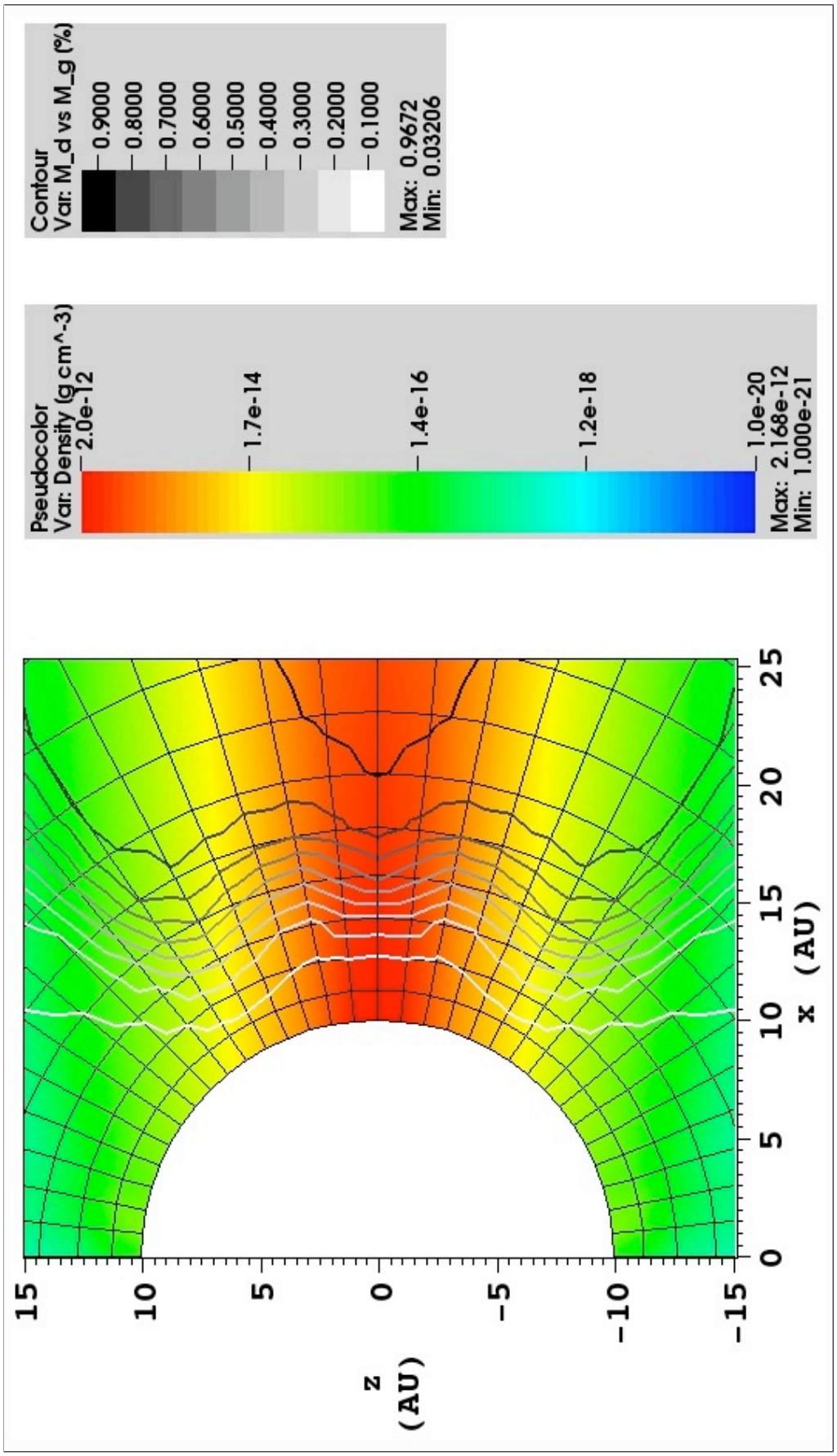

Figure 4.25: Gas density (colors), dust to gas mass ratio (contours) as well as the discretization (the numerical grid) in the innermost 25 AU. The transition from the dust depleted regions to the dusty disk midplane is resolved roughly within six grid cells. The image represents a slice through the x-z-plane of a three-dimensional collapse simulation of a 240 $M_\odot$ pre-stellar core after 1,500 yr.

4.4.2 The onset of radiation pressure driven outflows

The increase of stellar luminosity during the formation of the massive proto-star in the core center results in a strong heating of the stellar environment, especially directly behind the dust condensation front. The thermal radiative flux from these heated regions yields a forceful pressure on the surrounding dust grains. Assuming a tight coupling between the dust and the gas flow, the radiation pressure starts to drive a large-scale bipolar outflow, depleting the low-density environment. As identified in the two-dimensional axially symmetric simulations already, the formation of a massive circumstellar disk shields the internal accretion flow from the thermal radiative feedback basically by cooling in the vertical direction through the disk's atmosphere. The formation of the bipolar outflow, driven by radiation pressure, strongly depends on the dust physics (the absorption properties) of the stellar environment. The onset of acceleration in the radially outward direction occurs directly behind the dust condensation front. This fact is visualized in a sequence of snapshots in intervals of 100 years of the central region of the 240 $M_\odot$ collapse case in Fig. 4.26 on p. 126 and following. Each image shows on the left hand side the color-coded radial velocity distinguished in inward (dark blue to light blue) and outward motion (red to yellow). The right hand side of each panel shows the corresponding gas density (colors) as well as the dust to gas mass ratio (contour lines in steps of 0.1%). In the long term the radiation pressure driven outflow grows in the radial direction until it extends over the whole computational domain. Dragged behind, it grows in the polar direction as well. For shorter periods, the irruption of a mass flux into the outflow region enhances the density, yielding a higher evaporation temperature of the dust grains and therefore increases the local dust to gas mass ratio. If a sufficient amount of dust condensates locally, the majority of the stellar irradiation is absorbed at smaller radii again and the expansion of the low-density 'cocoon' or 'bubble' is stopped, even a temporary decrease set in. The dependence of the morphology of the outflow region on the proceeding physics in the high-density parts of the pre-stellar core is also reflected in the onset of non-axially symmetric modes in the circumstellar accretion disk, which yields a break of the axial symmetry of the radiation pressure in the vertical direction as well.

4.4.3 Disk fragmentation and binary formation

As known from the two-dimensional collapse simulations without the explicit treatment of viscosity ($\alpha = 0$), the increase of density in the massive accretion disk will result in the formation of an unstable ring. This instability occurs in the case of the three-dimensional collapse simulations of a 120 $M_\odot$ pre-stellar core roughly after 7.8 kyr. The instability is located at a short separation of 15 AU from the centrally forming massive star. Such a close-by fragmentation could not be resolved in previous numerical research due to the low resolution in the vicinity of the star. In case of the setup of Yorke & Sonnhalter (2002), this location is deeply buried inside the huge central sink cell used and, of course, the further evolution of this instability cannot be studied in axial symmetry anyway. In case of the simulations by Krumholz et al. (2007, 2009a), the formation of an unstable ring with a separation of 15 AU from the star cannot be reproduced on a cartesian grid with $(10\mathrm{AU})^3$ grid cells around a $(10\mathrm{AU})^3$ sink cell. The morphology of this unstable ring is displayed in Fig. 4.27 showing a face on view of the *x*-*y*-plane of the central core region at 7,920 yr after the beginning of the collapse. Additionally to the color-coded density, the figure contains iso-contours of the so-called Truelove criterion, introduced in Truelove et al. (1997), see also Sect. 2.4.1 for a brief description. The black, blue, and white contour lines embed the regions, in which the Jeans length λ_J is resolved by less than 12, 8, and 4 grid cells respectively. At

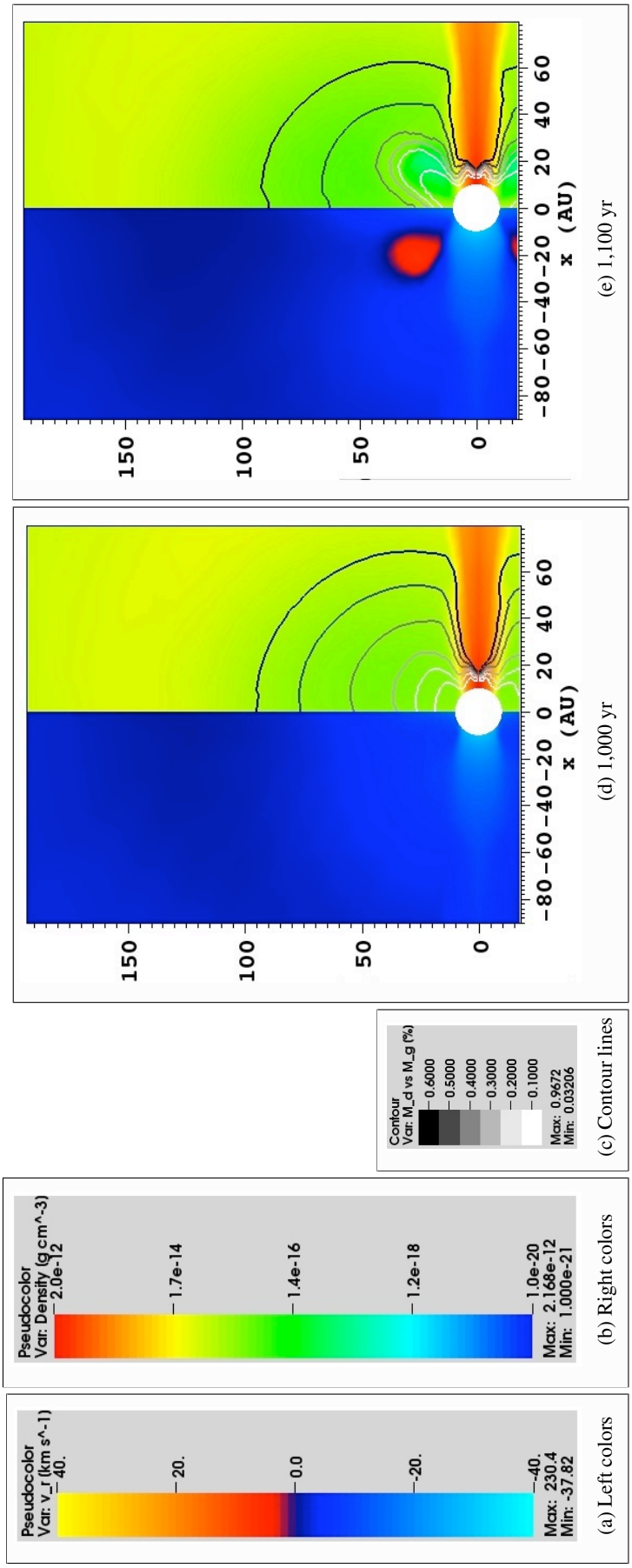

Figure 4.26: Radial velocity (colors on left half), gas density (colors on right half) and dust to gas mass ratio (contours) at the onset of the radiation pressure driven outflow formation. The images represent the x-z plane of the inner region from a three-dimensional collapse simulation of a 240 $M_\odot$ core at 1.0, 1.1, 1.2, 1.3, and 1.4 kyr. No deviations from axial symmetry have occurred in the circumstellar disk up to this epoch.

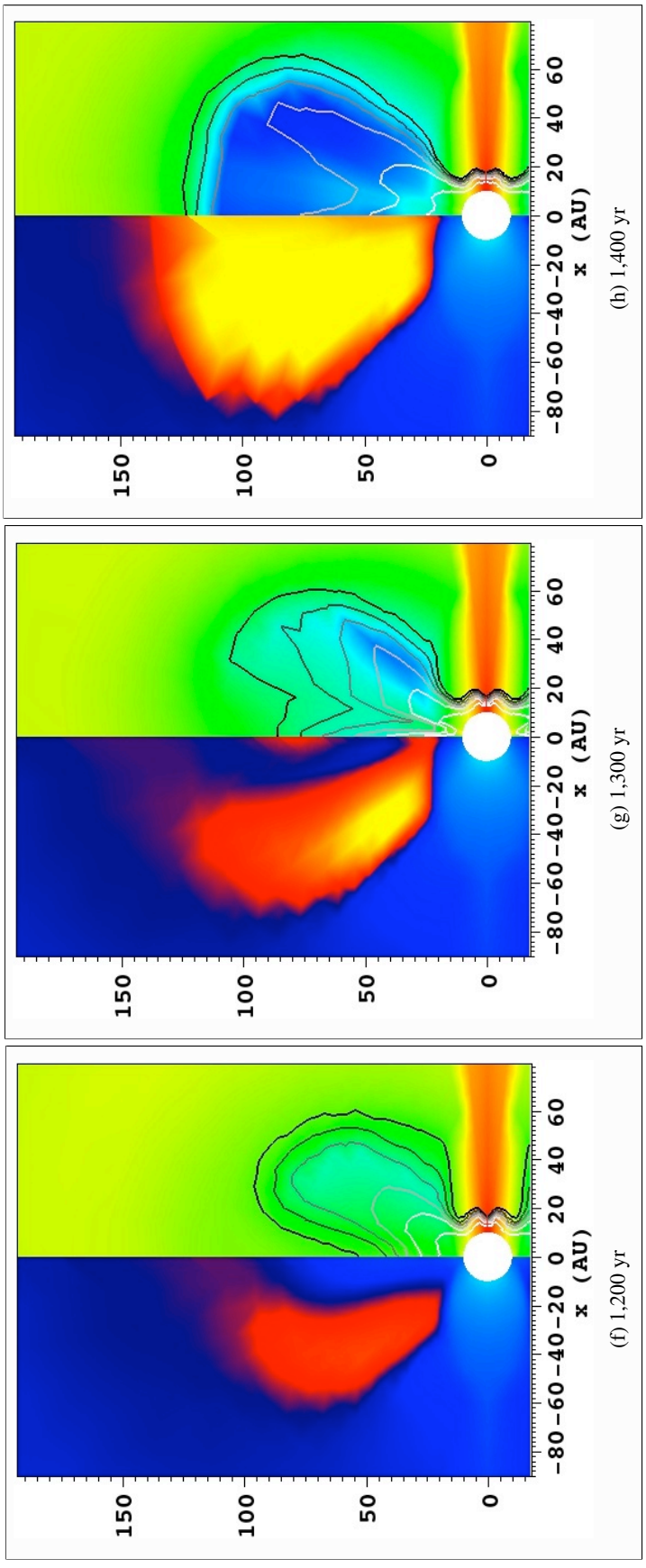
150
100
50
0
−80 −60 −40 −20 0 20 40 60
x (AU)
(f) 1,200 yr
(g) 1,300 yr
(h) 1,400 yr

least the small regions inside the white contour imply that although the onset of the disk fragmentation is truly resolved we cannot follow the fade of this unstable region further in time. The fast increase of density results in the violation of the Truelove criterion shortly after the onset of the gravitational instability. An even higher resolution of this specific region (or a sink cell paradigm) seems to be necessary to follow the evolution further in time.

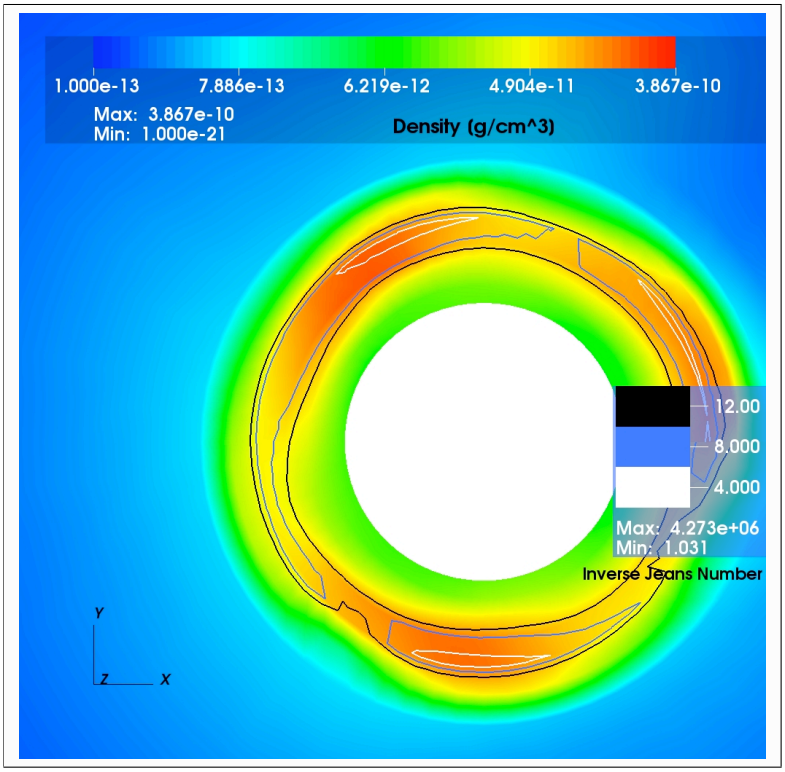

Figure 4.27: Face on view of the x-y-plane of the central core region shortly after the onset of a non-axial symmetric mode in the accretion disk. The image shows the logarithmically color-coded gas density as well as contour lines according to the Truelove criterion for Poisson solvers. The separation of the unstable ring from the centrally forming massive star is 15 AU.

Analytically a necessary criterion for stability is given by the Toomre criterion, introduced in Toomre (1964). The Toomre parameter Q is thereby given by

$$Q = \frac{\Omega\, c_\mathrm{s}}{2\pi\, G\, \Sigma} \tag{4.9}$$

with the local surface density Σ of the disk. A disk is prone to gravitational instabilities for a low value of Q. Thus, the probability of fragmentation grows if the circumstellar disk is slowly rotating, cold, and dense. To transfer this criterion to the accretion disk forming during our three-dimensional collapse simulations, we average the azimuthal velocity $\Omega(\theta = 90°)$ and the sound speed $c_\mathrm{s}(\theta = 90°)$ in the midplane layer as well as the local surface density Σ in the azimuthal direction:

$$\bar{\Omega} = \frac{1}{2\pi}\int_0^{2\pi} \Omega(r, \theta = 90°, \phi)\, d\phi \tag{4.10}$$

$$\bar{c}_s = \frac{1}{2\pi}\int_0^{2\pi} c_\mathrm{s}(r, \theta = 90°, \phi)\, d\phi \tag{4.11}$$

$$\bar{\Sigma} = \frac{1}{2\pi}\int_0^{2\pi} \Sigma(r, \phi)\, d\phi \tag{4.12}$$

The local surface density $\Sigma(r, \phi)$ is thereby calculated on the spherical grid by integrating the density distribution in the polar direction $\Sigma = \int_0^{\pi} \rho(\vec{x})\, r\, d\theta$. Deviations of this computation from integrating in the vertical direction cancels out for small angles beneath and above the midplane ($\sin(\theta) \approx \theta$ for small θ). Due to the fact that the density at larger angles above the disk's atmosphere is orders of magnitude lower than in the midplane, this simplified integration along the spherical coordinate axis is justified. The mean Toomre parameter $\bar{Q}$ is then given by the average values above:

$$\bar{Q} = \frac{\bar{\Omega}\, \bar{c}_s}{2\pi\, G\, \bar{\Sigma}}. \tag{4.13}$$

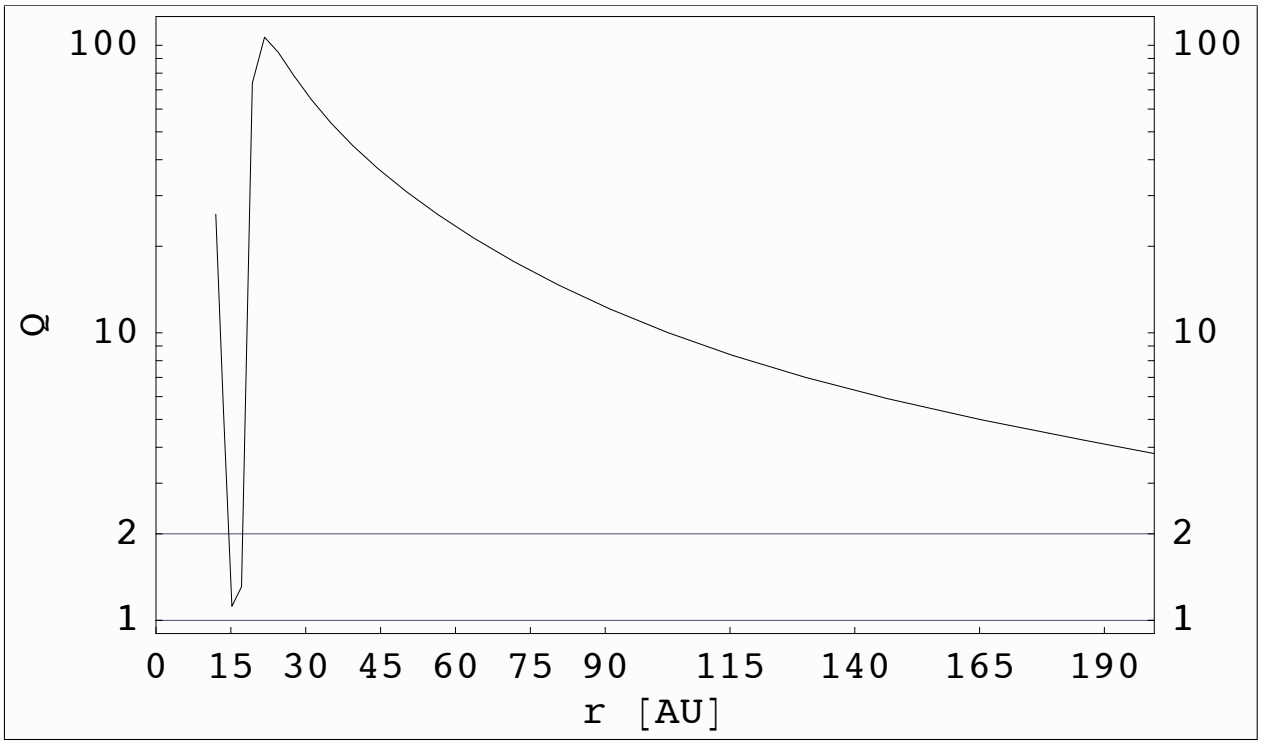

Figure 4.28: Mean Toomre parameter of the accretion disk formed during the 120 $M_\odot$ pre-stellar core collapse as a function of the radius. The accretion disk forms an instability in the three-dimensional simulation at roughly 15 AU from the central star. The snapshot is calculated at 7.92 kyr after the onset of the collapse. The massive star in the center has a mass of about 18.5 $M_\odot$ at this point in time.

The nature of the occurring instability can now be proved by analyzing the Toomre criterion for the massive disk. Fig. 4.28 shows the corresponding mean Toomre parameter as a function of the radius. The value of $Q < 2$ at 15 AU corresponds to the formation of a non-axial symmetric mode with $m \geq 1$. Potentially, if the cooling time in the unstable region is shorter than the dynamical time scale, the instability leads to the formation of a close-by companion. Zinnecker (2003) stated that disk fragmentation generally leads to binaries between 10 and 100 AU, corresponding to the radial disk extent. Observation of close spectroscopic binaries go even down to separations of less than 1.5 AU (Apai et al. 2007). Due to interplay of the two bodies, which will further accrete material from the high-mass surroundings, a reduction of their separation as well as a decrease of their mass ratio towards unity seems to be possible. The effect of the instability on the actual accretion rate during the three-dimensional simulation is further investigated in the next subsection.

4.4.4 Angular momentum transport and accretion in massive circumstellar disks

As stated in the description of the α-viscosity used in the two-dimensional simulations (see Sect. 2.3 and 4.3.3), the angular momentum transport in circumstellar accretion disks is aside from jets and winds mainly a result of developing intrinsic instabilities of the disk, which are e.g. caused by weak magnetic fields (Balbus & Hawley 1991; Hawley & Balbus 1991; Balbus 2003) or by strong self-gravity of the disk (Yang et al. 1991; Laughlin & Bodenheimer 1994; Bodenheimer 1995). Thereby, irradiation by the envelope or the star seems to suppress the

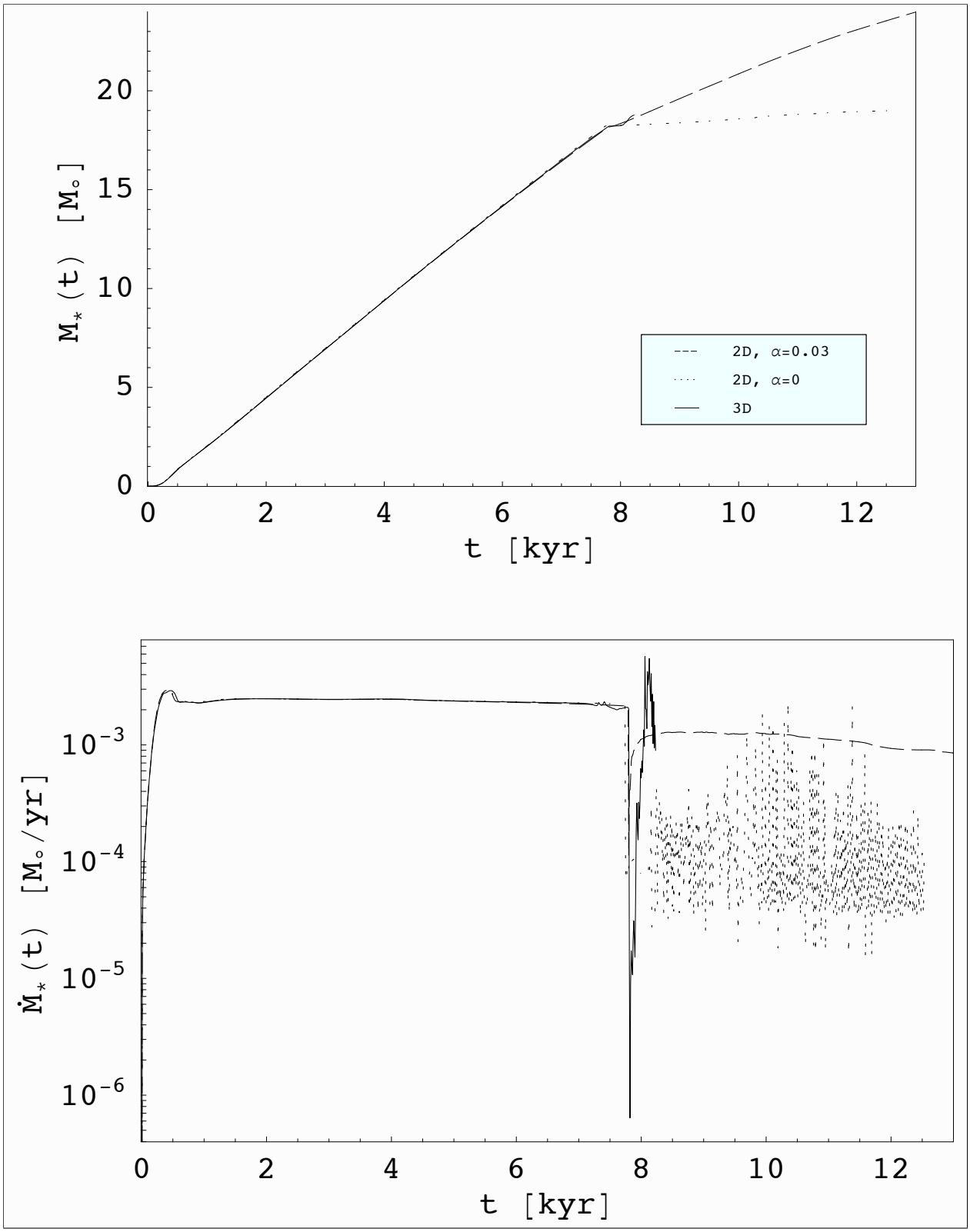

Figure 4.29: Stellar mass growth and accretion rate during the 120 $M_{\odot}$ pre-stellar core collapse as a function of time.
Dashed line: Two-dimensional simulation using a constant α-viscosity description.
Dotted line: Two-dimensional simulation without α-viscosity.
Solid line: Three-dimensional simulation yielding the formation of a gravitational instability in the accretion disk at roughly 7.8 kyr.

growth of the gravitational instability at least in low-mass proto-planetary disks (Cai et al. 2008, 2009). Kratter & Matzner (2006, 2008) argue in their semi-analytic models that disks around more massive stars including higher accretion rates are progressively more likely to fragment.

In our two-dimensional simulations, we assume a constant α-viscosity description, which mimics the effect of angular momentum transport and therefore maintains the accretion flow through stable viscous accretion disks. In the three-dimensional simulations, no shear or bulk viscosity is applied. The value of the accretion rate onto the massive star after the free fall phase is therefore determined by the nature of the gravitational instability, described in the previous subsection. Fig. 4.29 shows in comparison the resulting accretion history of the three-dimensional simulation as well as the evolution during the corresponding viscous and non-viscous two-dimensional runs in axial symmetry. The models started from the same initial conditions of a 120 $M_\odot$ pre-stellar core. All runs show an almost identical level of accretion during the free fall phase up to 7.8 kyr. The onset of the gravitational instability in the three-dimensional run is identified by a sharp, but transient, drop of the accretion rate. Shortly after, the induced angular momentum transport results in a strong increase of the mass flow into the central sink cell anew. The short separation of the instability from the central star of roughly 15 AU yields clearly visible fluctuations in the accretion history. Providing a deeper insight, Fig. 4.30 shows a zoom-in image of the upper panel of Fig. 4.29 at the onset of the instability. After the formation of the gravitational

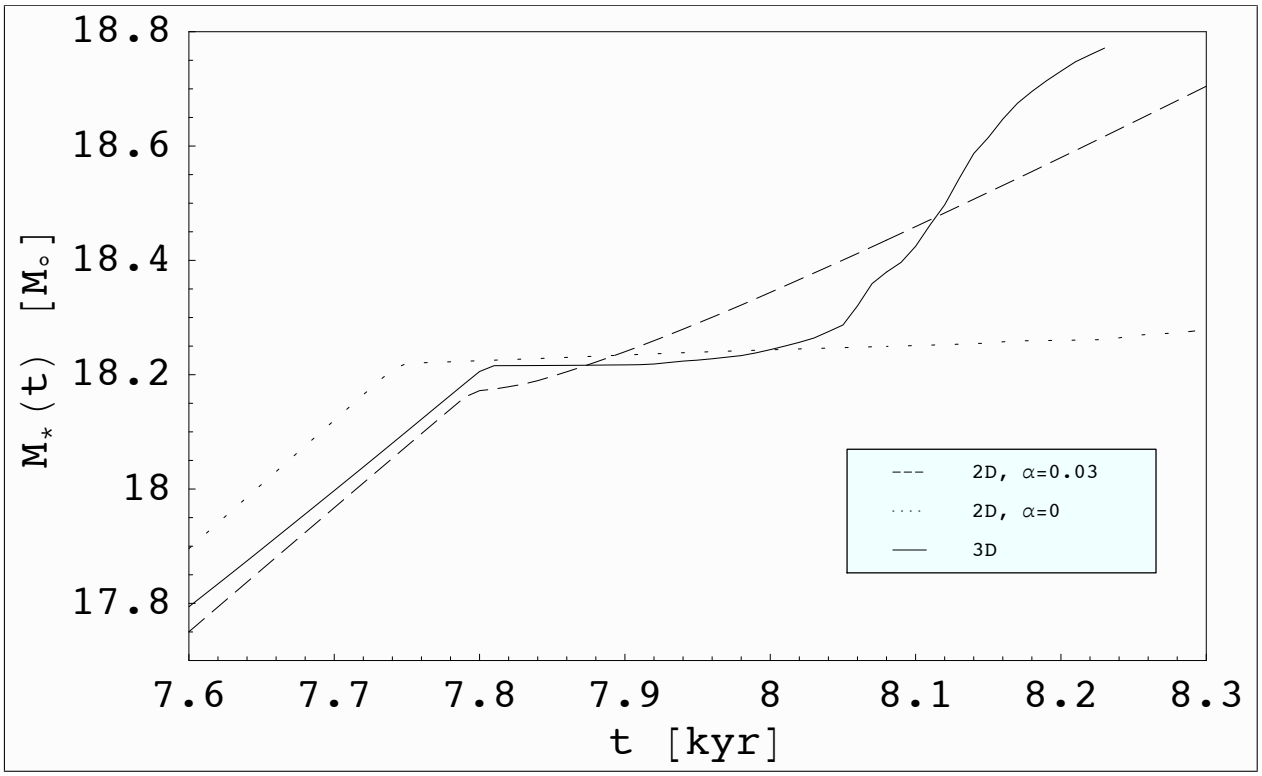

Figure 4.30: Zoom-in of Fig. 4.29: Accretion rate at the onset of instability as a function of time.
Dashed line: Two-dimensional simulation using a constant α-viscosity description.
Dotted line: Two-dimensional simulation without α-viscosity.
Solid line: Three-dimensional simulation yielding the formation of a gravitational instability in the accretion disk at roughly 7.8 kyr.

instability in the circumstellar disk, the accretion rate of the three-dimensional simulation drops sharply and the associated mass growth follows the result of the non-viscous two-dimensional simulation for roughly 200 yr. After this temporary episode, the actual stellar mass oscillates around the two-dimensional solution computed with a constant α-prescription. This behaviour of accretion in the three-dimensional simulations supports the general idea that the level of accretion is determined by the mass flux on the large scales or the feeding of the inner accretion disk by core accretion respectively. Already in the parameter scan of the α-viscosity in the two-dimensional simulations we found only a slight dependence of the accretion rate on the α-value for the case of stable accretion disks. Up to now, the three-dimensional simulations have reached 8,232 yr and 3,416 yr of evolution for the case of a $M_{\rm core}$ = 120 and 240 $M_\odot$ collapse respectively. We will investigate the further evolution of these runs in the near future.

5 Summary and outlook

5.1 Summary of the project

The Ph.D. research project "Modeling the formation of massive stars" covers in nearly equal parts the development as well as the testing of a frequency dependent radiation transport module for three-dimensional hydrodynamics simulations (Sect. 2.5) and its application to the radiation pressure problem in the formation of massive stars (Chapt. 4). Until now, the radiation pressure problem in the formation of massive stars has been studied either in strongly constrained symmetry, with very low spatial resolution, or under the simplifying assumption of frequency averaged (gray) radiation transport and the Flux Limited Diffusion (FLD) approximation. Ray-tracing radiative transfer was considered only in one-dimensional hydrodynamics simulations thus far.

Yorke & Sonnhalter (2002) studied the problem in two-dimensional simulations in a monolithic quiescent collapse scenario very similar to our own approach. Their simulation series covers the collapse of axially and midplane symmetric pre-stellar cores of three different masses (30, 60, and 120 $M_\odot$) examined with both, gray as well as frequency dependent radiation transport. The frequency dependent radiation transport equation is solved under the FLD approximation. With this research project they emphasized the need for the consideration of the frequency dependence of the forming massive star's irradiation spectrum to reproduce the radiation pressure feedback more precisely. Nevertheless, no frequency dependent radiation hydrodynamics study related to massive star formation was carried out in higher than one dimension since the work by Yorke & Sonnhalter (2002). Unfortunately, they performed these simulations with very low spatial resolution. They used a two-dimensional nested grid in cylindrical coordinates with a spatial resolution of the best resolved region around the forming star at the center of 40, 80, and 160 AU in the 30, 60, and 120 $M_\odot$ case respectively. It is highly doubtful that this resolution fulfills the requirement of a converged numerical result. For comparison, we refer to our extensive convergence simulations discussed in Sects. 4.2.1 and 4.3.1. From this simulation series we conclude that we achieve good convergence for a spatial resolution of the central region of the core of 1.2 AU

or below. Secondly, they use a huge central sink cell with sizes of 40, 80, and 160 AU respectively, which is identical to the spatial resolution, and much larger than the dust condensation radius. In doing so, they exclude the important first interaction of the stellar irradiation with the accretion flow from the computational domain. As shown in our parameter scan of the radius of the central sink cell (Sect. 4.3.2), this leads to an artificially high radiative feedback and explains the unphysically abrupt end of the accretion phase they found in their simulations. Finally, the extension of their research at a broader scan of the parameter space as well as higher resolution or three-dimensional runs fails due to the excessive amount of CPU time needed for the frequency dependent radiation transport solver.

The usage of a faster frequency dependent radiation transport method in the context of massive star formation was first published by Edgar & Clarke (2003). They recommend a splitting of the radiation field, which is in a similar fashion also used in our newly developed radiation transport module. To the best of our knowledge, this technique was introduced to the astrophysical community in the circumstellar disk analysis of Murray et al. (1994). The simulations by Edgar & Clarke (2003) were performed in one-dimension only and focused on Bondi-Hoyle accretion onto a massive star.

Numerical radiation hydrodynamics research in the field of massive star formation were later performed by Krumholz et al. (2007, 2009a,b) in the picture of an initially turbulent pre-stellar core. The time and space dependent grid resolution of the adaptive mesh refinement (AMR) technique used allows them to study the fragmentation of such a turbulent core. In Krumholz et al. (2007) they focus on the fragmentation of the pre-stellar core, while Krumholz et al. (2009a) is dedicated to the accretion process onto massive stars. Their simulations confirm the fact that the stellar radiative feedback suppresses the fragmentation of the pre-stellar core due to an increase of the Jeans mass by stellar heating. As an important improvement on the work by Yorke & Sonnhalter (2002) they used an appropriate size for the sink cells and followed the evolution of the pre-stellar core from a resolution of 966 or 645 AU in the regions of lowest spatial resolution down to 7.5 or 10 AU in the different simulations respectively. The radiative force is not able to stop accretion from the disk onto the star in their simulations as it is in Yorke & Sonnhalter (2002). Although Krumholz et al. (2009a) stated that this is due to the absence of axisymmetry in their accretion disks, we strongly believe that this is due to the appropriate sink cell size they used contrary to Yorke & Sonnhalter (2002). Unlike the conclusions in Krumholz et al. (2009a), we show in our simulations that radiative pressure is not able to stop accretion even in a two-dimensional axisymmetric setup if the radiation physics at the dust condensation front are resolved correctly. In the simulations of Krumholz et al. (2007, 2009a) the determination of the radiative feedback on the accretion flow suffers strongly from the approximate radiation transport method they used. Both the simplification of a gray radiation transport as well as the FLD approximation meet the requirements of the fragmentation feedback on the large scales, but surely fail to compute the details of the first absorption region in the vicinity of a massive star. For comparison we refer to the frequency dependent radiation benchmark test presented in Sect. 2.5.2, in which we show that even a gray ray-tracing plus FLD method is unable to reproduce the temperature profile in a circumstellar disk. Secondly, Krumholz et al. (2007, 2009a) unfortunately do not follow the evolution of the pre-stellar core all the way to the total depletion of the gaseous mass reservoir, which would be necessary to achieve the final stellar configuration and masses as well as the understanding of the end of the accretion phase and potentially the origin of the cut-off in the initial mass function (IMF) of stellar clusters. To our knowledge, they stopped their longest-lasting simulation in Krumholz et al. (2009a) at 57 kyr. At this point in time, the most massive star is part of a still accreting binary system and has a mass of less than 50 $M_{\odot}$. Thirdly, we would encourage an even higher spatial resolution for an in-depth analysis of the radiative feedback of the forming

star on the accretion flow.

In our simulations, we obtain a spatial resolution of about $(1.27\ \mathrm{AU})^3$ in the best resolved regions in the neighborhood of the forming massive star even in three-dimensional runs. To achieve such a jump in spatial resolution compared to previous research studies we decided to constrain ourselves on the investigation of the radiation pressure problem of a single forming star, the so-called monolithic collapse scenario. The usage of a spherical coordinate system with a logarithmically increasing radial resolution towards the center is therefore the natural choice, especially keeping in mind that the usage of a spherical coordinate system matches the proceeding gravitational and radiative dynamics perfectly. For further details and visualizations of the numerical grid used please see Sect. 2.1. To guarantee a broad survey of the huge parameter space, we had to develop a fast, robust, and accurate frequency dependent radiation transport module for hydrodynamics simulations. See Sect. 2.5 for a detailed description of the technique, the accuracy tests performed, as well as a parallel benchmark test. We attained the appropriate speed of the solver by splitting the radiation field into the frequency dependent stellar irradiation and gray thermal dust emission. We proved the accuracy of this splitting paradigm in a standard radiation benchmark test for Monte-Carlo or ray-tracing solver methods (Pascucci et al. 2004) and demonstrated its validity in the setup of a central star, a flared circumstellar disk, and an envelope. Additionally, the speed and the robustness of the FLD solver used for the thermal dust emission is further supported by using a modern Krylov subspace solver for sparse and linear matrix equations. The so-called generalized minimal residual (GMRES) solver is integrated into the framework of our radiation transport module by the open source library PETSc (Balay et al. 2001, 2004). The parallel efficiency of the implicit solver provided by the library even exceeds our own expectations. As an example, for a benchmark problem growing with the number of processors used and 64 CPUs, we gain a speedup factor of about 60 for the module. The accuracy of the final module is a consequence of its frequency dependent ray-tracing part. Therefore, we conclude that such a splitting paradigm combined with a frequency dependent ray-tracer provides an efficient and accurate tool to study the radiative feedback of star formation.

The equations of compressible hydrodynamics (Sect. 2.2), including full tensor viscosity (Sect. 2.3) in the case of the two-dimensional simulations, are solved by the open source MHD code Pluto3 (Mignone et al. 2007). The development of the (missing) Poisson solver (Sect. 2.4) was a straight forward extension to the radiative diffusion problem and makes use of the identical GMRES solving technique. The implementation of recently computed evolutionary tracks for accreting high-mass stars (Hosokawa & Omukai 2008) and appropriate frequency dependent opacity tables obtained from Laor & Draine (1993), described in Sect. 2.7 and 2.6 respectively, complete the numerical framework of our simulation research project.

Despite the high resolution and the complex radiation physics considered in our simulations, we have performed multiple simulation series in one, two, and three dimensions to scan the parameter space of numerical quantities such as the spatial resolution and the size of the central sink cell as well as physical initial conditions, particularly the initial mass of the pre-stellar core. Please see table 4.1 on p. 83f. for an overview of all runs discussed in this thesis. Opposed to earlier numerical research in this field, we have taken a step forward in spatial resolution down to $(1.27\ \mathrm{AU})^3$ focused on the vicinity of the forming massive star in the center of the pre-stellar core. In addition, we follow the dynamics of the pre-stellar cores for an evolutionary time up to several 100 kyr, which is much longer than ever done before. The consideration of frequency dependent radiation transport combined with the high resolution of the dust condensation front and the long-term evolution of the collapsing pre-stellar core studied gives access to a completely new parameter space in the research field of

massive star formation. Such improvements lead automatically to interesting new results:

First of all, we verified the upper mass limit for spherically symmetric accretion flows found in previous analyses (cp. Sect. 4.2.3) and showed that it is in fact the thermal radiation pressure which yields the reversal of the accretion stream. Quantitatively, this limit strongly depends on the stellar evolutionary model, the dust model applied, and the radiation physics considered. For the recently published stellar evolutionary tracks of accreting high-mass stars by Hosokawa & Omukai (2008), the dust opacities of Laor & Draine (1993), and frequency dependent radiative feedback we found an upper limit of the final stellar mass of $M_* \leq 40$ M$_\odot$ when starting from an initially steep density profile of the collapsing pre-stellar core of $\rho \propto r^{-2}$.

Especially in higher dimension runs, we demonstrate the need in radiation hydrodynamics simulations involving a sink cell paradigm for the forming massive star(s) to include the dust condensation front into the computational domain. This guarantees the correct reproduction of the radiative feedback on the accretion flow (see Sect. 4.3.2). Accordingly, we approximate analytically the relative importance of the radiation pressure feedback during the evolution of the forming star and estimate an expression for the dust condensation radius of a star with a specific luminosity (or mass) for the stellar evolutionary tracks and the dust model applied in our simulations in Sect. 3.4 and 3.5. From these derivations we conclude that it is appropriate to use a sink cell radius equal or below a size of 10 AU. We argue in a code comparison run with the simulations of Yorke & Sonnhalter (2002), presented in Sect. 4.3.4, that disregarding this first absorption region yields an artificially high radiative feedback leading to the abrupt and early end of the accretion phase in their simulations.

In two-dimensional axially and midplane symmetric runs, we apply the α-parametrization by Shakura & Sunyaev (1973) for the shear viscosity to account for the loss of angular momentum in circumstellar accretion disks. Details and formulas of the viscosity model are described in Sect. 2.3. Recent analytical estimates by Vaidya et al. (2009) on the viscous regime of stable massive accretion disks based on the Toomre parameter and the cooling time of the disk yield a range for the α-value of $\alpha = 0.01$ up to $\alpha = 0.1$. We verify this result numerically in a sequence of simulations scanning the α-parameter from $\alpha = 0$ and $\alpha = 10^{-3}$ up to $\alpha = 1$ (see Sect. 4.3.3).

The final parameter scan of the two-dimensional simulations in Sect. 4.3.5 examines the influence of the initial mass of the pre-stellar core on the resulting star mass (the star formation efficiency). We found that the slow-down of the accretion flow due to the reduction of gravity by centrifugal forces in slowly rotating pre-stellar cores is compensated by the bypass of the radiative feedback due to the disk geometry when going to higher mass cores. The maintenance of a steady accretion stream onto and through the radiatively shielded parts of the circumstellar disk allows the star to grow far beyond the limit found in the spherically symmetric runs. The final stellar masses obtained in the different runs are 27.4, 56.5, and 92.6 M$_\odot$ for the case of an initial core mass of 60, 120, and 240 M$_\odot$ respectively. The central star of the still running 480 M$_\odot$ collapse simulation has reached a mass of more than 112 M$_\odot$ by now. These simulation results clearly disprove the statement in Krumholz et al. (2009a) that it is the non-axisymmetry of the stellar environment that allows the star to grow beyond 40 or 50 M$_\odot$. Also, we suggest that bipolar cavities support the reduction of radiative force on the accretion flow, but are not mandatory. The main mechanism is that the radiative flux from the heated dust grains leaves the disk preferably in the vertical direction through the optically thin atmosphere and hence does not counteract on the accretion flow in the radial direction.

Generally, the onset of disk formation and the launching of a radiatively driven bipolar outflow causes major changes to the morphology of the stellar environment. These dramatic events leave their marks in the accretion history of the forming massive star and let us split the long-term evolution of the collapsing system

into a sequence of evolutionary epochs. We present these evolutionary sequences in Sects. 4.2.4 and 4.3.6 for initially non-rotating and rotating pre-stellar cores respectively.

Our study of non-axially symmetric effects in high-resolution, three-dimensional simulations of the formation of massive stars provides access to a completely new parameter space. The dust condensation front of the massive star and its radiative feedback on the inner rim of the dusty part of the accretion disk is resolved down to a few AU (Sect. 4.4.1). The onset of a radiation pressure driven outflow in the bipolar direction consolidates the differentiation of the stellar environment into an optically thin envelope and a dense, radiatively shielded disk layer (Sect. 4.4.2). The usage of the spherical coordinate system down to the radius of the central sink cell of 10 AU allows us to reveal the onset of a gravitational instability during the formation of the circumstellar accretion disk at a radius of 15 AU (Sect. 4.4.3). Such a close-by instability, potentially leading to the formation of a binary, could not be resolved in previous numerical research, but matches the observation of spectroscopic binaries (Zinnecker 2003; Apai et al. 2007). A Toomre analysis of the resulting accretion disk confirms the onset of non-axially symmetric modes ($m \geq 1$) in the disk.

Contrary to the axial symmetric runs, no physical shear viscosity is specified in the three-dimensional simulations. The accretion rate during the formation of the circumstellar disk is purely driven by the gravitational instability. We found an evidentiary agreement of the mean accretion rate induced by this loss of angular momentum when comparing the results from three-dimensional simulations with the axially symmetric collapse models including an α-viscosity (Sect. 4.4.4).

Summing up, we want to point out that the so-called radiation pressure barrier represents only an upper mass limit for perfectly spherically symmetric accretion flows. The formation of a circumstellar accretion disk, which is a natural outcome of the angular momentum conservation of the collapsing core, provides the geometry needed to shield the radiative flux from the accretion flow even in axially symmetric disks. Gravitational instabilities acting in the massive circumstellar disk drive a sufficiently high accretion rate (of roughly 10^{-3} $M_\odot$ yr^{-1} in the case of a 120 $M_\odot$ pre-stellar core collapse) to overcome the remnant radiation pressure in the radial direction.

5.2 Outlook on the future of the project

The further usage of our newly developed tool in the research field of massive star formation offers quite a wide range of prospects. Straightforward subsequent simulation series will include a parameter scan of the initial rotation speed of the pre-stellar core as well as its initial density profile. We also aim for an ongoing improvement of the numerics and physics considered in our code. The most important implementation step in the near future is the development of an interface to a dedicated stellar evolution code to achieve a fully consistent evolution of the central massive star and its feedback on the environment. We have highlighted this need already in the discussion of the parameter scan of the initial mass of the non-rotating spherically symmetric pre-stellar cores (Sect. 4.2.3). The importance of solving both, the evolution of the star and of the environment, consistently grows with the increase of the mass of the pre-stellar core considered. This reflects the fact that the accretion luminosity dominates the nuclear fusion luminosity from the start of the collapse up to the onset of the strong radiation pressure feedback.

A potentially long-term task includes the further improvement of the radiation transport module by implementing ionization and scattering during the frequency dependent ray-tracing step to account for the multi-phase environment of massive stars. The equation of state for the hydrodynamics should then be treated as time and space dependent. To consider even more details of the radiative feedback at the dust condensation front also an improvement of the hydrodynamics part of our code (Pluto3) would be necessary: the motion of the dust grains could be decoupled from the gas motion and either calculated by an n-body integration step or computed in an extra advection step, the so-called two fluid approximation. Observational evidence for dust gas decoupling in proto-planetary disks around intermediate stars was recently presented in e.g. van der Plas et al. (2008) and Fedele et al. (2008).

Furthermore, effects of magnetic fields are not considered in our simulations so far. Pluto3 supports solving the corresponding equations of magneto-hydrodynamics including a five-wave MHD Riemann solver and resistivity with ohmic heating as well as an intrinsic background field. Ambi-polar diffusion is not implemented yet. As stated in Banerjee & Pudritz (2008), primordial magnetic fields of the pre-stellar core lead to an early formation of outflow channels. This effect would presumably enhance the 'loss' of radiation pressure even during the early epochs. Additionally, the so-called photon bubble instability in magnetized disks with high radiation densities is able to transport radiation in the vertical direction very efficiently (Gammie 1998; Begelman 2001; Turner et al. 2003; Blaes & Socrates 2003; Turner et al. 2005, 2007). Furthermore, a large-scale magnetic field penetrating a pre-stellar core perpendicular to the midplane of the disk will produce a flatter and larger accretion disk. To study the effect of the magneto-rotational instability inside such a magnetized accretion disk formed during the global collapse, a huge increase of spatial resolution is necessary and therefore seems to be quite a difficult task to accomplish in the next few years.

Fortunately, the growing community of Pluto users worldwide and especially at our home institute offers quite an interesting field of overlapping research projects. Related Ph.D. projects using the Pluto MHD code at the Max-Planck Institute for Astronomy deal with the dynamics of outflows from young massive stars (by B. Vaidya), the formation of relativistic jets from slow disk-winds (by O. Porth), the simulation of planet-disk interactions with the objective to study different migration mechanisms of proto-planets (by A. L. Uribe), and the study of the magneto-rotational instability in circumstellar disks with non-ideal MHD and dynamical resistivity calculation (by M. Flock, see also Flock et al. (2009)).

Acknowledgements

During the time of my Ph.D. at the Max Planck Institute for Astronomy I received help from numerous people. First of all, I have benefited from a team of supervisors, thus I would like to thank ...

Hubert Klahr for answering my questions related to numerical hydrodynamics (and sometimes on 'real' physics, which quickly brought back the joy into the scientific workplace life).

Henrik Beuther for explaining to me all the beauty of the exciting research field of massive star formation as well as the really interesting key issues from an observer's perspective.

Cornelis 'Kees' Dullemond for giving me an understanding of radiation transport and for his permanent effort to break me of my habit to keep scientific text as short as possible.

Thomas Henning for giving the proper directions in time and suggestions of great importance.

Altogether they gave me the support I needed but allowed me great flexibility to make my own decisions, carry out and realize my own concepts.

In the context of supervision, I am really thankful for the Ph.D. Advisory Committee (PAC) at the Max Planck Institute for Astronomy as well as the thesis committee of the International Max Planck Research School for Astronomy and Cosmic Physics at the University of Heidelberg (IMPRS-HD). The opinion of the members (H. Beuther, M. Camenzind, C. Dullemond, T. Henning, C. Bailer-Jones, H. Klahr, H.-J. Rösner) on the progress of the project and the ideas of scientists from outside were always helpful and motivating.

Over the years, I learned a lot from Heidelberger colleagues in- and outside of the institute, particularly in the 'massive star formation splinter meetings', encouraged mostly by Henrik Beuther and Jürgen Steinacker. Furthermore, I gained much from fruitful discussions with Willy Kley, Mordecai-Mark Mac Low, Ralph Pudritz, Neal Turner, and Harold Yorke. In this regard, I received extra financial support, namely travel money, from IMPRS-HD and the Heidelberg Graduate School for Fundamental Physics (HGSFP).

I would like to thank Christian Fendt, the coordinator of the IMPRS-HD graduate school, for the huge amount of time he invests to solve the student's problems in his always friendly and open-minded manner.

Computer simulations for this thesis were performed at the RIO cluster and the PIA cluster at the computing center of the Max Planck Society in Garching. I wish to thank the system administrator Christian Guggenberger for his rapid replies and uncomplicated help with the everyday problems and more tricky challenges. Numerous day-to-day discussions with my colleague Mario Flock as well as E-Mail support by Andrea Mignone, the main developer of the Pluto code, helped me first to work, then to understand, and finally to enrich our version of the Pluto MHD code. I also have to mention the great and fast support of the PETSc (Portable, Extensible Toolkit

for Scientific Computation) mailing list, especially of Barry Smith. The performance of the solver finally achieved is simply due to his patient (and mostly physicist-friendly) explanations. The developed code and/or this thesis contain in part data from Takashi Hosokawa (the stellar evolutionary tracks) and Johannes Schönke (the double-check comparison data in the setup of Yorke & Sonnhalter (2002)). Thanks for their prompt and plentiful supply.

I thank Andrej Bicanski, Mario Flock, and especially Cassandra Fallscheer for the proof-reading of the thesis.

Not least, I want to express my gratitude to Gerhard Hoffmann for his ability to motivate me during the frustrating beginnings of the project (before I decided to switch to the Pluto code) and for his essential help on every computing related problem.

Thanks to my beloved partner Svenja for keeping me balanced amongst others due to her catching zest for life and a persistent lack of interest in computational astrophysics.

A

Constants, units, and variables

Constants

Variable	Value [cgs]	Name
a	$7.5657 * 10^{-15}$ erg cm^{-3} K^{-4}	radiation constant
c	$2.99792458 * 10^{+10}$ cm s^{-1}	speed of light in vacuum
G	$6.67428 * 10^{-8}$ cm^3 g^{-1} s^{-2}	graviational constant
k	$1.3807 * 10^{-16}$ erg K^{-1}	Boltzmann constant
N_A	$6.0221 * 10^{+23}$ mol^{-1}	Avogadro constant
$R_\mathrm{gas} = k * N_\mathrm{A}$	$8.31432 * 10^{+7}$ g cm^2 s^{-2} mol^{-1} K^{-1}	universal gas constant
$\sigma_\mathrm{SB} = 0.25 * a * c$	$5.670 * 10^{-5}$ erg cm^{-2} s^{-1} K^{-4}	Stefan-Boltzmann constant

Units

Unit	Value [cgs]
AU	$1.49597870691 * 10^{+13}$ cm
$\mathrm{R}_\odot$	0.004652 AU = $6.9593 * 10^{+10}$ cm
pc	206265.0 AU = $3.0857 * 10^{+18}$ cm
yr	$31,557,600$ s
$\mathrm{M}_\odot$	$1.9891 * 10^{+33}$ g
$\mathrm{L}_\odot$	$5.679 * 10^{+22}$ erg s^{-1}
Jy	10^{-23} erg cm^{-2} $\left(\mathrm{s}^{-1}\ \mathrm{Hz}^{-1}\right)$

Variables

Variable	Name
$\vec{d}$	acceleration
A	Poisson matrix
α	dimensionless viscosity parameter
B	Planck function
c_s	sound speed
c_V	specific heat capacity
D	radiative diffusion coefficient
δ_{ij}	Kronecker symbol
E	total energy density
E_int, E_thermal	internal energy density
E_kin	kinetic energy density
E_pot	gravitational energy density
E_R	diffuse radiation energy density
η	shear viscosity coefficient
η_b	bulk viscosity coefficient
$\vec{f}$	total force density
$\vec{f}_\mathrm{cent}$	centrifugal force density
$\vec{f}_\mathrm{grav}$	gravitational force density
$\vec{f}_\mathrm{pressure}$	thermal force density
$\vec{f}_\mathrm{rad}$	radiative force density
$\vec{F}$	diffuse radiation flux
$\vec{F}_*$	stellar radiation flux
$\vec{F}_\mathrm{tot}$	total radiation flux
γ	adiabatic index
H	local pressure scale height
H/R	aspect ratio of the disk
J	Jeans number
κ_R	Rosseland mean opacity
κ_P	Planck mean opacity
κ, κ_ν	frequency dependent opacity
L_acc	accretion luminosity
L_nuc	nuclear luminosity
L_*	total stellar luminosity
λ	diffuse radiation flux limiter ∧ wavelength
λ_J	Jeans length
M_core	initial mass of pre-stellar core
M_*	stellar mass
$M(r)$	mass inside the radius r
$M_\mathrm{dust}/M_\mathrm{gas}$	dust to gas mass ratio
μ	mean molecular weight
n	number of processors

Variable	Name
N	total number of grid cells
N_r	number of grid cells in the radial dir.
N_θ	number of grid cells in the polar dir.
N_ϕ	number of grid cells in the azimuthal dir.
$\dot{M}$	accretion rate
ν	frequency or dynamical viscosity
Ω	azimuthal angular velocity
Ω_0	initial rotation speed
Ω_K	keplerian angular velocity
p	gas pressure
Π	viscosity tensor
ϕ	azimuthal angle
Φ	total gravitational potential
Φ_*	stellar gravitational potential
Φ_sg	gravitational potential of gas mass
Q	Toomre parameter
Q^+	source terms of diffuse radiation energy
r	spherical radius
R	cylindrical radius ∧ dimensionless diffusion parameter
Δr	length of the grid cell in the radial dir.
$r\,\Delta\theta$	length of the grid cell in the polar dir.
$r\,\sin(\theta)\,\Delta\phi$	length of the grid cell in the azimuthal dir.
r_cent	centrifugal radius
r_cond	dust condensation radius
r_min	radially inner computational boundary
r_max	radially outer computational boundary
R_*	stellar radius
ρ	gas density
ρ_0	floor value of gas density
t	time
t_ff	free fall time
t_orbit	orbital period
T	temperature
T_*	effective stellar temperature
T_evap	local dust evaporation temperature
Δt	time step
τ	optical depth
θ	polar angle
$\vec{u}$	gas velocity
u_K	keplerian velocity

List of Figures

1.1 Observations of the star-forming region ISOSS J19357+1950. The image shows the 24 μm map of a part of the large scale cloud and the overlaid contours show the 450 μm emission visualizing the embedded cores. The extent of these cores in SMM1 North and SMM2 is roughly given by their FWHM of 0.3 to 0.4 pc (Author: Hennemann et al. (2008)). 14

1.2 The compact star cluster R136a embedded in the center of the Tarantula nebula (Author: ESO). 15

1.3 1.3 mm ^{12}CO(2−−1) outflow contours (red and blue) and the 1.3 mm dust continuum contours (gray) of the high-mass proto-stellar object IRAS 18151-1208 (Author: Fallscheer et al., *in prep*). 16

1.4 Rotated and zoomed-in image of Fig. 1.3 showing 1.3 mm dust continuum of IRAS 18151-1208, a high mass proto-stellar object at a distance of 3000 pc. A single pixel has an edge length of 300 AU. The integrated flux in the area is 0.4 Jy and the peak flux is 41 mJy. The image has linear scaling. The ellipse in the lower left corner is the beam size of the SMA. A large scale flattened structure perpendicular to the outflow direction (here vertically aligned) is revealed.
(Author: Fallscheer et al., *in prep*) 17

1.5 Schematic view of radiative forces onto the accretion flow in spherical symmetry. The radiative feedback is divided into direct stellar irradiation and secondary photons. 18

1.6 Schematic view of the different components of radiation pressure acting in an axially symmetric circumstellar disk geometry. 19

2.1 Two-dimensional grid (128 x 32) in spherical coordinates with logarithmically increasing radial resolution, a central sink cell of radius $r_{\rm min}$ = 10 AU and an outer boundary at $r_{\rm max}$ = 0.1 pc. . 25

2.2 Two-dimensional grid (64 x 16) in spherical coordinates with logarithmically increasing radial resolution, a central sink cell of radius $r_{\rm min}$ = 10 AU and an outer boundary at $r_{\rm max}$ = 0.1 pc. In three-dimensional simulations the resolution of this grid is retained and expanded in the azimuthal direction with the same angular resolution as in the polar direction. 25

2.3 Schematic setup of the one-dimensional self-gravity test: A sphere of iso-density ρ_0 with an outer radius r_2 and an empty inner hole of radius r_1. 29

2.5 Schematic setup of the two-dimensional static self-gravity test: An oblate (disk-like) spheroid with semiaxes $a = b > c$ in the x, y, and z direction respectively. 30

2.4 Static one-dimensional test results. Vertical lines mark the inner and outer sphere radii.
Upper panel: Resulting numerical (dots) and analytical solution (solid line) of the gravitational potential.
Lower panel: Deviation of the numerical solution from the analytic one. 31

2.6 Static two-dimensional test results along the long semiaxis in the *x*-*y* plane. The surface of the spheroid is reached at 100 AU.
Upper panel: Numerical (dots) and analytical solution (solid line) of the gravitational potential for the highest resolution run.
Lower panel: Deviation of the numerical solution from the analytic one at different resolutions. 33

2.7 Static two-dimensional test results along the short symmetry semiaxis in the z direction. The surface of the spheroid is reached at 50 AU.
Upper panel: Numerical (dots) and analytical solution (solid line) of the gravitational potential for the highest resolution run.
Lower panel: Deviation of the numerical solution from the analytic one at different resolutions. 34

2.8 Static three-dimensional test results along the x axis (100 AU).
Upper panel: Resulting numerical (dots) and analytical solution (solid line) of the gravitational potential for the highest resolution run.
Lower panel: Deviation of the numerical solution from the analytic one at different resolutions. 36

2.9 Static three-dimensional test results along the y axis (50 AU).
Upper panel: Resulting numerical (dots) and analytical solution (solid line) of the gravitational potential for the highest resolution run.
Lower panel: Deviation of the numerical solution from the analytic one at different resolutions. 37

2.10 Static three-dimensional test results along the z axis (25 AU).
Upper panel: Resulting numerical (dots) and analytical solution (solid line) of the gravitational potential for the highest resolution run.
Lower panel: Deviation of the numerical solution from the analytic one at different resolutions. 38

2.11 Schematic flow chart of the radiation module for a static problem. Exponents declare the timestep number n. The timestep used is denoted by $dt^n = t^n - t^{n-1}$. 42

2.12 Frequency dependent opacities $\kappa(\nu)$ in tabulated form from Laor & Draine (1993). 43

2.13 Radial cut through the temperature profile in the midplane in the most optically thin case ($\tau_{550\mathrm{nm}} = 0.1$).
Upper panel: Radial temperature slope of the gray irradiation routine (solid line) and the Monte-Carlo based comparison code (dots).
Lower panel: Differences between the two codes in percent. 50

2.14 Radial cut through the temperature profile in the midplane in the most optically thick case ($\tau_{550\mathrm{nm}} = 100$) without diffusion.
Upper panel: Radial temperature slope of gray irradiation (dashed line), frequency dependent irradiation (solid line) and the Monte-Carlo routine in the "one-photon-limit" (dots).
Lower panel: Deviations of the gray (dashed line) and frequency dependent (solid line) method from the Monte-Carlo code in percent. 51

2.15 Radial cut through the temperature profile in the midplane in the most optically thick case ($\tau_{550\mathrm{nm}} = 100$) including irradiation and Flux Limited Diffusion.
Upper panel: Radial temperature profile of gray irradiation plus Flux Limited Diffusion (dashed line), frequency dependent irradiation plus Flux Limited Diffusion (solid line) and the corresponding Monte-Carlo routine (dots).
Lower panel: Deviations of the gray (dashed line) and frequency dependent run (solid line) from the Monte-Carlo code in percent. 52

2.16 Polar cut through the temperature profile at $r = 2$ AU of the frequency dependent irradiation plus FLD run for the most optically thick case ($\tau_{550\mathrm{nm}} = 100$), reproducing the turnover point at a polar angle of $\theta \approx 19°$ above the midplane from the optically thin envelope to the optically thick disk region.
Solid line: Frequency dependent irradiation plus Flux Limited Diffusion.
Dots: Data from the corresponding Monte-Carlo comparison run.
The vertical axis covers only a small temperature range from 200 to 260 Kelvin to better visualize the small deviations. 53

2.17 Radial cut through the radiative force profile at a polar angle of $\theta \approx 27°$ from the midplane (to display the onset of the radiative force at the transition from the optically thin envelope to the optically thick disk) in the most optically thick case ($\tau_{550\mathrm{nm}} = 100$):
Upper panel: Radial radiative force profile of frequency dependent irradiation plus FLD (solid line with squares) as well as the results from the Monte-Carlo routine (solid line).
Lower panel: Deviations of purely stellar (dotted line with triangles) and stellar plus thermal radiative force (solid line with squares) from the Monte-Carlo run in percent. 55

2.18 Radial profile of the optical depth τ_R through the midplane in the most optically thick case ($\tau_{550\mathrm{nm}} = 100$). The optical depth $\tau_R(r) = \kappa_{\mathrm{R}}(T)\,\rho(r)\,\Delta r$ as a function of the Rosseland mean opacity is integrated from the outer edge of the disk towards the center. The plot clearly shows the low optical depth for the thermal component of the radiation field especially in the outer part of the disk, which results in an underestimation of the temperature in the transition region at roughly 200 AU due to the FLD approximation. 56

2.19 Regarding the frequency dependence of stellar irradiation feedback: frequency dependent opacities $\kappa(\nu)$ from Draine & Lee (1984), Planck mean opacities $\kappa_{\mathrm{P}}(T_*)$ and stellar black body spectrum $B_\nu(\nu, T_*)$ as functions of frequency ν. The usage of gray (frequency averaged) opacities results in an overestimation of the optical depth in the infrared part and an underestimation of the absorption in the ultraviolet part of the stellar spectrum. 57

2.20 Measured speedup factors $S = t_2/t_n$ and efficiencies $E = t_2/(t_n n) = S/n$ for a fixed (squares) and a growing (stars) problem size. 59

2.21 Radiative supercritical shock: Resulting density, pressure, velocity and temperature distributions at four different snapshots in time. Dashed lines represent the adiabatic runs, solid lines the radiative ones. The time snapshots are taken (from left to right) at 860 s, 4,000 s, 7,500 s, and 13,000 s after launching. Mostly horizontal lines at the lower border of the graphics refer to the initial setup. The snapshots at 4000 s are additionally marked by circles for every 10^{th} grid cell to illustrate the resolution used. The spatial axes are retranslated into the non-moving frame used in the visualization by Ensman (1994) for the sake of comparison. 62

2.22 Radiative subcritical shock: Resulting density, pressure, velocity and temperature distributions at five different snapshots in time. Dashed lines represent the adiabatic runs, solid lines the radiative ones. The time snapshots are taken (from left to right) at 350 s, 5,400 s, 17,000 s, 28,000 s, and 38,000 s after launching. The snapshot at 350 s shows approximately the initial setup. The snapshots at 4000 s are additionally marked by circles for every 10^{th} grid cell to illustrate the resolution used. The spatial axes are retranslated into the non-moving frame used in the visualization by Ensman (1994) for the sake of comparison. 63

2.23 Calculated Rosseland κ_{R} and Planck κ_{P} mean opacities as a function of temperature. The possible evaporation of dust grains at high temperatures (and/or low densities) is considered in the dust to gas mass ratio $M_{\text{dust}}/M_{\text{gas}}$ of each grid cell, see also Fig. 2.24. 64

2.24 Transition slope of the local dust to gas mass ratio as a function of temperature due to evaporation of dust grains for two different gas densities. 65

2.25 Polynomial fits to the nuclear fusion luminosity as a function of the stellar mass as calculated by Hosokawa & Omukai (2008). The data points represent an evolving massive star with an accretion rate of 10^{-3} $\text{M}_\odot$ yr^{-1}. The mass range was split into two regimes above and below 5.5 $\text{M}_\odot$ (at the sharp bend) and each part is fitted by a polynomial up to 10^{th} order (solid lines). 67

3.1 Equilibrium state of the stellar gravitational $\vec{f}_{\text{grav}}$, the thermal pressure $\vec{f}_{\text{pressure}}$, and the centrifugal $\vec{f}_{\text{cent}}$ force acting in a circumstellar disk perpendicular to the azimuthal direction. . . . 70

3.2 Derivation of the free fall time from Kepler's law of orbiting planets. 73

3.3 Sub-Eddington and Super-Eddington regimes for a massive star with a constant accretion rate of $\dot{M}_* = 10^{-3}$ $\text{M}_\odot$ yr^{-1} and $\dot{M}_* = 10^{-5}$ $\text{M}_\odot$ yr^{-1} respectively. The solid line marks the result if only the nuclear fusion luminosity of the forming star is taken into account. The dashed line identifies the result for the total luminosity (nuclear fusion plus accretion luminosity). 78

3.4 Dust condensation radius r_{cond} of a massive star as a function of the stellar luminosity for a high as well as a low value of the corresponding gas density of the stellar environment respectively. Stellar irradiation is the only heating process which is taken into account for the estimation of the dust condensation radius. The corresponding mass of the star at the upper axis is taken from the stellar evolutionary tracks by Hosokawa & Omukai (2008) for a forming star with a constant accretion rate of $\dot{M}_* = 10^{-3}$ $\text{M}_\odot$ yr^{-1}. 80

4.1 The formation of a self-gravitating ring instability in the massive accretion disk. The snapshot is taken at 7,820 yr of evolution of a collapsing pre-stellar core of 120 $\text{M}_\odot$. The radius of the ring is roughly 15 AU. The numerical grid is highlighted by dashed lines. The central sink cell is treated as transparent. 81

4.2 Volume rendering of an axially symmetric pre-stellar core of 120 $\text{M}_\odot$ at 10 kyr after the start of the collapse. The image shows the entire computational domain with a radius of 0.1 pc. The gas density is rendered in a logarithmic scale from 10^{-18} g cm^{-3} up the maximum value. The low-density gas $\left(\rho < 10^{-18} \text{ g cm}^{-3}\right)$ of the envelope is visualized in black. The positive radial velocity highlighting the radiation pressure driven outflow is rendered in a linear scale from dark blue to light blue and white. 82

4.3 Stellar mass M_* as a function of time for five different resolutions of the spherically symmetric pre-stellar core collapse simulations with an inner sink cell radius of $r_{\rm min} = 80$ AU. The number of grid cells N_r varies from 16 to 256, corresponding to a size of the smallest grid cell of $(\Delta r)_{\rm min} = 33.2$ AU down to 1.75 AU respectively. 88

4.4 Stellar mass M_* as a function of time for four different resolutions of the spherically symmetric pre-stellar core collapse simulations with an inner sink cell radius of $r_{\rm min} = 1$ AU. The number of grid cells N_r varies from 32 to 256, corresponding to a size of the smallest grid cell of $(\Delta r)_{\rm min} = 0.36$ AU down to 0.04 AU respectively. 89

4.5 Accretion rate (upper panel) and deviations of the accretion rates from the simulation run with the smallest sink cell radius of $r_{\rm min} = 1$ AU (lower panel) as a function of time for four different sizes of the spherical sink cell. The resolution of the grid is fixed to $\Delta r = 1$ AU up to a radius of $r = 100$ AU and decreases logarithmically afterwards in all simulations performed. 90

4.6 Accretion rate $\dot{M}$ as a function of the actual stellar mass M_* for four different initial pre-stellar core masses of $M_{\rm core} = 60\,{\rm M}_\odot$ up to $480\,{\rm M}_\odot$. The spherically symmetric accretion models yield an upper mass limit of the final star of $M_*^{\rm 1D} \leq 40\,{\rm M}_\odot$. 92

4.7 Snapshot of radial force densities in the innermost core region taken from the collapse simulation of a $M_{\rm core} = 120\,{\rm M}_\odot$ pre-stellar core at 20 kyr corresponding to a proto-stellar mass of about $M_* = 25\,{\rm M}_\odot$. Due to the superior radiative force the spherically symmetric accretion models yield an upper mass limit of the final star of $M_*^{\rm 1D} \leq 40\,{\rm M}_\odot$. 93

4.8 Integrated global potential, kinetic, and thermal energy as a function of time. Vertical lines identify transitions between different evolutionary epochs of the pre-stellar core collapse. . . . 94

4.9 Density $\rho(r)$, velocity $u(r)$ and temperature $T(r)$ as a function of radius r for the case of a 60 $\rm M_\odot$ pre-stellar core collapse at seven snapshots in time, representing distinguishable epochs of the evolution of the one-dimensional collapse. 100

4.10 Stellar mass M_* (upper panel) and accretion rate $\dot{M}_*$ (lower panel) as a function of time for five different resolution to determine the adequate number of grid cells necessary for the axially and midplane symmetric pre-stellar core collapse simulations. 102

4.11 Stellar mass M_* (upper panel) and accretion rate $\dot{M}_*$ (lower panel) as a function of time for different radii $r_{\rm min}$ of the central sink cell in the axially and midplane symmetric collapse simulation of a 60 $\rm M_\odot$ pre-stellar core. 105

4.12 Stellar mass M_* (upper panel) and accretion rate $\dot{M}_*$ (lower panel) as a function of time for different radii $r_{\rm min}$ of the central sink cell in the axially and midplane symmetric collapse simulation of a 120 $\rm M_\odot$ pre-stellar core. 106

4.13 Stellar mass M_* as a function of time for six different values of the strength of the α-viscosity in the axially and midplane symmetric pre-stellar core collapse simulations. 108

4.14 The resulting stellar mass M_* (upper panel) and accretion rate $\dot{M}_*$ (lower panel) from a collapse of a 60 $\rm M_\odot$ pre-stellar core with an outer radius of $r_{\rm max} = 0.1$ pc and an inner sink cell radius of $r_{\rm min} = 80$ AU using three different codes. 110

4.15 Accretion rate $\dot{M}_*$ as a function of actual stellar mass M_* for four different initial core masses $M_{\rm core}$ = 60 $M_\odot$, 120 $M_\odot$, 240 $M_\odot$, and 480 $M_\odot$. The two-dimensional axially and midplane symmetric collapse models of slowly rotating pre-stellar cores clearly break through the upper mass limit of the final star of $M_*^{\rm 1D} \leq 40$ $M_\odot$ found in previous spherically symmetric accretion models. 111

4.16 Total force density $|f_{tot}(r)|$ (upper panel) as well as density $\rho(r)$ and radial velocity $u_r(r)$ (lower panel) as a function of radius r through the disk's midplane. The snapshot was taken at 60 kyr after start of the simulation, corresponding to a central stellar mass of roughly 40 $M_\odot$. The individual force densities along this line of sight through the total and the inner core region are displayed in Figs. 4.17 and 4.18. 113

4.17 Gravity, centrifugal, and thermal pressure force as a function of radius through the disk's midplane. The snapshot was taken at 60 kyr after start of the simulation, corresponding to a central stellar mass of roughly 40 $M_\odot$. The radiative and viscous forces are orders of magnitude smaller than the illustrated ones, but become important in the inner disk region, where the stronger forces are in equilibrium. The radiative and viscous force densities along this line of sight through the inner core region are displayed in Fig. 4.18. 114

4.18 Viscous and radiative force density of the inner core region as a function of radius through the disk's midplane. The snapshot was taken at 60 kyr after start of the simulation, corresponding to a central stellar mass of roughly 40 $M_\odot$ 114

4.19 Total force density $|f_{tot}(r)|$ (upper panel) as well as density $\rho(r)$ and radial velocity $u_r(r)$ (lower panel) as a function of radius r at 30° above the disk's midplane. The snapshot was taken at 60 kyr after start of the simulation, corresponding to a central stellar mass of roughly 40 $M_\odot$. The individual force densities along this line of sight through the total and the inner core region are displayed in Figs. 4.20 and 4.21. 115

4.20 Gravity, centrifugal, thermal pressure, and radiative forces as a function of radius at 30° above the disk's midplane. The snapshot was taken at 60 kyr after start of the simulation, corresponding to a central stellar mass of roughly 40 $M_\odot$. The individual force densities along this line of sight through the inner core region are displayed in Fig. 4.21. 116

4.21 Gravity, centrifugal, thermal pressure, radiative, and viscous force density of the inner core region as a function of radius at 30° above the disk's midplane. The snapshot was taken at 60 kyr after start of the simulation, corresponding to a central stellar mass of roughly 40 $M_\odot$. . . 116

4.22 Global kinetic, thermal, and potential energy as a function of time for the collapse of a rotating axially and midplane symmetric pre-stellar core of 60 $M_\odot$. Vertical lines in the image of the first two free fall times (upper panel) identify transitions between distinguished evolutionary epochs of the collapse dynamics. The lower panel shows the long-term evolution of the energies up to 5 free fall times. 118

4.23 The onset of the radiation pressure driven bipolar outflow in the vicinity of the massive star (left panel) and its large scale extent at a more evolved state (right panel). The color coding in both panels is divided into the visualization of the temperature (colors on the left) and the density (colors on the right). Due to the different length scale of both panels also the color coding extents over different magnitudes. A separation into rotation and outflow dominated regions is highlighted by the $u_r = u_\phi$ iso-contour. Both images are from an axially and midplane symmetric collapse simulation of a 240 $M_\odot$ pre-stellar core. 120
4.24 Mass flux on the large scales (left image) as well as the accretion flow onto the star and the circumstellar disk (right image). The blue colored region on the right panel implies a radial velocity in the outward direction. Both images represent a snapshot of an axially and midplane symmetric collapse simulation of a 240 $M_\odot$ pre-stellar core at a highly evolved state at 30 kyr. 122
4.25 Gas density (colors), dust to gas mass ratio (contours) as well as the discretization (the numerical grid) in the innermost 25 AU. The transition from the dust depleted regions to the dusty disk midplane is resolved roughly within six grid cells. The image represents a slice through the x-z-plane of a three-dimensional collapse simulation of a 240 $M_\odot$ pre-stellar core after 1,500 yr. 124
4.26 Radial velocity (colors on left half), gas density (colors on right half) and dust to gas mass ratio (contours) at the onset of the radiation pressure driven outflow formation. The images represent the x-z plane of the inner region from a three-dimensional collapse simulation of a 240 $M_\odot$ core at 1.0, 1.1, 1.2, 1.3, and 1.4 kyr. No deviations from axial symmetry have occurred in the circumstellar disk up to this epoch. 126
4.27 Face on view of the x-y-plane of the central core region shortly after the onset of a non-axial symmetric mode in the accretion disk. The image shows the logarithmically color-coded gas density as well as contour lines according to the Truelove criterion for Poisson solvers. The separation of the unstable ring from the centrally forming massive star is 15 AU. 128
4.28 Mean Toomre parameter of the accretion disk formed during the 120 $M_\odot$ pre-stellar core collapse as a function of the radius. The accretion disk forms an instability in the three-dimensional simulation at roughly 15 AU from the central star. The snapshot is calculated at 7.92 kyr after the onset of the collapse. The massive star in the center has a mass of about 18.5 $M_\odot$ at this point in time. 129
4.29 Stellar mass growth and accretion rate during the 120 $M_\odot$ pre-stellar core collapse as a function of time.
Dashed line: Two-dimensional simulation using a constant α-viscosity description.
Dotted line: Two-dimensional simulation without α-viscosity.
Solid line: Three-dimensional simulation yielding the formation of a gravitational instability in the accretion disk at roughly 7.8 kyr. 130
4.30 Zoom-in of Fig. 4.29: Accretion rate at the onset of instability as a function of time.
Dashed line: Two-dimensional simulation using a constant α-viscosity description.
Dotted line: Two-dimensional simulation without α-viscosity.
Solid line: Three-dimensional simulation yielding the formation of a gravitational instability in the accretion disk at roughly 7.8 kyr. 131

List of Tables

2.1 Resolution of different radiation hydrodynamics simulations of a collapse of a slowly rotating massive pre-stellar core. The simulations of Yorke & Sonnhalter (2002) were performed on a non-adaptive two-dimensional grid in cylindrical coordinates with three nested levels. The given resolution (Δr x Δz) of Yorke & Sonnhalter (2002) represents the case of a $M_{\rm core}$ = 60 $M_\odot$ pre-stellar core. The resolution for the lower mass $M_{\rm core}$ = 30 $M_\odot$ collapse was a factor of two better. The resolution for the higher mass $M_{\rm core}$ = 120 $M_\odot$ collapse was a factor of two worse. The simulations of Krumholz et al. (2007, 2009a) were performed on a three-dimensional cartesian adaptive mesh refinement (AMR) grid. The given resolution (Δx x Δy x Δz) represents the lowest and highest resolution during the simulation. The resolution of our own grids in spherical coordinates is given in units of arc length (Δr x ($r\ \Delta\theta$) x ($r\ \sin(\theta)\ \Delta\phi$)) in the midplane. . . 24

2.2 Monte-Carlo comparison runs: The overview table of the comparison runs performed with the Monte-Carlo based code RADMC contains the corresponding optical depth of the test case and the configuration of the Monte-Carlo code used. 48

2.3 Overview of runs using the proposed approximate radiation transport: The table contains the corresponding optical depth of the test case and the Monte-Carlo run, which is used for comparison (see also table 2.2 and the corresponding comparison Sects.). Furthermore the applied radiative modules (gray or frequency dependent absorption as well as possible diffusion) of our proposed approximate radiation transport method and the corresponding sections, in which these modules and the final results are discussed, are given. The deviations in the resulting temperature slopes of the approximate radiation transport from the corresponding Monte-Carlo comparison run are shown in the lower row. 48

4.1 Overview of massive pre-stellar core collapse simulations presented. The table is structured in blocks of topics and their corresponding sections. For each run the label, the dimension, the number of used grid cells, the resolution of the best resolved regions in the midplane $(\Delta r \text{ x } r\ \Delta\theta \text{ x } r\ \sin(\theta)\ \Delta\phi)_{\min}$, the size of the central sink cell $r_{\min}$ (the location of the inner boundary of the computational domain), the strength of the so-called α-viscosity if applied (cp. Sect. 2.3), the initial mass of the pre-stellar core M_{core}, its corresponding free fall time t_{ff} (cp. Sect. 3.2), and the period of evolution simulated t_{end} are given. If results of a single run are used in several sections, only a link to the final evaluation is given. Simulations, which were at least performed until the accretion rate onto the central star has dropped to zero, are marked by an additional '$*$' in the t_{end} column; most of these runs contain no mass in the computational domain anymore. Simulations, which are still running, are marked by an additional '+' in the t_{end} column. 83
4.1 Continuation of table 4.1 on p. 83. 84
4.1 Continuation of table 4.1 on p. 83f. 85
4.2 Overview of default physical initial conditions used in the collapse simulations of massive pre-stellar cores. 86

Bibliography

Apai, D., Bik, A., Kaper, L., Henning, T., & Zinnecker, H. 2007, ApJ, 655, 484

Balay, S., Buschelman, K., Eijkhout, V., et al. 2004, PETSc Users Manual, Tech. rep., revision 2.1.5

Balay, S., Buschelman, K., Gropp, W. D., et al. 2001, PETSc Web page, http://www.mcs.anl.gov/petsc

Balay, S., Gropp, W. D., McInnes, L. C., & Smith, B. F. 1997, Birkhäuser Press, 163

Balbus, S. A. 2003, ARA&A, 41, 555

Balbus, S. A. & Hawley, J. F. 1991, ApJ, 376, 214

Bally, J. 2008, in: Massive Star Formation: Observations confront Theory, ed. H. Beuther, H. Linz, T. Henning, 387, 158

Bally, J. & Zinnecker, H. 2005, AJ, 129, 2281

Banerjee, R. & Pudritz, R. E. 2008, in: Massive Star Formation: Observations confront Theory, ed. H. Beuther, H. Linz, T. Henning, 387, 216

Bate, M. R. 2009a, MNRAS, 392, 1363

Bate, M. R. 2009b, MNRAS, 392, 590

Begelman, M. C. 2001, ApJ, 551, 897

Beltrán, M. T., Cesaroni, R., Codella, C., et al. 2006, Nat, 443, 427

Beltrán, M. T., Cesaroni, R., Neri, R., et al. 2004, ApJ, 601, L187

Beltrán, M. T., Cesaroni, R., Neri, R., et al. 2005, A&A, 435, 901

Beuther, H., Churchwell, E. B., McKee, C. F., & Tan, J. C. 2007, in: Protostars and Planets V, ed. B. Reipurth, D. Jewitt, & K. Keil, 165

Beuther, H. & Sridharan, T. K. 2007, ApJ, 668, 348

Beuther, H., Sridharan, T. K., & Saito, M. 2005a, ApJ, 634, L185

Beuther, H. & Walsh, A. J. 2008, ApJ, 673, L55

Beuther, H., Walsh, A. J., Thorwirth, S., et al. 2008, A&A, 481, 169

Beuther, H., Zhang, Q., Sridharan, T. K., & Chen, Y. 2005b, ApJ, 628, 800

Bik, A., Kaper, L., Hanson, M. M., & Smits, M. 2005, A&A, 440, 121

Bik, A., Kaper, L., & Waters, L. B. F. M. 2006, A&A, 455, 561

Bik, A., Lenorzer, A., Thi, W. F., et al. 2008, in: Massive Star Formation: Observations confront Theory, ed. H. Beuther, H. Linz, T. Henning, 387, 78

Bik, A. & Thi, W. F. 2004, A&A, 427, L13

Birkmann, S. M., Krause, O., Hennemann, M., et al. 2007, A&A, 474, 883

Birkmann, S. M., Krause, O., & Lemke, D. 2006, ApJ, 637, 380

Bjorkman, J. E. & Wood, K. 2001, ApJ, 554, 615

Black, D. C. & Bodenheimer, P. 1975, ApJ, 199, 619

Blaes, O. M. & Socrates, A. 2003, ApJ, 596, 509

Bodenheimer, P. 1995, ARA&A, 33, 199

Bodenheimer, P., Yorke, H. W., Rozyczka, M., & Tohline, J. E. 1990, ApJ, 355, 651

Boley, A. C., Durisen, R. H., Nordlund, Å., & Lord, J. 2007, ApJ, 665, 1254

Bondi, H. & Hoyle, F. 1944, MNRAS, 104, 273

Bonnell, I. A. & Bate, M. R. 2002, MNRAS, 336, 659

Bonnell, I. A., Bate, M. R., & Zinnecker, H. 1998, MNRAS, 298, 93

Bonnell, I. A., Vine, S. G., & Bate, M. R. 2004, MNRAS, 349, 735

Cai, K., Durisen, R. H., Boley, A. C., Pickett, M. K., & Mejía, A. C. 2008, ApJ, 673, 1138

Cai, K., Durisen, R. H., & Zhu, Z. 2009, AJ, 213, 313

Cesaroni, R., Felli, M., Testi, L., Walmsley, C. M., & Olmi, L. 1997, A&A, 325, 725

Cesaroni, R., Galli, D., Lodato, G., Walmsley, C. M., & Zhang, Q. 2007, in: Protostars and Planets V, ed. B. Reipurth, D. Jewitt, & K. Keil, 197

Cesaroni, R., Neri, R., Olmi, L., et al. 2005, A&A, 434, 1039

Chini, R., Henning, T., & Pfau, W. 1991, A&A, 247, 157

Chini, R., Hoffmeister, V. H., Nielbock, M., et al. 2006, ApJ, 645, L61

Davis, C. J., Moriarty-Schieven, G., Eislöffel, J., Hoare, M. G., & Ray, T. P. 1998, AJ, 115, 1118

de Koter, A., Heap, S. R., & Hubeny, I. 1998, ApJ, 509, 879

Draine, B. T. & Lee, H. M. 1984, ApJ, 285, 89

Dullemond, C. P. & Dominik, C. 2004, A&A, 421, 1075

Dullemond, C. P. & Turolla, R. 2000, A&A, 360, 1187

Edgar, R. & Clarke, C. 2003, MNRAS, 338, 962

Edgar, R. & Clarke, C. 2004, MNRAS, 349, 678

Efstathiou, A. & Rowan-Robinson, M. 1990, MNRAS, 245, 275

Ensman, L. 1994, ApJ, 424, 275

Fedele, D., van den Ancker, M. E., Acke, B., et al. 2008, A&A, 491, 809

Flock, M., Dzyurkevich, N., Klahr, H. H., & Mignone, A. 2009, eprint arXiv, 0906, 5516

Fromang, S., Balbus, S. A., Terquem, C., & Villiers, J.-P. D. 2004a, ApJ, 616, 364

Fromang, S., Balbus, S. A., & Villiers, J.-P. D. 2004b, ApJ, 616, 357

Gammie, C. F. 1998, MNRAS, 297, 929

Harvey, P. M., Campbell, M. F., Hoffmann, W. F., Thronson, H. A., & Gatley, I. 1979, ApJ, 229, 990

Hawley, J. F. & Balbus, S. A. 1991, ApJ, 376, 223

Hayes, J. C., Norman, M. L., Fiedler, R. A., et al. 2006, ApJS, 165, 188

Hennemann, M., Birkmann, S. M., Krause, O., & Lemke, D. 2008, A&A, 485, 753

Hennemann, M., Birkmann, S. M., Krause, O., et al. 2009, ApJ, 693, 1379

Henning, T. 2008, in: Massive Star Formation: Observations confront Theory, ed. H. Beuther, H. Linz, T. Henning, 387, 452

Henning, T., Lapinov, A., Schreyer, K., Stecklum, B., & Zinchenko, I. 2000, A&A, 364, 613

Ho, P. T. P. & Haschick, A. D. 1986, ApJ, 304, 501

Hoffmeister, V. H., Chini, R., Scheyda, C. M., et al. 2006, A&A, 457, L29

Hosokawa, T. & Omukai, K. 2008, in: Massive Star Formation: Observations confront Theory, ed. H. Beuther, H. Linz, T. Henning, 387, 255

Isella, A. & Natta, A. 2005, A&A, 438, 899

Jijina, J. & Adams, F. C. 1996, ApJ, 462, 874

Kahn, F. D. 1974, A&A, 37, 149

Kellogg, O. D. 1929, Barman Press, New York

Keto, E. R. 2003, ApJ, 599, 1196

Keto, E. R., Ho, P. T. P., & Reid, M. J. 1987, ApJ, 323, L117

Klahr, H. H. & Bodenheimer, P. 2003, ApJ, 582, 869

Klahr, H. H., Henning, T., & Kley, W. 1999, ApJ, 514, 325

Klahr, H. H. & Kley, W. 2006, A&A, 445, 747

Klessen, R. S., Krumholz, M. R., & Heitsch, F. 2009, eprint arXiv, 0906, 4452

Kley, W. 1989, A&A, 208, 98

Kratter, K. M. & Matzner, C. D. 2006, MNRAS, 373, 1563

Kratter, K. M. & Matzner, C. D. 2008, in: Massive Star Formation: Observations confront Theory, ed. H. Beuther, H. Linz, T. Henning, 387, 262

Krumholz, M. R., Klein, R. I., & McKee, C. F. 2005a, in: Protostars and Planets V, ed. B. Reipurth, D. Jewitt, & K. Keil, 8271

Krumholz, M. R., Klein, R. I., & McKee, C. F. 2007, ApJ, 656, 959

Krumholz, M. R., Klein, R. I., McKee, C. F., Offner, S. S. R., & Cunningham, A. J. 2009a, eprint arXiv, 0901, 3157

Krumholz, M. R., Klein, R. I., McKee, C. F., Offner, S. S. R., & Cunningham, A. J. 2009b, Science, 323, 754

Krumholz, M. R., McKee, C. F., & Klein, R. I. 2005b, ApJ, 618, L33

Landau, L. D. & Lifshitz, E. M. 1987, Pergamon Press, Oxford, 552

Laor, A. & Draine, B. T. 1993, ApJ, 402, 441

Larson, R. B. & Starrfield, S. 1971, A&A, 13, 190

Laughlin, G. P. & Bodenheimer, P. 1994, ApJ, 436, 335

Lebouteiller, V., Bernard-Salas, J., Brandl, B., et al. 2008, ApJ, 680, 398

Levermore, C. D. & Pomraning, G. C. 1981, ApJ, 248, 321

Lodato, G. 2008, New Astr. Rev., 52, 21

Lyder, D. A., Belton, D. S., & Gower, A. C. 1998, AJ, 116, 840

McKee, C. F. & Ostriker, E. C. 2007, ARA&A, 45, 565

McKee, C. F. & Tan, J. C. 2003, ApJ, 585, 850

Mignone, A., Bodo, G., Massaglia, S., et al. 2007, ApJS, 170, 228

Mihalas, D. & Mihalas, B. W. 1984, Oxford University Press. Dover Publications edition 1999.

Murray, S. D., Castor, J. I., Klein, R. I., & McKee, C. F. 1994, ApJ, 435, 631

Nakano, T. 1989, ApJ, 345, 464

Nielbock, M., Chini, R., Hoffmeister, V. H., et al. 2007, ApJ, 656, L81

Pascucci, I., Wolf, S., Steinacker, J., et al. 2004, A&A, 417, 793

Patel, N. A., Curiel, S., Sridharan, T. K., et al. 2005, Nat, 437, 109

Pillai, T., Wyrowski, F., Hatchell, J., Gibb, A. G., & Thompson, M. A. 2007, A&A, 467, 207

Pollack, J. B., Hollenbach, D., Beckwith, S., et al. 1994, ApJ, 421, 615

Ramsey, A. 1961, Cambridge University Press, Cambridge, 40

Rathborne, J. M., Jackson, J. M., Chambers, E. T., et al. 2005, ApJ, 630, L181

Rathborne, J. M., Jackson, J. M., & Simon, R. 2006, ApJ, 641, 389

Rathborne, J. M., Jackson, J. M., Zhang, Q., & Simon, R. 2008, ApJ, 689, 1141

Rathborne, J. M., Johnson, A. M., Jackson, J. M., Shah, R. Y., & Simon, R. 2009, ApJS, 182, 131

Rodón, J. A., Beuther, H., Megeath, S. T., & van der Tak, F. F. S. 2008, A&A, 490, 213

Saad, Y. & Schultz, M. H. 1986, SIAM Journal on Scientific Statistical Computation, 7, 856

Schreyer, K., Henning, T., van der Tak, F. F. S., Boonman, A. M. S., & van Dishoeck, E. F. 2002, A&A, 394, 561

Schreyer, K., Semenov, D., Henning, T., & Forbrich, J. 2006, ApJ, 637, L129

Shakura, N. I. & Sunyaev, R. A. 1973, A&A, 24, 337

Shu, F. H., Lizano, S., & Adams, F. C. 1987, in: Star forming regions, ed. M. Peimbert, J. Jugaku, 115, 417

Sincell, M. W., Gehmeyr, M., & Mihalas, D. 1999a, Shock Waves, 9, 391

Sincell, M. W., Gehmeyr, M., & Mihalas, D. 1999b, Shock Waves, 9, 403

Spitzer, L. 1942, ApJ, 95, 329

Steinacker, J., Chini, R., Nielbock, M., et al. 2006, A&A, 456, 1013

Strang, G. 1968, SIAM Journal on Numerical Analysis, 5, 506

Toomre, A. 1964, ApJ, 139, 1217

Torrelles, J. M., Ho, P. T. P., Moran, J. M., Rodriguez, L. F., & Canto, J. 1986, ApJ, 307, 787

Truelove, J. K., Klein, R. I., McKee, C. F., et al. 1997, ApJL, 489, L179

Tscharnuter, W. M. & Boss, A. P. 1993, in: Protostars and Planets III, ed. E. H. Levy, J. I. Lunine, 921

Tscharnuter, W. M., Schönke, J., Gail, H. P., & Lüttjohann, E. 2009, eprint arXiv, 0903, 4580

Turner, N. J., Blaes, O. M., Davis, S. R., & Socrates, A. 2003, AJ, 7, 660

Turner, N. J., Blaes, O. M., Socrates, A., Begelman, M. C., & Davis, S. R. 2005, ApJ, 624, 267

Turner, N. J., Quataert, E., & Yorke, H. W. 2007, ApJ, 662, 1052

Turner, N. J. & Stone, J. M. 2001, ApJS, 135, 95

Vaidya, B., Fendt, C., & Beuther, H. 2009, eprint arXiv, 0906, 5493

van der Plas, G., van den Ancker, M. E., Fedele, D., et al. 2008, A&A, 485, 487

van Leer, B. 1979, JCP, 32, 101

Vasyunina, T., Linz, H., Henning, T., et al. 2009, A&A, 499, 149

Vázquez-Semadeni, E., Ballesteros-Paredes, J., Klessen, R. S., & Jappsen, A. K. 2008, in: Massive Star Formation: Observations confront Theory, ed. H. Beuther, H. Linz, T. Henning, 387, 240

Wang, W. X. 1988, Journal of Physics A: Mathematical and General, 21, 4245

Wang, W. X. 1989, Journal of Physics A: Mathematical and General, 22, 1459

Whitney, B. A. 2005, Nat, 437, 37

Wolfire, M. G. & Cassinelli, J. P. 1986, ApJ, 310, 207

Wolfire, M. G. & Cassinelli, J. P. 1987, ApJ, 319, 850

Wu, Y., Zhang, Q., Chen, H.-R., et al. 2005, AJ, 129, 330

Yang, S., Durisen, R. H., Cohl, H. S., Imamura, J. N., & Toman, J. 1991, Icarus, 91, 14

Yorke, H. W., Bodenheimer, P., & Laughlin, G. P. 1995, ApJ, 443, 199

Yorke, H. W. & Krügel, E. 1977, A&A, 54, 183

Yorke, H. W. & Sonnhalter, C. 2002, ApJ, 569, 846

Zel'Dovich, Y. B. & Raizer, Y. P. 1967, New York, Academic Press. Dover Publications edition 2002

Zhang, Q. 2005, in: Massive star birth: A crossroads of Astrophysics, ed. R. Cesaroni, M. Felli, E. Churchwell, and C. M. Walmsley, 227, 135

Zhang, Q. & Ho, P. T. P. 1997, ApJ, 488, 241

Zhang, Q., Hunter, T. R., Beuther, H., et al. 2007, ApJ, 658, 1152

Zhang, Q., Hunter, T. R., & Sridharan, T. K. 1998, ApJ, 505, L151

Zhang, Q., Hunter, T. R., Sridharan, T. K., & Ho, P. T. P. 2002, ApJ, 566, 982

Zinnecker, H. 2003, in: A Massive Star Odyssey: From Main Sequence to Supernova, ed. K. van der Hucht, A. Herrero, and C. Esteban, 212, 80

Zinnecker, H. & Yorke, H. W. 2007, ARA&A, 45, 481